VON KARMAN INSTITUTE FOR FLUID DYNAMICS
AERONAUTICS AND AEROSPACE DEPARTMENT

UNIVERSITÉ DE LIÈGE
DEPARTMENT OF AEROSPACE AND MECHANICAL ENGINEERING

Aerothermodynamics of Pre-Flight and In-Flight Testing Methodologies for Atmospheric Entry Probes

Cover: QARMAN full scale testing at VKI Plasmatron. (art by Can Akyurek)

Thesis presented by Isil Sakraker in order to obtain the degree of "Doctor of Philosophy in Aerospace Engineering", Université de Liège, February 2016.

Supervisors: Prof. Olivier Chazot (von Karman Institute for Fluid Dynamics, Belgium) and Prof. Gaëtan Kerschen (Université de Liège, Belgium)

Doctoral Committee:

Prof. Paolo Barbante (Politecnico di Milano, Italy)
Prof. Olivier Chazot (von Karman Institute for Fluid Dynamics, Belgium)
Dr. Ali Guelhan (Deutsches Zentrum fr Luft- und Raumfahrt Cologne, Germany)
Prof. Gaetan Kerschen (Université de Liège, Belgium)
Prof. Thierry Magin (Université de Liège and von Karman Institute for Fluid Dynamics, Belgium)
Prof. Pierre Rochus (Centre Spatial de Liege and Université de Liège, Belgium)
Prof. Vincent Terrapon (Université de Liège, Belgium)

A selection of doctoral theses published by the von Karman Institute:

Development and applications of the Light Extinction Spectroscopy technique for characterizing small particles
(I. T. Horváth, Université Libre de Bruxelles, Ecole Polytechnique de Bruxelles, October 2015)

Numerical simulation of aerothermal flows through ablative Thermal Protection Systems
(P. Schrooyen, Université catholique de Louvain, November 2015)

Material response characterization of low-density ablators in atmospheric entry plasmas
(B. Helber, Vrije Universiteit Brussel, January 2016)

Semi-analytical methodologies for airfoil noise prediction
(L. Dantas de Santana, KU Leuven, September 2015)

Longshot hypersonic wind tunnel flow characterization and boundary layer stability investigations
(G. Grossir, Université Libre de Bruxelles, École Polytechnique de Bruxelles, July 2015)

Adjoint-based error estimation for adaptive Petrov-Galerkin finite element methods. Application to the Euler equations for inviscid compressible flows
(S. D'Angelo, Université Libre de Bruxelles, École Polytechnique de Bruxelles, March 2015)

Experimental investigation of cavitation in a safety relief valve using water. Extension to cryogenic fluids
(J. Pinho, Université Libre de Bruxelles, École Polytechnique de Bruxelles, April 2015)

A full catalogue of publications is available from the library.

Aerothermodynamics of Pre-Flight and In-Flight Testing Methodologies for Atmospheric Entry Probes

Keywords: experimental aerothermodynamics, high enthalpy flows, plasma, CubeSats

D/2016/0238/669, T. Magin, Editor-in-Chief
Published by the von Karman Institute for Fluid Dynamics with permission.

ISBN 978-2-87516-102-4

“Ce qui embellit le désert, c’est qu’il cache un puits quelque part...
What makes the desert beautiful, is that somewhere it hides a well...”

Le Petit Prince - Antoine de Saint-Exupéry

Road trippin' on Işılmobile

Işılmobile is my imaginary converted cozy van where I have lived for the past years. It is painted with all the colors of nature and I have traveled with all very lovely people. The initial destination, I thought, was a place called "PhD", which I figured has been the road itself.

I passed through the jungles and deserts, cities and villages, rivers and mountains; most of the time bumpy roads, lots of climbing and certainly breath taking.

Although the green Işılmobile runs mostly on solar power, a refuel was needed especially on cloudy days. Luckily, Olivier Chazot stations were all over the place, welcoming me together with the associates Gaetan Kerschen, Thierry Magin, Alessandro Turchi, Vincent Leroy, Damien Le Quang and Zuheyr Alsalihi.

I was often traveling with a circus company called Plasmatron. We, then, all wore big shirts with flames and did kickass on-the-road-performances where people watched us with special goggles. Our leader was the almighty Pascal Collin; and us, the crew, Bernd, Damien, Alan, Francesco at the gorgeous stage, Plasmatron. I enjoyed each gig very much guys! Thank you!

Then, there was this lego baby, its name is QARMAN. Yes yes, with a Q. She wore a funny hat made of wine stopper and a skirt. We brought her to life together with Cem, Vincent, Ertan, Thorsten, Gilles and Paride. Soon we will have to tell her goodbye on her journey to space... How cool is that??

Once every year, I passed through different cities called IPPWs. So many wonderful people lived there. They showed me many new destinations and made me see so many new horizons. My sincere thanks to Ozgur Karatekin, Ethiraj Venkatapathy, Bernard Bienstock, Anita Sengupta, Michelle Munk and Ali Guelhan for showing me the cool tricks.

Every now and then, I took young hitchhikers onboard; Pedro, Roger, Eray, Deniz, Pablo, Thomas.. We exchanged many good stories along our ride. When the police stopped for checking the documents, the genius bass player Dr. Kemal and the reputable Prof. Erdal were always there to pass me the correct papers, all the way from US and Singapore. Thanks!

Sometimes, we pulled over in different cities to take a swim in the weirdest beaches, did picnics and partied around a camp fire under the stars. It was wonderful to have you around Sophia, Timoté, Barış, JB, Ceyhun, Cansev, Alessia, Elvan, Fabrizio, Clara, Chiara, Imre, Ugur, Marina, Bernd, Ertan, Alessandro-and-Chiara, Elif, Sinan, Dilay and Tugba.. JB, there are still a lot of magic trails in the world, we gotta hurry!

And sometimes, I needed a pit stop, which often happened in the cows-y areas of Leuven. The rakı-table was always prepared and long discussions were in front of us. It was delicious, Hakan, Erkan, Erdal and Nedim.

Have I told you that a bunch of beautiful upside down dwellers was continuously riding and playing on top of Işılmobile? Haein, Geoff, Tadeusz, Christina, Tatjana, Zsuzsanna.. I very often found myself upside down, a lot in danger too indeed, and it was so much fun! Namaste my dears, forever..

I would also like to mention the people, who walked with me to the departure point of my journey. Dr. Cem Asma, Prof. Fırat Oğuz Edis, Prof. Cihat Baytaş, Prof. Rüstem Arslan and Prof. Okşan Çetiner. And of course, thank you for the parting gift Hyunwoo Krassilchikoff.

Işılmobile could never be built if my parents, Tülay and Tahsin, had not provided me the tools and the how-to recipes since I was a little girl. Likewise, never without the support and fun of my forever-little brother Deniz. İyi ki varsınız!

All along the way, a warm bright beam of sunshine, my haku Seçkin traveled with me. He helped me changing so many torn tires, gave a hand while I was covered with the black dust fixing the engine. With all my heart, thank you..

It is now time to take off to new mysterious adventures.

To all lovely people, with gratitude..

Işıl
Brussels, 2015

Abstract

Spacecraft, returning back to Earth, experience a very harsh environment during the encounter with the particles of the atmosphere. One of the major issues of the atmospheric entry is the extreme aerodynamic heating and the exothermic chemical reactions due to the gas-surface interaction at hypersonic free stream velocities. There is a constant effort by the space agencies to increase the understanding of the re-entry flight dynamics to optimize the spacecraft and especially its thermal protection system design. During the design process, ground tests and numerical tools are extensively used for their low cost and controlled environment abilities. However, real flight tests are indispensable for ground test and numerical tools validation. Due to high costs, such missions are rarely launched and thus there is an increasing interest in small affordable entry probes. Such platforms, once matured enough, may serve as an easily accessible tool to produce experimental data.

It is the aim of this dissertation to propose tools to improve ground test capabilities and on the other hand to present the design, and using the developed tools, the testing of aerothermodynamic experimental payloads to collect flight data with a small entry probe. QARMAN (QubeSat for Aerothermodynamic Research and Measurements on AblatioN) is a triple unit CubeSat with ablative and ceramic thermal protection systems. It will perform an atmospheric entry with 7.7 km/s and a peak heat flux of 1.7 MW/m^2. The aim of the in-flight experiments is to retrieve real flight data on ablator efficiency (temperature, pressure, recession) and temperature-pressure measurements for transition on the side panels.

The peculiar squared geometry of QARMAN led to the development of a Flight-to-Ground Duplication methodology accounting for spacecraft geometries. It allows duplicating fully the stagnation region of a spacecraft with an arbitrary geometry in subsonic plasma wind tunnels. As a requirement of this methodology, free stream characterization techniques, specifically enthalpy measurement techniques are introduced. Experimental and numerical databases are built.

A thorough ablation characterization campaign in VKI Plasmatron is conducted to provide input for building material response models. The cork P50 ablator is studied in terms of surface and sub-surface temperatures, emissivity, mass loss, char-pyrolysis layers, outgassing species and recession and swelling profiles. Similar in-flight experiments are proposed for QARMAN flight for in-depth temperature and pressure. Methods to build models for advanced data treatment are proposed.

A full picture of post-flight analysis strategy is described for each study to relate the ground tools and flight data.

Contents

List of Figures

List of Tables

Nomenclature

Roman Symbols

A_{ul}	Einstein coefficient	[s^{-1}]
C_p	Isobaric specific heat	[J kg^{-1}K^{-1}]
C_v	Isochoric specific heat	[J kg^{-1}K^{-1}]
Da	Damköhler number	[-]
du/dx ; β	Velocity gradient	[s^{-1}]
E	Energy level	[cm^{-1}]
g	Degeneracy	[-]
h	Total enthalpy per unit mass	[J kg^{-1}]
h	Planck constant	[m^{2} kg s^{-1}]
J_{ul}	Emission intensity	[mW cm^{-3} sr^{-1}]
K	Zoby constant	[g cm$^{-3/2}$ s^{-1} atm$^{-1/2}$]
k	Thermal conductivity	[Wm^{-1}K^{-1}]
k_B	Boltzmann constant	[m^{2} kg s^{-2} K^{-1}]
Kn	Knudsen number	[-]
k_p	Barker effect	[-]
L	Radiance	[W sr^{-1} m^{-2}]
Le	Lewis number	[-]
$\dot{m}$	Mass flow rate	[g s^{-1}]
P	Power	[W]
Pr	Prandtl number	[-]
p	Pressure	[Pa]
$\dot{q}$	Heat flux	[W m^{-2}]
R	Radius	[m]
Re	Reynolds number	[-]
$\dot{s}$	Recession rate	[m s^{-1}]
t	Time	[s]
T	Temperature	[K]
u	Velocity in x-direction	[m s^{-1}]
V	Velocity	[m s^{-1}]
v	Velocity in y-direction	[m s^{-1}]
y_i	Mole fraction of species i	[-]

Greek Symbols

β	Velocity gradient	[s^{-1}]

γ	Recombination Efficiency	[-]
γ	Specific heat ratio	[-]
Δ	Shock standoff distance	[m]
δ	Finite boundary layer thickness	[m]
ϵ	Emissivity	[-]
λ	Wavelength	[nm]
μ	Dynamic viscosity	[Pa s]
ρ	Density	[kg m^{-3}]
σ	Stefan-Boltzmann constant	[W m^{-2} K^{-4}]
τ	Duration	[s]
τ	Characteristic time	[s]

Subscript

0	Total
∞	Free stream
c	Char
$chem$	Chemical
$cond$	Conduction
D	Dissociation
$diff$	Diffusion
dyn	Dynamic
e	Edge
eff	Effective, equivalent
g	Gas
H	Hypersonic
l	Lower
m	Model
rad	Radiation
S	Subsonic
s	Torch exit
s	Solid
u	Upper
v	Virgin
w	Wall

Acronyms

AeroSDS	Aerodynamic Stabilization and De-orbiting System
BL	Boundary Layer
CFD	Computational Fluid Dynamics
CJC	Cold Junction Compensation

COTS	Components Off The Shelf
DAQ	Data AcQuisition system
EM	Engineering Model
ESA	European Space Agency
FM	Flight Model
ICP	Inductively Coupled Plasma
ISS	International Space Station
LHTS	Local Heat Transfer Simulation
LTE	Local Thermochemical Equilibrium
MNT	Modified Newtonian Theory
NDP	Non Dimensional Parameter
PCB	Printed Circuit Board
QARMAN	Qubesat for Aerothermodynamic Research and Measurements on AblatioN
TC	ThermoCouple
TP	Thermal Plug
TPM	Thermal Protection Material
TPS	Thermal Protection System
XPL	eXperimental PayLoad
VKI	von Karman Institute for Fluid Dynamics

Chapter 1.

Introduction

One of the major goals of the aerospace research field is to increase the safety and efficiency of the manned and unmanned space missions whether they travel to or from another planet or wander around the Earth. A very big challenge of such travels is the encounter with the atmosphere of a planet. When spacecraft approaches the atmosphere at hypervelocity, it comes across a very harsh environment: a completely different stability regime than in continuum atmosphere, telecommunication blackout and extreme temperatures due to aerodynamic heating as well as exothermic chemical reactions at the surface of the spacecraft. These phenomena are studied under the research field of the *aerothermodynamics*. Hence, spacecraft have to be protected by Thermal Protection Systems (TPS). When designing and sizing TPS, material engineers must be very conservative to ensure the safety of the crew or the payload since the aerothermochemical environment and its physics are complex to be accurately predicted. This leads to inefficiently over-sized designs with reduced available mass and volume budgets that would otherwise be used for crew, propellant, payload, and scientific instrumentation.

An overview of hypersonic aerothermodynamics is given in this section as an introduction to the physics and the terminology used in this thesis. Then the phenomena and the investigation tools are briefly discussed in order to place the motivation behind the developed testing methodology and the in-flight experiment in the big picture.

1.1. Hypersonic Space Flight - Atmospheric Entry

1.1.1. Basics of Aerothermodynamics

Hypersonic flows are traditionally known as flows faster than Mach 5. There are three main applications being atmospheric entry from planetary orbits (also known as “re-entry”), hypersonic cruise and launch vehicles. The cruises and launchers involve propulsion systems while the re-entry is the mission phase to slow down the vehicle. The characteristics of the hypersonic flow environment highly depend on the mission profile, thus vehicle type and application. Our focus in this study is the blunt re-entry vehicles of a variety mission concepts such as Earth returns from orbit or other bodies, and landing on other planets or moons with atmosphere. Specifically, a small blunt entry probe mission to Earth atmosphere will be discussed.

At hypersonic velocities, a strong detached bow shock appears in front of the blunt vehicle. Consequently, the temperatures become very high in the regions behind the shock wave. The internal energy of the gas molecules are excited resulting in a plasma flow where dissociation and ionization occur. When modeling hypersonic flows, one should take into account the effects of dominant physico-chemistry in different regions of the flow. Therefore, it is important to classify and define the general characteristics of the gas during a spacecraft's re-entry.

Spacecraft are subjected to different flow regimes along their entry trajectory from orbit to the planet's surface. Fig. 1.1 depicts examples of different entry trajectories. The rarefied "free molecular regime", "continuum regime" and "transitional regime" between the two, are distinguished by Knudsen number range. At high altitudes, the atmosphere is so rarefied, thus low density, that mesoscopic scales should be taken into account with a statistical approach. The conventional no-slip wall condition is no longer valid since there is a big temperature and velocity gradient between the wall and the adjacent fluid particle. However, since this "jump" at the wall is a function of both the Knudsen number and vehicle size, no strict separation can be done between continuum and non continuum regimes. In fact, the re-entry problem is a combination of all since the Knudsen number can vary in the shock region and the afterbody. The flow in the stagnation region can be in continuum while the wake of the entry capsule can be in rarefied regime due to fluid mechanical phenomena. Fig. 1.2 shows the applicability of different flow models (equations) at different Knudsen numbers.

For re-entry flows, it is very important to include the chemistry of the flow in the models in order to define the governing equations. The shock shape and standoff distance are highly affected by chemistry since the temperature, thus density, depends on these phenomena. Although the direct effect of chemistry in pressure is smaller, the integrated effect on the pitching moments, lift and drag force can be high [4]. The active high temperature chemical phenomena in hypersonic flows are often called "real gas effects" by many authors (including Bertin [5], Cambel et al. [6] etc.). This term sometimes creates confusion since according to Anderson [7] a real gas means only the environment where the intermolecular forces are important, mainly at high pressures and low temperatures. The state of the gases at high pressures can be divided in two groups: real gas and perfect gases. However the focus of this thesis is the high temperature effects and the high pressure cases will not be further discussed. At high temperatures, the gases can behave thermally or calorically perfect or imperfect. These models take into account the dissociation and ionization. For air, above 800 K, due to the excitation of vibrational states, the specific heats of the gas, C_v and C_p, are no longer constant (and the specific heat ratio, γ, equal to 1.4 in the case of "calorically perfect gas") but are functions of temperature, which

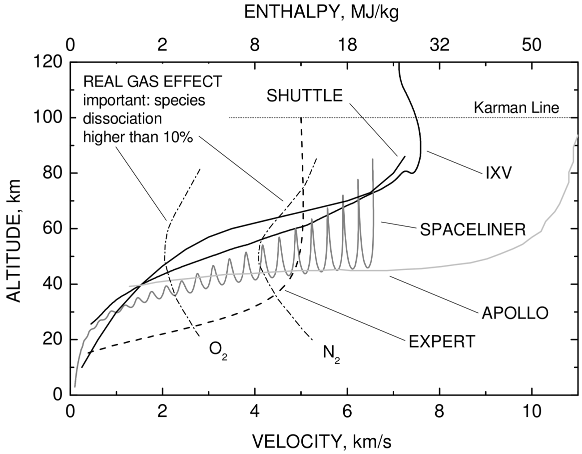

Figure 1.1.: Different Earth entry trajectories taken from [1] and the boundaries Nitrogen/Oxygen molecule dissociation by [2].

become "thermally perfect gas". At even higher temperatures, dissociation and ionization processes occur and γ becomes a function of two thermodynamic properties, e.g pressure and temperature. It should be noted that the dissociation of oxygen molecule starts between 2000 - 4000 K and the nitrogen molecule above 9000 K.

Imagine the particles in a flow field through a bow shock. They undergo chemical reactions and exchange energy through different translational, vibrational, rotational and electronic modes. All these processes happen when the particles are colliding with each other. Obviously, the collision chances are higher in high density than at high altitudes where the density is lower. Two characteristic times can be defined as follows:

- **Characteristic time of the flow,** τ_{flow}, also known as "transit time" by [5], is the time the particles take to cross a characteristic length of the fluid.
- **Characteristic time of chemistry,** τ_{chem}, also known as "accommodation time" is the time required for a process to accommodate itself to the local conditions. It is determined by the collision frequency.

The characteristic times can be used to define the Damköhler number:

$$Da = \frac{\tau_{flow}}{\tau_{chem}} \tag{1.1}$$

Then the two extremes can be given in terms of Damköhler number

1. Equilibrium: $\tau_{chem} \ll \tau_{flow}$, Da $\rightarrow \infty$

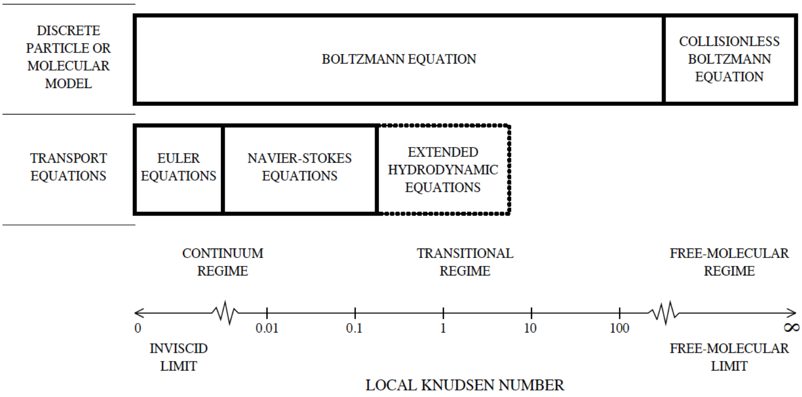

Figure 1.2.: Knudsen number limits [3].

2. Frozen: $\tau_{chem} > \tau_{flow}$, Da $= 0$
3. Non-Equilibrium: All intermediate cases, also known as “finite chemistry”

At higher densities passed the shock wave where sufficient collisions occur, the energy equilibrates between different modes. Knowing two thermodynamic properties is enough to define the thermodynamic state and chemical composition of the gas. This is called *thermochemical equilibrium* and there is only one temperature which is $T = T_{translational} = T_{vibrational} = T_{rotational} = T_{electronic}$. It may also happen that there is not enough collisions to achieve equilibrium by the time the particles move away, such as crossing a shock or a rapid expansion. In non-equilibrium conditions, the chemical composition of the gas can affect the dynamic behavior as mentioned previously. So, when modeling non-equilibrium flows, one should take into account different energy modes and their own temperatures [9].

A practical approximation when modeling the hypersonic flow is the “local equilibrium and non-equilibrium”. The gas is in local thermodynamic equilibrium (LTE) when the internal energies of each species follow a Boltzmann distribution at the local translational temperature [5] and when the reaction rates are faster than the characteristic time of the flow and the chemical species concentrations are function of only two local intensive thermodynamic variables.

During re-entry, the gas particles passes through areas with different properties between the bow shock and the wall as sketched in Fig. 1.3. The region right after the shock, namely the shock layer, is called the relaxation zone and the flow is at thermal and chemical non-equilibrium. The flow is then in LTE until the edge of the boundary layer. Unlike other flow regimes, the

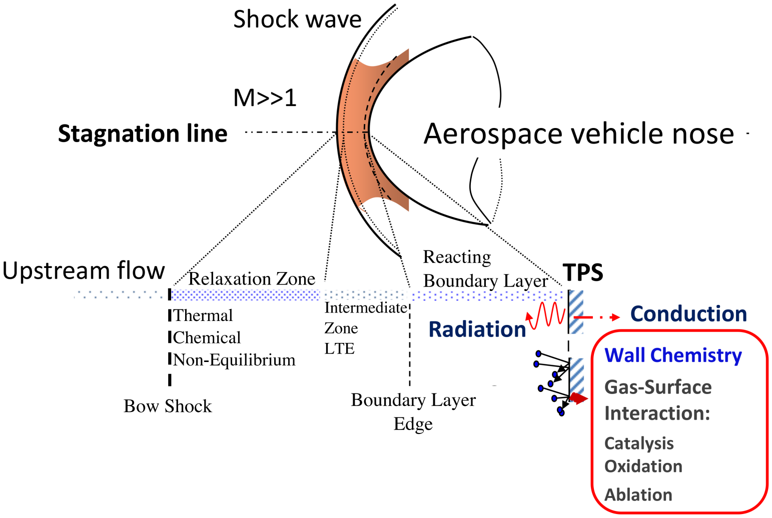

Figure 1.3.: Hypersonic flow in front of the blunt vehicle. Sketch taken from [12].

boundary layer is a reactive boundary layer, which affects the surface of the vehicle leading to very high impinging heat fluxes. This is why the vehicles must be protected by special shields called Thermal Protection Systems (TPS).

1.1.2. Thermal Protection Systems

The selection of the suitable thermal protection materials of spacecraft depends highly on the mission profile. The kinetic energy of the spacecraft, which is directly related to the departure location (orbit, moons or another planet), determines the amount of energy dissipated in the form of heat and thus determines the chemical processes needed to overcome the excessive heating problem. They are required to have high melting temperatures, lightweight and resistance to strong shear forces.

Different classifications can be found in literature [13], however a broad separation can be given as *reusable* and *ablative* TPS materials [14]. The reusable materials are typically used in lower speed entries, i.e ISS return, or suborbital flights. They are usually made of carbon, silica or boron in form of ceramic matrix composites. They do not undergo high mass or property changes, thus can theoretically be re-used. The emissivity of their coating is very important since a large amount of heat coming from radiative and convective processes is re-radiated. Then the rest of the heat is transferred through conduction, so it is the thermal conductivity of the material that determines the TPS thickness.

Ablators on the other hand are used for higher speed entries like Moon (Apollo) or Mars returns. They can withstand higher heat rates and heat loads since they change phase and lose mass, which help dissipating heat away from the surface. They are made of fibers and a binder. Most ablative TPS materials use reinforced composites in organic resin binders. The material is consumed during the entry therefore cannot be re-used. The next section covers more details on the ablation process since a cork based ablator is used in the test case of this thesis.

All the thermal protection materials interact with the chemically reacting boundary layer flow behind the bow shock. Depending on the mission profile, the phenomena at the gas-surface interface may affect the selection of the TPS material. Next, the gas-surface interaction phenomena are introduced.

1.1.3. Gas-Surface Interaction Phenomena

The dissociated atoms coming from the shock layer reach the boundary layer and eventually the surface passing through numerous processes. Once they reach the surface, they undergo additional reactions together with the surface particles. The particles coming off the surface (gas, liquid or solid) are also introduced in the boundary layer. The main gas-surface interaction phenomena can be grouped as catalysis, oxidation/nitridation, sublimation and ablation.

The catalytic properties of the wall can recombine the dissociated atoms back to molecules. The recombination efficiency, or "catalycity" γ[1], is defined as the ratio of the recombined atoms to the sum of impinging atoms. A fully-catalytic wall promotes a significant increase in the heat flux on the wall due to the exothermic recombination reactions [15]. Oppositely, the extreme case of a non-catalytic wall would significantly reduce the heat rates. The catalytic effects on the blunt body stagnation point heat fluxes are discussed in Sec. 2.1.1.

The oxidation can be observed alone more easily in the ceramic TPS materials. It is the crucial process of the surface material interaction with the surrounding oxygen atoms in gas phase. The oxidation of a TPS can be harmful but also helpful. Depending on the environmental conditions, the TPS can experience two different oxidation phenomena that would result in surface chemistry changes [16]. For example for a silica based TPS, passive oxidation occurs when the SiC surface interacts with the incoming oxygen and forms a protective solid or liquid silica (SiO_2) layer on top of the material surface. Thus, there is a net mass increase. Active oxidation on the other hand corresponds to a net mass loss due to the formation of gaseous silicon monoxide (SiO) where the silicon leaves the surface and the material is subjected to erosion. In case of carbon surfaces, it leaves the surface in

---

[1] The catalycity is also shown by γ symbol and should not be confused with the specific heat ratio.

form of CO. Active oxidation happens at high temperature and low pressure conditions (inducing non equilibrium which favors surface reactions). Oxidation reactions are exothermic reactions that causes increase in temperatures. Nitridation and sublimation on the other hand, have a weaker effect than oxidation [13]. The carbon on the material surface can leave the surface in form of CN with the incoming atomic nitrogen. Sublimation of carbon results in mass loss in form of C_3. For the example of graphite in Hayabusa, it has been shown that even though there is more atomic nitrogen in air plasma than atomic oxygen, the mass loss due to oxidation is higher than nitridation and also sublimation [17]. The nitridation and sublimation phenomena on carbon surfaces are also studied extensively at VKI [18].

Ablation phenomenon as a whole contains oxidation and nitridation processes [13]. However ablation is the description of multiple processes. When ablators are exposed to heat, three fundamental processes happen [19], they:

- pyrolyze: release of gaseous products due to chemical decomposition of the resin. (no free stream particles involved)
- ablate: combination of surface reactions, vaporization and sublimation which change the phase of the solid and liquid to gas.
- fail: erosion and loss of the material in solid (spallation) or liquid forms (melting).

The pyrolysis gas products, which are mainly hydrocarbons, travel gradually inside the porous material by diffusion and convection to the surface and are injected into the boundary layer. The pyrolysis of the resin is an endothermic reaction, therefore when the gaseous products leave the material, they take away heat from the surface. The pyrolysis products change the chemistry of the boundary layer by reducing the convective heat transfer and by reacting with the species in the boundary layer. The carbon is left behind in the structure and this residue is called “char”. The surface material also undergoes chemical reactions with the boundary layer species and consume the surface, which is called “ablation”. These surface reactions can affect the heat transfer to the surface since oxidation is an exothermic reaction while vaporization or sublimation are endothermic [14]. The surface can also be mechanically removed from the surface which is called spallation [20].

Ablation modeling is quite complex and is usually split into different sections. The solid phase phenomena are modeled in material response codes [21, 22]. The surface phenomena are usually computed by separate models and codes. A material response model is presented in Chapter 3. There are also codes that couple both [22, 23]. The fact that ablative TPS materials change shape during the re-entry adds more complexity to the models. Some efforts on shape change analysis can be found in [24, 25].

1.2. Investigation Tools for Hypersonic Entry Aerothermodynamics

1.2.1. Aerothermodynamic Design Cycle

Aerospace scientists and engineers try to understand the aerothermodynamic flight conditions around space vehicles for an efficient thermal design interacting with other disciplines such as flight trajectory analyses, guidance-navigation and control system design, aeroelasticity, propulsion systems etc [26]. There are three powerful interacting tools for a reliable Thermal Protection System design as well for other critical items such as aerodynamic forces and moments, telecommunications blackout and stability. *Ground tests* and *numerical simulations* are the everyday application while the *flight tests* are the third rare and valuable tool. All three methods are connected to each other, sometimes directly depending on the case and sometimes through "models" as illustrated in Fig. 1.4. This approach is however subjective to the modelers or ground test experts and is highly dependent on the research goals. For example, for design purposes, the three main tools may be ground tests, numerical simulations and models since the ground tests and the flight conditions are viewed as experimental data for validation. Instead, for the author of this thesis, how the flight conditions are related to the ground test environment is a major concern and it is the primary research objective.

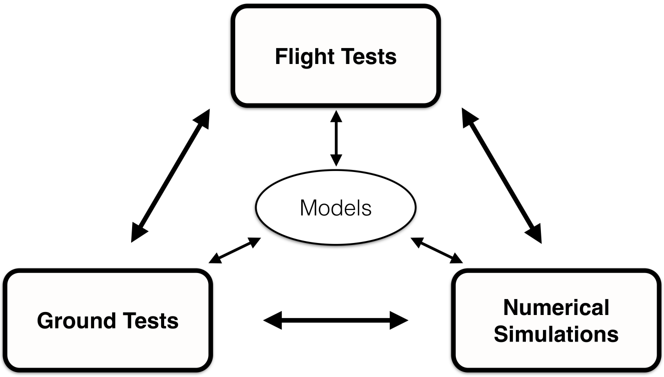

Figure 1.4.: Aerothermodynamics investigation tools overview.

The numerical simulations are the cheapest among all but they initially suffer from reliability issues as they need to be validated by physical information coming from the ground or flight experiments. With more validation cases and high computation capabilities, the computational tools are preferred to other expensive tools since it is not possible to perform experiments for all possible flight conditions. For validation of any model or numerical method, the experiments are indispensable. The biggest advantage of the ground tests is that the test environment can be controlled. Nevertheless unlike low speed aerodynamics, high enthalpy flows cannot be simulated in one single ground facility type but only partial experiments are possible [7]. Furthermore, steady free stream experiments are often done and they have limitations on dynamic testing for a full re-entry trajectory simulation. As mentioned previously, it is of great importance to relate the ground test conditions to the real flight environment and therefore reliable measurement techniques must be developed to understand accurately the features of the flow reproduced in the ground facilities. Furthermore, our capabilities on ground, both numerical and experimental, are necessary to build high quality aerodynamic and aerothermodynamic databases for an efficient vehicle design.

Flight tests are unique opportunities to test all aspects of the re-entry physics and build relevant aerothermodynamic databases. Within a limited range of availability, they are the most valuable among all three main tools given in Fig. 1.4. Flight data are collected either from real missions like Apollo or designated test flights. The experimental flights come with very high costs so they are rarely launched. On the other hand, this thesis discusses the QARMAN test flight mission, which is a low-cost small CubeSat platform, fit to collect aerothermodynamic data during Earth atmospheric entry. Small entry probes, such as CubeSats, are currently under development for atmospheric entry research. Once they are advanced enough, they can be launched frequently and can become the new convention for experimental data generation. A brief overview of the past flight experiments and the focus of this thesis, QARMAN mission, are discussed in the next section.

1.2.2. Flight Experiments and QARMAN Mission

The flight experiments dedicated to atmospheric entry data collection, started in 1960s. Almost all of them were spherical cones or sounding rockets and came in "bigger" sizes than the aforementioned CubeSat platforms [2]. FIRE II experiment was launched in 1965 as a demonstrator to test the heating environment for Apollo missions [27] and its aerothermal in-flight data are still used by engineers and scientists today. It weighed 86.5 kg and had a nose diameter of 0.672 m. It carried on board calorimeters, thermocouples and pressure sensors and its experiment configuration set a baseline to the following flight experiments. A series of Apollo missions followed FIRE II, and some had basic instrumentation like thermocouples and pressure sensors (e.g. Apollo AS-201 and Apollo AS-202 in 1966, Apollo 4 in 1967). In 1971, Reentry F, that is a sharp half cone of 5°, was launched to measure the turbulence heating and the transition onset [28]. It made pressure and

---

[2] For the terminology in this thesis, a micro-probe is defined as a vehicle with 10 to 100 kg total mass, a nano-probe is 1 to 10 kg and a pico-probe is around 1 kg or less.

temperature measurements on 21 stations along the cone and additional heat flux and pressure measurements in the base region for a beryllium TPS material. This as well was a large probe of 272 kg. A smaller yet a 62.1 kg spherical cone micro-probe Planetary Atmospheric Experiment Test (PAET) was launched in 1971 [29]. It had a diameter of 0.914 m and had heat shield plugs, temperature and pressure measurements both in fore and afterbody heat shield. Even though it made an entry to Earth, its mission objective was to test the configurations for atmospheric properties measurements onboard so that the vehicles perform well during the missions to other planets. It also carried onboard a radiometer, a mass spectrometer and atmospheric temperature/pressure sensors.

In the meantime, the Buran programme started in 1960s. This was the Soviet space shuttle programme and prior to the manned flights had a series of scaled unmanned demonstrator flights called BOR-1 (1969) to BOR-5 (until 1988) to collect atmospheric entry data [30]. In 1970s, both US and Soviets started to send vehicles to Mars and Venus. Some of these vehicles were instrumented for entry measurements however very restricted to accelerometers and a few temperature and pressure measurements for TPS health monitoring.

A Japanese capsule, OREX, re-entered Earth in 1994 to make wall catalycity measurements in addition to TPS temperature measurements to support the Japanese space shuttle programme HOPE [31]. It was a spherical cone of 3.4 m diameter and 761 kg total mass.

In 1997, the German MIRKA mission, which was a 1 m diameter sphere of 154 kg with ablative TPS, entered Earth [32] as the first successful mission from western Europe. It had a number of attitude determination instrumentation and also carried 24 thermocouples, RAFLEX and PYREX payloads, which were pressure, temperature and heat flux sensors, and pyrometric temperature measurements. Later in 1998, the European Atmospheric Reentry Demonstrator (ARD) re-entered Earth's atmosphere to increase the space flight capabilities in Europe with emphasis on re-entry technologies [33]. It had a number of thermal plugs with 3 to 5 thermocouples and pressure sensors on board of this 2 m diameter spherical cone of a total mass 2715 kg.

Important flight experiment missions such as European HERMES, X-33, X-34 and X-38 were canceled or failed due to high costs or the ambitious scientific and engineering problems. This led US, Europe and Australia to make use of the sounding rockets for atmospheric experiments below 100 km altitude [34]. Between 1998 and 2015 eight sounding rockets were launched in SOAREX programme testing a variety of instrumentation and hypersonic technologies [35, 36]. In 2002, HyShot sounding rocket experiment was successful at the second launch in Australia [37]. In 2005, the German Aerospace Center (DLR) launched the first adapted sounding rocket of the SHEFEX flight test programme SHEFEX I and the second one SHEFEX II in 2012 [38]. These sharp edge vehicles collected flight data at 1.4 to 2.8 km/s speeds. SHEFEX II carried on board a Flush air data system (FADS) experiment, a Guidance, Navigation and Control (GNC) experiment and an aerodynamic flight control. Between 2010 and 2012, five HIFiRE flight tests were performed by US and Australia in a wide range of scientific and engineering objectives for improving hypersonic flight capabilities [39–42]. Like SHEFEX, HIFiRE programme also consisted of sounding rockets.

The nano-probes gained more attention in the past two decades not only to reduce even further the flight data costs but also to find an affordable and reliable way to bring back cargo from International Space Station (ISS) that would mainly be the biological and non-biological microgravity experiments. Another important goal for developing such technology is the applicability of these platforms in other planets. A very interesting mission in terms of miniaturization came up in 1999, Deep Space 2 (DS-II) mission to Mars [43]. It consisted of two identical nano-probes of 3.6 kg spherical cones of 0.35 m diameter. The mission objective was to be jettisoned from Mars Polar Lander and penetrate to Mars. The instrumentation were related to geophysical research. Although after both probes left the main spacecraft, no communication was established, this mission has demonstrated that nano-sized probes are indeed feasible and promising for future interplanetary missions. The nano-probe Reentry Breakup Recorder (REBR) was launched from ISS during the re-entry of the Japanese HTV2 supply vehicle in 2011 [44]. This spherical cone of 4.4 kg and diameter 0.31 m, carried on board a sensor suite including 3 thermocouples for TPS measurements. Interesting for the QARMAN mission studied in this thesis, it used the IRIDIUM network to downlink the flight data before it reached the ground, thus no recovery was required. There are also on-going projects like MIRKA2 [45] from Germany which is a spherical cone capsule fitting in the 1 unit of a 3U[3] CubeSat. Other similar conceptual projects are Small Probes for Orbital Return of Experiments (SPORE) [46] fitting in 1 to 4U CubeSats and Recovery of In-Space CubeSat Experiments (RICE) [47] in minimum 2U with expected weights of 1 to 4 kg.

Mars Science Laboratory (MSL) successfully landed on Mars in 2012 with MSL Entry Descent and Landing (EDL) Instrumentation (MEDLI) suite [48]. It carried on board recession sensors, thermal plugs and pressure measurements. Although not flown, NASA's Small Probe Reentry Investigation for TPS Engineering (SPRITE) nano-probe is worth mentioning here. SPRITE capsule introduced the “fly what you test” concept, which suggests that if the vehicle is small enough to fit in the hypersonic ground facility, it is possible to fly the same test object [49]. SPRITE test model can fit in the arcjet facilities of NASA AMES thanks to its 0.35 m diameter size and 11 kg mass. Its objective is to provide a low cost test bed for testing TPS materials. It was tested successfully in NASA Ames' arcjet in 2010 and 2011. Its instrumentation suite is based on the MEDLI instrumentation configuration of the Mars Science Laboratory.

---

[3] 1U Cubesat corresponds to 10x10x10 cm unit volume. The sizes of CubeSats are defined as multiples of 1 unit as 2U, 3U, etc.

In 2014, Orion's first flight test Exploration Flight Test-1 (EFT-1) was performed [50]. This future multipurpose crew vehicle is expected to perform in Earth orbit as well as Mars or other destinations. The EFT-1 flight made measurements on a wide range of re-entry phenomena including aerothermodynamics, aerodynamics and GNC. Another recent example from Europe is the Intermediate eXperimental Vehicle (IXV) [51], launched in February 2015. They collected important amount of aerothermochemical data and the outcomes will be very useful for validation purposes.

It can be seen that most of the flight data are collected from flight tests, which were very big in size. This increases not only the hardware development, manufacturing and testing costs but also the launch costs. The von Karman Institute for Fluid Dynamics (VKI) is currently working on a low cost technology demonstration mission on a CubeSat platform to perform an atmospheric entry to Earth. QARMAN (QubeSat for Aerothermodynamic Research and Measurements on AblatioN) [52] is a spacecraft respecting the triple unit CubeSat standards [53]; a rectangular prism weighing 4 kg with dimensions 34x10x10 cm depicted in Fig. 1.5. It will be deployed together with the QB50 mission [54] at 380 km then will enter the atmosphere with a speed of 7.7 km/s and a peak heat flux of 1.7 MW/m^2 at the stagnation region. It is protected with Cork P50 material at the nose and a SiC based ceramic TPS on the side panels. The ablative nose radius of curvature is 23 cm and the corner radius is 1.2 cm.

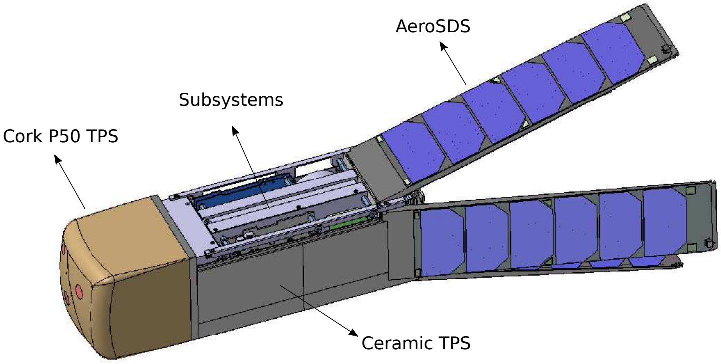

Figure 1.5.: QARMAN vehicle overview. The size of the vehicle before opening the AeroSDS panels is 34x10x10 cm and it weighs 4 kg.

Off the shelf components are mainly used as subsystems except the unique payloads such as aerothermodynamic in-flight experiments and the Aerodynamic Stability and De-orbiting Device (AeroSDS). The AeroSDS is a passive attitude control system, which allows QARMAN to follow the designed entry trajectory shown in Fig. 1.6. The stabilization and de-orbiting maneuver will be performed using aerodynamic forces and moments by the opening panels shown in Fig. 1.5.

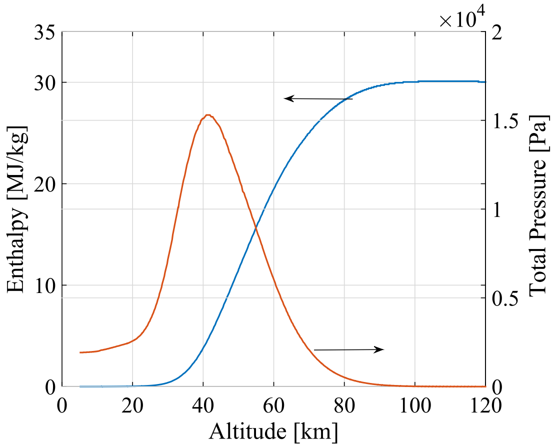

Figure 1.6.: Enthalpy and total pressure of QARMAN entry trajectory.

A number of TPS materials from low density ablators to heavier cork based materials are considered for the first QARMAN flight. An overview of the cork based TPS materials can be found in [55]. The experimental TPS selection campaign resulted in the choice of Cork P50 as the best available fit for QARMAN mission profile especially for its relatively low heat flux trajectory and a rectangular prism geometry.

QARMAN carries on board a number of in-flight experiments to collect real flight data that will be used to improve experimental and numerical tools. The objectives of the in-flight experiments are to retrieve data on ablator behavior and aerothermal environment in the stagnation region in terms of temperature, pressure, recession and radiation, and temperature/pressure/skin friction measurements for transition on the side panels. More details on the experimental payloads can be found in Chapter 4. Overall, this challenging mission targets to contribute to atmospheric entry research with nano and pico satellite technology offering a very flexible system with wide range launch opportunities and reduced costs. Once the concept is proven, different thermal protection materials, guidance, navigation and control algorithms, subsystems, aerothermodynamic instrumentation, etc. can be tested and flight qualified.

1.3. Thesis Scope and Objectives

This thesis focuses on an analysis starting from the pre-flight testing methodology until the design and tests of in-flight measurements with a post-flight data analysis strategy for arbitrary hypersonic entry vehicles. At the *pre-*

flight phase, a methodology is developed for accurate duplication of the stagnation aerothermochemistry of the spacecraft in subsonic plasma wind tunnels. It is presented with new flow characterization techniques and is demonstrated for the QARMAN flight experiment test case. It continues with a thorough experimental characterization of QARMAN's TPS material. The *flight* phase of QARMAN includes the design and testing of aerothermodynamic in-flight experiments for making measurements relevant to the ground experiments. QARMAN mission is still to be launched in early 2016 therefore a *post-flight* strategy is proposed for validation of the developed methods.

The Chapter 2 starts with a literature survey on the convective stagnation heating of entry vehicles to understand the heat transfer mechanisms and the thermo-chemical phenomena of the hypersonic flight so that we can duplicate them in our ground facility. The chosen ground facility, Plasmatron at von Karman Institute for Fluid Dynamics, is described. The flow created in the wind tunnel should be accurately characterized in terms of enthalpy and velocity gradient, thus an enthalpy probe concept is tested as well as an optical emission spectroscopy tool. An experimental database with heat flux and enthalpy measurements is built in addition to a numerical database where the flow in Plasmatron is computed by an in-house plasma flow solver. Finally a *Flight-to-Ground Duplication* method on how the flight flow conditions can be duplicated in the plasma wind tunnel is proposed. The method is valid for any given spacecraft geometry and its validity is demonstrated using the built databases with the test case of QARMAN that has a peculiar nose and body shape. The perspectives of dynamic testing are discussed and how the methodology can be iterated with the flight data is elaborated.

After covering the high enthalpy flow part, Chapter 3 discusses the solid material and its surface. An extensive experimental campaign on ablation characterization is presented to provide input for future material response models and investigate the effects of the LHTS parameters on the ablative behavior. The material response equation sets and their boundary condition at the gas-surface interface are given. The test matrix consists of a range of free stream conditions of pressure-heat flux and a range of sample geometries as suggested by the developed Flight-to-Ground Duplication methodology. The surface and sub-surface temperatures, swelling/recession, mass loss, emissivity and species behaviors are monitored by a number of experimental techniques and the expected performance during the flight is elaborated. The aspects of dynamic testing of ablators are elaborated and a post-flight analysis strategy is proposed for the validation of the material response model.

Since the tools we use on ground need to be validated by real flight data, the opportunity to fly relevant experiments is taken with QARMAN mission. The Chapter 4 discusses the design, development and testing of two in-flight experiments. While one makes measurements of in-depth material heating at three locations (XPL01), the other measures pressure at three points in the ablative nose (XPL02). XPL01 consists of *thermal plugs*, meaning each plug makes temperature measurements at five different depths from surface. XPL02 incorporates bare holes on the TPS that is aligned with a pressure spool inserted from the back, connected to a low range pressure sensor. Since both payloads are placed in the stagnation region, its flight data can be related to the ground test experiments of Chapter 3. QARMAN, as a test flight mission, has other aerothermodynamic in-flight experiments however they are out of scope of this thesis. A data reduction methodology is briefly discussed for the flight data processing after the launch of QARMAN in 2016.

Finally the work is concluded in Chapter 5 with the contributions of the thesis and perspectives for future work.

The objectives of the dissertation are to answer the following questions:

- How to duplicate the entry flight conditions of arbitrary spacecraft's stagnation region in plasma wind tunnels.
- How to characterize accurately the duplication parameters of the flow, i.e. enthalpy and velocity gradient, in the wind tunnel.
- How to characterize a mission tailored ablative TPS material behavior in a plasma wind tunnel to provide input for material response models.
- How to make relevant aerothermodynamic in-flight experiments for ground tools validation.
- How to treat the flight data in the future for ground tools validation.

Chapter 2.

Ground Testing Methodology for Aerothermodynamics

For efficient and safe space travel, it is crucial to have a good understanding of the atmospheric entry aerothermodynamic environment prior to the flight by accurate ground tests and numerical simulations. This chapter begins with the details of the stagnation heating during the atmospheric entry. The generic ground testing methodology used in VKI Plasmatron facility, Local Heat Transfer Simulation (LHTS), is introduced which requires accurate characterization of the free stream in the test chamber. A new enthalpy measurement technique, the enthalpy probe, is introduced and compared to other methods. An experimental database is built with the testing conditions in addition to a numerical database which consists of simulations of the flowfield in the test chamber. Finally, an extensive ground testing procedure for the entry of an arbitrary spacecraft into an arbitrary atmosphere is demonstrated. This iterative process allows one to determine the testing conditions and the test sample geometries that are unique per spacecraft and per altitude on the entry trajectory.

2.1. Stagnation Region Heating in High Enthalpy Flows

2.1.1. A Literature Survey

The stagnation region of a vehicle is almost always the critical region as it is exposed to the highest heating rates. The flow dissociates behind the detached bow shock of the blunt vehicle, and recombines at a certain rate in the shock layer and the boundary layer until the catalytic wall. Since 1950s, a large number of scientists investigated how to compute the heat transfer at the stagnation region with the aim of sizing the TPS of a wide variety of vehicles in a wide range of planetary atmosphere configurations. The stagnation region allows similar boundary layer solutions, however deriving analytical solutions for laminar heat transfer was only possible with certain assumptions. The convective and radiative heating are studied extensively in literature however the convective heating phenomena will be the focus in this section.

Initially in 1952, an exact solution of the heat transfer was given by Sibulkin [56] for incompressible flow on hemisphere-cylinders with isothermal surfaces. Prior to 1956, a limited number of experimental laminar heat transfer data were available on hemisphere-cylinders taken in supersonic Mach numbers. For example, Korobkin [57] measured the effective recovery temperature distributions on hemispherical surfaces and later Eber [58] and Stine and Wanlass [59] showed that the recovery factor is a function of the square root of the Prandtl number outside of the boundary layer. In 1956, Lees [60] proposed formulations for laminar heat transfer of dissociated flows considering atomic diffusion in the two extreme conditions of thermodynamic equilibrium and frozen flows, extending the simplifications by transformations of the similar compressible flow equations by Cohen and Reshotko [61] and Hayes [62].

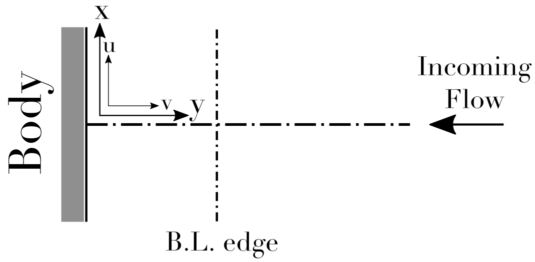

Figure 2.1.: Reference coordinate frame for the stagnation point heating and boundary layer equations.

In 1957, Crawford and McCauley [63] made an experimental campaign in hypersonic flow and widened previous work to non isothermal surfaces. They applied a modification to the method of Sibulkin by using the diameter and the conditions behind the normal shock and had a good agreement with the experiments. One year later Fay and Riddell [64] published the famous work on stagnation heating in fully dissociated air for equilibrium and non equilibrium with fully catalytic and non catalytic walls. This work has become the reference for research and industry to which all the theoretical and experimental progress are compared as it will be shown shortly. For dissociated air and where Prandtl number is not necessarily equal to 0.71, the Fay and Riddell equation is given below in the reference frame depicted in Fig. 2.1.

$$\begin{aligned}\dot{q}_w &= 0.763 Pr^{-0.6} \left(\rho_e \mu_e\right)^{0.4} \left(\left.\frac{du_e}{dx}\right|_{edge} \right)^{1/2} \left(\rho_w \mu_w\right)^{0.1} \\ &\quad \times \left(h_{0,e} - h_w\right) \left[1 + \left(Le^{\alpha} - 1\right) \left(\frac{h_{D,e}}{h_{0,e}}\right)\right] \qquad (2.1)\end{aligned}$$

where ρ is mass density, μ is the absolute viscosity, du_e/dx is the velocity gradient, h is the enthalpy per unit mass, Pr is the Prandtl number and the subscripts 0, e and w describe the total, the conditions at the edge of the boundary layer edge and at the wall respectively. $h_{D,e}$ is the dissociation enthalpy and is the product of the enthalpy of formation, $\Delta h^0_{F,i}$, of species i and its mass fraction $y_{i,e}$:

$$h_{D,e} = \sum_{i=1}^{N} y_{i,e} \Delta h^0_{F,i} \tag{2.2}$$

The exponent of Lewis number, Le, in Eq. (2.1) α is given 0.52 for an equilibrium boundary layer and 0.63 for a frozen boundary layer with fully catalytic wall. The latter is suggested as 2/3 by Lees [60]. Rose and Stark [65] compared experimental results on a hemisphere-cylinder probe in a shock tube and found a better agreement with Fay and Riddell [64] than Lees [60] when they used the velocity gradient correlation of Boison and Curtiss [66].

The same year, Stoney [67] presented experimental results on flat faced, concave and hemisphere cylinders and Goulard [68] suggested a similar heat flux equation to Fay-Riddell for frozen boundary layer with arbitrary catalytic efficiencies at the wall and at any degree of dissociation:

$$\dot{q}_w = 0.664 Pr^{-2/3} \left(\frac{du_e}{dx} \rho_e \mu_e \right)^{1/2} h_{0,e} \times \left[1 + \left(Le^{2/3} \phi - 1 \right) \left(\frac{h_{D,e} y_e}{h_{0,e}} \right) \right] \tag{2.3}$$

where y_e is the atom mass fraction at the boundary layer edge and ϕ introduces the catalytic efficiency at the wall.

Each term in the above equations requires special attention. The velocity gradient, $\frac{du}{dx}$ or β, is a major parameter and it is discussed in detail in Sec. 2.1.3. It is the derivative of the velocity component normal to the stagnation line, shown as u in Fig. 2.1, in the x-axis direction, along the stagnation line. It affects the convective characteristic time of the flow ($\tau_{flow} = \beta^{-1}$) determining how fast the flow is deviated from stagnation region [7, 64]. Therefore, recalling the definition of the Damköhler number, $Da = \tau_{flow}/\tau_{chem}$, it can be shown that β is a key parameter to quantify how likely are the gas-phase chemical reactions to occur. Although the β value in the above heating equations is defined as the boundary layer edge value, depending on several applications in literature such as experiments or inviscid computations, it is occasionally determined at the wall. The details of which β along the stagnation line should be used are also given in Sec. 2.1.3.

The studies continued by extending the existing correlations to other gas mixtures and to improve the high temperature air models for the computation of the thermodynamic properties appearing in the stagnation heating equations. Beckwith and Cohen [69] took special care for the high temperature air using the thermodynamic properties of Moeckel and Weston [70].

Fay and Kemp [71] studied partially ionized diatomic gas computing equilibrium and frozen boundary layers. They first considered nitrogen and extended it to air comparing their results to the work of Pallone and Van Tassell [72]. Their results for equilibrium nitrogen disagreed with the calculations of Scala and Warren [73] due to the difference of the charge-exchange cross section assumptions. In addition to the theoretical work of Bade [74] on Argon, many experimental results are reported for different gas mixtures such as Horton and Babineaux [75] investigated experimentally the influence of gas mixtures on heat transfer for carbon dioxide and nitrogen, Nerem et al. [76] who considered carbon dioxide atmosphere, Reilly [77] xenon-argon mixture, and Pope [78] helium and argon. More experimental results can be found in [79, 80].

In 1968, Zoby [81] proposed general empirical relations for a range of arbitrary atmospheric compositions of different planet entries. The proposed form is the following:

$$\dot{q}_w \sqrt{\frac{R}{p_0}} = K \left(h_{0,e} - h_w \right) \tag{2.4}$$

where p_0 is the total pressure, R is the nose radius, K is given for different gas mixtures:

$$K = \frac{0.763 Pr^{-0.6} A^{0.5} 2^{0.25}}{R^{0.25}} \left(\frac{\rho_w \mu_w}{\rho_e \mu_e} \right)^{0.1} \tag{2.5}$$

where A is a coefficient from Sutherland law of viscosity.

A study that combines ablative boundary conditions of wall mass transfer to the stagnation heating is made by Yoshikawa [82]. Sutton and Graves [83] later extended the range of atmospheric compositions to arbitrary gas mixtures of i.e helium, neon, ammonia, methane etc, for chemical equilibrium flows around axisymmetric blunt bodies considering the mass fractions, molecular weights and transport parameters.

In the meantime, studies on specific missions were also reported. Holloway and Dunavant [84] made experiments on Scout Flight Experiment vehicle on two models at two Mach numbers and a range of angles of attack. The test models were not hemisphere cylinders but staged axisymmetric bodies with curved corners. They took as reference the modified Sibulkin method by Crawford and McCauley [63] and showed to match well the heat transfer predictions by Lees [60] at the stagnation point. They also observed that the heating in the corners of their model was more than the stagnation point heating which is interesting for the QARMAN vehicle discussed in this thesis because it has have sharp corners. This verified the prediction of the corner heating phenomenon by Lees [60] and Beckwith and Cohen [69] however the measured corner heating was less than the theoretical values. Two years later a study on FIRE reentry experiment was reported by Stainback [85]. The reader is advised to visit the review of Tauber [86] published in 1989 for further reading.

A recent study by Brandis and Johnston [87] considering both radiative and convective heating rates is worth mentioning due to its simplicity. They compared the existing correlations of Fay and Riddell [64] and Sutton and Graves [83] to the shock tube experimental data and proposed an updated correlation for convective heating as below for two sets of entry speeds.

- For 3 km/s$\leq$V<9.5 km/s:

$$\dot{q} = 7.455 \times 10{-}9\rho^{0.4705}V^{3.089}R^{-0.52} \tag{2.6}$$

- For 9.5 km/s$\leq$V$\leq$17 km/s:

$$\dot{q} = 1.270 \times 10{-}6\rho^{0.4678}V^{2.524}R^{-0.52} \tag{2.7}$$

2.1.2. Local Heat Transfer Simulation

The stagnation heating is a crucial parameter in the hypersonic entry and it is important to reproduce the flight conditions in the ground test facility as accurately as possible. Studying the Eqs. (2.1) and (2.3) from the previous section, it is seen that the density ρ, the velocity gradient du/dx or β, the total enthalpy h_0 and the chemical composition at the boundary layer edge (hidden in the $h_{D,e}$ term) as well as the wall conditions of enthalpy and catalycity are in common. These can be treated as the *similitude* or more correctly as the *duplication* parameters. To satisfy the duplication criteria at the wall, the following can be done:

- **Catalycity:** If the actual flight TPS material is tested in the ground facility, the wall catalycity is the same as the flight conditions; given the sample is exposed to the same stagnation region flow.

- **Enthalpy at the wall:** For a given TPS material, thus material composition and properties, Goulard [68] states that for equilibrium, the enthalpy at the wall, h_w, can be given as a function of the enthalpy, pressure and velocity gradient at the boundary layer edge. Therefore, if the flight TPS material is used in the test chamber, h_w is a dependent variable, $h_w = f(h_{0,e}, p_e, \beta_e)$, at equilibrium conditions.

When the same wall conditions are assured, to reproduce the the flight heat flux in the test chamber there are four independent parameters to be determined at the boundary layer edge: ρ_e, β_e, $h_{0,e}$ and $h_{D,e}$. In order to be consistent with the assumption of h_w computation, one should assume local thermodynamic equilibrium (LTE). Then, the species concentration, $f(h_{D,e})$, the density, ρ_e, and the viscosity, μ_e, at the boundary layer edge become functions of pressure and enthalpy.

$$h_{D,e} = f(y_{i,e}) = f(h_{0,e}, p_e) \tag{2.8}$$

$$\rho_e = f(h_{0,e}, p_e) \tag{2.9}$$

$$\mu_e = f(h_{0,e}, p_e) \tag{2.10}$$

Finally, there are only three independent variables left for LTE: p, h, and β. This is expressed as Local Heat Transfer Simulation (LHTS) by Kolesnikov [88]. If these three independent parameters at the boundary layer edge of a hypersonic vehicle are duplicated in a ground facility on a TPS, then the heat flux and the boundary layer aerothermochemistry are the same. A sketch of the LHTS logic is given in Fig. 2.2 for the case of a subsonic plasma tunnel testing. Thus the LHTS methodology provides the means of transition between ground tests and the flight conditions as given in Eqs. (2.11) to (2.13).

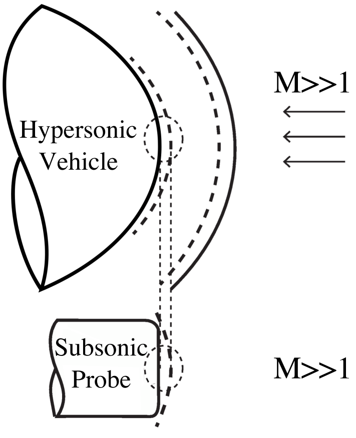

Figure 2.2.: Local Heat Transfer Simulation (LHTS) approach. The boundary layer behind the normal shock in the hypersonic flight can be fully reproduced in a subsonic plasma wind tunnel if the enthalpy, h, pressure, p and the velocity gradient, β at the boundary layer edge are duplicated.

$$\text{Enthalpy} : h_e^{flight} = h_e^{ground} \tag{2.11}$$

$$\text{Pressure} : p_e^{flight} = p_e^{ground} \tag{2.12}$$

$$\text{Velocity gradient} : \beta_e^{flight} = \beta_e^{ground} \tag{2.13}$$

The enthalpy and the pressure are functions of the free stream that are required to be reproduced in the ground facility. One can determine h_e and

p_e from the free stream flight conditions using the energy and the momentum equations as follows [89]:

$$h_\infty^{flight} + \frac{1}{2}(V_\infty^{flight})^2 = h_e^{ground} \tag{2.14}$$

$$p_\infty^{flight} + \rho_\infty^{flight}(V_\infty^{flight})^2 = p_e^{ground} \tag{2.15}$$

where the term h_∞^{flight} in Eq. (2.14) and p_∞^{flight} in Eq. (2.15) can be neglected since at hypersonic speeds $h_\infty^{flight} \ll \frac{1}{2}(V_\infty^{flight})^2$ and $p_\infty^{flight} \ll \rho_\infty^{flight}(V_\infty^{flight})^2$. To summarize, the enthalpy and pressure link the incoming flow conditions during the flight to the ground test free stream which requires accurate characterization the flow in the test chamber. The pressure and enthalpy measurement techniques and their accuracies are further discussed in Sec. 2.2.

On the other hand, the determination of the last parameter of the LHTS the velocity gradient, β, is more complicated and is explained in the dedicated Sec. 2.1.3. Unlike pressure and enthalpy, the velocity gradient depends not only on the free stream characteristics but also on the spacecraft and test sample geometry too. It was discussed in the previous section that the probe geometry affects how the flow is deviated, and through the Damköhler number, modifies the chemical reactions in the boundary layer. So it is the parameter linking a wind tunnel experiment to the atmospheric entry of a specific spacecraft geometry.

Depending on the application, the direction of the LHTS methodology changes from a "Ground-to-Flight Extrapolation" [90] to a "Flight-to-Ground Duplication" which are in practice very different than each other unless the flying body is a sphere. Ground to Flight extrapolation is performed when a TPS material is required to be characterized without aiming a specific spacecraft's entry trajectory or body shape. The generic TPS characterization experiments are often performed with ESA standard probe with a fixed geometry [91]. Given the testing conditions of p, h and the incoming flow on the probe, one can determine β^{ground} and so β^{flight}, thus *which spacecraft geometry the experiment corresponds to.* Examples of this application can be found in [1, 90] and the determination of β^{ground} is elaborated in Sec. 2.2.2. However in the case of Flight-to-Ground duplication, one needs to determine β^{flight} for a given spacecraft geometry at a given entry trajectory point and make sure to duplicate the same velocity gradient in the ground facility in addition to the correct enthalpy and pressure boundary layer edge. The determination of β^{flight} is discussed in detail in the next Sec. 2.1.3. This means one must use different test sample geometries or different test configurations for different missions and even for different trajectory points of the same atmospheric entry. Sec. 2.3 consists of a Flight-to-Ground Duplication methodology, allowing for arbitrary spacecraft geometry and demonstrates with a test case of QARMAN mission, how the ground testing conditions and the sample geometries are determined.

2.1.3. Velocity Gradient

The definition of the velocity gradient is introduced in the previous section. The β profiles differ in different flow regimes. The Fig. 2.3 shows the velocity gradient behaviors in subsonic and hypersonic conditions. From the qualitative point of view, the two curves exhibit a totally different behavior. In the subsonic regime the velocity gradient asymptotically tends to zero upstream. In approaching the stagnation point it rises up to a maximum value and then it goes to zero at the wall. Alternatively, in the hypersonic case it is null in the free stream, it jumps to its maximum value right after the shock, and then decreases monotonically in the subsonic region.

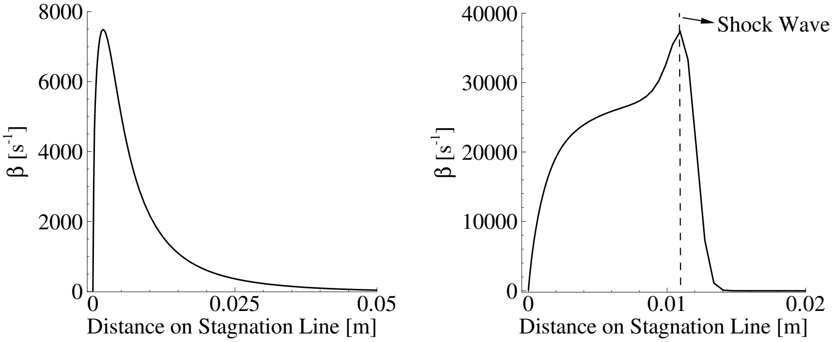

Figure 2.3.: Velocity gradient profile examples in front of a probe in subsonic test conditions (left) and in front of a hypersonic vehicle (right).

Our focus is to determine the β^{flight} for a given spacecraft and for a given entry trajectory location. This was a struggle for all the studies presented in Sec. 2.1.1 since as shown by Holden [92] there has always been a discrepancy of theory and experiments where experimental heat fluxes were higher than the theory. According to Olivier [93], heat flux over-estimation is due to the velocity gradient approximations and the difference cannot be solely due to wind tunnel noise as explained by Fay and Riddell [64].

In 1957, Lees [94] pointed out in detail how "excellent" the modified Newtonian pressure distribution is for the spherical portion of the noses by comparing his results with the experimental work of O'Bryant and Machell [95] where the pressure distribution around the spherical nose is measured for a range of yaw angles. The modified Newtonian Theory (MNT) is widely used in many theoretical, experimental and industrial works among those mentioned in the Sec. 2.1.1 such as [60, 63–65, 68, 71, 81, 83].

The MNT considers the one-dimensional momentum equation for the streamlines in the vicinity of the stagnation line where the pressure term is obtained from the sphere pressure distribution of the Newtonian theory, $C_p = 2cos^2\phi = (p_e - p_\infty)/q_\infty$, where ϕ is the angle between the normal to the surface and the free stream direction. Additionally assuming an incompressible inviscid flow at the stagnation point, β can be expressed as:

$$\beta_e = \frac{1}{R}\sqrt{2\frac{(p_e - p_\infty)}{\rho_e}} \tag{2.16}$$

(for full derivation, see p255-256 in [7]).

Immediately after, Boison and Curtiss [66] published their experimental pressure measurements in the stagnation region of axisymmetric blunt bodies at supersonic Mach numbers [66]. They compare their experimental results to a combination of the MNT and Bernoulli equations. A series of blunt shapes, consisting of spherical segments with varying radii and common cylindrical after body of radius r^*, was analyzed. Defining x^* as the axial distance between the stagnation point (on the spherical segment) and the beginning of the after-body cylinder, they found that for body configurations with high bluntness ($x^*/r^* < 0.25$) the MNT no longer applies if the nose radius of curvature is *directly* used in Eq.(2.16). This study was extended later in 1969 by Trimmer and Clark [96] to hypersonic flows on axisymmetric models with changing bluntness and reached the same conclusion. Later in 2006, Fletcher and Playez [97] use the velocity gradient scaling coefficients of Trimmer and Clark for hypersonic and subsonic flows as given in [98] for a blunt, yet axisymmetric body and compared hypersonic and subsonic ground test facility measurements.

In 1960, instead of using the Newtonian pressure distribution Truitt [99] considered potential flow solution in concentric spheres where the outer sphere would be the detached bow shock. Using the method of Truitt, Topham [100] measured the shock standoff distance and related it to the tangential velocity gradient.

In 1966, Zoby and Sullivan [101] investigated analytically the effects of the corners on stagnation point velocity gradient determination from flat face cylinders to hemisphere-cylinders. Using the work of Boison and Curtiss [66], they state that if the stagnation region pressure distribution is the same for a given flight condition, an *effective radius* can be found with a simple relation as follows:

$$\frac{\frac{d(U_e/U_\infty)}{d(s/R_B)}_{Blunt\,Body}}{\frac{d(U_e/U_\infty)}{d(s/R_B)}_{Hemispherical\,Body}} = \frac{R_B}{R_{eff}} = constant \tag{2.17}$$

Zoby [81] based his empirical correlation on the R_{eff} assumption, which is given as R in Eq. (2.4). Ellison [102] in 1969 studied the corner effect experimentally on Apollo-like capsule shapes with different nose, corner and cone radius at different angles of attack. He followed the logic of Boison and Curtiss by measuring pressure distribution around the body at Mach 8. As Boison and Curtiss [66] he also found a significant discrepancy between

MNT method and the experimental pressure distributions passed a bluntness parameter threshold. For MNT computations he used the effective radius approach of Zoby and Sullivan given in Eq. (2.17). He showed, for spherical cone capsule geometries, that the effective radius decreases with decreasing nose radius and increasing corner radius.

Parallel to these works, a number of studies were published on heat and mass transfer by three dimensional stagnation flow computations. These studies took the example of shuttle-like vehicles and considered two radii of curvature on two radial axes. The works of Howarth [103] , Reshotko [104] and Libby [105] defined coefficients based on the ratio of the radii of curvature in two axes. These studies are later used to relate the axisymmetric body heating to the three dimensional heating with these coefficients. For example, DeJarnette and Cheatwood [106] reported a velocity gradient expression as:

$$\beta_{e,x} = \frac{V_\infty}{R_x}\sqrt{1.85\frac{\rho_\infty}{\rho_e}} \tag{2.18}$$

where x can be replaced by z for the velocity gradient of the other axis. Later in 1975, Lunev [107] in Russia, proposed a similar approach to MNT theory however based on Thin Shock Layer theory:

$$\beta_e = \frac{1}{R}\sqrt{\frac{8}{3}\frac{(p_e - p_\infty)}{\rho_e}} \tag{2.19}$$

Moreover the study of Olivier [93] has mass and momentum equations written in polar coordinates for a sphere starting from a general expression as stated in the book by Probstein and Hayes [108] where real gas effects, vorticity behind the detached shock and compressibility effects are considered. As a result, the velocity gradient expression is derived as follows:

$$\beta_e = \frac{1}{R}\frac{\left(1+\overline{\Delta}\right)}{\overline{\Delta}}\frac{p_{0,2}-p_2}{\rho_\infty u_\infty}\frac{\rho_{0,2}}{\rho_s} \tag{2.20}$$

where the subscript 2 corresponds to the conditions after the shock, and $\overline{\Delta} = \Delta/R$ is the normalized shock standoff distance.

All the above mentioned approaches apply almost always to spherical nosed axisymmetric vehicles and a few in blunt axisymmetric bodies. Axisymmetry is a strong assumption since the aim is to provide a Flight-to-Ground Duplication Methodology independent of the spacecraft geometry. A practical different example is the design of QARMAN vehicle shown in Fig. 1.5. The unconventional rectangular prism shape of QARMAN required a specific study to assess a suitable approach for determining the velocity gradient in case of a non-axisymmetric and non-spherical body. In the case of QARMAN the bluntness is 0.1 and so, accordingly to the work of Boison and Curtiss [66], the nose curvature radius of 23 cm cannot be used directly to compute the β value through Eq. (2.16). However, although Eqs. (2.16), (2.17), (2.19) and (2.20) are functions of the radius R which is of a sphere, they can still be valid if an effective radius at hypersonic flow, $R_{eff,H}$, can be found and is used instead of the nose curvature radius. The exception of axisymmetry assumption in the expression of DeJarnette and Cheatwood in Eq. (2.18) cannot be used for QARMAN either since QARMAN has multiple curvature radii, a squared cross section and has corners; no unique R can be defined in either axes.

For any given β expression, there is one equation and two unknowns being β and R_{eff} for an *arbitrary* vehicle geometry. Therefore, with the final objective of defining a hemispherical test sample radius to allow the β duplication in the ground facility, and so the stagnation-point heat flux reproduction, the problem turns into the computation of the effective radius $R_{eff,H}$ (by inverting one of Eqs. (2.16)-(2.20)) provided that the β value in the flight conditions is known.

Unfortunately the extraction of β directly from hypersonic numerical solution is not trivial since the boundary layer edge is not evident to determine as depicted previously in Fig. 2.3. Sec. 2.3 discusses the Flight to Ground Duplication methodology that is considering all the aspects mentioned above and its application on the squared QARMAN geometry utilizing Lunev formulation given in Eq.(2.19) formulation which is also used by Kolesnikov [88].

2.2. Flow Characterization at VKI Plasmatron Facility

Prior to the introduction of the Flight-to-Ground Duplication, the VKI Plasmatron facility and its tools are described since the scope of this study is the improvement of the ground testing pertinence and accuracy. It was shown that the pressure and enthalpy are the major elements to provide a relevant free stream environment in the facility, hence they need to be accurately characterized. The pressure measurements and the conventional enthalpy determination method are explained. Two enthalpy measurement techniques are introduced with their results in comparison to each other. Finally, the built experimental and numerical databases are presented.

2.2.1. Facility Characteristics and Operations

The Plasmatron facility is a plasma wind tunnel generating an inductively coupled plasma flow [109]. A sketch of the facility is presented in Fig. 2.4. The torch is a quartz tube with a coil wrapped around it. While a cold gas is injected, a high voltage and high frequency current is supplied to the coil.

Hence, an electromagnetic field is formed inside. The electromagnetic field heats up the gas by the Joule effect which promotes excitation and ionization of particles. Then, the gas leaves the torch in form of a plasma jet to the chamber, which is held initially in vacuum. The starting gas is Argon due to its suitable ionization feature. Once the argon plasma is stable, air or the testing gas is injected gradually and eventually a stable continuous air plasma is obtained. The testing gas can be argon, air, N_2 and CO_2.

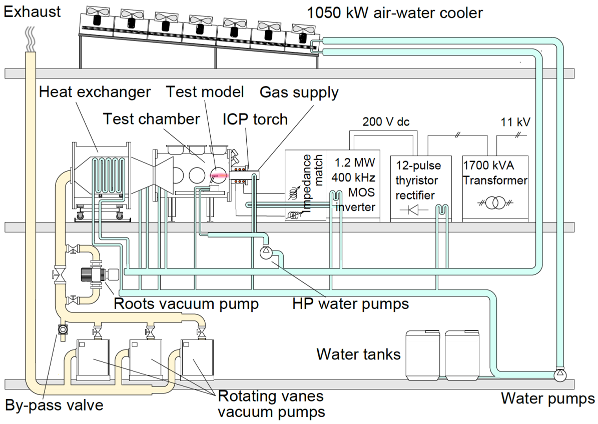

Figure 2.4.: VKI Plasmatron facility. Courtesy to [1].

The Plasmatron facility uses a high frequency, high power, high voltage (400 kHz, 1.2 MW, 2 kV) solid state (MOS technology) generator, feeding the single-turn inductor of the 160 mm diameter plasma torch. The chamber is large enough to accommodate big test samples. There are three sample holders allowing three probes to be exposed to plasma during one run. Additionally, there is a cooling box to keep the TPS samples unaffected by the plasma jet heat before injection. However some sample holders are too long to fit in as in the case of some ablation measurements presented in Chapter 3.

The test matrices usually consist of static pressure and heat flux ranges. After the plasma onset, the static pressure is adjusted with the vacuum pumps shown in Fig. 2.4. The static pressure envelope of the facility is between 1000 Pa and 80000 Pa. For a generic TPS test configuration, the heat flux probe is injected and the facility power is regulated until the required heat flux is measured. Finally, the TPS sample is injected from the cooling box in the upper sample holder. All the data are recorded in the Plasmatron data acquisition system MX100.

The heat flux is measured by different sized probes equipped with copper water cooled calorimeters. The heat fluxes measured with the ESA standard probe geometry [91] can vary between 90 kW/m^2 and 10 MW/m^2. Other configurations with converging or supersonic nozzles at the torch exit can lead up to 16 MW/m^2. The inlet and outlet temperatures of the cooling water is measured by type E thermocouples. A Yokogawa rotameter is used to regulate the water flow rate, which is calibrated prior to each test run. The cold wall heat flux is then determined in real time as follows:

$$\dot{q} = \frac{\dot{m} \cdot C_p \cdot (T_{out} - Tin)}{A} \tag{2.21}$$

where the A is the surface area of the copper calorimeter surface and $\dot{m}$ is the water flow rate. A thorough uncertainty quantification on heat flux measurements is performed by Panerai [1]. The error on the heat flux can be evaluated from partial differentials:

$$\frac{\delta \dot{q}}{\dot{q}} = \left[\left(\frac{\delta \dot{m}}{\dot{m}} \right)^2 + \left(\frac{\delta C_p}{C_p} \right)^2 + \left(\frac{\delta (T_{out} - T_{in})}{T_{out} - T_{in}} \right)^2 + \left(\frac{\delta A}{A} \right)^2 \right]^{1/2} \tag{2.22}$$

The typical uncertainties associated to each term with 1.95 σ confidence interval are given in Table 2.1 following the work of [1]. These values result in ±10% accuracy in the heat flux using Eq. (2.22).

Table 2.1.: Uncertainties of heat flux measurement by calorimeter probe with $\pm 1.95\sigma$ confidence interval as given in [1].

Quantity	Uncertainty
$\dot{m}$	$\pm 0.5 \times 10^{-3}\,\mathrm{g.s^{-1}}$
ΔT	$\pm 0.8\,\mathrm{K}$
C_p	$\pm 0.1\,\mathrm{J.kg^{-1}.K^{-1}}$
A	$\pm 4.4 \times 10^{-6}\,\mathrm{m^2}$ (1/10 mm in diameter)

There are other heat flux gages available such as Gordon gauges and copper slug calorimeters, however they are not considered in this study.

2.2.2. Non-Dimensional Hydrodynamic Parameters and Numerical Simulations

The numerical tools used in Plasmatron were originally developed to determine the catalytic properties of TPS materials tested in Plasmatron. The boundary layer equations are convenient to compute a numerical heat flux and the boundary layer profiles, which would then be matched with the experimental heat flux to compute the flow around a probe in the ground facility. The boundary layer equations facilitate this procedure since they reduce to ordinary differential equations in the vicinity of the stagnation point [89]. However, the classical boundary layer equations are suitable for the high Reynolds number flows because the terms having $Re^{-1/2}$ are neglected in their derivation [7, 110]. In the case of the low Mach, high temperature and high viscosity flow in Plasmatron, the Reynolds numbers are very low (∼150) and one must consider the higher order terms with $Re^{-1/2}$, hence the costly Navier-Stokes equations are needed. Barbante uses the equation sets such as second order boundary layer equations or the viscous shock layer equations [89]. He proves in his PhD thesis that in the vicinity of the stagnation point, the higher order equation sets reduce exactly to first order boundary layer equations, which require less computational effort.

Kolesnikov states that one can solve the outer flow with Navier Stokes equations in LTE and match it to first order boundary layer equation solutions at a finite boundary layer thickness [111]. The choice of the boundary layer thickness, δ, can be arbitrary as long as the matching point lies in the linear part of the normal velocity component, u, profiles. In summary, it is more convenient to solve the outer flow and boundary layer separately.

The link between the two solutions are the non-dimensional hydrodynamic parameters (NDPs) defined at a distance δ. They indicate the hyrodynamic nature of the stagnation point flow. They are defined from the LTE Navier-Stokes computations and are used as boundary conditions in the boundary layer equations. It is convenient to define the boundary layer edge at the inflection point of the normal velocity gradient, $\partial u/\partial x$ [111] since the second order derivatives, such as the stress tensor, would go to zero. The exact determination of the inflection point is rather flexible according to Thoemel [112], who computed the boundary layer profiles and the heat flux by defining the δ with ±20% shift from the inflection point in either direction along the stagnation line and found very good agreements.

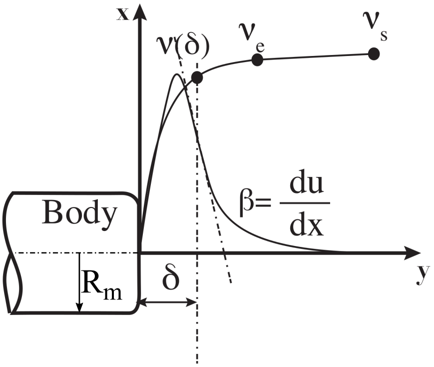

Figure 2.5.: The boundary layer velocity profiles in front of a probe in subsonic flow. Reference frame for Non-Dimensional hydrodynamic Parameter (NDP) calculation.

The boundary layer velocity profiles in front of a probe in subsonic plasma are depicted in Fig. 2.5. Although three independent NDPs are sufficient as shown by Degrez et al [113], the current in-house codes have a convention of five NDPs [114]. The derivation of the NDPs can be found in [113, 114]. With the reference frame given in Fig. 2.5, the five NDPs are defined as follows at the boundary layer edge defined at location δ:

$$NDP1 = \frac{\delta}{R_m} \tag{2.23}$$

$$NDP2 = u_{1e} = \frac{\partial u}{\partial x} \cdot \frac{R_m}{v_s} \tag{2.24}$$

$$NDP3 = u_{1y} = \frac{{R_m}^2}{v_s} \cdot \frac{\partial}{\partial y}\left(\frac{\partial u}{\partial x}\right) \tag{2.25}$$

$$NDP4 = \overline{v} = \frac{v(\delta)}{v_s} \tag{2.26}$$

$$NDP5 = \frac{v(\delta)}{v_e} \tag{2.27}$$

The three velocities defined as v_s, v_e and $v(\delta)$ are the torch exit velocity, the free stream velocity if there was no probe in the chamber and finally the velocity at the boundary layer edge given by the distance δ which is the inflection point of the velocity gradient profile. [1]

Conventionally at VKI, two distinct in-house codes, ICP CoolFluiD and CERBOULA, are used to solve the outer flow to determine NDPs, and a boundary layer code to compute the numerical heat flux and the boundary layer profiles, respectively. The flow in the Plasmatron chamber impinging on a probe is numerically simulated by ICP CoolFluiD code [115]. It simulates the equilibrium conditions in the chamber starting from the inductively coupled plasma torch until the downstream of the sample by solving steady and laminar Navier-Stokes equations. It accounts for the Joule effect and the Lorentz forces caused by the magnetic field and the magnetic induction. It is coupled with Mutation++ [116], the thermodynamic and transport

---

[1] The velocity gradient parameter is important and emphasized in this thesis. Therefore, it is important to mention how this variable is identified in the numerical codes. The velocities called v_s, v_e and $v(\delta)$ in Fig. 2.5, are called V_{torch}, V_s and V_e respectively in NEBOULA. Hence by the code notation, the velocity gradient at the boundary layer edge (at distance δ) is given as:

$$\beta = \frac{V_{torch}}{R} \cdot NDP2 = \frac{V_e}{NDP4} \cdot \frac{NDP2}{R} = V_s \cdot \frac{NDP5}{NDP4} \cdot \frac{NDP2}{R}$$

The above definition corresponds simply to the below equation with the notation given in Fig. 2.5:

$$\beta = NDP2 \cdot \frac{v_s}{R_m}$$

properties library for equilibrium air plasmas and the chemistry models can be adapted. In this study an 11 species air model is used. A code-to-code validation is performed at VKI with the code of the Institute for Problems in Mechanics of Moscow.

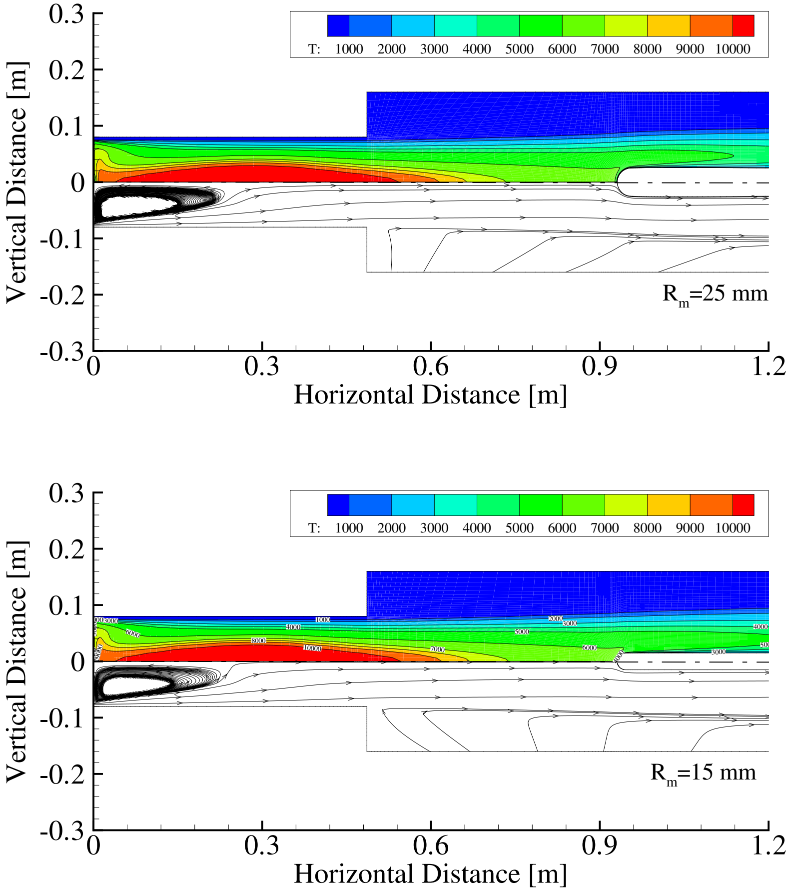

Figure 2.6.: Subsonic plasma temperature field and streamlines in Plasmatron chamber computed by ICP with two different probes of 25 mm (top) and 15 mm (bottom) radius at 6180 Pa and 95 kW Power (the amount going into the flow only).

The flow is solved on a 2D axisymmetric mesh. A grid convergence study is performed for three flat faced probes of 15, 25 and 57.5 mm radii [117]. The generic mesh for the 25 mm radius hemispherical probe is based on these and is widely used at VKI. Two examples of ICP computations are shown in

Fig. 2.6. The simulation times are typically 4-5 days for a new mesh; and 4 to 6 hours to run a different operating condition from a converged solution using the same mesh. The details of the reference 25 mm hemispherical probe and other meshes genereted in this thesis are given in Appendix C.1.

The second in-house code is the boundary layer equations solver CERBOULA [89]. It is a combination of two codes; NEBOULA and CERBERE. NEBOULA solves axisymmetric reacting boundary layers in chemical non-equilibrium and thermal equilibrium. CERBERE, on the other hand, uses the experimental heat flux and pressure data, and rebuilds the boundary layer edge properties by iteration on the boundary layer edge temperature, T_e. The iteration is converged when the numerical heat flux matches the experimental one.

CERBOULA's finite thickness boundary layer model configuration is used in this study but the code can also solve classical boundary layers. It can solve 2D axisymmetric bodies however only the 1D stagnation line solver is exploited here. The chemical models for the reaction rates can be user-defined and Park-1985 [118] model is implemented. The code is coupled with the PEGASE library [119] to compute the thermodynamic and transport properties.

It is important to note that in addition to the heat flux computations, the hydrodynamic NDPs are also needed for the iterative procedure for boundary layer edge enthalpy determination and the Flight-to-Ground Duplication discussed in Sec. 2.2.4.1 and in Sec. 2.3 respectively.

2.2.3. Pressure Measurements

For the subsonic plasma jet, the static pressure in the test chamber is measured with an absolute pressure sensor, Membranovac DM12 from Oerlikon Leybold Vacuum. It has a sensor accuracy of $\pm$ 70 Pa, which corresponds to ± 0.4 to 2% sensor error over the operational sub-atmospheric pressure range of Plasmatron. The performance and the stability of the Plasmatron vacuum pumps also affect the required static pressure value. During the test campaigns presented in this thesis, the mechanical instabilities caused typical fluctuations of $\pm 0.05\,\text{to}\,2.4\%$.

The dynamic pressure is determined by differentiating mechanically the total pressure measured by a Pitot probe and the static pressure port in the test section. The differential pressure is measured by a DP-15 Validyne, a variable reluctance pressure sensor. The magnitude of the dynamic pressure is very low compared to the static one. For a generic testing condition of 10^4 Pa, the resulting dynamic pressure is about $0.1-0.2\%$ of the static pressure. The measurement error on dynamic pressure has been evaluated 15% through the measurement chain. Although its effect for total pressure determination is negligible, its contribution to the presented Flight-to-Ground Duplication procedure can be important and is discussed in Section 2.3.

2.2.4. Enthalpy Determination Techniques

One of the three duplication parameters of LHTS is the enthalpy. This section covers first the classical method to rebuild the boundary layer edge enthalpy using the experimental data. Then, the proposed Enthalpy Probe technique principles are presented. Additionally, the application of two optical emission spectroscopy methods for temperature, thus enthalpy determination is given. Several experimental campaigns are conducted and their data contributed to the experimental and numerical databases discussed in the Sec. 2.2.5 and 2.2.6.

2.2.4.1. Classical Approach: Enthalpy Rebuilding

Conventionally in Plasmatron, the boundary layer edge properties are determined from an iterative postprocessing method and the boundary layer profiles are rebuilt numerically after the experiments. The in-house rebuilding code CERBOULA [89] is used for this purpose as described in Sec. 2.2.2.

The rebuilding procedure requires measured values of heat flux with a given probe, and the dynamic and static pressures. However, it also requires additional inputs such as the non-dimensional hydrodynamic parameters (NDPs), the catalytic efficiency of the heat flux probe (which is often called "reference catalycity of copper") and the surface temperature of the water cooled probe. The NDPs are computed with the ICP Code [115] specific to the experiment configuration as discussed in Sec. 2.2.2. The reference catalycity of copper includes the recombination of nitrogen and oxygen atoms at the wall. This is a source of error in the rebuilding procedure since the catalytic efficiency is a function of the free stream conditions and not accurately known. In this thesis, the values taken from [1] are used. Finally the wall temperature of the probe is set to 350 K thanks to the cooling water circuitry.

Table 2.2.: Reference catalycity values for enthalpy rebuilding procedure for flat faced copper heat flux probes at different static pressure ranges [1].

Pressure Range	Probe Radius		
	57.5	25	15
Pa		mm	
$1200 < p_s \leq 5000$	0.05	0.1	0.1
$5000 < p_s \leq 10000$	0.005	0.01	0.01
$10000 < p_s$	0.001	0.005	0.005

The uncertainty of this method is computed by a detailed uncertainty quantification study by Villedieu et al. [120]. They concluded that the heat flux and dynamic pressure measurement errors have the highest impact on the rebuilt enthalpy. Additionally they found out that for reference copper catalycities lower than 0.15, the resulting uncertainties of edge total enthalpy become larger around 6.3%. Nawaz et al. [121] show that the copper catalycities for the most conditions discussed here are lower than 0.1, which is in agreement with the values given in Table 2.2. For other cases with reference copper catalycities higher than 0.1, an uncertainty of 6% is assumed.

2.2.4.2. Enthalpy Probe

The “enthalpy probe” is a means of direct intrusive measurement for local enthalpy determination. The experimental setup is summarized in Fig. 2.7. It is a heat exchanger tube of 6 mm inner diameter, that is surrounded by an insulating water cooled jacket with the outer dimensions of the ESA standard probe [91] of 25 mm radius flat face cylinder with rounded corners of 11.75 mm radius as shown in Fig. 2.8. The probe is connected to a vacuum pump and the free stream plasma is sucked inside the heat exchanger. The heat is only exchanged at the inner wall of the heat exchanger where the plasma is flowing, thanks to the insulation between the water circuits. Between the vacuum pump and the enthalpy probe, there is a rotameter to measure the plasma flow rate which is adjusted by the two valves as depicted in Fig. 2.9. Since the calibration of rotameter devices rely strongly on the inlet pressure, a mercury manometer is also placed at the inlet.

The complexity of the aerothermodynamics of a chemically reacting plasma in VKI Plasmatron was discussed earlier. Before going any further with the measurement technique details, one has to make the following assumptions in order to relate the exchanged heat inside the probe to the free stream enthalpy:

- The testing gas is a chemically reacting perfect gas mixture.
- The special case of local thermodynamic equilibrium is valid.
- The enthalpy is a function of two intensive state variables [7] which are chosen as temperature and pressure, and at a given pressure is given as:

$$h_i(T) = C_{p,i}(T)T + \Delta h^0_{F,i} \tag{2.28}$$

$$h = \sum_{i=1}^{N} y_{i,e} h_i \tag{2.29}$$

where h_i is species specific enthalpy (enthalpy per unit mass), h is the total specific enthalpy, C_p is the specific heat, T is temperature and p is pressure. (Note that the perfect gas state equation $pv = RT$ is also valid for chemically reacting perfect gases, for each species, and specific volume, v, could be chosen instead of p.)

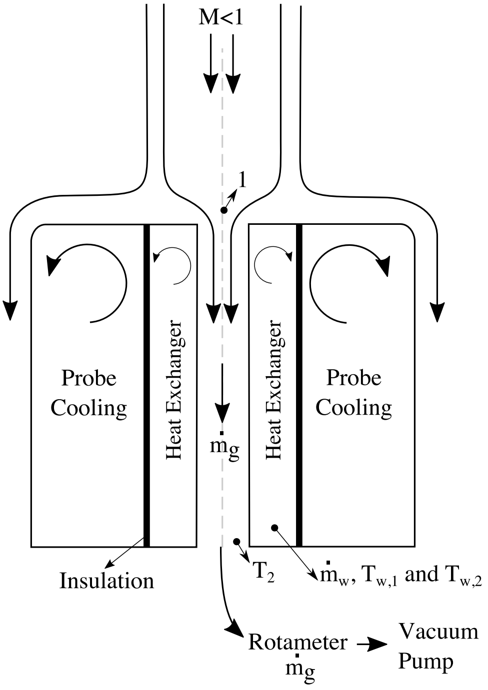

Figure 2.7.: Enthalpy probe setup. The plasma is sucked in the 6 mm diameter orifice with a vacuum pump. The heat is transferred along the 14 mm outer diameter heat exchanger. T_2, $T_{w,1}$ and $T_{w,2}$ are measured with a type E thermocouple and the flow rates $\dot{m}_g$ and $\dot{m}_w$ are measured with a rotameter.

- The term corresponding to the heat of formation of each species i, $\Delta h^0_{F,i}$ is taken into account.

Using the above assumptions, the heat balance between the hot plasma sucked inside the heat exchanger and the heated water inside the heat exchanger reads:

$$h_1 = h_2 + \frac{\dot{m}_w}{\dot{m}_g} C_{p,water} \left(T_{w2} - T_{w1}\right) \tag{2.30}$$

where h_1 is the enthalpy at the inlet location shown as 1 in Fig.2.7, T_{w1} and T_{w2} the water temperatures at the inlet and outlet of the cooling circuit, and $\dot{m}_w$ and $\dot{m}_g$ are the water and plasma flow rates respectively. The term $h_2 = C_{p,g}T_2$ corresponds to the enthalpy at the back of the heat exchanger. It is later confirmed by the experiments that the temperature in the back of the heat exchanger is low enough that no dissociation occurs and one can

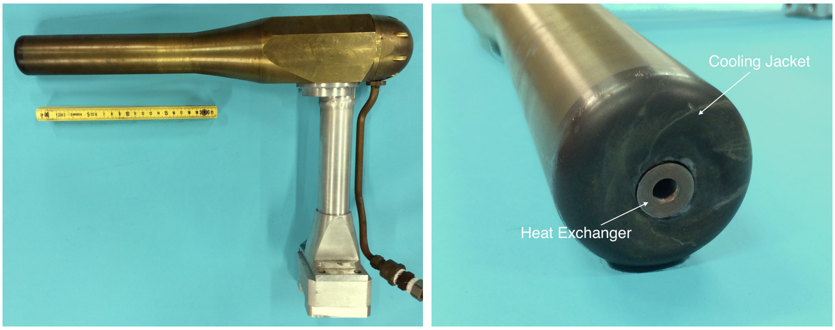

Figure 2.8.: Enthalpy probe and the front view with the heat exchanger.

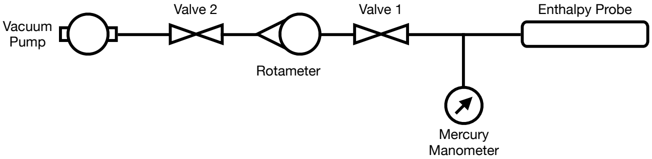

Figure 2.9.: Enthalpy probe experimental setup overview. Courtesy: Thomas Rees [122].

show that $\Delta h^0_{F,i} = 0$. Therefore the enthalpy at the exit can be determined as $h_2 = C_{p,g}T_2$. The inlet and outlet water temperatures as well as the sucked plasma temperature at the back of the heat exchanger T_2, are measured by a type E thermocouple. $C_{p,g}$ is computed by VKI in-house library Mutation++ [116], the thermodynamic and transport properties library for equilibrium air plasmas.

To make sure h_1 is the enthalpy at the boundary layer edge, one has to define the correct suction rate in order not to disturb the outer flow. As will be shown by the experimental data, a lower suction rate leads to a too high enthalpy reading while a higher suction leads to a too low enthalpy reading. Fig. 2.10 shows the stream lines in front of the probe and how the flow can be affected.

The balanced suction rate is unique for each test condition and unknown prior to the actual measurement. During the experiment, a number of suction rates is applied by means of a rotameter and the correct suction rate is found by an iterative post-processing method. The iterative procedure solves two equations correlating the specific enthalpy seen by the probe and the sampled plasma suction rate. The correlation function between the suction rate and the measured enthalpy is of the following form, inversely proportioned as mentioned previously:

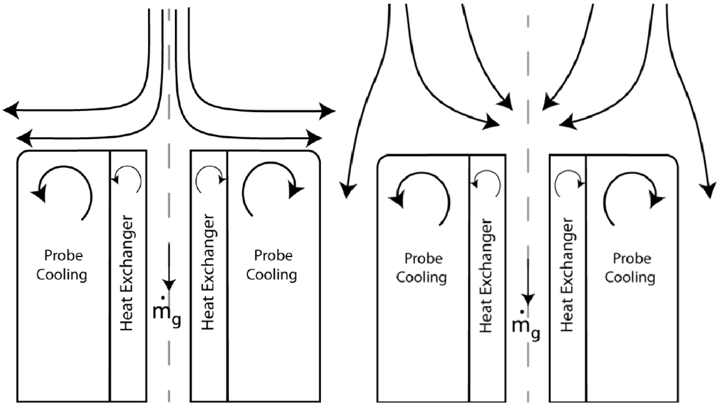

Figure 2.10.: Effect of plasma suction on the streamlines. Left: Low suction. Right: High suction.

$$h_{read} = A\frac{1}{\dot{m}_g} + B \tag{2.31}$$

while the plasma sampling rate reads:

$$\dot{m}_g = \rho_{@h_{read}} VS = \rho_{@h_{read}} \sqrt{\frac{2P_{dyn}}{\rho_{@h_{read}} k_p}} \pi R^2 \tag{2.32}$$

where V is the velocity in the stagnation ring (assumed constant), S is the surface of the inner ring, P_{dyn} is the dynamic pressure, R is the radius of the heat exchanger, k_p is the Barker correction coefficient and ρ is the density of the hot gas. The dynamic pressure is measured by means of the Pitot probe available in Plasmatron facility. The Barker coefficient takes into account the effect of viscosity, thus Reynolds number, in Pitot-like probes [123], such as the enthalpy probe. Barker showed that the viscous interaction between the flow and the probe leads to high pressure measurements for low Reynolds numbers (below ∼100) as it is the case in Plasmatron. The correction coefficient k_p is taken 1.1 in this study.

First h_{read} is determined for each measured $\dot{m}_g$ from Eq. (2.30). Then, the measurement points are fitted into the form given in Eq. (2.31) and the coefficients A and B are found. The correct suction rate $\dot{m}_g$ should satisfy both Eqs. (2.31) and (2.32). They are solved iteratively for plasma sampling rate $\dot{m}_g$ and the enthalpy h. Since the enthalpy does not appear explicitly in Eq. (2.32), the matching is made on the density, $\rho_{@h_{read}}$. The enthalpy at the density (and the measurement pressure) determined from Eq. (2.32), is computed by Mutation++ library. Finally, this enthalpy is compared to the h_{read} in Eq. (2.31) until both equations are satisfied. An example is shown in Fig. 2.11, where the experimental suction rates are fit to the correlation and the correct specific enthalpy is iteratively calculated.

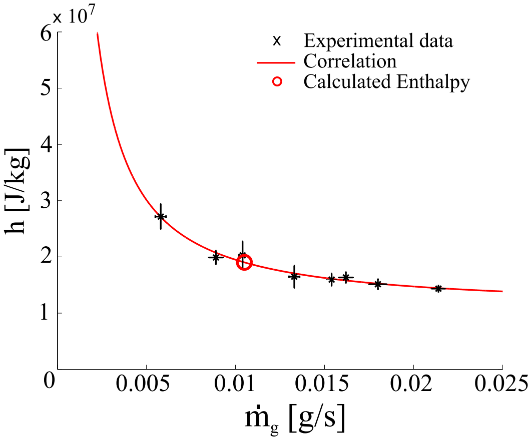

Figure 2.11.: Correct suction rate computation of a test case 4b of 6180 Pa and 651 kW/m^2 with hemispherical 25 mm radius heat flux probe. The Plasmatron power is 170 kW.

The testing procedure follows the steps below:

1. The static pressure is set according to the test matrix.
2. The required reference heat flux is set by water cooled copper calorimeter measurement.
3. The dynamic pressure is measured by the Pitot probe at the free stream conditions set by the pressure and heat flux given above.
4. Once the enthalpy probe is injected, the suction rate should be adjusted starting from the lowest value possible and increasing step by step to the highest value possible.
5. Before recording each mass flow rate, a minimum settling time of 4 seconds should be allowed. This is an observed value from the presented test matrix. It is determined as the time until the plasma temperature T_2 reaches the steady state.
6. The heat exchanger temperatures should be measured for a minimum duration of 10 seconds where the rotameter level is stable.
7. A minimum number of 8 to 10 measurements should be done for each free stream condition to be able to fit the curve in Eq. (2.31) (or Fig. 2.11) more accurately.

8. Since the rotameter calibration cannot be done simultaneously, the mercury manometer values should be noted down together with the rotameter levels.

9. (Optional) The "mark" tool of the Plasmatron data acquisition system is recommended between different suction rates for an easier data reduction at post-processing.

The free stream enthalpy is measured with the enthalpy probe in a testing envelope of pressures from 6180 to 23482 Pa and reference heat fluxes (25 mm hemispherical probe) from 360 up to 1030 kW/m^2. A rudimentary Monte Carlo analysis is also performed to quantify the sensitivity of different input elements on the resulting enthalpy. The errors are given as 2σ and a gaussian distribution is assumed. The major sources of error are the calibration of the Yokogawa KL1 rotameter for plasma suction, the water rotameter, the temperature measurements and the dynamic pressure measurements. The plasma suction rotameter error and the manometer reading error are taken as 0.5 mm. The water rotameter error is taken 3% of the measured flow rate. The temperature errors are taken as the measurement fluctuations as this error was bigger than the thermocouple calibration error. Finally the dynamic pressure error is assigned individually for each flow condition since the error deviates a lot for lower and higher chamber pressures. Table 2.3 shows the test matrix, the experimental results together with the maximum measurement error result of the Monte Carlo analysis and the converged $\dot{m}_g$ values.

The test cases 6c, 8a and 8b show quite high errors when compared to other test cases. The error is much higher when the suction rate *samples* during the test do not cover a wide enough range for an accurate fit. The fitted curves for the cases 6c and 8a are depicted in Fig. 2.12. Both reveal a similar type of inaccurate curve fitting. In both cases, there is not enough data points at low suction rates. The first point of the case 6c has a very big uncertainty and all the points for case 8a stay on the right side of the converged solution. The experiments presented here give an order of magnitude to the converged suction rates in a wide range of chamber pressures. In the future, these tests can be repeated with these preliminary values by focusing on the lower suction rates.

It can be seen in Table 2.3 that no testing condition below 6180 Pa is available. The main reason for that is the performance of the vacuuming procedure. At lower pressures, even at 6180 Pa, it is very difficult to keep the plasma suction steady since the rotameter floater is bouncing. A damping tank inserted between the vacuum pump and the rotameter was not enough to damp the unsteadiness. Therefore, the current experimental setup has a lower Plasmatron chamber pressure limitation. It should also be mentioned that the lower suction rates induces more instability in the rotameter. This bouncing did not allow acquiring enough data points for an accurate curve fit. This was taken into account in the error estimation and for some cases

Table 2.3.: Enthalpy probe test conditions, measured mean enthalpies and associated errors. All measurements are taken at 16 g/s Plasmatron air mass flow rate. $\dot{q}_{std}$ corresponds to the flat faced standard probe with 25 mm radius and P_{Static} is the static pressure in the test chamber. The individual suction rate measurements are detailed in Appendix A.1 for each test condition.

Test	P_{Static} [Pa]	Power [kW]	$\dot{q}_{std}$ [kW/m^2]	$\dot{m}_g$ [mg/s]	Enthalpy [MJ/kg]	Max. Error (2σ) [MJ/kg]
4b	6180	164	651.73	10.5	19.02	2.81
4bbis6	10000	146	460.50	8.4	18.37	3.18
4bbis	10000	168	642.68	9.5	20.42	3.05
4bbis4	10000	192	858.06	9.7	28.24	3.08
4bbis5	10000	214	1039.64	11.0	28.01	3.18
5a	11967	140	384.24	8.8	12.62	3.14
5c	11967	175	727.43	10.2	23.60	4.04
6b	17143	162	582.97	8.3	18.10	8.36
6c	17143	184	813.49	9.2	23.39	10.71*
7a	19815	142	381.79	7.3	13.75	1.91
7b	19815	147	425.87	10.3	13.09	4.79
7c	19815	184	714.68	10.0	17.07	4.25
8a	23482	142	364.85	6.3	14.87	12.36*
8b	23482	163	559.32	7.5	17.91	13.77*
8c	23482	181	781.97	9.1	21.12	2.59

*High errors as a result of insufficient or poor set of data points.

and wrong enthalpy values were found. For example the case 4a, not shown here, with 6180 Pa and 150 kW power converged to an enthalpy of 203.16 MJ/kg which is taken out of the test matrix. This was due to the fact that only five suction rate samples were recorded and those were at quite high rates which resulted in a wrong hyperbolic curve fit.

Another limitation of the procedure is the high heat fluxes. This is simply due to the design of the heat exchanger and the efficiency of the water cooling. There is a recirculation bubble forming inside of the front bearing which is exposed to the plasma flow. The original design could not take cold wall reference heat fluxes above 600 kW/m^2 and the heat exchanger often melted at the bearing. A new heat exchanger was designed and the test matrix given in Table 2.3 was built. However, when the probe was exposed to a plasma of pressure 10000 Pa and 1700 kW/m^2, the bearing could not stand the heat and melted. For the moment, no new design is proposed for higher heat flux applications.

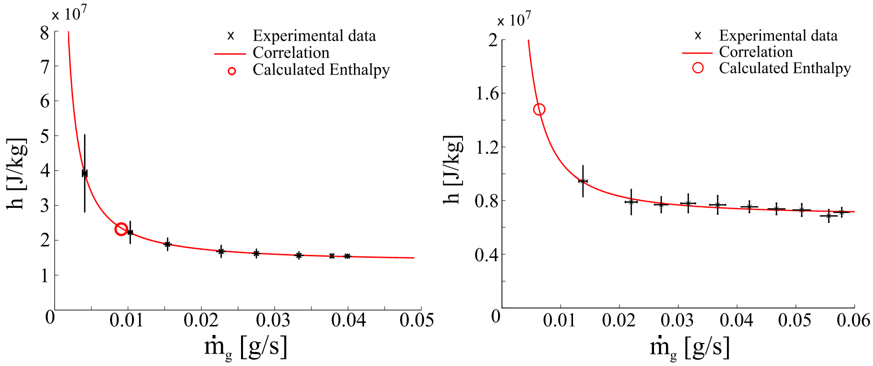

Figure 2.12.: Examples of poor hyperbolic fits for iterative solution for the case 6c (left) at 17143 Pa and 190 kW, and the case 8a (right) at 23482 Pa and 150 kW.

2.2.4.3. Optical Emission Spectroscopy

Under the assumption of LTE, if the temperature at a given location in the plasma jet can be determined, one can determine the enthalpy knowing the pressure using the Mutation++ [116]. Two optical measurement techniques based on emission spectroscopy is considered in this study. ARTEmiS works with the Boltzmann method with hydrogen lines and REDES with CN violet and N_2^+ molecular lines.

ARTEmiS: Acquisition of Real-Time Temperature by Emission Spectroscopy

ARTEmiS acquires the visible spectral range and processes the data in real time to provide the plasma temperature, thus enthalpy. ARTEmiS is initially developed for Argon-Hydrogen plasma and it uses H_α (656.27 nm) and H_β (484.12 nm) atomic emission lines in the Balmer series [124]. The temperature can be detected from the very well known Boltzmann technique; it is a function of the measured intensities and known spectroscopic data of the selected emission lines.

ARTEmiS tool works significantly well in Argon-H_2 plasmas, however the test case in this thesis is QARMAN and it will perform an atmospheric to Earth. Thus the applicability of the method in air plasma is investigated. Although some experiments (mainly at low pressures and high heat fluxes) in air plasma at Plasmatron facility showed good results, the atomic hydrogen lines are not easily detected next to the strong emission of other species. Water injection to the air plasma was tried however despite the high temperatures, due to the low chamber pressure the water often turned to solid ice particles which changed the flow nature. Different injection locations and flow rates as well as other hydrogenated species are tried however no satisfactory setup was accomplished. Therefore, the idea of using ARTEmiS in air plasma was abandoned and another method based on ratios of molecular emission lines is introduced. The details of the method are not further discussed here but can be found in Appendix A.2 with its application to Argon-Hydrogen plasma in VKI Minitorch facility.

REDES: Real-time Enthalpy Determination with Emission Spectroscopy REDES is an optical emission spectroscopy tool to measure the plasma temperature in real-time, thus enthalpy under LTE assumption as it was the case for ARTEmiS. The tool is made to work with low cost low resolution Ocean Optics HR4000 spectrometer in LabView environment. It is known that the molecular emission line features such as the peak and the integral area under the peaks is sensitive to temperature [125]. REDES uses a method adopted from Fletcher [125] for generic air plasma. Cipullo [126] applied it to Plasmatron conditions however not as a real-time tool. It is based on comparing a theoretically computed spectrum to the measured one during the plasma test.

The theoretical spectra are generated at a given pressure, for a range of temperatures, thus for equilibrium plasma. There is a number of codes in literature to compute theoretical spectra; in this study we used Specair [127].

Having the theoretical database ready for the facility chamber pressure, REDES measures the experimental emission lines of N_2^+ first negative ($\Delta\nu = 0$) and CN violet ($\Delta\nu = 0$) molecules. Both of these transitions occur around 390 nm in wavelength. The two lines are shown in Fig. 2.13. REDES has two modes to determine the equilibrium temperature: it processes the ratio of the peaks of these two features and the integrated area under them, referred as integral ratio from now on. Fig. 2.13 also shows the peak locations and the integrated areas. To determine the area, the intensities are integrated over 387.41 and 389.27 nm wavelength for CN and over 390.07 and 392.19 nm for N_2^+.

The two theoretical databases consist of the peak ratio over temperature and the integral ratio over temperature for a given pressure. Fig. 2.14 shows examples of these two curves. REDES then compares instantaneously the ratio to the theoretical curve to determine the temperature. To convert the temperature to enthalpy, just like ARTEmiS, it uses a premade library from Mutation++ at the testing pressures. A measurement example is given in Fig. 2.15 at 20000 Pa and 1.95 MW/m^2 (by standard heat flux probe).

To summarize, it allows us to monitor the realtime temperature and enthalpy during the test. This is specially useful if one need to adjust the Plasma operating condition to a free stream enthalpy. The test matrix for QARMAN testing is built in this way; taking the entry trajectory pressure and enthalpy, and converting it to Plasmatron operating conditions: pressure and power. As presented in Sec. 2.2.5, for each pressure, enthalpy over a range of power is measured to build the test conditions. The results are shown in Sec. 2.2.5 in comparison with other methods. Additionally, the

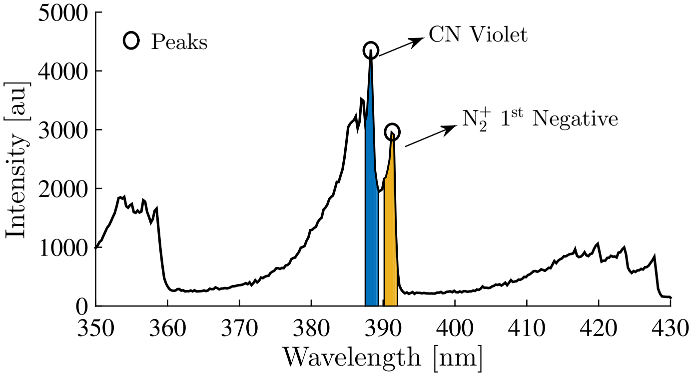

Figure 2.13.: CN violet and N_2^+ 1^{st} Negative emission line intensities as a function of wavelength for 20000 Pa and 1.94 MW/m^2. The peaks and the integrated areas for the peak/integral ratio method are also shown.

details of each test condition are given in Appendix A.3.

A limitation of the method is the temperature bound. As it can be seen in Fig. 2.14, the theoretical curves for both peak and integral ratios stay constant at about 8000-8500 K. This means that there is no unique ratio to be matched to the experimental curve. The limitation for the lower temperature is the signal to noise ratio. As the temperature of the plasma decreases, the emission gets weaker so the acquired spectrum is too noisy to make accurate measurements. The error of the measurement is in the range of 10% in intensity as was the case in the previous technique. The estimated measurement errors specific to the test conditions are presented in Sec. 2.2.5.

It should be noted that the ratio method is a line of sight, steady measurement. This is a disadvantage since the plasma jet fluctuates at a certain frequency. This plasma jet fluctuation frequency is highly pressure dependent and the complete characterization of this frequency over Plasmatron operating conditions is still missing although Cipullo [126] made a study to measure the dominant frequencies over a range of conditions. The spectrometer integrates the emission over a time period and even averages some scans, which results in an acquisition frequency of about 2 or 4 Hz depending on the plasma power. Although never published, the effect of integration time on temperature measurements was studied internally at VKI. It is found that the peak ratio is much more sensitive to the fluctuations than the integral ratio method. However there is a significant overshoot of enthalpy for both cases. This is simply because the temperature found from integrating emission over a time period is not the same as if we take instantaneous temperature measurements and average it over time. Cipullo [126] stated this is either due to the LTE assumption validity or due to the fluctuations.

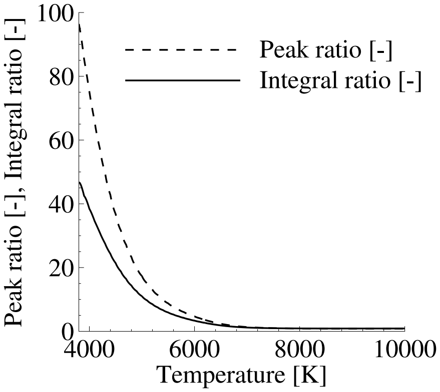

Figure 2.14.: Theoretical integral and peak ratios computed for 20000 Pa by Specair 2.2 [127].

According to Lequang [128], the high pressure cases in Plasmatron can be considered LTE. However, the results with REDES show that even at high pressures, both methods overshoot [129]. Therefore, it can be concluded that the overshoot is caused by jet fluctuations.

No quantification of the overshooting is performed and its pressure dependence is not studied further. Instead a new technique is currently being investigated at VKI, which uses high speed 2D imaging of the plasma torch, using a filter for the atomic oxygen line at 777 nm. It is intended to overcome the jet unsteadiness problem by making high speed acquisitions at frequencies higher than the fluctuation frequencies. The setup was originally based on the work of Bachmann et al. [130], using a more complex setup. The preliminary results are reported in [131]. Improvements are still on-going at VKI, by using a CCD array to 2D image the temperature field with the oxygen triplet at 777 nm.

2.2.5. Experimental Database

This section summarizes the results of the experimental campaigns conducted with the enthalpy probe and the optical emission spectroscopy tool described previously. The results are also compared to the rebuilding procedure and another emission spectroscopy method using oxygen triplet at 777 nm. Moreover, the required inputs for building the numerical database and eventually for the Flight-to-Ground duplication methodology (Sec. 2.3) are developed.

All the test conditions are derived from QARMAN entry trajectory given in Table 2.4. The test names given previously in Table 2.3 also come from these cases by keeping the pressures same but changing the power of the

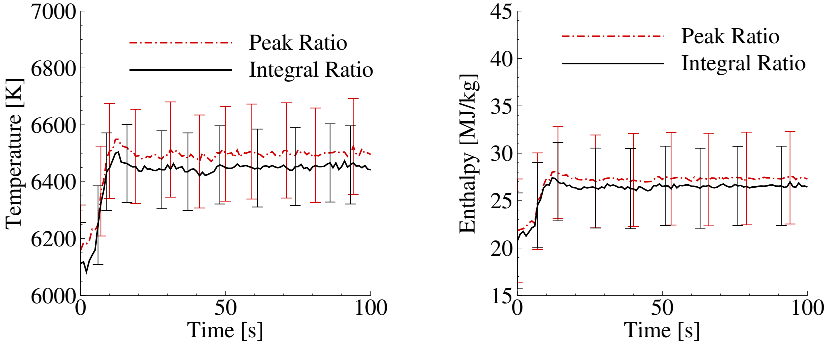

Figure 2.15.: Temperature and enthalpy measurements at 20000 Pa and 1.94 MW/m^2.

Table 2.4.: Experimental test cases based on QARMAN trajectory.

Case Name	P$_{dyn}$ [Pa]	Altitude [km]	Velocity [km/s]	Enthalpy [MJ/kg]
1	1035.05	80	7.51	28.20
2	2127.6	75	7.33	26.86
3	4156.7	70	7.07	24.99
4	6180.3	66	6.84	23.39
5	11967.9	60	6.25	19.53
6	17143.4	55	5.67	16.07
7	19815.3	53	5.34	14.26
8	23482.9	50	4.81	11.57

facility. The basic idea behind is to match the total pressure and the free stream enthalpy in the test facility with the flight conditions. Prior to tests, the enthalpy values are not known. The real-time measurement tool REDES is therefore used to build the initial conditions. The chamber pressure was fixed and the power is modified until the target enthalpy is measured. Of course, due to the enthalpy measurement uncertainties, multiple powers are taken in the test matrix to allow enough points for an interpolation if necessary.

Due to Plasmatron operation techniques, it is always better to calibrate a test condition using pressure and heat flux. Based on the philosophy of the flight to ground duplication technique, for a given free stream, data from different heat flux probe radii are necessary. These probes are conventionally called as Damköhler probes; *frozen* probe with 15 mm radius, *standard* probe with 25 mm radius and *equilibrium* probe with 57.5 mm radius[2]. Since the facility can accommodate only three probes at a time, the enthalpy probe measurements had to be conducted separately than the heat flux measurements. The frozen hemispherical probe of 15 mm radius is kept in the facility for all tests to provide a reference. All the test conditions including the power and heat fluxes measured by different sized probes are provided in detail in Appendix B.

Some cases for the enthalpy probe, optical emission spectroscopy and rebuilding are plotted together in Fig. 2.16 for 10000 Pa and 23400 Pa. For the full set, refer to Table A.3. In both plots, the increase in heat flux is evident except the integral ratio technique. The plot for 23400 Pa includes the enthalpy probe data of 8a and 8b which have quite large uncertainties as explained previously and shown in Fig. 2.12, however the mean values are consistent with the heat flux increase and the rebuilding data. It can also be seen that the ratio method often has smaller error margins and they often do not overlap with other methods. The main reason is that the time integration of the spectroscopic measurements lead to an overshoot of temperature and this overshoot is not quantified therefore not considered in the error estimation.

Fig. 2.16 also includes the spectroscopic data from the oxygen triplet at 777 nm[3]. This experimental method consists of measuring the spectral radiance of the excited oxygen triplet at the predicted boundary layer edge by numerical simulation of the test chamber. The spectral emission is then rebuilt through Abel inversion and straightly related to a temperature assuming LTE [132]. Knowing the pressure and temperature, the thermodynamic properties of the gas mixture at equilibrium can be then computed including enthalpy. The applicability of LTE is limited by Plasmatron operating conditions. The test case considered in this study can be assumed LTE according to [128] where the electron densities are measured and compared with the Griem threshold [132]. The accuracy of the measurements is calculated around 7%. Associated error bars are also given in Fig. 2.16.

Fig. 2.16 depicts a trend that the integral and peak ratios give higher enthalpies than the rebuilding, enthalpy probe and O777 method. When enough suction rate points are present, the enthalpy probe measurements have a good agreement with the O777 method and the rebuilding (See Table A.19 for the full dataset). It should be noted that the enthalpy probe and the O777 methods are more cumbersome than the ratio method due to the required post processing efforts. The ratio method does not rely on Abel inversion and does not require intensity calibration. Once the theoretical ratio databases are built, the enthalpy is provided in real time. Instead the O777 method setup has to be calibrated and more sophisticated spectrometers have to be used for instantaneous and line-profile acquisitions for Abel

---

[2] Only hemispherical Damköhler probes are used in this thesis.

[3] These experiments are performed by Dr. Damien Le Quang Huy at VKI Plasmatron facility

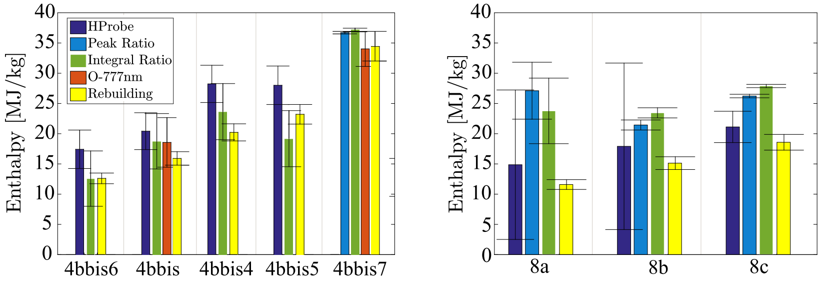

Figure 2.16.: Comparison of enthalpy measurements at 10000 Pa (left) and 23400 Pa (right). The data for all cases are given in Appendix A.4.

inversion. However, as discussed in the previous section, the ratio method constantly overshoots.

In summary, the experimental database provides the pressure-power configuration of Plasmatron operations that gives a certain free stream enthalpy. This enthalpy is targeted from the QARMAN entry trajectory. Determination of the most accurate enthalpy measurement method is still an on-going study at VKI Plasmatron, which is not constrained with the techniques presented here.

Additionally, the dynamic pressure is measured at those free stream conditions. The power and the dynamic pressure measurements are necessary for building the numerical database of Plasmatron simulations, which are required for the flight-to-ground duplication methodology described in the next section and the ablation characterization campaign analysis in Chapter 3.

2.2.6. Numerical Database

A large experimental database was constructed based on the vehicle entry trajectory. The same is done here numerically to determine the NDPs for each of these conditions both as input to the enthalpy rebuilding and to the Flight-to-Ground duplication methodology discussed in the following section. Conventionally, each time an experiment is done in Plasmatron, the NDPs are not computed with the tie consuming ICP. Instead, the existing regressions [1] are often used to determine the NDPs to be inserted in the rebuilding code CERBOULA. Unfortunately, the regressions only exist for a fixed probe geometry and allow only to modify pressure or power. The Flight-to-Ground Duplication methodology specifically necessitates a “fitting” procedure including the probe radius.

A large number of ICP computations were performed with different hemispherical probes at a large range of test conditions. The built envelope ranges and probe sizes are given in Table 2.5. It was mentioned in Sec. 2.2.2

that three mesh with 57.5, 15 and 6 mm radii probes are generated based on the reference mesh of hemispherical 25 mm probe. The details of the mesh can be found in Appendix C.1. A total number of 221 computations were conducted with ICP CoolFluiD code, combining the pressures, powers and radii. The inlet air mass flow rate is kept constant to 16 g/s. The air-11 chemistry model is used and the probe is always placed 445 mm away from the torch exit. The computed NDPs are given in Appendix C.2.

Table 2.5.: Test condition ranges of the ICP computations for building the numerical database. All computations are done for a mass flow rate of 16 g/s.

Pressure $[Pa]$	ICP Power $[kW]$	Probe Radius $[mm]$
1500	60	6
2127	65	15
4156	67.5	25
6180	70	57.5
7500	75	
8500	85	
10000	95	
11968	105	
12500	115	
13500	120	
15000	130	
16000	135	
17143	145	
18015	155	
19815	165	
21415	175	
23483	195	

Building an artificial neural network (ANN) for NDP computations is an ongoing study at VKI [133]. The network is used to compute the NDPs instantly without running the time consuming ICP computations. In order to increase the accuracy of such system, a large number of data points is required. Performed simulations are the first inputs to the ANN program. The ANN has the following input variables: pressure, power, probe radius, probe distance to the torch, mass flow rate and test gas. In the interest of this thesis, so the Flight-to-Ground Duplication methodology, only three input variables are considered: pressure, power and probe radius. A separate network is built for each NDP and they are used in the iteration process of the Flight-to-Ground Duplication as explained in Sec. 2.3.

It is also important to note that the ICP power is not equal to the Plasmatron power discharge in the previous section. The ICP power is the power going to the plasma only. Plasmatron has a certain efficiency, which changes with test conditions but the efficiency is in average around 50%. The power efficiencies of the experimental cases can be found in Appendix B.

2.3. Flight to Ground Duplication

A “Flight to Ground” duplication methodology is proposed in this section in order to duplicate accurately the three similitude parameters; p, h and β. The main improvement compared to existing methodologies, discussed in Sec. 2.1.3, is that no assumption of spacecraft geometry is made in terms of nose radius or axisymmetry. Although the example of QARMAN vehicle is discussed in this study, the procedure is applicable to any entry probe.

2.3.1. Iterative Procedure Overview

The work logic of the proposed iterative approach for an accurate aerothermochemical duplication is presented in Fig. 2.17. The procedure starts by computing the flight conditions of the vehicle along its atmospheric entry trajectory. An equivalent sphere flying at hypersonic velocities is defined by the stagnation line properties of the computed flight trajectory. An equivalent *hypersonic* sphere has identical stagnation line profiles with the actual entry vehicle and is unique for a given altitude and vehicle, thus changing along the trajectory together with the free stream parameters. Once the equivalent hypersonic sphere is found, β can be determined from Eqs. (2.16)-(2.20). Next, an equivalent *subsonic* sphere is defined for the subsonic plasma flow using the experimental data of pressure and enthalpy introduced in Sec. 2.2.5. The subsonic equivalent sphere also has the same stagnation region aerothermochemistry as the hypersonic vehicle and the equivalent hypersonic sphere. Using the equivalent subsonic sphere, the model geometry for the plasma wind tunnel conditions is determined. To do so, the boundary layer models used for computations are adapted according to the appropriate Reynolds number regime in the test facility. Finally, an iterative process takes place for converging the computed ground test conditions and the model geometry found from the procedure making use of the numerical database presented in the previous section. Each step of the methodology is detailed in the next section with application to QARMAN entry probe at its trajectory point of 66 km altitude.

2.3.2. Hypersonic CFD and Boundary Layer Approach for Stagnation Flows

The 3D numerical aerothermodynamic database for QARMAN is provided to the author by the QARMAN team. It consists of the steady computa-

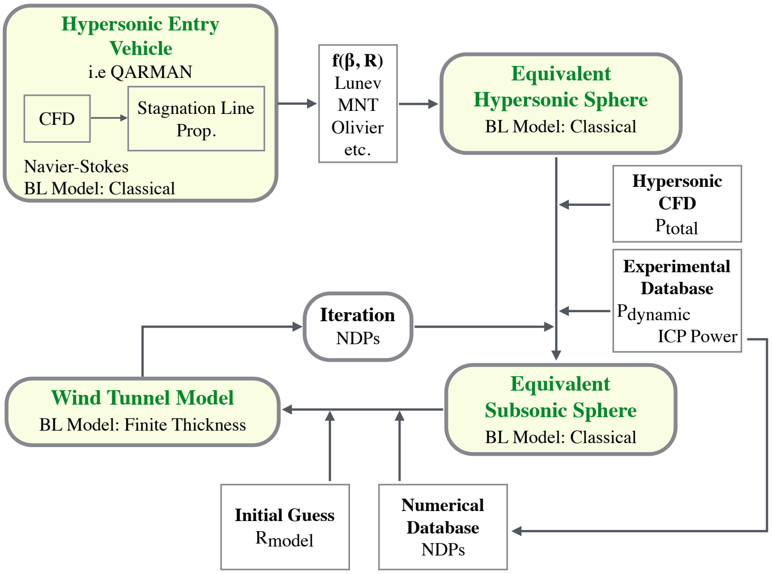

Figure 2.17.: Overview of the iterative Flight to Ground Duplication procedure.

tions of the different locations of the QARMAN entry trajectory with the commercial code CFD++ [134]. CFD++ solves Navier-Stokes equations and the computations are done, assuming thermal equilibrium and chemical non-equilibrium with a 7-species air model (Park 1985 [118]), for a non-catalytic wall in radiative equilibrium. The fine 3D hemisphere mesh has the front unit of QARMAN vehicle and it has 1267807 mesh points in total. The wall proximity is well resolved with the first grid point being 5 μm away from the wall. Although coarsely, the shock position is captured. The test case presented here corresponds to the 66 km altitude trajectory point computed as well with a non-catalytic surface with a radiative equilibrium boundary condition applied at the TPS surface. The free stream conditions are provided in Table 2.6.

Table 2.6.: Free stream conditions for 66 km altitude.

V_∞	6845.59	m/s
P_∞	8.66	Pa
ρ_∞	$1.32075.10^{-4}$	kg/m^3
T_∞	228.925	K

This computationally expensive analysis was carried out omitting any aspects related to the ablative TPS used in the QARMAN mission (e.g., vehicle shape change, pyrolysis gas blowing effect on attitude, etc.). A more detailed analysis would consider these aspects to quantify their effects on the aerothermodynamic database generation. However, the virgin shape of the vehicle was considered suitable for the purpose of the present analysis, which intends to describe the development of the Flight-to-Ground Duplication methodology. It is also important to stress that the presented methodology should be consistent with the gas surface interaction phenomena. Ref. [135] shows to this respect that the LHTS methodology can be applied even in the presence of ablation.

In order to apply the proposed Flight-to-Ground duplication methodology, we have to demonstrate first that a boundary layer could be defined around the stagnation point, at hypersonic conditions, in terms of the classical boundary layer model [110]. In other words, we have to show that the boundary layer equations are relevant along the stagnation line so that we can use the available Navier-Stokes and boundary layer solvers. To do that, computations from a full Navier-Stokes solver and a classical boundary layer equation solver are compared with the same boundary conditions.

For the boundary layer solver, the boundary layer thickness is defined by temperature linearity method that is discussed in the next section and the edge conditions at this point are taken from the stagnation-line solution of the 3D CFD++ calculation. These conditions, together with the obtained surface temperature, are given as boundary conditions to NEBOULA [89].

Fig. 2.18 shows temperature and density profile comparisons between the two codes. The two solutions show a very satisfactory agreement, and the profiles are practically superimposed through the boundary layer. The species concentrations, shown in Fig. 2.19, are also in a very good agreement. Thus, one can treat the stagnation flow with parabolic boundary layer formulation. What is interesting to see is that on the stagnation line, the profiles do not behave asymptotically as the generic boundary layer profiles on walls, which supports the argument of hypersonic velocity gradient distribution shown in Fig. 2.3.

2.3.3. QARMAN geometry to Hypersonic Equivalent Sphere

In order to apply the LHTS, an effective radius as presented with different approaches in Section 2.1.3 needs to be determined. To do so, one has to define the velocity gradient at the edge of the boundary layer. The approach is to select the point where the temperature profile stops to be linear after the shock. The relevance of this approach can then be confirmed by verifying that the selected point corresponds to the location where the velocity gradient computed for an inviscid case differs from that of a viscous case profile.

Fig. 2.20 shows the velocity gradients along the stagnation line of QAR-

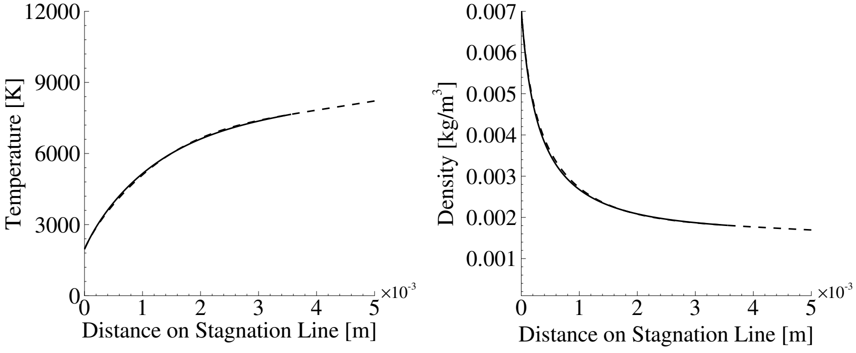

Figure 2.18.: Stagnation line temperature and density profiles comparison of Navier-Stokes solver (CFD++), shown with dashed lines, and Boundary Layer solver (NEBOULA) for QARMAN trajectory at 66 km altitude, shown by solid line.

MAN. The CFD cases of both viscous and inviscid flow together with the temperature profile of the viscous case only are presented. It is interesting to note that this boundary layer edge location defined on the basis of the temperature profile agrees very well with the deviation point of the two velocity gradients. This behavior confirms the analogy between the kinetic and the thermal boundary layer in the actual hypersonic conditions (p127 in [110]).

Once the boundary layer edge has been defined, the $R_{eff,H}$ value can be easily computed from Eq. (2.19) using the value of β obtained from viscous simulation. This computation returns an $R_{eff,H}$ value of 12.4 cm for 66 km.

Fig. 2.21 shows the temperature and density profiles in the boundary layer computed in hypersonic CFD of QARMAN squared shape and the hypersonic equivalent sphere computed by the Stagnation Line Code [136] [4]. One can see that there is a very good agreement between the density profiles and for the temperature by a maximum of 4% difference. However it should be noted that this procedure aims to test the in-flight experiments and the TPS of spacecrafts. Higher slope of temperature means that the heat flux is slightly higher and this leads to a considerably conservative approach.

Fig. 2.22 shows the species concentration profiles comparison. Both results from QARMAN CFD++ and hypersonic sphere computation by Stagnation Line Code computations are done by using the 7 species air model by Park [118]. The species in consideration are O_2, O, N_2, N, NO, NO^+

---

[4] A code-to-code comparison is performed between CFD++ and Stagnation Line Code on the same hypersonic sphere and a good agreement is found. The Stagnation Line code is used from here on thanks to its short computation time. The same chemistry model of CFD++ is used in the simulations.

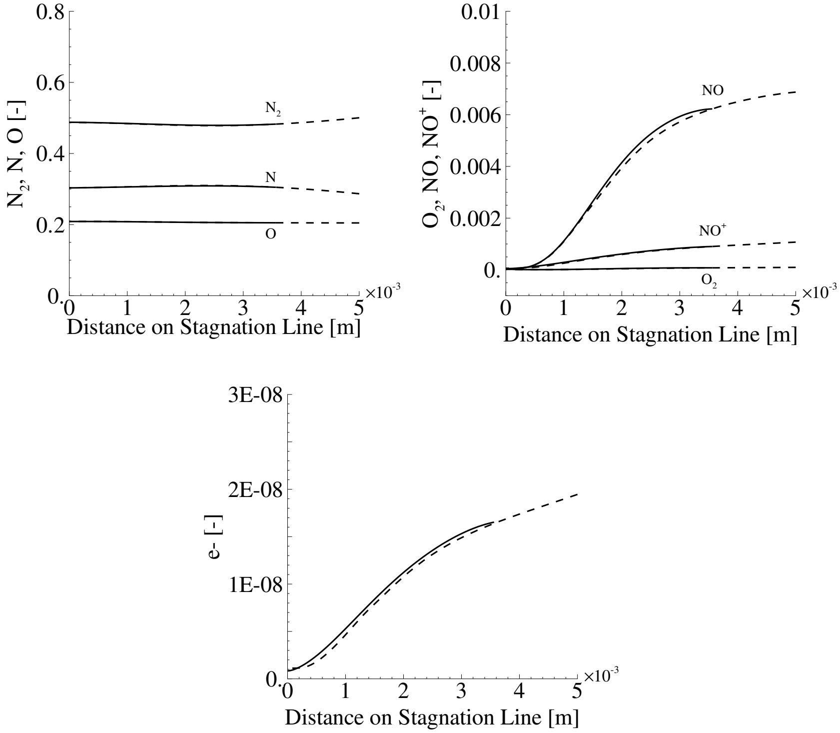

Figure 2.19.: Stagnation line molecular and atomic species concentration profiles comparison of Navier-Stokes solver (CFD++), shown by dashed lines, and Boundary Layer solver (NEBOULA) for QARMAN trajectory at 66 km altitude, shown by solid line.

and electrons. All profiles show a good agreement except NO, however they have a good agreement close to the wall. N_2 and NO have a difference of 2% and 3.3% close to the wall respectively. This can be explained with the fact that the hypersonic sphere and hypersonic QARMAN shock configurations are not matched, as the focus is the region close to the wall. The difference in shock position is also depicted in β profiles in Fig. 2.20.

The hypersonic equivalent sphere radius value is subjected to a sensitivity analysis and is detailed in Sec. 2.3.6. The error source here is the pick-up location of the β and the codes used so far are considered validated and without errors.

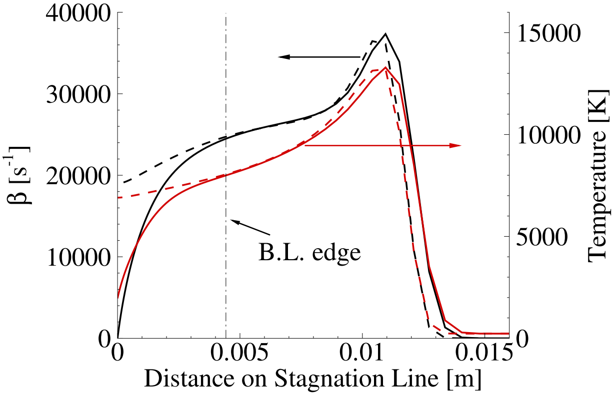

Figure 2.20.: Viscous and inviscid stagnation-line velocity gradient and temperature profiles of the squared QARMAN shape for conditions at 66 km altitude computed by CFD++.

2.3.4. Hypersonic Equivalent Sphere to Subsonic Equivalent Sphere

This step is where we pass from hypersonic to subsonic regime according to the operation mode of the VKI Plasmatron. Thus the aim is to find the radius of a subsonic sphere which is equivalent to the hypersonic sphere found in the previous step.

Applying Eq. (2.1) for the hypersonic and subsonic cases, one could notice that total enthalpy, total pressure and velocity gradient should be respected in both regimes, to retrieve the same total heat flux at the surface. It is important to note that the convective heat flux and the diffusive flux are also exactly reproduced in both regimes. The major difference in applying the heat transfer equation for the two cases is the expression of the velocity gradient since the pressure distributions around the stagnation point in both situations are expressed with different models.

The stagnation point heating equation by Fay and Riddel (Eq. (2.1)) was reformulated by Zoby [81] as Eq. (2.4). Rewriting the K coefficient as K_H and introducing the hypersonic equivalent sphere radius $R_{eff,H}$ instead of R, the hypersonic stagnation point heating can be given as:

$$\dot{q}_w \sqrt{\frac{R_{eff,H}}{p_0}} = K_H \left(h_{0,e} - h_w\right) \tag{2.33}$$

where K_H is:

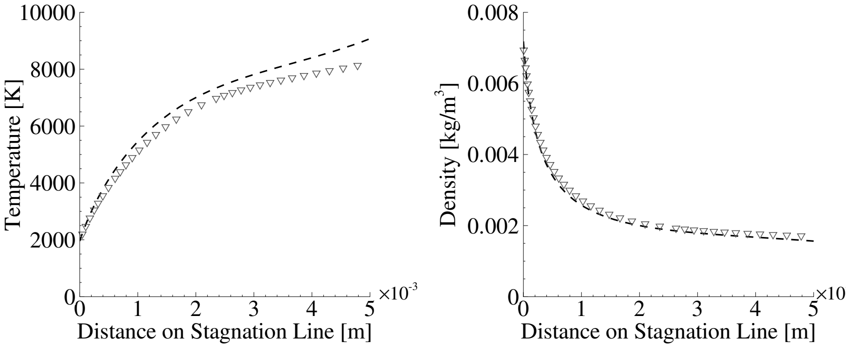

Figure 2.21.: Temperature profiles in boundary layer for squared QARMAN shape by CFD++ (shown by the gradient symbol) and equivalent hypersonic sphere of 12.4 cm radius by S-L code (shown by dashed lines).

$$K_H = \frac{0.763 Pr^{-0.6} A^{0.5} 2^{0.25}}{R_{eff,H}^{0.25}} \left(\frac{\rho_w \mu_w}{\rho_e \mu_e}\right)^{0.1} \tag{2.34}$$

where A is a constant coming from Sutherland's law of viscosity.

The aim is to find a similar expression in the subsonic regime so that we can equate the heat flux terms. The velocity gradient parameter in Eq. (2.1) can be analytically evaluated combining potential flow theory and Bernoulli's law for a sphere of radius $R_{eff,S}$. The pressure, p, over a sphere is given by potential flow theory [137] as:

$$p = p_e - \frac{9}{4} sin^2\theta \left(p_e - p_\infty\right) \tag{2.35}$$

Starting from Bernoulli equation, like Boison and Curtiss [66], one can differentiate the velocity u with respect to x to obtain an expression for velocity gradient. It is assumed that x is the curvilinear abscissa that follows the surface starting at the stagnation point; and θ being the angle between the stagnation point and a given point x on the surface. At the stagnation region, θ is very small so $x = R_{eff,S}\,\theta$ holds. Thus:

$$\beta_e = \frac{du}{dx} = \frac{3}{2} \frac{1}{R_{eff,S}} \sqrt{\frac{2p_e}{\rho_e}\left(1 - \frac{P_\infty}{p_e}\right)} \tag{2.36}$$

Introducing Eq. (2.35) in the above equation and replacing the velocity gradient term in Eq. (2.1), one can obtain the following expression:

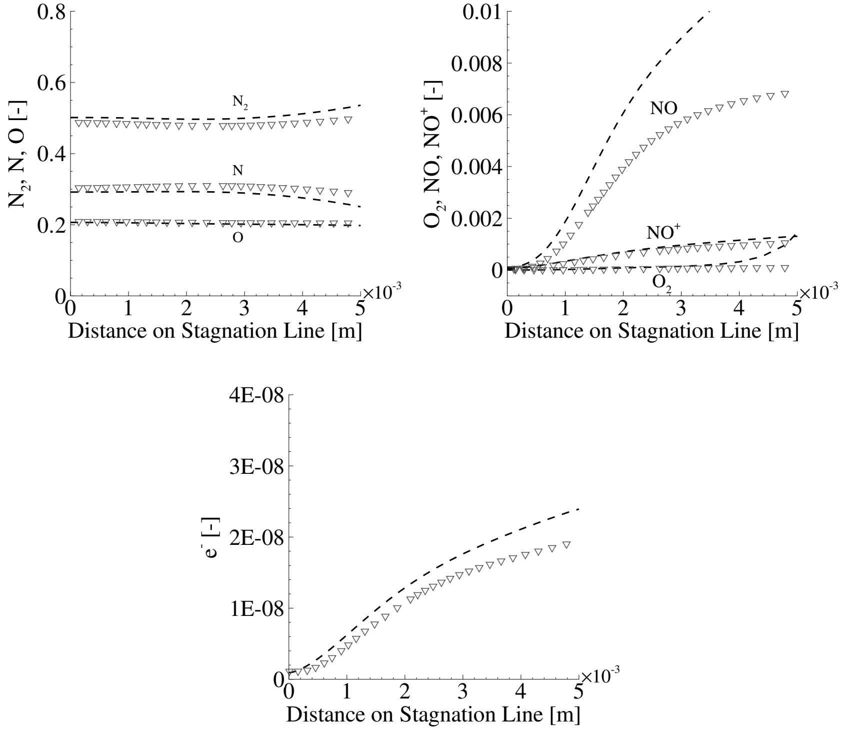

Figure 2.22.: Molecular and atomic species concentration profiles in boundary layer for squared QARMAN shape by CFD++ (shown by the gradient symbol) and equivalent hypersonic sphere of 12.4 cm radius by S-L code (shown by dashed lines).

$$\dot{q}_w \frac{\sqrt{R_{eff,S}}}{\sqrt[4]{p_e.\Delta p}} = K_S \left(h_{0,e} - h_w\right) \tag{2.37}$$

where K_S:

$$K_S = \frac{0.763 Pr^{-0.6} A^{0.5} 2^{0.25} \sqrt{\frac{3}{2}}}{R_{eff,S}^{0.25}} \left(\frac{\rho_w \mu_w}{\rho_e \mu_e}\right)^{0.1} \tag{2.38}$$

The K_H and K_S parameters include the terms given in Eq. (2.1) except the velocity gradient at the boundary layer edge du_e/dx. It is seen that the velocity gradient is expressed as a function of a spherical radius and pressure quantities in both hypersonic and subsonic cases. The two parameters K_H

and K_S are shown to be equivalent in hypersonic and subsonic regimes from the experiments conducted in many hypersonic ground test facilities and subsonic plasma wind tunnels [138] as shown in Fig. 2.23. Using the two expressions in Eqs. (2.33) and (2.37), a relation between the hypersonic and subsonic effective radii is deduced as follows:

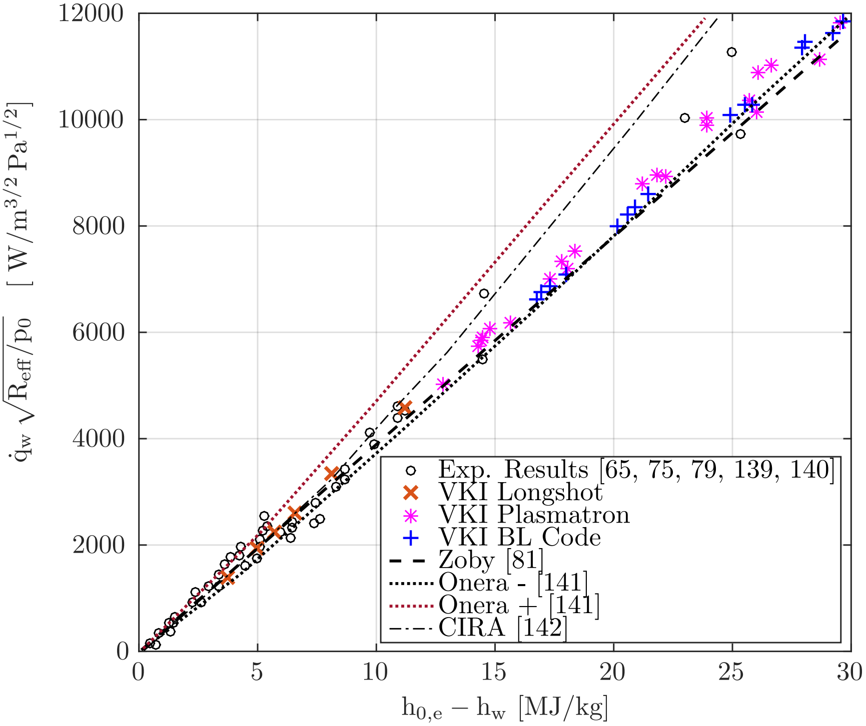

Figure 2.23.: Comparison of the numerical and experimental stagnation point heating rates for subsonic and hypersonic flows. The slope of the presented data correspond to K_S and K_H parameters. The plot is remade from [138]. The hypersonic cases are VKI Longshot, Zoby, Onera and CIRA.

$$R_{eff,Subsonic} = R_{eff,Hypersonic} \times \frac{\sqrt{p_e \Delta p}^{ground}}{p_{0,e}^{flight}} \tag{2.39}$$

where $p_{0,e}$ is taken from hypersonic CFD computations of squared QARMAN geometry.

To apply Eq. (2.39), one needs to know the dynamic and static pressure in the ground facility. The static pressure is directly taken from the trajectory data and the facility is operated in the same condition. The dynamic pressure is a parameter that depends on the free stream values including enthalpy as it appears from LHTS. Finding the correct combination of enthalpy (power) and pressure for operating the plasma wind tunnel requires additional experimental campaigns where the dynamic pressure is measured. The experimental database constructed in Sec. 2.2.5 is used to have the correct dynamic pressure of the free stream conditions at the trajectory point by using the enthalpy measurement techniques given in Sec. 2.2.4. However, one should keep in mind that the measurements have an associated uncertainty, which is not constant at different testing conditions. The errors on enthalpy and pressure measurements are addressed in the sensitivity analysis in Section 2.3.6.

Combined with the experimental campaign in the VKI Plasmatron, the hypersonic effective radius for 66 km altitude returns a subsonic sphere radius of 8.31 mm. It is important to note that there is no assumption concerning the used boundary layer model until this step therefore this radius remains computed with the classical boundary layer model, adapted for high enough Re numbers.

2.3.5. Subsonic Equivalent Sphere to Hemisphere-Cylinder Test Sample

Recalling that the $R_{eff,H}$ is found using Classical boundary layer theory (which was shown to be equivalent to Navier-Stokes solutions in Section 2.3.2), it is also the case for the passage from $R_{eff,H}$ to $R_{eff,S}$. The classical boundary layer model is suitable for high Reynolds number flows [110]. However, the plasma flow in the VKI Plasmatron facility has low Reynolds numbers. The finite thickness boundary layer model is more appropriate [89] and the approach needs to be adapted to model accurately the flow around the tested sample. This last treatment leads to the definition of the final probe radius, which allows the duplication of the hypersonic boundary layer in a subsonic plasma wind tunnel.

The flow characteristics at the stagnation line in front of the hemispherical probe in the Plasmatron chamber can be represented using five non-dimensional parameters (NDPs) defined for a finite thickness boundary layer given in Eqs. (2.23) to (2.27) as mentioned earlier. The numerical database built for a wide range of operating conditions was presented in Sec. 2.2.6. At this step, we will find the equivalent hemisphere-cylinder geometry, that is the test sample for Plasmatron. Since the equivalent test sample geometry is unknown prior to the procedure, one must have a correlation in function of not only the free stream conditions (power and pressure) but also the probe geometry. This is why a wide range of hemisphere radii of 6 - 57.5 mm were included in the numerical database. Recalling the equations of NDPs that are determined at the boundary layer edge δ:

$$NDP1 = \frac{\delta}{R_m} \tag{2.23}$$

$$NDP2 = \frac{\partial u}{\partial x} \cdot \frac{R_m}{v_s} \tag{2.24}$$

$$\mathrm{NDP3} = \frac{{R_m}^2}{v_s} \cdot \frac{\partial}{\partial y}\left(\frac{\partial u}{\partial x}\right) \tag{2.25}$$

$$\mathrm{NDP4} = \frac{v(\delta)}{v_s} \tag{2.26}$$

$$\mathrm{NDP5} = \frac{v(\delta)}{v_e} \tag{2.27}$$

The R_m value corresponds to the radius of the cylindrical afterbody of the probe. This is also the nose radius when a hemispherical probe is used.

Considering the x-momentum equation at the finite thickness boundary layer edge where the external inviscid flow and the boundary layer are matched:

$$\frac{\partial p}{\partial x} = -\rho u \cdot \frac{\partial u}{\partial x} - \rho v_e \cdot \frac{\partial u}{\partial y} \tag{2.40}$$

and stating that at the stagnation point it is possible to assume:

$$u = \frac{\partial u}{\partial x} \cdot x \tag{2.41}$$

and equating this pressure gradient to the one at the inviscid wall, where $v = 0$, introduces directly $R_{eff,S}$ using the definitions given in Eq. (2.23) to (2.27) as a function of NDPs and the model radius R_m,

$$R_{eff,S} = \frac{R_m}{\mathrm{NDP2} \cdot \left(1 + \frac{\mathrm{NDP5} \cdot \mathrm{NDP3}}{\mathrm{NDP2}^2}\right)} \tag{2.42}$$

$$R_{eff,S} = \frac{R_m}{f\,(\mathrm{NDP})} \tag{2.43}$$

One can now compute an $\mathrm{R_m}$ with the function of NDPs which comes from solving the flow in Plasmatron by ICP code with an initial guess of a hemispherical probe geometry: $\mathrm{R_{m,guessed}}$. It should be noted that even if the $\mathrm{R_{eff,S}}$ is given, NDP2 and NDP3 are functions also of $\mathrm{R_m}$. So Eq. (2.43) should be solved iteratively as there is no closed-form solution to $\mathrm{R_m}$. Practically, although $f\,(NDP)$ changes with the geometry and the flow conditions, the change is around 6-7 % for 40% change in guessed radius which makes the iteration process rather fast and easy.

For subsonic plasma test conditions corresponding to the trajectory point of 66 km, an educated guess of $R_{m,guessed}$ is used to run an ICP computation of the chamber. Since a hemispherical probe will be used, the first guess was the widely used $R_{m,guessed} = 25$ mm. Then the process is iterated until the $R_{m,found}$ through Eq. (2.43) is the same as the $R_{m,guessed}$ with the NDPs are extracted from the NDP regressions if the ICP computation does not exist for the precise geometry. For this condition, the R_m is converged to 10.52 mm. For $Pressure_{ICP} = 6180.27$ Pa and $Power_{ICP} = 95$ kW (which is the net power going into the plasma discharge), the NDPs are given in Table 2.7.

Table 2.7.: NDPs for the converged R_m 10.52 mm.

NDP1	0.2984
NDP2	0.2520
NDP3	0.6410
NDP4	0.2654
NDP5	0.4011

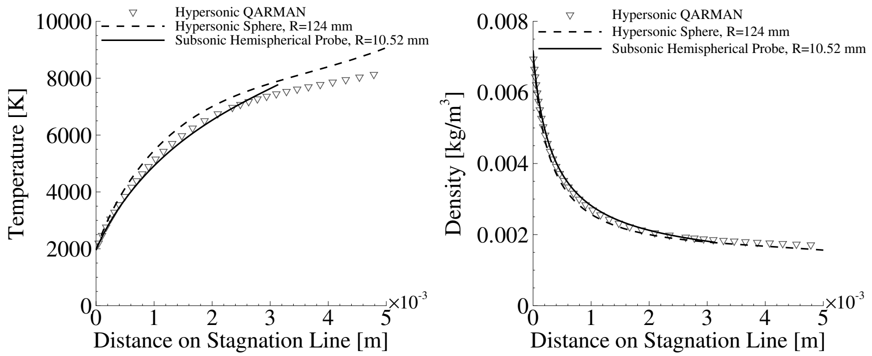

Figure 2.24.: Temperature and density along stagnation line. Comparison of the squared hypersonic QARMAN by CFD++, the hypersonic equivalent sphere 1D solution by S-L code and the hemispherical model in subsonic plasma by NEBOULA computations for 66 km conditions.

The boundary layer flow properties of the newly defined hemispherical probe are solved by the in-house NEBOULA code which computes finite thickness boundary layer equations [89]. The change in the boundary layer model is automatically introduced by the NDP1 given in Eq. (2.23).

Fig. 2.24 shows the result of the iterative procedure in terms of temperature and density distributions along the stagnation line. One can also see that the flow in front of the hemispherical probe in Plasmatron conditions shows a very good agreement close to the wall for both temperature and density. This is a driving parameter for the heat flux and the chemistry at the stagnation region. Fig. 2.25 depicts the molecular and atomic species profiles. The subsonic hemispherical probe profiles show a better agreement with the hypersonic QARMAN shape than the hypersonic sphere. Overall, it can be concluded that the procedure provides a good duplication of the boundary layer at the stagnation region. How sensitive the solution is to each step of the procedure is further assessed in Sec. 2.3.6.

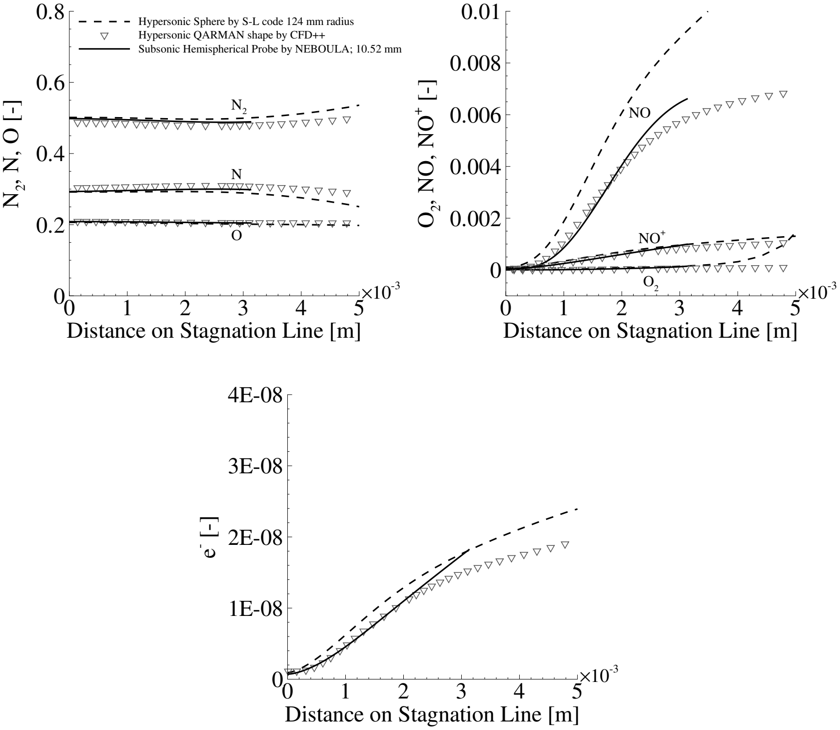

Figure 2.25.: Molecular and atomic species concentration profiles along stagnation line. Comparison of the squared hypersonic QARMAN by CFD++, the hypersonic equivalent sphere 1D solution by S-L code and the hemispherical model in subsonic plasma by NEBOULA computations for 66 km conditions.

A very interesting outcome is to see how much the geometry is changing from the actual hypersonic vehicle to the probe geometry to be used in a subsonic plasma facility. The original QARMAN shape had a square cross section of 10x10 cm while the equivalent geometry to be put in the subsonic plasma test facility is a 10.52 mm radius hemispherical probe. The change in geometrical parameters are sketched to scale in Fig. 2.26.

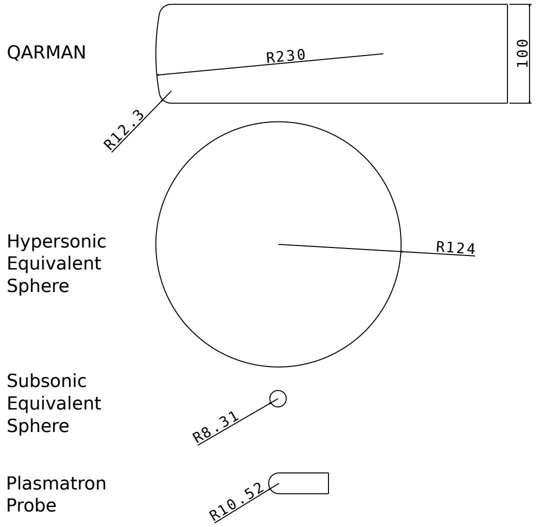

Figure 2.26.: Change in geometrical parameters in millimeters at each step of the Flight-to-Ground Duplication Methodology.

2.3.6. Sensitivity Analysis

The sensitivity analysis is done on the same trajectory point at 66 km of altitude as described in the previous section. First, the error sources are determined for each step. The errors of the validated numerical codes (CFD++, Stagnation Line Code, ICP and NEBOULA), the error of atmospheric model for p_∞, ρ_∞, p_0 values used in trajectory analysis and the 7-species air model are neglected. The considered error sources are summarized in Table 2.8. It is seen that there are three major error contributions and to each is assigned an error applied to the nominal value, resulting in three values per parameter. To keep the sensitivity analysis simple, out of the nine values computed at each step, the minimum, nominal and maximum values are taken to the next step. Each of these values and the assigned errors are specified in Table 2.8.

The first source of error is the β pick-up location, δ, which is the point where the temperature profile stops to be linear. This point can be determined by the derivative along the stagnation line and a 10% error is assigned on the δ location towards the wall and away from the wall. The main parameters that are directly affected by δ are the computed $R_{\mathrm{eff,H}}$ and

Table 2.8.: Error sources affecting the converged R_m solution and their assigned values.

Step	Uncertainty source	Affected Term	Uncertainty[a]	$R_m/\overline{R}_m$[b]
Vehicle shape to $R_{eff,H}$	Velocity gradient pick-up location	β	-10% to $\overline{\delta}$	1.02
			$+10\%$ to $\overline{\delta}$	0.99
$R_{eff,H}$ to $R_{eff,S}$	Ground test measurements	$\sqrt{p_e\ \Delta p}$	-2% to $\overline{P_e}$ -15% to $\overline{\Delta p}$	0.89
			$+2\%$ to $\overline{p_e}$ $+15\%$ to $\overline{\Delta p}$	1.11
$R_{eff,S}$ to R_m	Plasmatron power (Pwr.)	$f(NDP)$	-11% to $\overline{\text{Pwr.}}$	0.99
			$+11\%$ to $\overline{\text{Pwr.}}$	1.01

[a] Overbarred values represent the nominal values for the input variables: $\overline{\delta} = 4.28$ mm, $\overline{P}_e = 6180.2$ Pa, $\overline{\Delta P} = 26.01$ Pa, and $\overline{\text{Pwr.}} = 95$ kW.

[b] Nominal value for the final quantity of interest is $\overline{\mathrm{R}}_\mathrm{m} = 10.52$ mm

the boundary conditions given at the boundary layer edge to NEBOULA at the last step where the model geometry profiles are compared to QARMAN. The effect of the pick-up location is isolated by fixing the rest of the parameters ($\sqrt{\mathrm{p_e}\Delta\mathrm{p}}$ and power). The resulting probe diameters are given in the Table 2.8 being: $\mathrm{R_{m,nominal}}$=10.52 ± 0.16 mm and the boundary layer temperature profile for pick-up locations $\mathrm{x_1} = \overline{\delta} - 10\%$, $\mathrm{x_2} = \overline{\delta}$ and $\mathrm{x_3} = \overline{\delta} + 10\%$ are shown in Fig. 2.27.

The second term is the effect of pressure measurement errors, $\sqrt{\mathrm{p_e}\Delta\mathrm{p}}$, on the calculation of $\mathrm{R_{eff,S}}$ that appears in Eq. (2.39). Its effect is isolated by fixing the pick-up location and the Plasmatron power and by using the minimum, nominal and maximum values given in Table 2.8 for simplification. This is the largest effect among all three sources. As shown in Table 2.8, the resulting probe radii are $\mathrm{R_{m,nominal}}$=10.52 ± 1.2 mm. This is the largest effect among all three sources and the boundary layer temperature profiles are depicted in Fig. 2.28.

The last term is the power of Plasmatron facility which not only affects the f(NDP) computed by the ICP code but also drives the boundary layer edge enthalpy in the facility since the free stream enthalpy is adjusted by power. The power margin to be imposed in ICP computation is deduced from the enthalpy uncertainty through the experimental database. It corresponds to 11% margin on the nominal power of 95 kW, that gives $\mathrm{h_e}$ = 23.57 kJ/kg at the reference condition. This margin includes the QARMAN trajectory condition at 66 km that has an enthalpy of 23.43 kJ/kg. By fixing the pick-

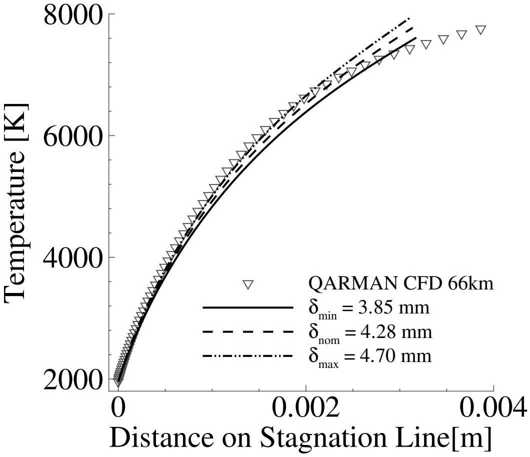

Figure 2.27.: Influence of the pick-up location, thus the boundary layer edge, on temperature profile. All the curves are for $R_{\text{eff,S}} = 8.31\,\text{mm}$ and Power = 95 kW which correspond to the nominal values of pressure and power. The boundary layer profiles are computed with NEBOULA.

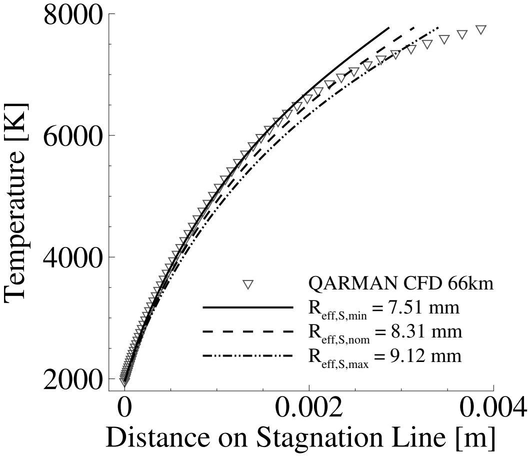

Figure 2.28.: Influence of the pressure, determining the $R_{\text{eff,S}}$, on temperature profile. All the curves are for $\delta_{\text{nom}} = 4.28$ mm and Power = 95 kW which correspond to the nominal values of the the pick-up location and power. The boundary layer profiles are computed with NEBOULA.

up location and the pressure terms to nominal, the effect of power on the R_m and temperature profiles is found to be smaller than the previous sources as shown in Fig. 2.29. The resulting R_m values are $R_{m,nominal}$=10.52 ± 0.12 mm as given in Table 2.8.

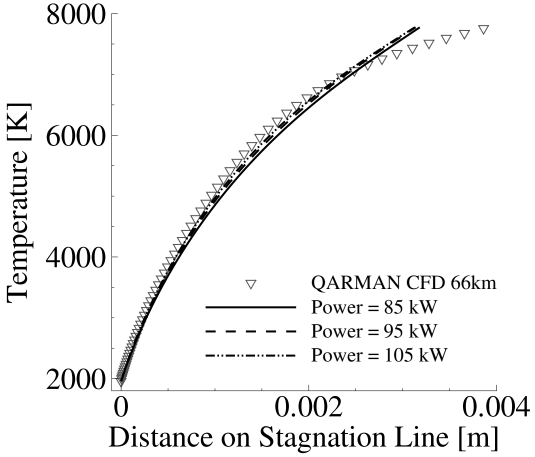

Figure 2.29.: Influence of the power on temperature profile. All the curves are for $\delta_{nom} = 4.28$ mm and $R_{eff,S,nom} = 8.31$ mm which correspond to the nominal values of the pick-up location and pressure. The boundary layer profiles are computed with NEBOULA.

How the combination of different error source terms affects the temperature profiles is also investigated. The highest extreme case is found to be the combination of $\overline{\delta} + 10\%$ location, $R_{eff,S,min}$ and the highest power of 105 kW leading to R_m=9.45 mm. Additionally, the lowest extreme case is the combination of $\overline{\delta} - 10\%$ location, $R_{eff,S,max}$ and the lowest power of 85 kW leading to R_m=11.68 mm. These two extremes are plotted in Fig. 2.30 together with the nominal case and QARMAN CFD. These extremes are considered as the total interval of the uncertainty. Taking the maximum deviation; the uncertainty on the final model radius is R_m=10.52 ± 1.2mm.

2.3.7. More QARMAN Trajectory Points

The Flight-to-Ground duplication methodology is also applied to other entry trajectory points of QARMAN given in Table 2.4. The summary of the computed model radii at different altitudes are given in Table 2.9. The sensitivity analysis showed previously that the largest error is introduced in the pressure term coming from the ground test experiments as seen in Table 2.8. The error in dynamic pressure is kept constant to 15%. Since

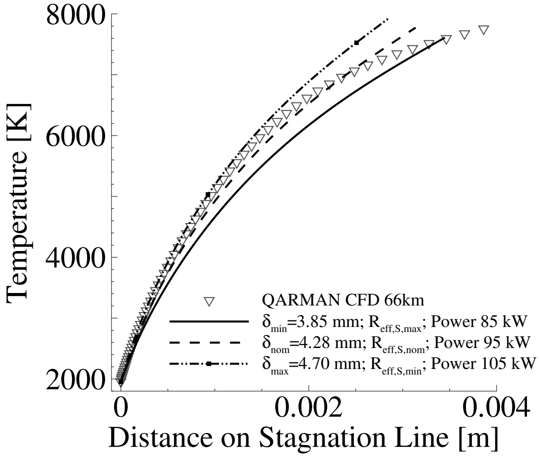

Figure 2.30.: The combination of errors leading to cases where the temperature profiles showed the extreme low and high values. The lowest temperature case has $\mathrm{R_m} = 11.68$ mm, the nominal case has $\mathrm{R_m} = 10.52$ mm and the highest temperature case has $\mathrm{R_m} = 9.45$ mm. The pick-up locations are depicted $\delta_{\mathrm{min}} = \overline{\delta} - 10\%$, $\delta_{\mathrm{nom}} = \overline{\delta}$ and $\delta_{max} = \overline{\delta}+10\%$ for legend simplicity. The boundary layer profiles are computed with NEBOULA.

as we get lower in altitude, the total pressure increases and in return at Plasmatron the dynamic pressure decreases, the error in the model radius gets smaller with lower altitudes. However it should be noted that the pressure term error is still the largest.

It is seen in Table 2.9 that the required sample geometry is very small at 60 km and below. Making tests with such small sized samples can lead to high 3D heating which would prevent satisfying the basic 1D stagnation heating assumption of the methodology. To overcome this problem, bigger sample geometries can be used if the entire methodology is repeated using a different air mass flow rate than 16 g/s. Plasmatron testing envelope allows a range of air mass flow rate from 2 to 28 g/s. Since it requires additional experiments and numerical simulations, the full analysis is not performed here. The trajectory pressure and enthalpy can be set in the wind tunnel with the presented measurement techniques. This is investigated by making numerical simulations at the same free stream power-pressure and three mass flow rates for the same probe geometry 8, 16 and 20 g/s, and also two different hemispherical probe geometries. The boundary layer edge conditions are summarized in Table 2.10. Two trends are observed which are consistent with the perfect gas law and the mass conservation.

- At constant pressure, as mass flow rate increases, β, v_δ, T_δ decreases,

Table 2.9.: Model radius computation from Flight to Ground Duplication methodology along QARMAN entry trajectory.

Altitude km	R_m mm	Maximum Error ±mm	Relative Error [%]
70	18.33	1.73	9.44
66	10.52	1.20	11.41
60	6.53	0.56	8.57
55	5.37	0.47	8.75
53	5.19	0.46	8.86
50	3.38	0.26	7.69

and ρ_δ increases.

- At constant pressure and mass flow, as probe size increases, β, v_δ, T_δ decreases, and ρ_δ increases.

In conclusion, to match the velocity gradient of the lower altitudes with a *bigger* sample size, a *lower* air mass flow rate should be used. Alternatively, the procedure can be repeated with other geometries than hemisphere cylinders.

Table 2.10.: ICP simulations at 11967 Pa and 75 kW ICP power with the flat standard probe of R_m=25 mm at 8, 16 and 20 g/s, and three hemispherical probes of 6, 15 and 25 mm radius.

	Mass Flow Rate g/s	β s^{-1}	v_δ m/s	T_δ K	ρ_δ kg/m^3
Flat Standard R_m = 25 mm	8	1464.43	37.35	6224.63	$4.15.10^{-3}$
	16	1130.05	30.77	6033.72	$4.52.10^{-3}$
	20	956.96	26.90	5917.65	$4.75.10^{-3}$
Hemispherical R_m = 6 mm	16	6158.16	31.69	6027.62	$4.53.10^{-3}$
Hemispherical R_m = 15 mm	16	2575.06	28.437	5937.96	$4.71.10^{-3}$
Hemispherical R_m = 25 mm	16	1734.24	25.97	5935.06	$4.72.10^{-3}$

2.3.8. Flight-to-Ground Duplication Iteration with Flight Data

The Flight-to-Ground duplication application was thoroughly detailed previously. Note that the process is using the virgin TPS geometry since no accurate shape change analysis could be performed because no material re-

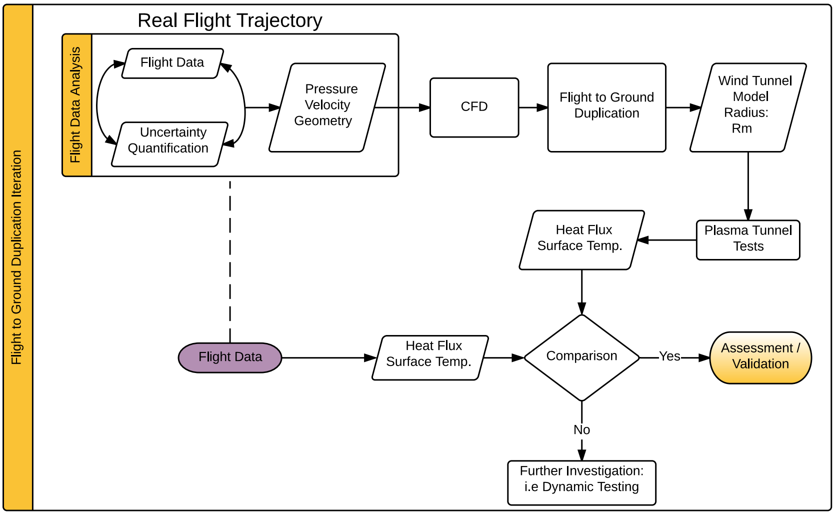

Figure 2.31.: Postflight Flight-to-Ground Duplication with the actual trajectory and nose geometry.

sponse model has been used at this stage. The flight data from QARMAN can reveal the shape change.Together with the shape change information and the actual trajectory, new CFD computations can be made so that the Flight-to-Ground duplication methodology can be repeated to find wind tunnel model radii corresponding to the actual flight free stream conditions. This will lead to a real trajectory duplication where the material performance in the ground tests can be compared to the flight. If the real trajectory and the resulting sample geometries are very different from the ones used to generate the databases, additional experiments should be performed and added to the database. In case steady plasma wind tunnel testing is not sufficient, dynamic testing up to some extent can be considered. The schematic of the proposed procedure is depicted in Fig. 2.31.

2.4. Dynamic Testing Considerations

Dynamic testing, as a term, stands for the procedure of testing a TPS or a payload, at the conditions of the re-entry trajectory, respecting the change of heat flux, enthalpy, pressure, velocity gradient and entry duration. Before going any further with the dynamic testing aspects, it is important to recall the capabilities and limitations of the plasma wind tunnel. Similar to many others, the VKI Plasmatron facility has the capability for an automated power (thus, enthalpy and heat flux) change at a prescribed rate. However the pressure in the chamber is adjusted by valves of the vacuum pumps. Although the automated system can adjust the valves to achieve the required pressures, the response time is much longer than the change of power since it takes more time to settle the chamber pressure. This prevents simultaneous modifications of pressure and enthalpy. Similarly, once the sample is put inside, its geometry is not changeable.

The nature of the re-entry profiles, that we need to duplicate in our facility, should be investigated to understand the requirements. A number of entry trajectory examples were given in Fig. 1.1; here we will take the example of QARMAN trajectory to demonstrate the dynamic testing approach. In a non-skipping trajectory, it was shown in Fig. 1.6 that the enthalpy has a constant decrease while the total pressure increases until a peak (around 41 km) and then starts decreasing as the vehicle slows down. The heat flux on the other hand has also a peak around 60 km, as will later be shown in detail Sec. 4.4.2. The last entry profile term in question is the velocity gradient. The velocity gradient and the corresponding terms were determined in Sec 2.3 for the QARMAN entry trajectory using the Flight-to-Ground Duplication methodology. The model radii were given in Table 2.9. The velocity gradient for the hypersonic flow decreases as the vehicle lowers altitude, so do the subsonic velocity gradient and the model radii required to make accurate boundary layer duplications.

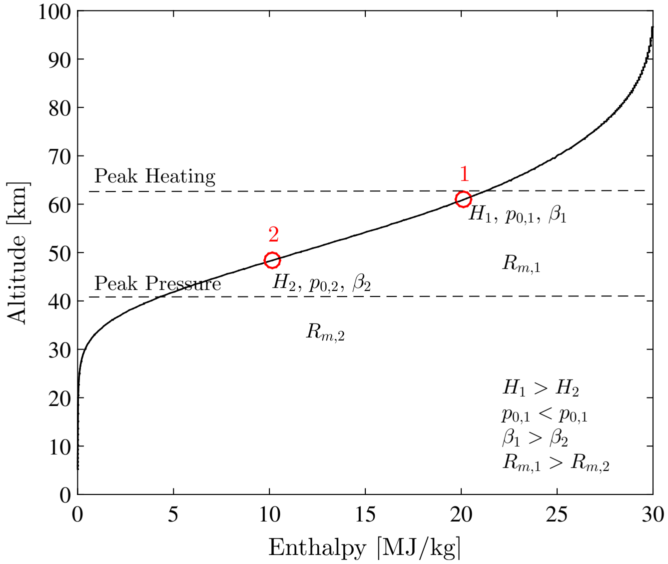

Figure 2.32.: Simplified overview of the dynamic trajectory simulation.

The aim of the dynamic testing along a trajectory can be summarized in Fig. 2.32. The vehicle approaches the ground with a certain enthalpy, total pressure and velocity gradient. All these free stream values with the given vehicle geometry correspond to a wind tunnel model radius that should be used to simulate that specific trajectory point. In a real campaign, the number of the investigated trajectory points are higher, however as a qualitative approach, a simplified version will be used here and we simply go from point 1 to point 2 (See Fig. 2.32). One should recall that the total pressure profile has a peak after which it starts to decrease. Therefore, the region before and after the peak pressure altitude should be treated differently. Since the vehicle significantly slows down in the region after the peak pressure, the enthalpy is low and thus only the part before this peak is discussed here.

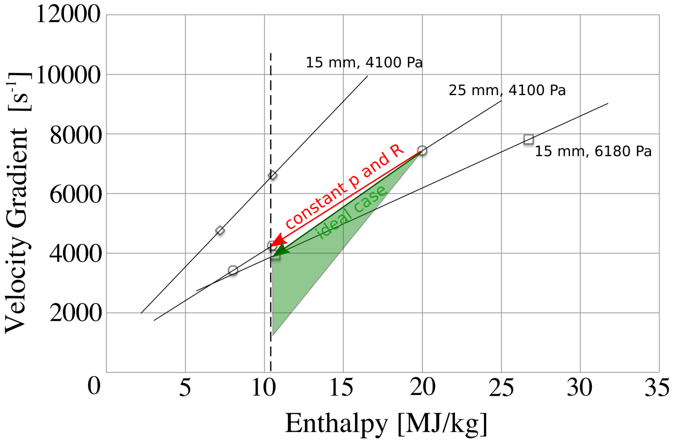

Figure 2.33.: Possible test approach and the ideal case. (The velocity gradient and enthalpy measurements are taken from the ablation campaign and the experimental database.)

Considering the capabilities of the facility presented previously, the possible testing scenarios are investigated. Going from one trajectory point to a lower altitude, as depicted in Fig. 2.32, one should adjust a decreasing enthalpy (or power), an increasing pressure and a decreasing model radius. With a qualitative approach shown in Fig. 2.33, let's imagine that our trajectory point 1 is 20 MJ/kg and the point 2 is at 10 MJ/kg; and the Flight-to-Ground duplication method revealed model radii of 25 mm and 15 mm respectively. Ideally, the testing conditions should be changed according to the green line given in Fig. 2.33. A green triangle is put to show qualitatively where this line can end up if the sample geometry for the point 2 is different than the shown data. This ideal case triangle, with a qualitative range of possibilities for the velocity gradient (model radius), will always stay below the constant pressure-radius line because the velocity gradient and the model radius for the lower altitude will always be lower.

Although decreasing the enthalpy in the wind tunnel is feasible, changing radius and pressure simultaneously is not within the current capabilities. What is possible to do is to follow the red line, which means to keep a constant radius and pressure but changing the enthalpy. Qualitatively speaking, since the velocity gradient shows a monotonous decrease along the entire trajectory, one can make sure that the arriving point will have a lower velocity gradient. However, it was also seen that increasing pressure tends to decrease the velocity gradient when exposed to the same enthalpy. Therefore, if the radius and pressure are kept constant, one can make sure that the arriving point will have a higher β value. As a matter of fact, this means that the model radius corresponding to this higher velocity gradient will be smaller. Hence, the impinging heat flux will be higher. So, one can conclude that a conservative test can be performed following the red line depicted in Fig.2.33.

As a future work, the aspects of real time mass flow rate stepping should also be considered. At this stage, there is no existing experimental or numerical database for an accurate prediction and reasoning. As it was discussed in the previous section, changing the mass flow rate could compensate for the change in radius. However it should also be noted that changing the mass flow rate prolongs the heat flux calibration process prior to the experiments. The settling times after increasing or decreasing the mass flow rate in the plasma wind tunnel should also be investigated thoroughly.

2.5. Concluding Remarks

The Local Heat Transfer Simulation (LHTS) dictates the need to duplicate pressure, enthalpy and velocity gradient for an accurate simulation of the stagnation region of an entry vehicle in a ground facility. The pressure and enthalpy are free stream magnitudes that necessitates an accurate flow characterization. To improve the knowledge of the incoming flow, new measurement techniques are needed. The pressure can be determined accurately with 2% uncertainty but the enthalpy requires more attention. The conventional rebuilding methodology was presented where the heat flux measurements by a cold wall copper calorimeter is used in combination with static/dynamic measurements and numerical simulations of the facility. Since the resulting error in enthalpy is about 7% or higher [120], new measurement techniques are investigated.

Initially an enthalpy probe concept was tested. It is a heat exchanger tube surrounded by a cooling jacket, having the same dimensions of the heat flux and dynamic pressure probes, that intakes plasma and allows a heat exchange along the inner walls of the heat exchanger. Measuring the inlet and outlet temperatures of the heat exchanger water and the sucked plasma inside, one can deduce the plasma enthalpy at the inlet making some assumptions. Since the suction rate is unique to the test condition and is not known before the test, a range of rates are applied and the correct rate and the enthalpy are solved iteratively after the test. Measurements are made in a wide range of pressures and it was seen that the existing setup has a lower pressure limitation of about 6000 Pa because the plasma suction is not steady below. It is also seen that the inner design of the heat exchanger cannot handle heat fluxes of 1700 kW/m^2 due to a recirculation just behind the front bearing. However, for the conditions for which enough suction rates could be sampled and the errors are lower, the results agree very well with other methods and the probe is shown to be a promising measurement technique.

To extend the applicability of the probe to a wider range of pressures and heat fluxes, a new design of the heat exchanger should be done. Traditionally, roughness elements could be added to the inner channels to induce turbulence and increase the cooling efficiency. The design of the front bearing should be improved by making detailed cooling water simulations inside the tubes to determine exactly the recirculation areas. In order to make low pressure measurements, a new rotameter and damping system can be considered. A flowmeter could also be added to the system to damp the instabilities. An immediate knowledge of the plasma flow rate is also useful to see the range at the time of the measurements. For the presented experimental database, the necessary plasma flow rates are determined at least in terms of order of magnitude. Considering these flow rates as a baseline, a new experimental campaign, with a new heat exchanger design and a damping system, should be performed covering more of the Plasmatron operational range and compare to other existing methods. In addition to the sensitivity analysis presented here, a more elaborated uncertainty quantification (UQ) can be done and compare to the UQ results of the rebuilding method [120].

Later, an optical emission spectroscopy method, REDES, is presented, which uses the CN violet and N_2^+ emission lines. The ratio of their peaks or the integrated area under them are compared to the theoretical air spectra computed with Specair [127] which corresponds to a temperature at a given pressure. The temperature and pressure are then converted to enthalpy using the Mutation++ database [116]. Since it is a realtime measurement tool, the idea was to calibrate the facility power until the desired free stream enthalpy is reached. Indeed the test conditions presented in this thesis are built in this way. However, when compared to other methods, it was seen that the measured enthalpies were too high. The reason was the long integration time of the spectrometer acquisition when compared to the frequency of the jet fluctuations. The overshooting is not quantified over the operation envelope.

The existing enthalpy determination methods are compared and it was seen that the enthalpy probe measurements agree with the oxygen triplet method and the rebuilding procedure. The peak and integral ratio methods were always higher than the others. To determine the enthalpy in the test conditions of ablation campaign, the most accurate method is chosen per test condition. The edge conditions of species and density are then computed by CERBOULA matching the enthalpy of the most accurate method per case.

In addition to the free stream parameters pressure and enthalpy, the LHTS methodology requires a match of velocity gradient as well. The velocity gradient is the parameter that links a ground test with a given spacecraft geometry. A thorough literature survey is presented on its determination. It was seen that all existing expressions has the axisymmetry assumption. The test case presented here, QARMAN, is a blunt rectangular prism, with a curvature at the nose and at the corners. No existing expression could be applied to the case of a squared model as QARMAN. From here a need of a ground testing methodology that can account for arbitrary spacecraft geometries came up. A four step methodology is developed and validated combining analytical solutions, numerical simulations of the flight and the ground facility, and experimental data.

The flight velocity gradient is determined by defining the boundary layer edge as the location where the temperature stops to be linear. Using the velocity gradient at that location, an effective radius is computed by Lunev expression given in Eq.(2.19). This equivalent hypersonic sphere is then converted to an equivalent subsonic sphere by equating the heat fluxes using Eq. (2.39). A final transformation is applied to pass from high Reynolds flows to low Reynolds regime, as the flow in Plasmatron, by changing the boundary layer model from classical to finite thickness. The last step is iterated by means of ICP computations, thus NDPs, until the hemisphere cylinder sample geometry is obtained that is shown to have the same boundary layer as the hypersonic vehicle. A detailed sensitivity analysis is also performed.

The results showed that the required sample radii can be very small below certain altitudes for QARMAN geometry and entry trajectory. Small samples would be less easy to test and instrument hence are not preferred. A way to test with bigger samples and still respecting the LHTS parameters is elaborated. All the numerical computations and experiments were performed for an mass flow rate of 16 g/s. It is shown that if new experiments and simulations are performed at lower mass flow rates, the same boundary layer can be retrieved with bigger samples. Other sample geometries than hemisphere cylinders can as well be considered. However, these require a significant computational work and it is left as future work.

Thanks to the numerical and experimental database, the methodology could be applied to QARMAN mission. If the detailed geometry, hypersonic CFD and experimental data can be made available, the methodology should be applied to other missions as well, such as ARD, IXV or Hayabusa that also have flight data provided that their trajectory conditions fall on the performance envelope of the facility.

A dynamic testing perspective is given for the VKI Plasmatron with the current capabilities and corresponding limitations. At the VKI Plasmatron, there is a possibility to perform tests with enthalpy (heat flux, power) steps but at a constant pressure, and naturally starting from one sample geometry. It is shown that as the vehicle decreases altitude (and enthalpy), if the same sample geometry is exposed to the re-entry heat flux profile at constant pressure, the test condition corresponding to the lower altitude will always result in a higher velocity gradient than the ideal case. The ideal dynamic testing would be decreasing the model radius and enthalpy while increasing the pressure simultaneously according to the results of the Flight-to-Ground Duplication methodology and the entry trajectory. This means that the sample will be exposed to a higher heat flux at the given enthalpy if a constant pressure constant radius test is conducted. This can be advantageous if one wants to focus on the surface parameters such as wall temperature or emissivity.

Chapter 3.

Pre-Flight: Experimental Ablation Characterization Campaign

The previous chapter discusses how the stagnation region flow conditions of the hypersonic flight can be rebuilt in the subsonic plasma wind tunnels. This chapter talks about estimating the gas-surface interface and the material behavior at these flow conditions, which cannot be included in the CFD computations due to the unavailable knowledge on material properties and fully coupled ablation-fluid numerical tools. An inverse methodology is presented here for building the material response models using experimental data. A number of plasma experiments are performed to extract the behavioral trends of the ablator cork P50 material under different pressure, heat flux and sample radius conditions, which are the three parameters of the LHTS. Additionally, a thermogravimetric analysis is performed on the cork P50 sample to extract some material properties. How the contribution of each experimental data will be used to build the material response model is elaborated. The expected flight performance is discussed for the flow environment of QARMAN atmospheric entry and an overview is given on dynamic trajectory testing aspects. Finally, a methodology for validation with flight data is discussed.

3.1. Motivation

The Flight-to-Ground Duplication method allows us to duplicate the stagnation region flow in front of the spacecraft in a ground facility. The next step is to analyze the phenomena happening at the interface between the fluid and the ablative surface, and inside the solid when exposed to a high enthalpy flow. In order to understand how the TPS material reacts to this harsh environment, ground tests are indispensable as the flight-like conditions can be provided. Ground test data help us build material response models. These models can be improved and validated by ground test experiments, and later be compared to flight data, be validated in dynamic response and be used for designing safe and efficient future missions' TPS.

In the case of QARMAN, there is no flexibility on TPS sizing. The maximum available space in the standard CubeSat launch pod is filled with TPS material. Since QARMAN is a test bed for providing flight data for validation, the importance of its ablator characterization is to make sure the thickness is safely sufficient to accomplish its mission and to provide flight data for validation of the ground testing methodologies and the material response models.

For QARMAN mission profile, the cork based ablator Cork P50 from Amorim is chosen as the most suitable material to fit in the thermal insulation requirements. Cork P50 consists of high percentages of cork agglomerated with a plasticized phenolic resin. The amount of phenolic resin is in the range of 1/4 of total weight. The plasticizer is a glycol and is added to the composition in order to give some flexibility to the material [147]. It recesses and unlike many other ablators swells when exposed to plasma.

The motivation behind this experimental campaign is to provide the necessary inputs for the material response model for the selected TPS material for QARMAN. In this section, first the material response model basic equations are described, then the necessary boundary condition of the surface energy balance is detailed. Solving these equations require knowledge of some material properties that are currently not available to the author. Therefore, an inverse methodology is proposed to determine them using Plasmatron experimental data. It should be noted that building the material response model and its implementation in a material response code are out of the scope of this thesis.

3.1.1. Material Response Models

The common method for predicting the TPS material behavior during reentry is to measure the thermo-chemical properties of the ablator, make models and use them in the material response codes which are later iterated with experimental data of high enthalpy wind tunnels. If the vehicle flying this TPS material, has an on-board recession, temperature and pressure measurement suite, the material model could be validated. A relevant example is the PICA material initially used in Stardust mission [143], which is later used in Mars entry of MSL with the MEDLI instrumentation, validating the PICA material models [144].

A number of material response codes with different levels of fidelity can be found in literature [22]. Most of the numerical models consist of three equation sets which are the mass, momentum and heat balance equations. As will be seen in this chapter, the TPS of QARMAN, Cork P50 is a swelling material. Most of the models do not consider this complex behavior because new generation low density ablators such as PICA or ASTERM are not swelling. A model that takes it into account is proposed by Pinaud and van Eekelen [145] for cork based materials[1]. This is taken as an example in this

---

[1] This model is implemented in finite element software SAMCEF: AMARYLLIS. It has a module called SUPERVISOR, which takes into account the intumescing nature. So, the software couples the thermo-chemical and mechanical processes.

chapter however other models could as well be used since they contain same (or more) physical properties.

The governing equations of the Pinaud and Eekelen model are presented to relate the contributions of each result of the experimental campaign for building a material response model in the future. It was explained in Sec. 1.1.3 that the ablators decompose chemically when exposed to heat and as a result, the mass density is decreasing. This can be described by multiple Arrhenius laws, that relate the chemical reactions with temperature (by the notation of [145]):

$$\partial_i \alpha_i = A_i \left[\frac{\rho_v - \rho_c}{\rho_v} \right]^{N_i - 1} (1 - \alpha_i)^{N_i} \, e^{\frac{-E_i}{RT}} \tag{3.1}$$

where α_i is the advancement of the i^{th} pyrolysis reaction, A_i is the frequency or the pre-exponential factor of the i^{th} Arrhenius law, ρ is the mass density with subscripts v and c for virgin and char, N is the order of reaction, E_i is the activation energy of the i^{th} Arrenhius law, R is the perfect gas constant and T is the temperature. From here the change of total mass density, ρ, in time can be written as follows:

$$\partial_t \rho = - \sum_{N_{arrh}} \Delta \rho_i \partial_t \alpha_i \tag{3.2}$$

where N_{arrh} is the number of Arrhenius laws. From here one can write the mass conservation equation in the solid phase as follows:

$$\partial_t \rho + \partial_t \rho_g + \partial_x \overrightarrow{\dot{m}_g} = 0 \tag{3.3}$$

where $\partial_t \rho_g$ is the generated pyrolysis gases due to decomposition and $\overrightarrow{\dot{m}_g}$ is the mass flow rate vector. One can assume a steady state ablation, so the mass density of the pyrolysis gases does not change in time, and omit the second term, $\partial_t \rho_g$. The first equation of the equation sets, the mass conservation then becomes:

$$\partial_t \rho + \partial_x \overrightarrow{\dot{m}_g} = 0 \tag{3.4}$$

The second equation is the momentum conservation of the gaseous phase which can be given by Darcy equation:

$$\overrightarrow{\dot{m}_g} = -K_p \partial_x P \tag{3.5}$$

where K_p is:

$$K_p = \frac{\beta}{\mu_g \rho_g} \tag{3.6}$$

where β is the permeability and μ is the dynamic viscosity. Thirdly, the conservation of energy under heterogeneous equilibrium of the pyrolysis gases can be written as:

$$\partial_t \rho h + \partial_t \rho_g h_g = \partial_x \cdot \left(\overline{\overline{\lambda}}\, \partial_x T \right) - \partial_x \left(\overrightarrow{\dot{m}_g} h_g \right) \tag{3.7}$$

where $\overline{\overline{\lambda}}$ is the effective thermal conductivity tensor. The left hand side of the above equation indicates the unsteadiness and the chemistry of the pyrolysis gases. The first term on the right hand side is the effective conduction in macroscopic scale, therefore can be taken as the combination of the conductivity of the raw phase accounting for porosity, the tortuosity and the dispertion which takes into account the velocity of the gas phase flow inside the material, so it is a function of the geometry. By neglecting the viscous dissipation of the pyrolysis gas flow through the solid porous matrix and applying steady state simplifications the energy equation turns into:

$$\rho \partial_t h - \overline{H}_p \partial_t \rho = \partial_x \cdot \left(\overline{\overline{\lambda}}\, \partial_x T \right) - \overrightarrow{\dot{m}_g} \cdot \partial_x h_g \tag{3.8}$$

where $\overline{H}_p$ is the heat of pyrolysis defined as:

$$\overline{H}_p = h_g - \frac{\rho_v h_v - \rho_c h_c}{\rho_v - \rho_c} \tag{3.9}$$

With Eqs. (3.4), (3.5) and (3.8), one can model the temperature distribution in the material, recession and with the additional module, the swelling in time. To solve these equations, boundary conditions are needed. The boundaries are the back wall and the surface that is reacting to the incoming flow. The surface is more complicated to analyze since it is a coupled problem of the material response and the reacting boundary layer. The surface energy balance should be solved. To do so, the transfer coefficient approach is suggested and it is detailed in the next section.

3.1.2. Surface Energy Balance

Our interest is to model the transient temperature distribution and eventually the recession of the TPS material in time. The surface energy balance equation is the boundary condition to solve the energy equation Eq. (3.8) given in the previous section. To get an idea of the mechanisms of heating, we consider a control volume positioned at the ablative material surface. The control volume includes a portion of fluid and material, and has the surface in the middle as shown in Fig. 3.1. Thus, the control volume moves as the surface swells or recesses. The incoming and outgoing heat can be given as follows [23]:

$$\begin{aligned}\dot{q}_{cond,fluid}+\dot{q}_{diff}+\cancel{\dot{q}_{rad,in}}+\dot{m}_g h_{g,w}+\dot{m}_s h_{sw}\\ =\rho_w u_w h_w+\dot{q}_{rad,out}+\dot{q}_{cond,solid}+\cancel{\dot{m}_F h_{F,w}}\end{aligned}\tag{3.10}$$

where the incoming heat is in form of conduction from the fluid, diffusion, radiation, energy due to pyrolysis blowing and also a convective term due to the material recession $\dot{m}_s h_{s,w}$. The incoming radiation from the flow to the surface can be neglected making the optically thin plasma assumption. The heat leaves the surface in form of $(\rho u)_w h_w$ which is the energy taken by the mass that leaves the control volume in response to the recessing surface, and also in forms of outward radiation and conduction towards inside of the material. There is also the energy shown by $\dot{m}_F h_{F,w}$ which is the energy removed due to the mechanical erosion, thus failure, however it is neglected as the samples were intact during all experiments.

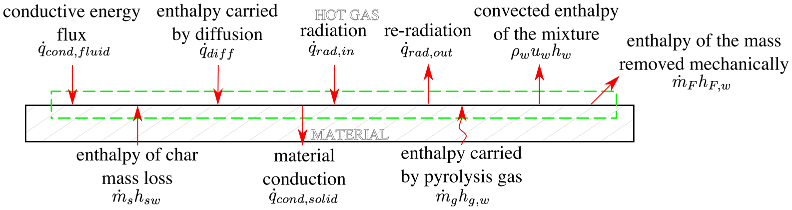

Figure 3.1.: Energy fluxes at the surface of a generic ablator, adapted from [23].

If one considers a steady state conduction through the solid; the last term on the right hand side of Eq. (3.10) becomes:

$$\dot{q}_{cond,solid}^{steady\,state}=\dot{m}_g h_{g,w}-\dot{s}\left(\rho_{v,T_0}h_{v,T_0}-\rho_c h_{c,w}\right)\tag{3.11}$$

where the $\dot{s}$ is the recession rate, the subscript v, T_0 stands for the virgin material far from the surface at temperature T_0, and the subscript c is the char. Inserting Eq. (3.11) in 3.10, the energy due to pyrolysis gas injection in the boundary layer cancel out. Eq. (3.11) also has the assumptions of 1D heat conduction, that the material properties at the surface are constant with temperature and that the location at the far back of the sample stays at constant temperature T_0 so no thermal wave reaches the back surface.

Another useful approximation is that the surface only recedes from the charred surface. Therefore, one can write the following expressions:

$$\dot{m}_s h_{sw}=\dot{m}_c h_{cw}\tag{3.12}$$

$$\dot{s}=\frac{\dot{m}_c}{\rho_c}\tag{3.13}$$

Similarly, since we deal a lot with the reference heat fluxes, which are done by non-ablative cold wall measurements, it is important to give the heat balance for the heat flux probe. The total heat flux would read:

$$\dot{q}_{measured} = \dot{q}_{cond,fluid} + \dot{q}_{diff} \tag{3.14}$$

where the measured heat flux is the conduction of copper to the cooling circuit. The radiative terms are evaluated as negligible due to the cold wall and because the incoming radiation from the flow is reflected.

Solving the surface energy balance equation (Eq. (3.10)) is not trivial since it requires knowledge of material response and the reacting flow which are transient phenomena that are dependent on each other. This can be solved via coupled CFD and material response codes but it is a costly process. Another solution which is well proven is the “transfer coefficients” approach which provides a link between the two problems. Heat and mass transfer coefficients can be used to represent the heat and mass transfer rates at the ablating surface and the two problems can be decoupled. Furthermore this method is shown to be useful for correlating the theoretical and experimental transfer values.

The surface energy balance, in terms of the heat and mass transfer coefficients, C_h and C_m respectively, can be given as follows for a pyrolyzing ablator and in case of no spallation [146][2]

$$\begin{aligned}\rho_e u_e C_h \left(h_r - h_w\right)_e + \rho_e u_e C_m \sum_{i=1}^{N} \left(y_{e,i} - y_{w,i}\right) h_{w,i} + \dot{m}_c h_c + \dot{m}_g h_g \\ + q_{rad,in} = \left(\rho v\right)_w h_w + \dot{q}_{rad,out} + \dot{q}_{cond}\end{aligned} \tag{3.15}$$

where h_r is the recovery enthalpy (denoted as $h_r = h_e + r_c \frac{u_e^2}{2}$, where r_c is the recovery factor) and $\dot{q}_{rad,out} = \sigma \epsilon T_w^4$. This equation is valid for arbitrary Pr and Le numbers. The problem is now reduced to the determination of the transfer coefficients C_h and C_m. They are approximately related by:

$$C_m = C_h Le^{2/3} \tag{3.16}$$

The heat transfer coefficient C_h depends on the total mass blowing rate due to the ablative surface. If we define a new heat transfer coefficient for a non-blowing surface, C_{h0}, then it relates to C_h by:

$$C_h = C_{h0} \left[\frac{ln\left(1 + 2\lambda \dot{m} / \rho_e u_e C_h\right)}{2\lambda \dot{m} / \left(\rho_e u_e C_h\right)} \right] \tag{3.17}$$

---

[2] The derivation of this equation can be found in [146]. His derivation is for non-pyrolyzing materials, therefore the above equation is modified accordingly for pyrolyzing materials.

where λ is the empirical blowing rate parameter and can be taken 0.5 for laminar and 0.4 for turbulent flows [146]. For the case of Plasmatron, the C_{h0} can be determined from the non ablating heat flux probe where the enthalpy at the wall and at the boundary layer edge can be determined by the Rebuilding Code described in Sec. 2.2.2,

$$C_{h0} = \frac{\dot{q}_{cold\,wall}}{(h_e - h_w)} \tag{3.18}$$

Further simplifications can be done with Prandtl and Lewis number approximations. For laminar flows the recovery factor r_c is equivalent to $\sqrt{Pr}^3$. If one can assume that the heat conduction is equal to the viscous dissipation in the boundary layer, thus for $Pr = 1$, the recovery enthalpy will be equal to h_0. Moreover, if one can assume that the thermal and mass diffusivities are the same, thus $Le = 1$, then the heat and mass transfer coefficients are equal $C_h = C_m$.

It is also worth mentioning the non-dimensional mass blowing parameters for pyrolysis and char, being B'_g and $B'c$ respectively. Some material response codes take B' values as input. They are defined as:

$$B'_g = \frac{\dot{m}_g}{C_m \rho_e u_e} \tag{3.19}$$

$$B'_c = \frac{\dot{m}_c}{C_m \rho_e u_e} \tag{3.20}$$

3.1.3. Objectives

To solve the equations given in the previous sections, the material properties of the cork P50 material must be known. However, the elemental composition is unknown and performing extensive material property measurements was not possible with little exceptions discussed in the following sections. The complex behavior and composition of the material make the modeling very difficult. Therefore an inverse methodology is proposed here to characterize and predict its behavior: Experimental data from VKI facilities will be used to solve Eq. (3.10). The approach consists of two steps.

Step 1 To use the experimental pressure, recession and surface temperature to solve Eq. (3.10), with the material properties of a similar material, i.e P45 from Amorim. The thermal conductivity, k, is considered as the only unknown and an iteration will be performed on it until the computed in-depth temperatures match the experimental in-depth measurements as depicted in Fig. 3.2.

---

[3] For turbulent boundary layers $r_c = Pr^{1/3}$.

Step 2 This time, the transfer coefficients C_m and C_h will be computed and will be used as inputs together with the recession profiles in Eq. (3.15) to compute the surface temperature, T_w. An iteration will be performed on C_h until the computed T_w matches the measured surface temperature.

The objectives of the experimental campaign discussed in this chapter can be summarized as follows:

- Providing the experimental data to build the material properties with an iterative process as input to the material response models/codes
- Characterize the material for the three parameters of the Flight-to-Ground Duplication methodology, investigate the effect of pressure, enthalpy and velocity gradient on ablation related phenomena
- Provide a post-flight analysis strategy for validation of the material response model with the transient flight data.

A series of plasma experiments are performed in a given envelope, including QARMAN entry. A total number of 24 samples were exposed to plasma in the VKI Plasmatron and the dependency on pressure, heat flux. Different from generic TPS characterization campaigns, the dependency on the velocity gradient is investigated to take into account the Damköhler number effect. Furthermore, the thermogravimetric analysis (TGA) is performed on two cork samples to determine the mass change of the material with temperature.

First, the test conditions are determined. Then the experimental setup and Plasmatron configuration are described. Finally, the extensive experimental study on the selected Cork P50 material is presented by showing the behavior trends of the material. How the experimental data will be of use for material response modeling and how the three LHTS parameters p, h and β affect ablative characteristics are discussed. QARMAN entry trajectory is compared to the test envelope to roughly predict the surface temperatures. The possibilities for making a full trajectory simulation in a ground facility is elaborated. Finally, how the flight data can be used to validate the material response code is discussed.

3.2. Building Testing Conditions

The testing conditions are a combination of the QARMAN entry trajectory and the application of the Flight-to-Ground duplication methodology. Some test cases were discussed in section 2.2.5 and 2.2.6.

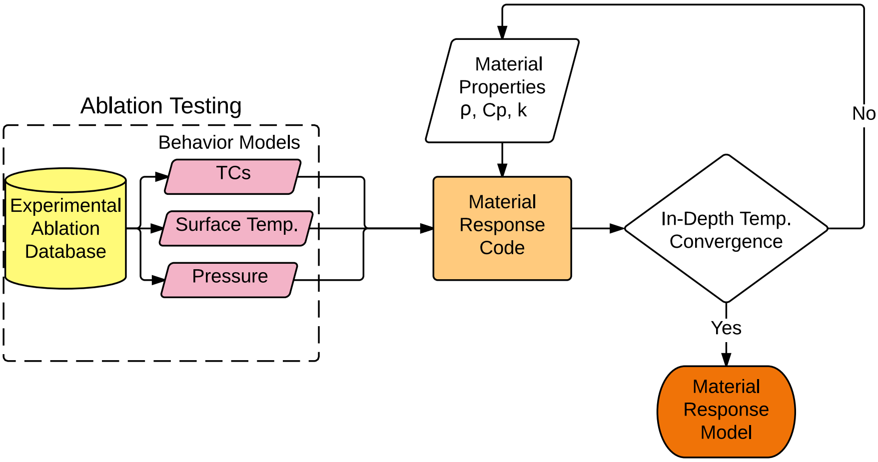

Figure 3.2.: Material response model building methodology.

3.2.1. Free Stream: Pressure and Enthalpy

The free stream conditions are determined based on the QARMAN trajectory data. However the heat flux and pressure envelopes are kept much larger in order to build a global model from which the QARMAN trajectory points can later be interpolated. The chamber static pressure values are 1500, 4100, 6180 and 20000 Pa. On the other hand, the reference heat fluxes, measured by the hemispherical 25 mm probe, are between 280 and 3250 kW/m^2.

3.2.2. Sample Geometry: Velocity Gradient

The flight-to-ground duplication methodology applied to the test conditions given in Table 2.4 resulted in hemispherical probe geometries. The details for 66 km were discussed in Sec. 2.3. The test sample radii for other altitudes are given in Table 2.9. It can be seen that the required samples are very small. In contrast with the philosophy to simulate the stagnation line and its vicinity, smaller sample radii in the big Plasmatron jet would induce significant heating from the side walls. This would prevent the 1D heat conduction assumption and would alter the material response. The application of the Flight-to-Ground duplication with bigger samples were discussed previously and are not included here.

Finally, three sample sizes are considered in the ablation characterization campaign. The smallest sample has a radius of 11 mm in addition to the conventional “frozen” radius of 15 mm and “standard” radius of 25 mm. Although 25 mm sample is not present in the computed sample radii in Table 2.9, it provides an upper bound to the testing envelope. The samples smaller than 11 mm are not included in the matrix due to the 3D effects.

3.3. Experimental Setup and Measurement Techniques

The experimental setup consists of a number of measurement techniques and is depicted in Fig. 3.3. The heat flux is measured by the 25 mm hemispherical probe with a water cooled copper calorimeter. The experimental database is used to scale the target heat fluxes. The dynamic pressure is measured by the Pitot probe.

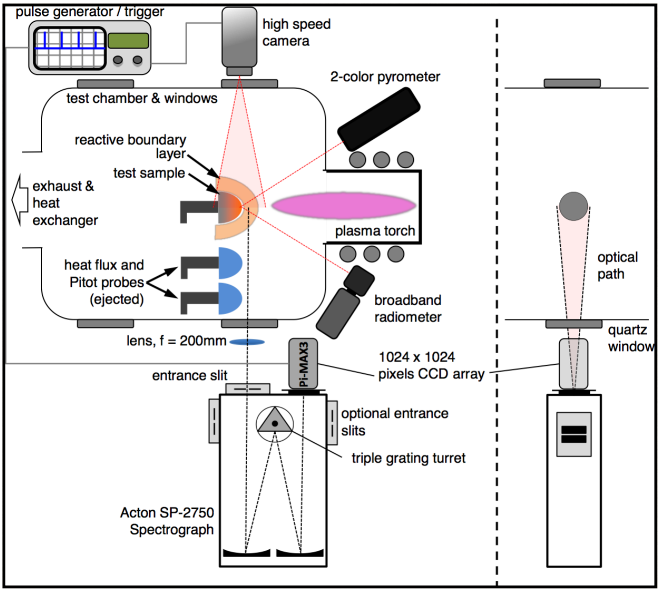

Figure 3.3.: Experimental setup of VKI Plasmatron TPS testing. Courtesy of: Bernd Helber.

As mentioned previously, the samples are hemispherical cylinders with 11, 15 and 25 mm radii. During the heat flux measurements, the samples are kept in the cooling box of Plasmatron chamber so that the samples do not start pyrolyzing do to heating. However, the samples of 25 mm and 11-15 mm were placed on a different sample holder. The sample holder for 25 mm probe was the only one to fit the cooling box.

The samples are each 48 mm in length and have 20 mm deep 7 mm radius cylindrical hole in the back which provides space for thermocouples and mounting on the sample holder. The samples have an average virgin density of 460 $\mathrm{kg/m^3}$. The surface temperature evolution during the plasma exposure are recorded with a two color pyrometer (independent of emissivity) and an infrared radiometer (function of emissivity). The Raytek Marathon (RAYTEK MR1S-C) two color pyrometer performs measurements in a wavelength range of 0.75 - 1.1 μm and 0.95 - 1.1 μm and a temperature range of 1000 - 3000°C while the infrared Heitronics KT19 radiometer functions in the wavelength range of 0.6 - 39 μm and provides as output the integrated thermal radiation over this spectrum, within a temperature range of 0 - 3000°C. The pyrometer outputs can be assumed to be independent of emissivity since the two colors are overimposed in a narrow band, while the radiometer temperature measurement is emissivity dependent. By comparing the results of the two measurement techniques and by suitable data processing and hypothesis, the total emissivity of the test specimen at test conditions can be calculated.

The in-depth temperature of the samples are measured at 4, 8 and 12 mm away from the initial surface with type K and type E thermocouples. The mass change and char-pyrolysis layer thicknesses are determined for each case. A high speed camera is used to determine the swelling and recession rates at 10 frames per second. Additionally, for some of the tests, a high resolution photo camera is used at 2 Hz acquisition to monitor possible spallation and mechanical erosions. The optical emission spectroscopy is used to determine the species behavior (mainly CN and C_2) along a vertical line in front of the sample. For some test cases, three additional spectrometers were placed at the rear side of the sample at three different distances to monitor the pyrolysis gas ejection.

3.4. Results

The material test TGA and plasma wind tunnel test results are presented here. The plasma measurement test matrix and the results are summarized in Table 3.1 by the techniques described in the previous section. Each measurement is further elaborated from here on by pointing out their contributions to solve the material response equations (Eq. (3.4) to Eq. (3.8)) and its boundary condition, the surface energy balance Eq.(3.10) to (3.15).

3.4.1. Thermogravimetric Analysis (TGA)

Thermogravimetric analysis (TGA) is a technique where the mass of a sample is measured continuously under an imposed temperature history. The thermal analyzer STA 449 F3 Jupiter from Netzsch is available at VKI. It operates with two identical alumina crucibles; one is left empty as reference and the sample is put in the other one. A microbalance measures the mass difference between the two crucibles while the sample is exposed to a pre-defined temperature gradient between 25 - 1500°C. The sample undergoes changes like evaporation or decomposition due to temperature increase. Various atmospheres can be applied during the procedure. In the case of cork testing, Argon is used in order to prevent any oxidation or nitridation and to isolate the pyrolysis mechanisms. There is a constant flow inside the vacuum-tight test chamber to purge the gaseous products. However the

Table 3.1.: Test matrix and the summary of experimental results. R, radius, p, pressure, P, power, $\dot{q}_{\mathrm{ref}}$, reference cold wall heat flux, τ, duration, $T_{Surface}$, surface temperature, $\dot{m}$, total mass loss rate and $\dot{s}$, recession rate.

Test	R mm	p Pa	P kW	$\dot{q}_{\mathrm{ref}}$ kW/m^2	τ s	$T_{Surface}$ K	$\dot{m}$ kg/m^2/s	$\dot{s}$ 10^{-5}m/s
13	15	1500	139	524.52	82	1832.86	0.026	5.20
14	25	1500	188	1176.26	48	2003.94	0.028	7.10
14R	25	1500	193	1000.61	48	2037.19	0.028	3.50
15	15	1500	170	1025.64	37	1961.17	0.044	7.60
16	11	1500	175	1029.26	27	2003.13	0.053	28.70
18	15	1500	290	2120.16	13	2307.45	0.139	14.50
18RR	15	1500	365	2907.36	13	2625.34	0.136	62.00
17	25	1500	369	3122.68	17	2454.04	0.055	N/A
22	11	4100	104	292.06	120	1682.75	0.014	12.70
21	15	4100	116	317.09	132	1644.94	0.016	14.20
20	25	4100	120	364.11	171	1588.02	0.011	4.20
19	25	4100	131	520.80	103	1709.20	0.016	2.90
23	15	4100	140	525.12	82	1809.34	0.024	4.30
3R	15	6180	114	432.02	82	1780.94	0.021	N/A
3	15	6180	128	677.97	65	1848.47	0.024	3.68
9R	25	6180	112	449.25	100	1721.71	0.015	N/A
9	25	6180	120	483.30	82	1729.78	0.018	5.20
27	11	6180	115	474.02	60	1804.68	0.023	9.10
5	15	6180	183	1246.73	46	2114.27	0.035	4.90
7R	15	6180	380	2923.64	13	2714.03	0.149	N/A
7	15	6180	410	3227.02	10	2765.37	0.197	18.49
12	25	10000	158	1030.41	120	1986.10	0.019	6.70
24	15	20000	144	484.70	82	1714.62	0.020	7.82
25	15	20000	194	1026.60	37	2030.89	0.036	6.00
26	15	20000	266	3038.02	13	2548.71	0.084	None

incoming flow does not impinge on the sample in the crucible and therefore the sample is considered not affected by any flow.

The TGA was performed on two cork P50 samples to observe its decomposition and reactions as it was heated. Two tests were performed for repeatability and the initial sizes of the samples were 1.8x2.2x3 mm and 2x2.5x2.3 mm. Both samples were heated with a rate of 10 K/min in Argon. Fig 3.4 shows that the pyrolysis begins around 430 K with the mass reduced to 98% and the samples are fully charred at 780 K with the mass down to 24.5%. The char mass is then constant at 20% until the end of the test at 1650 K. The derivative of the mass loss rate is also computed to see the major reactions that would appear in the slope changes and is depicted in Fig 3.4. There is a slight change at around 350 K which is attributed to moisture volatilization by [148]. Then a larger reaction occurs at 488-500 K according to the two sample data. Around 620 K a very small reaction occur and finally at 700 K the major one takes place. These reaction locations are consistent with data for a similar material cork P45, which has the same constituents but a different elemental composition.

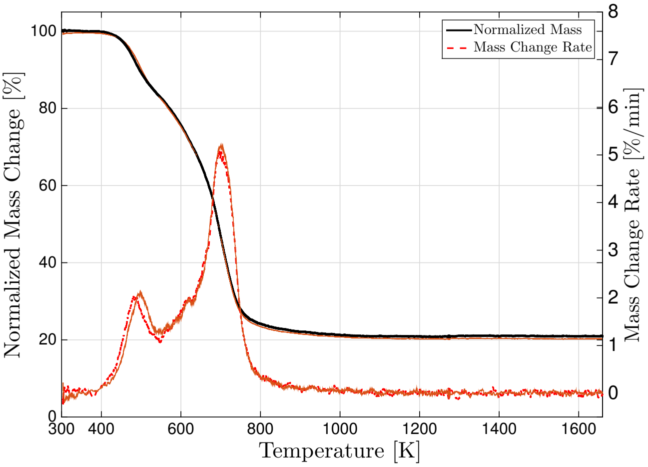

Figure 3.4.: TGA data for two samples with 10 K/min heating rate. The thick lines show the data of sample 1 and the thin lines of sample 2. The normalized mass loss profile for both samples are very similar.

For both samples, the virgin density and the char density can be determined to implement in Eq. (3.1), (3.9), (3.11) and (3.13). The virgin densities, ρ_v are 466.66 and 464.53 kg/m^3 as expected. The char densities, ρ_c are 298.38 and 279.90 kg/m^3.

One can also determine the coefficients of the Arrhenius laws, given in Eq. (3.1), using TGA data. There are two distinctive reactions happening therefore two Arrhenius laws can be fit. The coefficients that are determined by this fitting procedure are, the pre-exponential factor A, the density different term $d\rho = \frac{\rho_v - \rho_c}{\rho_v}$, the order of the reaction N and finally the activation energy of the chemical reaction E. The fitting results for both reactions for both TGA tests are given in Table 3.2

Table 3.2.: Arrhenius law coefficients fitted on the TGA data shown in Fig. 3.4.

	A	$d\rho$	N	E
Test 1	4987.26	227.15	1.07	82678.65
	9999.98	146.03	3.57	51439.49
Test 2	3779.21	266.68	1.15	80561.28
	6317.36	99.28	1.59	58009.70

3.4.2. Boundary Layer Edge Conditions

Prior to present the experimental data from Plasmatron experiments, it is important to determine the free stream conditions at the edge of the boundary layer since they will be useful in a number of applications as will be further discussed in this section and also to determine the non-blowing heat transfer coefficient C_{h0} to compute C_h and C_m as given in Eq. (3.18). The edge conditions are rebuilt using the VKI rebuilding code CERBOULA [89] with catalycities taken from Table 2.2. The rebuilt edge enthalpies, temperatures and species concentrations can be found in Table 3.3. The rebuilt enthalpies are compared to the available enthalpy probe and O-777 data discussed in Sec. 2.2.5 and found to have a good agreement.

3.4.3. Visual Inspection and In-Depth Layers

Although not directly used in the material response modeling, the test samples were monitored with a photo camera in addition to the high speed camera. The changes in the dimensions of each sample after plasma exposure are measured. First of all, it is important to confirm that no material was removed mechanically during the tests so the $\dot{m}_F h_{F,w}$ can indeed be neglected in Eq. (3.10). Secondly, the changes in the surface texture may be important for tuning and improving the material response models especially to see the behaviors during swelling and recessing. Finally, the in-depth char and pyrolysis layer measurements are important to confirm if the samples ablate uniformly around the stagnation region or not, and also to compare with the in-depth temperature measurements to deduce when the pyrolysis or char layers reach the measurement locations.

No significant mechanical erosion was observed except very small scale spallation. All the samples first swelled when they were exposed to plasma

Table 3.3.: Boundary layer edge enthalpy, density, temperature and species concentrations rebuilding with copper catalytic efficiencies using CERBOULA [89].

Test	γ	h_e	ρ_e	T_e	$[O_2]$	$[N_2]$	[NO]	[NO+]	[O]	[N]	$[e^-]$
		MJ/kg	g/m^3	K	$\times 10^{-4}$						$\times 10^{-10}$
13	0.1	11.42	0.880	4670.06	1.02	7089.71	36.00	0.78	2308.55	563.95	14
14	0.1	22.96	0.598	5540.77	0.10	4162.89	12.41	3.82	2320.42	3500.36	70
14R	0.1	19.76	0.653	5371.39	0.15	4999.90	15.74	2.96	2319.05	2662.19	54
15	0.1	20.36	0.642	5404.63	0.14	4843.29	15.05	3.12	2319.34	2819.06	57
16	0.1	20.43	0.641	5408.36	0.14	4825.42	14.97	3.14	2319.38	2836.95	57
18	0.1	41.75	0.331	7873.13	0.00	24.98	0.27	17.36	2319.77	7637.62	318
18RR	0.1	46.83	0.251	10388.76	0.00	0.52	0.02	34.23	2310.91	7654.32	626
17	0.1	48.55	0.232	11239.39	0.00	0.20	0.01	40.39	2307.63	7651.76	739
22	0.1	6.97	3.660	3341.70	371.11	7536.78	282.14	0.01	1807.62	2.34	0
21	0.1	7.20	3.566	3404.87	288.42	7544.18	264.36	0.01	1899.80	3.24	0
20	0.1	8.02	3.209	3709.04	81.21	7572.24	182.57	0.04	2150.59	13.34	1
19	0.1	10.51	2.472	4643.35	3.04	7322.43	62.26	0.57	2292.64	319.06	10
23	0.1	10.53	2.470	4646.06	3.01	7320.17	62.09	0.57	2292.75	321.40	10
3R	0.01	10.71	3.644	4741.66	3.45	7300.58	69.46	0.64	2288.35	337.53	12
3	0.01	15.83	2.898	5417.26	0.61	6124.24	35.50	2.31	2308.40	1528.94	42
9R	0.01	11.22	3.466	4847.77	2.17	7128.56	58.86	0.91	2295.13	514.37	17
9	0.01	11.71	3.438	4936.41	2.03	7095.88	57.37	0.96	2296.05	547.72	18
27	0.01	11.65	3.449	4926.23	2.08	7108.76	57.94	0.94	2295.69	534.58	17
5	0.01	26.74	2.120	6112.23	0.14	3336.54	15.40	6.01	2317.63	4324.29	110
7R	0.01	49.34	0.922	11633.93	0.00	0.56	0.03	43.30	2306.07	7650.04	792
7	0.01	52.31	0.817	13122.78	0.00	0.15	0.01	54.52	2300.10	7645.22	998
12	0.005	24.97	3.523	6149.39	0.21	3848.22	20.91	5.75	2314.74	3810.16	105
24	0.005	34.07	5.456	6966.24	0.11	1679.98	12.20	10.77	2316.81	5980.12	197
25	0.005	40.48	4.517	7821.96	0.04	344.29	3.79	16.68	2318.22	7316.98	305
26	0.005	49.52	2.959	11728.24	0.00	1.64	0.10	44.00	2305.66	7648.60	805

and then started recessing. The only exception was the 15 mm radius sample Test 7 tested at the highest heat flux, which directly started recessing during its short exposure. Moreover, it was observed that for most cases the samples are bigger at the end of the test, so the sample swelled and then recessed but the test was stopped before it recessed further. The reason was that the test matrix is built in the way that all the samples are exposed to the same heat load which resulted in different test durations. Therefore, it is more logical to study the high speed images that clearly show the swelling and recession.

The test sample surfaces significantly changed after the plasma tests. An example image is given for virgin material and tested material for Test 9R in Fig. 3.5. The test photos show that as soon as the sample is in the plasma jet, the cracks occur suddenly. The surface between the cracks (called *cells* from here on) does not change geometry but move away from each other as the sample swells and then get back closer as the sample recesses. It is also seen that the cell surfaces start as concave and later during char recession become convex. This means that the crack sides are higher and the center is lower. This suggests that the pyrolysis gas products are traveling towards the surface along these cracks and due to the cooling effect of the pyrolysis blowing there is less recession in these adjacent areas. However,

Figure 3.5.: Change of cork P50 surface topology from virgin (left) to char cracks (right) after Test 9R.

this hypothesis means that the pyrolysis ejection continues even though the surface is completely charred. This would mean that there is still virgin material beneath the thin char layer. The pyrolysis mechanism is further analyzed in this section by other experimental data as well.

The dimensions of the samples were also measured before and after the plasma tests. It is seen that the swelling is a volumetric phenomenon since the diameter of the sample is also changing along the height. All the test samples were sectioned to identify the char layer thickness as well as in-depth layers of pyrolysis and virgin thicknesses. Fig. 3.6 shows the sections of two samples. It can directly be noticed that there is still a very large amount of virgin material inside and the ablation thicknesses are much smaller. The fact that non charred material is still close to the surface, is consistent with the previous finding of the char ablation concerning the convex surface geometries. The char layer is easy to determine since the cracks start there. It is also seen that the char thickness is quite uniform from stagnation region to the sample aft. Pyrolysis layers are determined from the color change of the virgin material which are still not completely charred. Table 3.4 shows the layer thicknesses for all tests.

3.4.4. Surface Temperatures

For all test cases, the pyrometer was pointed at the stagnation point. Each surface temperature profile indicated a sharp increase shortly after plasma exposure and then reached a steady temperature. The mean steady temperatures taken at the plateau are given in Table 3.1.

The surface temperatures are required to solve the material response equations as well as the second step where an iteration will be performed for C_h for matching purposes.

To analyze the effect of the LHTS parameters (pressure, enthalpy and velocity gradient), one should perform a fitting study so that the compar-

Figure 3.6.: Cross sections of Tests 14R (left) and 26 (right) with radii of 25 and 15 mm respectively. 11 mm samples were completely charred and could not be removed intact from the sample holder.

isons can be investigated at the same conditions. For instance, if we want to see the effect of pressure on surface temperature, we should make sure to isolate the pressure parameter by providing data at the same heat flux and radius. However, due to the nature of the experiments, the reference heat fluxes are not exactly the same, therefore the surface temperature behavior should be interpolated at the required heat flux for a given pressure and model geometry. These free stream and radius dependence will be discussed in Sec. 3.5.3 and 3.5.4.

To perform these fits, each time one parameter is changed and others kept constant. For example, Fig. 3.7 shows how surface temperature changes at a fixed radius and pressure. This is repeated for all test conditions and the fitting coefficients are given in Table 3.5. Linear fits are found suitable within the range of the measurements. Other experiments need to be done to extend the validity of the fits since they may be changing nature from linear to a polynomial. It should be noted that each of these points corresponds to an experiment at VKI Plasmatron and the total number of tests is constrained by the mission budget. Thus it was not possible to increase the number of the experiments although more accurate fits could be done with more points. Given the constraints, for some cases such as for 11 mm radius samples, there is not enough test cases to make fits for heat flux at a fixed pressure, therefore the effect of pressure is omitted and the fit is performed for all pressures as can be seen in Table 3.5. On the other hand, for the pressure 4100 Pa, only low heat fluxes are included in the test matrix so an extrapolation is needed for high heat fluxes and is not preferred as the errors would be very large.

Temperature Errors

Before investigating the effect of pressure or radius by using the fits, it is worth examining the errors of the surface temperature measurements and the fits. The pyrometer device has a measurement error of ±10 K which results on the error bars given in Fig. 3.8. Moreover, the measurement is

Table 3.4.: Sample dimensions before and after test, and char, pyrolysis and virgin thicknesses. $\varnothing$ and l correspond to diameter and height at the stagnation point respectively with subscripts i and f for "initial" and "final", s is the total change in the height, Δ is the thickness with subscripts c, p and v for char, pyrolysis and virgin layers. All units are in mm.

Name	$\varnothing_i$	$\varnothing_f$	l_i	l_f	s_{tot}	Δ_c	Δ_p	Δ_v
3	30	30.6	47.8	49.4	-1.6	4.4	1.5	43.6
3R	30	30.5	47.8	47.8	0.0	2.2	1.0	44.6
5	30	31.8	47.8	48.7	-0.9	4.0	1.1	43.6
7	30	30.3	47.8	51.4	-3.6	4.5	1.7	45.3
7R	30	30.1	47.8	51.0	-3.2	4.5	3.0	43.5
9	50	51.0	47.8	48.6	-0.8	N/A	N/A	N/A
9R	50	50.7	47.8	50.7	-2.9	3.0	1.0	46.7
12	50	50.7	47.8	46.7	1.2	4.1	2.0	40.6
13	30	30.1	47.8	N/A	N/A	3.4	1.1	N/A
14	50	50.8	47.8	45.5	2.3	1.7	0.6	43.2
14R	50	51.1	47.8	44.0	3.8	2.0	0.5	41.5
15	30	30.8	47.8	49.0	-1.2	1.5	1.0	46.5
16	22	N/A	47.8	N/A	N/A	1.4	1.8	N/A
17	50	50.7	47.8	48.3	-0.5	1.7	0.5	46.1
18	30	31.0	47.8	50.4	-2.6	3.7	1.3	45.4
18RR	30	30.5	47.8	50.5	-2.7	3.4	1.7	45.4
19	50	50.7	47.8	46.6	1.2	2.4	1.1	43.1
20	50	50.7	47.8	46.2	1.6	2.7	1.9	41.7
21	30	29.9	47.8	49.2	-1.4	3.5	2.0	43.7
22	22	N/A	47.8	N/A	N/A	Fully	0.0	0.0
23	30	31.0	47.8	49.3	-1.5	2.7	1.1	45.5
24	30	30.8	47.8	49.3	-1.5	2.7	2.1	44.5
25	30	31.0	47.8	49.1	-1.3	2.5	1.4	45.3
26	30	31.1	47.8	49.8	-2.0	2.0	1.1	46.7
27	22	N/A	48.0	N/A	N/A	3.0	1.0	N/A

fluctuating during the plasma exposure as shown in Fig. 3.9 for Test 3. The standard deviation from the mean steady value for Test 3 is 26.48 K which is larger than the typical pyrometer device error of 10 K. The fluctuation ranges depend on the test case and should be considered individually. Finally, another source of error is the one coming from the linear fit which changes with the test case as well. The error value is defined as the maximum error of the overall heat flux range of the used fit. For Test 3, the maximum error in the linear fit is 38.09 K over the whole heat flux range.

In conclusion, there are three sources of errors which are the instrument error, the measurement fluctuations and the fitting errors. The instrument error and the standard deviation of the fluctuations can be coupled as ($\pm\,10\,\mathrm{K} + \sigma$) which is equal to 36.48 K for Test 3. However the error coming

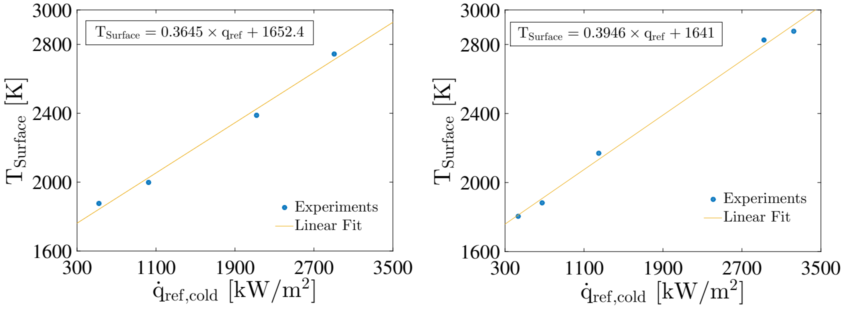

Figure 3.7.: Change of surface temperature with heat flux for a fixed pressure and sample geometry of 15 mm radius. Pressure 1500 Pa (left) and 6180 Pa (right).

Table 3.5.: Surface temperature linear fits in function of reference cold wall heat flux. The form is: $T_{Surface} = a \times q_{ref} + b$.

Pressure [Pa]	Radius mm	Number of Points -	a -	b -	R^2 -
1500	15	4	0.3317	1636	0.9938
6180	15	5	0.3622	1628	0.9959
20000	15	3	0.3078	1631	0.9672
1500	25	3	0.2109	1793	0.9803
*4100	25	2	0.7734	1306	-
*6180	25	2	0.2370	1615	-
All	11	3	0.4165	1581	0.9784
All	15	14	0.3485	1612	0.9758
All	25	7	0.2916	1606	0.9173
1500	All	8	0.2751	1709	0.9404
**4100	All	5	0.5099	1481	0.4803
6180	All	8	0.3734	1597	0.9923
20000	All	3	0.3078	1631	0.9672

*The fits are invalid due to insufficient number of experiment points.
**The fit is invalid due to very narrow heat flux range.

from the fit is independent of the measurement errors. So the overall error is defined as the maximum between the coupled error and the error of the used fit. For a data point where Test 3 would be used, the error bar would indicate ±38.09 K. All the error bars in figures of Sec 3.5.3 and 3.5.4 are defined as explained here however the details are not shown further.

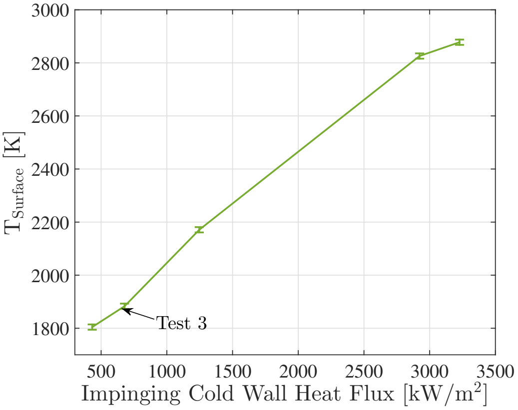

Figure 3.8.: The pyrometer device error on the tests with the 15 mm radius sample at 6180 Pa pressure.

3.4.5. Emissivity

The emissivity appears explicitly in the surface balance equations (3.15) and (3.10). The two color IR pyrometer measures the temperature independent of the emissivity whereas the radiometer measures spectral radiance in the range of 0.6-39 μm. Therefore the emissivity of the sample, locally at the measurement point can be calculated as follows [1]:

$$\varepsilon'_{(0.6-39)} = \frac{L'_{(0.6-39)}}{L^0_{(0.6-39)}} \tag{3.21}$$

where L is the radiance and 0 stands for the blackbody radiance. For the wide spectral range of 0.6-39 μm and an emissivity 1 seen by the radiometer, this can be approximated for radiative equilibrium as:

$$\varepsilon'_{(0.6-39)} = \left(\frac{T_{radiometer}}{T_{pyrometer}}\right)^4 \tag{3.22}$$

Note that this method makes a gray body assumption, which means that the emissivity is constant at the measurement wavelength range.

The emissivity values computed from the averaged temperatures at the steady state are given in Appendix D. It should be noted that these values are only preliminary because of two reasons: the radiometer calibration and the gray body assumption. While the pyrometer calibration was made up to 3000 K, it was only possible to calibrate the radiometer with a black body up to 1770 K due to wavelength limitations of higher temperature black body devices. For surface temperatures above this value, the calibration is

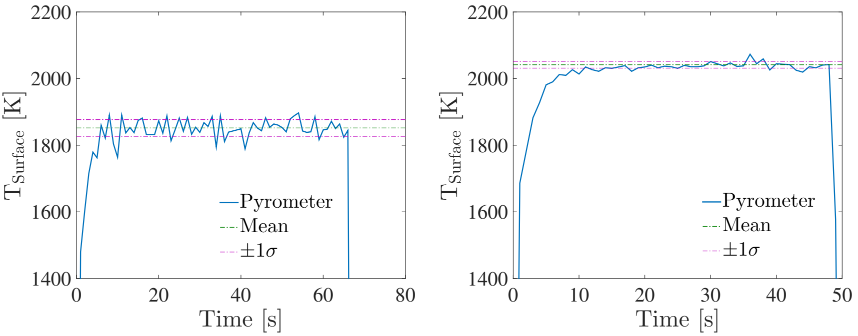

Figure 3.9.: Surface temperature measurements with the pyrometer for Test 3 (left) where the mean temperature is 1882 K and the standard deviation is 26.48 K, and Test14R (right) where the mean temperature is 2037 K and the standard deviation is 10.49 K. (See Table 3.1 for the test details)

extrapolated, leading to errors. Secondly, the radiometer measures the radiance over a wide range of wavelengths. Although if one computes the Planck radiance curves for typical TPS surface measurements with emissivity 1, it can be seen that the radiance is almost constant only after 10 μm, this can still suggest that gray body assumption may not be valid between 0.6 and 10 μm.

To determine the emissivity by other means, an effort is made by Helber [151] to determine the spectral radiance by an emission spectrometer to fit Planck curves, and by an infrared camera working in 8 - 9 μm range (and lower maximum temperature limit ~1500 K). Another possibility is to use the one color of the pyrometer, assuming it is emissivity dependent, and the two color as a blackbody to deduce the emissivity. Even if the emissivities computed with these different methods agree with each other, the only conclusion to be drawn on the gray body assumption is limited in narrow wavelength bands and cannot be generalized to the full measurement range of 0.6 - 39 μm with the current capabilities at VKI. In conclusion, assuming gray body assumption is valid, the emissivity values may be used as a preliminary data to implement in the expressions discussed in Sec. 3.1.2 for surface temperatures lower than 2000 K where the radiometer is calibrated.

3.4.6. In-Depth Temperatures

The in-depth temperatures provide comparison datasets for the solution of the material response equations. It was stated that the first step is to determine the thermal conductivity, k appearing in $\overline{\overline{\lambda}}$ in Eq. (3.8), with an iterative procedure. The iteration is continued until the computed in-depth temperature distribution matches the experimental ones.

All samples were equipped with three in-depth thermocouples. They were mounted at 4, 8 and 12 mm away from the surface of the virgin sample. As the sample swells or recesses, the surface position changes and the thermocouples stay where they initially were since the extensions are fixed to the sample holder. Therefore, throughout the test the thermocouple depths change with respect to the surface but in the plots presented in this study, they will be named after the initial positions.

Fig. 3.10 shows the surface and in-depth temperature profiles of Test 23 as an example. The temperature immediately at 4 mm depth is much lower than the surface temperature. This suggests that the thermocouple is not in the ablating char layer. The final char thickness for this test case is 2.7 mm as given in Table 3.4. It is also seen that the final sample height is larger than the original. Assuming the thermocouples do not change position when the sample is swelling or recessing, the first thermocouple is still in pyrolysis layer. Indeed the TGA data showed that the pyrolysis is apparent above 430 K, which is the measured temperature range by this thermocouple.

For the cases where the char layer is thicker and there is a thermocouple in it, the temperature rises above the measurement range of type K to a value closer to the surface temperature. A good example of this is the Test 22 where the sample almost completely charred and broke into pieces while removing from the sample holder. The temperature profiles can be seen in Fig. 3.10 where the first two thermocouples were in char layer and failed to provide data. Usually, the measurement junction opens when the temperature rises above its operational limit, and later when the sample cools down the two thermocouple wires are soldered back together and start working as can be seen after 125 seconds. The same thermocouples may be re-used in other tests[4].

Coming back to the Test 23 example, the first and although not very visible, the second thermocouple data show a "hump" after a certain time as if a thermal wave arrived. This behavior has also been reported for other materials such as NASA's PICA, Phenolic Impregnated Carbon Ablators [149]. The term "hump" is also used by Milos and Chen [149] referring to the treatment of PICA data first in arcjet tests and later the real flight data from Mars Science Laboratory thermal plugs by Mahzari et al. [144].

It can be seen that a certain exothermic reaction occurs at those moments with an incoming thermal wave. One possibility of exothermic reactions would be the oxidation reactions reach subsurface areas due to the cracks or the charring surface which changes the surface porosity. By definition, the pyrolysis reactions are endothermic, which is the main reason ablative materials are good insulators. To cross check, TGA data are considered; apparent reactions had occurred at 488 and 700 K. The hypothesis is that the endothermic reactions observed during the TGA analysis are responsible for "cooling down" the material and decreasing the in-depth temperatures.

The location and the timing of these humps are examined as the pressure

---

[4] It was seen that this event does not affect the calibration of the thermocouples.

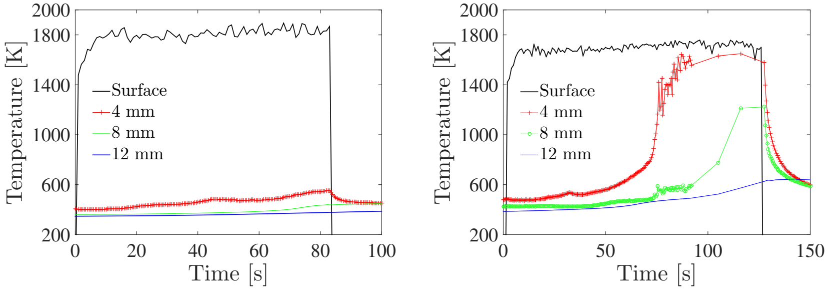

Figure 3.10.: The surface and in-depth temperatures of Test 23 (left) and Test 22 (right).

and sample radii are changed. Fig. 3.11 show the 4 mm thermocouple data for two cases having the same sample radius but the same reference heat flux suggesting same surface temperatures. Regardless of the pressure, the three humps occurred almost at the same time and temperature. A similar behavior is seen when the reference heat flux (thus same surface temperature) kept constant and the sample radius is changed as depicted in Fig. 3.11. In both cases a hump occurs around 41 s but at different temperatures. For all the test cases, humps are seen around 490 K and for those that increases enough, at 700 K. These data agree very well with the TGA data. However, during the plasma tests, an additional hump occurred consistently around 430-440 K as well.

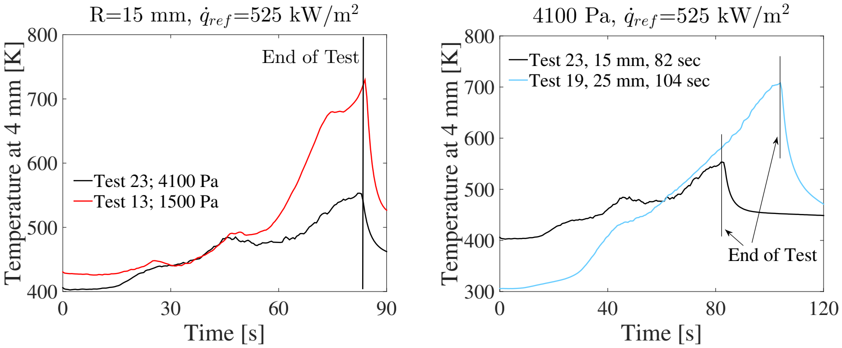

Figure 3.11.: The "humps" in thermocouple data at 4 mm depth for two cases of different pressures but the same radius and same reference heat flux (left); and for two cases of different radii (also different test duration) but the same pressure and same reference heat flux (right). Note that the 15 mm radius samples could not fit in the cooling box, therefore are subjected to a pre-heating.

3.4.7. Swelling and Recession Profiles

The recession information is required in the equations (3.11) and (3.13). We provide the recession rate as input in both k and C_h computation iterations. The recession profiles also play a role in the mass blowing rate determination approach discussed in the next section.

The swelling and recession profiles were captured with a high speed camera throughout the plasma exposure. First, the edges of the sample are determined. Then the time evolution of the stagnation point along the horizontal line is tracked as shown in Fig. 3.12 during the swelling and recessing processes of Test 19. Test 19 sample swelled until t = 24.85 s and recessed until 99.85 s, when the plasma was stopped. The top image in Fig. 3.12 shows the events of test onset, end of swelling, and end of the test. A chessboard calibration sheet image is acquired prior to each experiment to convert the pixels to mm.

The recession rates were determined from the slopes once the swelling is over and there is an apparent recession. These rates are given in Table 3.1. Three recession profiles at a fixed pressure and sample radius are depicted in Fig. 3.13 for an increasing heat flux. It is seen that at higher heat fluxes, thus surface temperatures, the recession rates are higher. It is also seen that the swelling takes longer time at lower heat fluxes. Due to the test durations, it was not always possible to accurately determine the recession rates. Fig. 3.14 shows three recession profiles with similar heat fluxes but at different pressures. It is seen that as pressure gets higher, the swelling duration is longer and the swelling thickness is larger.

A different behavior is also observed when the heat flux and the pressure are kept the same but the radius is changed from 15 to 25 mm. The recession profiles are given in Fig. 3.15. The swelling durations seem to be similar but the total recession is higher for the smaller sample.

During the tests, it is seen that the material surface directly chars and the surface temperatures stay constant after a very short time for all tests. From here it can be assumed that the char layer at the surface ablates constantly even though the sample is overall swelling as seen by the high speed camera. Therefore, the high speed camera cannot determine the recession rate until the sample stops swelling. This is also taken into account when the mass loss of each sample is further analyzed in Sec. 3.4.8.

3.4.8. Mass Blowing Rates

When studying the mass loss of each sample, primarily it is important to justify that the ablation, thus mass loss, is only due to thermo-chemical processes; indeed no mechanical failure is observed for any of the test cases. Since the surface is fully charred when injected in the plasma jet, its recession is also only due to the thermo-chemical processes of the reactions at the wall and inside the sample creating gaseous products that leave the sample

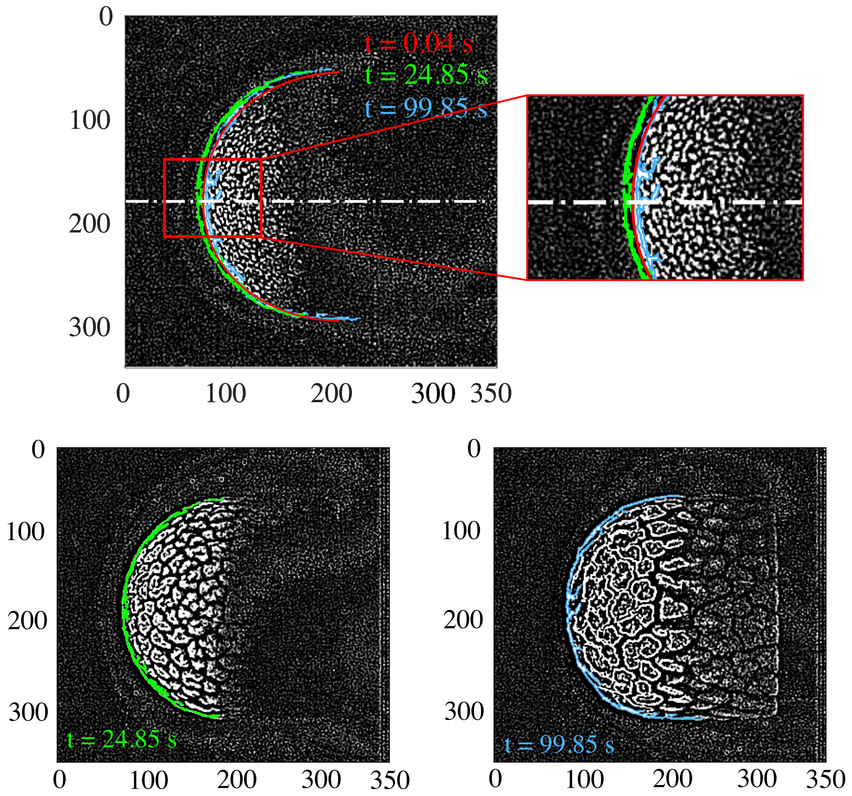

Figure 3.12.: Determination of swelling and recession of Test 19 by high speed camera. The top image shows the sample at the beginning of the test, t = 0.04 s. The sample swells until t = 24.85 s (bottom left) and recesses until the end of the test, t = 99.85 s (bottom right). The top image also shows the change of the surface location throughout the test with a zoom on the stagnation point. Each pixel shown in the axes correspond to 0.23 mm.

leading to mass loss. Therefore, the total mass loss is due to pyrolysis outgassing and char ablation.

The mass of each sample is measured before and after each test. The mass loss rate computation methods differ in literature based on the materials. Conventionally, the pyrolysis and char blowing rates can be separately estimated when the non-dimensional blowing rates B'_c and B'_g are known. When they are not known, Smith et al. [148], who studied the cork P45 material for a rocket engine application, preferred to compute the total mass loss rate as the mass difference before and after the test, divided by the test duration and sample surface area. They could not determine the recession

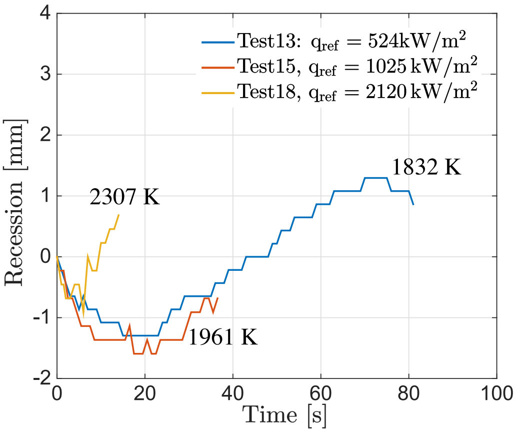

Figure 3.13.: Swelling and recession profiles from high speed camera of cases with the same radii (15 mm) and pressure (1500 Pa) but different reference heat fluxes. Positive values correspond to recession and negatives mean swelling. The steady state surface temperatures are also indicated.

rates due to the swelling behavior. Furthermore, they presented the char and pyrolysis rates in distance per second, using the final char and pyrolysis layer thicknesses.

Having the identical problem of swelling, the global mass loss rates are computed from the total change in mass before and after per exposure area per unit time as:

$$\dot{m}_{tot} = \frac{m_i - m_f}{\tau A} \tag{3.23}$$

where τ is the test duration, m_i and m_f are the initial and final mass, and A is the total surface area of the hemispherical sample.

Since the first assumption is that all mass loss is due to pyrolysis and the oxidation of the char, this could be treated as the total value. To analyze which portion of the total mass loss come from which process, the dimensional char blowing rates are computed. One approach is to consider the recession occurs at the constant rate since the beginning of the test even though it is not visible on the high speed camera images initially due to swelling. This assumption agrees well with the constant surface temperature during the whole test. Eq (3.13) could be used to determine the char blowing rates. The char density was measured by TGA, the question is then to accurately determine the recession rate. A first method can be the char recession rates are taken as the slopes of high speed camera data after the swelling finishes. Alternatively, following the proposal of Smith et al. [148], the char and pyrolysis layers can be determined by the depth between the

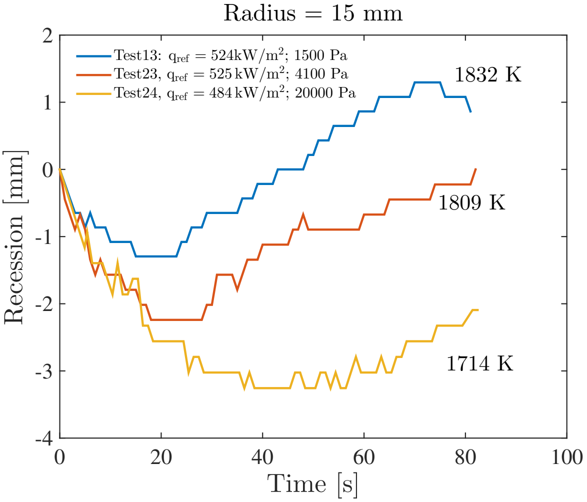

Figure 3.14.: Swelling and recession profiles from high speed camera of three cases with the same radii (15 mm) and similar heat fluxes but different pressures. Positive values correspond to recession and negatives mean swelling. The steady state surface temperatures are also indicated.

virgin surface and the final surface below the char/pyrolysis thicknesses divided by the test duration. The second method does not always provide results for the test matrix presented here because of the swelling. For many cases, the test was not long enough to have a severe recession. This also affects the accuracy of the high speed camera data handling where the slopes are determined.

Using the high speed camera data as a basis, and when not available the Smith approach [148], the char blowing rates are computed. The total mass loss and the char mass rates are shown in Fig. 3.16. For literature convention, it is also normalized with the sample radius and the pressure at the boundary layer edge. The difference between the total mass loss rates and the char rates can be attributed to the pyrolysis blowing rates. For some cases the total mass loss has almost the same value with the char rates so the char blowing rates could not be determined accurately. The reason is the volumetric swelling that conceals accurate recession measurements.

According to Metzger et al. [152] when the mass loss rate is normalized by radius and pressure, the term is a function of temperature. Metzger et al [152] studied the non pyrolyzing graphite, therefore the char ablation was only due to the oxidation processes. They observed a reaction limited process up to 1500 K where the mass loss rate increases gradually depending on the sample radius; then the rates reach a plateau until 2800 K where the radius and pressure no longer affects the mass loss rate even with increasing

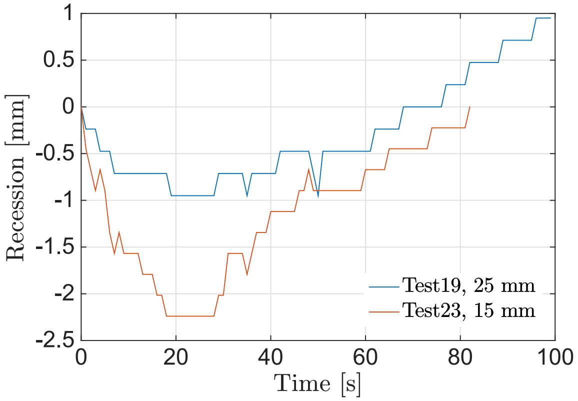

Figure 3.15.: Swelling and recession profiles from high speed camera of cases with the same reference heat flux (525 kW/m^2) and pressure (4100 Pa) but different radii. Positive values correspond to recession and negatives mean swelling.

surface temperature, suggesting a diffusion-limited process. After 2800 K, sublimation starts and the mass loss is increasing again as a function of temperature and also pressure. Metzger et al. suggest for graphite that the smaller sample radius and higher pressures move the curves towards higher temperatures. However, for cork P50, these trends are the opposite: as sample radius gets smaller, the temperatures are lower and higher pressures have the same effect. Overall it can be said that as the surface temperature increases, the mass loss rate also increases by an order of magnitude and no plateau is observed as for graphite ablation shown by Metzger et al [152].

In summary, it was seen that the swelling behavior and the pyrolysis effects changed significantly the complexity of the measurements and the results deviated a lot from the expected behavior in absence of pyrolysis. A dedicated campaign in the future could be performed by exposing the samples for much longer times to plasma to increase the accuracy of the recession rate measurements. For flight safety, it can be concluded that even when the samples lost considerable amount of mass during the test, they have not recessed much so to increase the temperatures at the back. One could also say that the volumetric swelling, although cannot be put in an accurate prediction model yet, would keep the hot char layer away from the back surface, which would protect the back shell for a longer time.

3.4.9. Optical Emission Spectroscopy

Although the optical emission spectroscopy results do not contribute directly to the solution of the previously mentioned equations, it is worth mentioning

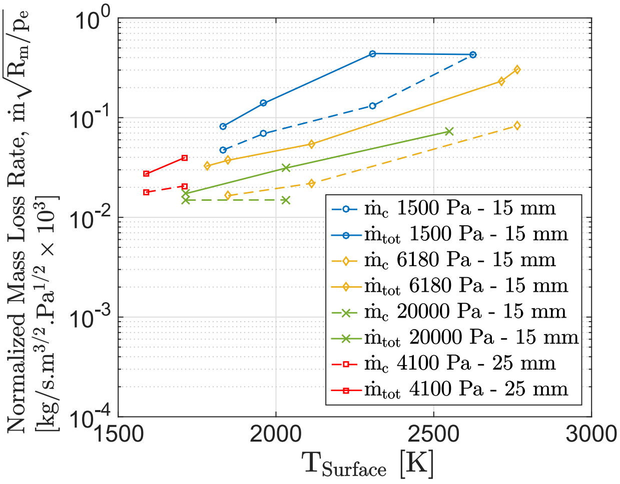

Figure 3.16.: The normalized total and char mass rates with surface temperatures.

for qualitative reasons. The gaseous products captured by the spectroscopic tools can be usef in the future to identify the chemical reactions. Two emission spectroscopy setup were implemented during the experiments. One was the vertical profile of the stagnation region and the other was the three spectrometers. They are briefly described here with an emphasis on the pyrolysis product outgassing.

Stagnation Region During the experimental campaign, the locally resolved emission intensities in the ablation boundary layer are measured by Helber [18] with focus on the data treatment to obtain mole fractions of reaction products. An intensified camera with a 2D CCD array connected to an Acton Series spectrograph recorded the full radial and spectrally resolved boundary layer emission profile. Under the assumption of axisymmetry and an optically thin medium, the inverse Abel transformation yielded locally resolved emission intensities of ablation products such as CN and C_2 Swan. Both assumptions were examined and found to be valid. The detailed investigation on the measurement techniques and the results can be found in the work of Helber et al. [18].

An interesting outcome can be seen in Fig. 3.17 for the emission of the pyrolysis product C_2 Swan for Test 19. When heated, the hydrocarbon alkyne acetlyene present in the material C_2H_2 undergoes the following chemical reactions and break up into C_2 and hydrogen [150],

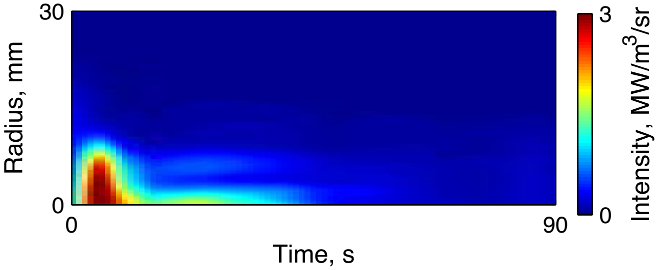

Figure 3.17.: C_2 emission along a vertical profile in front of the test sample for Test 19.

$$C_2H_2 + M \leftrightharpoons C_2H + H + M \tag{3.24}$$

$$C_2H + M \leftrightharpoons C_2 + H + M \tag{3.25}$$

which can be detected by the spectrometer.

The high speed camera data show that the Test 19 sample front moved forward for 25 seconds about 1 mm then recessed backwards for 2 mm where the test ended. The spectrometer was located 2 mm away from the stagnation point and was not moved during the test. At 25 s, the surface is the closest to the spectrometer line of sight by 1 mm. From the C_2 Swan profiles, it is seen that there is a high emission until 15 s and the C_2 disappears at about 42 s. The fact that swelling continues until 25 s and the C_2 intensity significantly drops at 15 s, show that the pyrolysis gas products are reduced since the sample surface still gets closer to the spectrometer until 25 s. Indeed at 25 s, there is again a slight increase of C_2 which decays as the surface moves away from the surface. The pyrolysis production can also be seen by the photographs. These data are analyzed further in detail with the side spectrometers in the following section.

Sample Side Wall In addition to the stagnation spectroscopy, three Ocean Optics HR4000 spectrometers were placed at the aft of the sample to monitor the emission species in a wavelength range of 350 - 1100 nm. Fig. 3.18 shows the experiment timeline of Test 26 with photos including the three spectrometer locations shown by red dots. It can be seen that a light color layer is surrounding the sample. At the beginning this layer is visible at the stagnation point as well but later during the plasma exposure, it can only be seen on the sides and it gets smaller and smaller. It should also be noted that the three spectrometers are in this bright layer at the beginning but towards the end the far spectrometer stays in the darker plasma layer. The spectrometer integration times are 200 ms for the close (C19) and middle

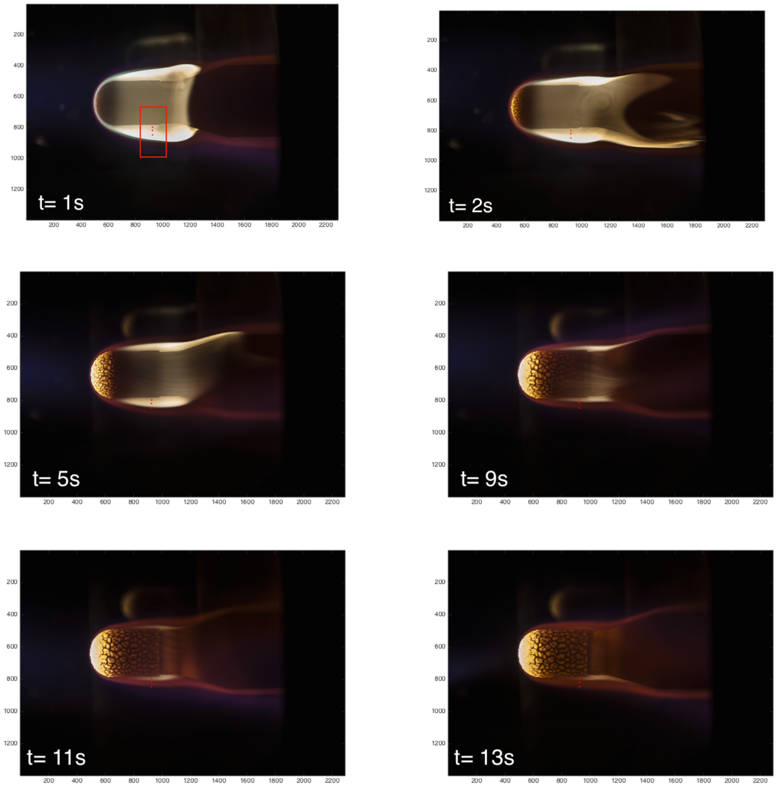

Figure 3.18.: Plasma exposure of Test 26. Test duration, 13 s. The red dots, depicted in the red box of the first image, show the position of the three side spectrometers.

(M14) spectrometers and 100 ms for far (F71) spectrometer. It is known that the Plasmatron jet fluctuates and the fluctuation frequencies at 20000 Pa are higher than the integration time, but instantaneous spectra could not be acquired with the used spectrometers.

The emission peaks are analyzed to check the differences between these locations. CN and C_2 are the prominent radiating species. CN lines were visible throughout the entire test for all spectrometers while C_2 Swan feature between 485 - 520 nm is shown in Fig. 3.19. The fact that this feature is still present at the end of the test shows that the pyrolysis process is still on going as shown by other experimental data. On the other hand, CH emission, plotted in Fig. 3.20, is also visible in the far spectrometer while it appears only at 18 s for the middle and close ones.

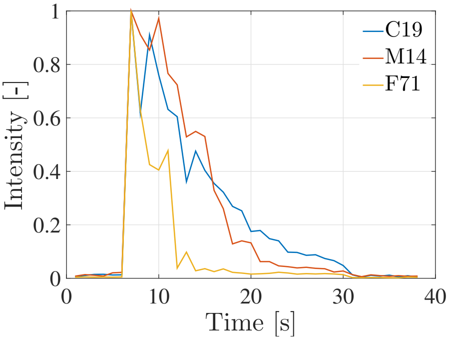

Figure 3.19.: Normalized C2 Swan emission acquired by three spectrometers at 516 nm. C19 is the closest one, M14 is the middle one and F71 is the far spectrometer.

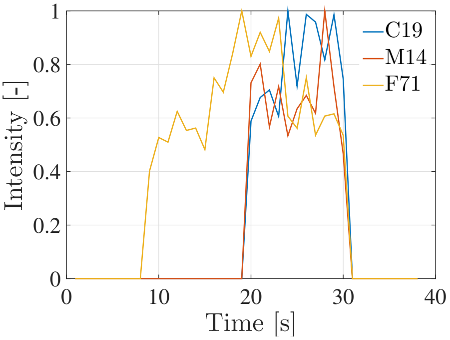

Figure 3.20.: Normalized CH emission acquired by three spectrometers at 431 nm wavelength. C19 is the closest one, M14 is the middle one and F71 is the far spectrometer.

During the test, the photo camera and the spectrometers were not synchronized so the spectra of the different color layers cannot be acquired precisely due to plasma fluctuations. However, it is clear that the chemistry differs and the presence and absence of pyrolysis products deserve further attention with a dedicated experimental campaign.

3.5. Discussion

3.5.1. Contributions to Material Response Model

The details for building material response models were discussed previously in Sec. 3.1. To provide the necessary information, an extensive experimental campaign is conducted for characterizing the ablative cork P50 material. Table 3.6 summarizes which experimental data contribute to the solution of which equation.

Table 3.6.: Contributions of the experimental data for building the material response model.

Location	Quantity	Equation/Purpose
Flow	$\dot{q}_{cold\,wall}$	(3.18), LHTS parameter investigation
	h_e	(3.18), LHTS parameter investigation
	h_w	(3.18), LHTS parameter investigation
	p, p_{dyn}	Thermodynamic variable computation, LHTS parameter investigation
	$y_{i,e}$	Thermodynamic variable computation
Surface	T_w	(3.10), (3.15) and Comparison Data for Step 2 (Sec. 3.1.3)
	ϵ	(3.10), (3.15)
	$\dot{s}$	(3.11), (3.13)
In-Depth	ρ_v	(3.9)
	ρ_c	(3.9), (3.11), (3.13)
	Arrhenius coefficients	(3.1)
	Temperature by TCs	Comparison Data for Step 1 and 2 (Sec. 3.1.3)

3.5.2. Effect of Edge Enthalpy

VKI Plasmatron facility is operated by adjusting the power and pressure as previously mentioned. At a fixed pressure, increasing the power directly increases the free stream enthalpy therefore, the resulting heat flux increases as well. At this point, the effect of the sample radius is neglected and the experiments results are evaluated for fixed geometry, thus velocity gradient at a given free stream. It was clearly seen in Sec. 3.4.4 that at fixed pressure, the surface temperature increases linearly with the heat flux. This also means that the temperature increases with the edge enthalpy. The rebuilt enthalpies were shown in Table 3.3 and the linear fits are not further given here.

3.5.3. Effect of Pressure

The effect of pressure on surface temperature is investigated by fixing the rest of the variables which are the sample radius and reference heat flux. The 15 mm sample is chosen as more data are available at different pressures and heat fluxes. In order to fix the heat fluxes, the previously discussed fits are used because not all experiments were conducted at the exact same heat flux. Fig. 3.21 shows the change of surface temperature with pressure at a number of fixed heat flux values. It can be seen that at a constant heat flux, the effect of pressure is quite small. At lower heat fluxes the maximum difference is about 45 K while at high heat fluxes the maximum difference is 150 K. As expected, the effect of pressure is quite smaller than increasing the heat flux at a constant pressure as shown in Fig. 3.7. It is also seen that there is a decrease of temperature of about maximum 80 K when the pressure is increased from 1500 Pa to 20000 Pa. This is consistent with other low density ablator experimental data where a decrease between 60 to 160 K was observed [151] for 1500 and 20000 Pa pressures.

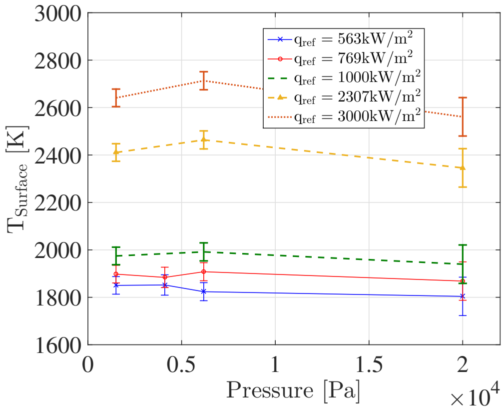

Figure 3.21.: Effect of pressure for 15 mm radius sample tests at fixed reference heat fluxes. The error bars indicate the maximum of the measurement and the fitting.

An interesting outcome concerns the boundary layer edge enthalpies. Each of the pressure and heat flux couples correspond to a boundary layer edge enthalpy. Fig. 3.22 shows the enthalpy values for three heat fluxes. As the pressure increases, the amount of power that should be given to the

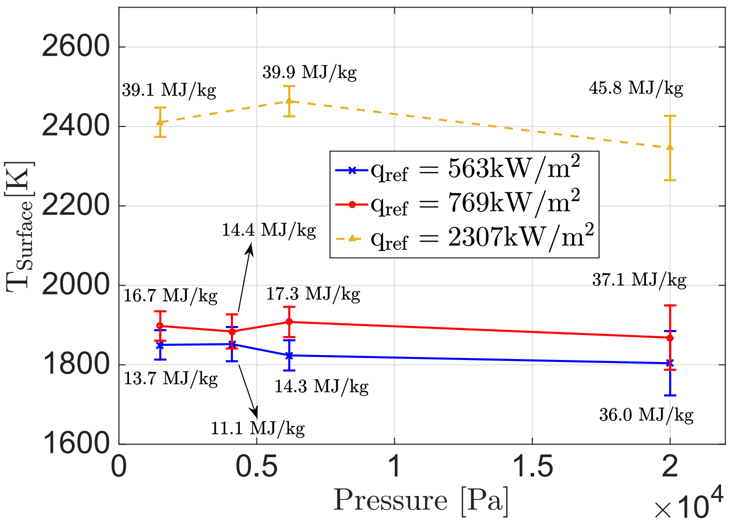

Figure 3.22.: Effect of pressure with boundary layer edge enthalpies for 15 mm radius samples.

plasma gets higher if we want to keep the heat flux same. This is simply because there are more gas particles in the chamber. Thus, at constant heat flux, at high pressures the edge enthalpy is also higher, while the velocity gradient becomes smaller.

To understand these effects, we can study each term in the energy balance equation at the surface given in Eq. (3.10) with the steady state solid conduction assumption given in Eq. (3.11). The conduction term is a function of the thermal conductivity k and the temperature gradient ∇T. As the pressure increases, the experimental data show that the surface temperature almost stays constant, or decrease about maximum 80 K. On the other hand, the temperature at the boundary layer edge increases significantly. For instance, considering the Tests 15 and 25, having the same probe geometry and reference heat flux, but tested at pressures 1500 and 20000 Pa respectively, the edge temperature increase from 5404 K up to 7821 K. This increase of 2417 K is much larger than the change in the surface temperature. The temperature along the boundary layer is computed for a cold wall as in Fig. 3.23 and it shows that the temperature gradient on the conduction term increases significantly. The thermal conductivity is also changing however its effect is expected to be smaller and overall, the conduction increases when the heat flux is kept constant but the pressure is increased.

The diffusive term on the other hand is a function of the diffusion coefficient D and the species concentration gradient ∇y_i. According to [3] the

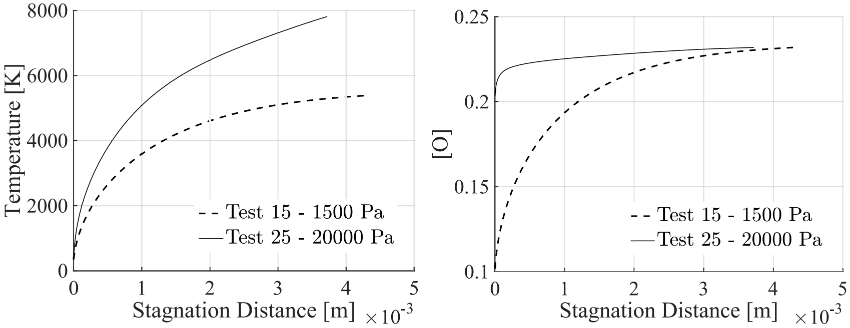

Figure 3.23.: The boundary layer temperature and oxygen mass concentration profiles, for tests 15 and 25 having the same radius, reference heat flux but tested at 1500 and 20000 Pa respectively.

diffusion coefficient increases with increasing temperature and decreasing pressure. The species concentrations were checked for Test 15 and 25 (cold wall) as plotted in Fig. 3.23 and one can conclude that the diffusive term is decreased with increased pressure. Note that the surface concentrations are not the same since the surface catalycity is changing with the pressure [1].

The change in the convective term $\dot{m}_s h_{s,w}$ can be deduced from the experimental data if one considers that the surface recession is due to char ablation. So this term is then equal to $\dot{s}\rho_{char}$ where $\dot{s}$ is the recession rate and the second term is the char density measured from TGA. Continuing from the example of Test 15 and 25, one can see that the recession rates are both 0.06 mm/s and the char density is constant. Therefore this term is not changed with higher pressure.

The first term on the right hand side of the Eq. (3.10) is equivalent to the convective term discussed above. The second term is the radiative heat flux, which is a function of temperature and emissivity and if the temperature decreases slightly, this term decreases as well. The last term is the conduction inside the solid, which is measured during the plasma tests with the in-depth thermocouples. Fig. 3.24 depicts that the temperature slope is higher for the high pressure case so the conductive term is increasing.

In summary, the described heating mechanisms seem to be balancing each other which results in the same or slightly lower surface temperatures for increasing pressure. One could also speculate that although it is said that the heat flux is kept constant, only the *cold wall* heat flux is constant. It may well be that the hot wall heat fluxes are not equal. Unfortunately, due to unknown material elemental composition and the lack of models to simulate the swelling behavior, most of the above terms cannot be computed to make a quantitative comparison.

Another observation is that although the recession rates are not changing, the total swelling and recession thicknesses and the swelling durations are

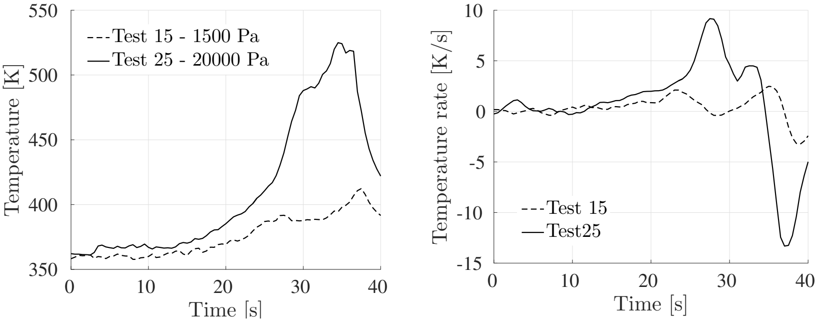

Figure 3.24.: The in-depth temperature and the temperature rate data of the thermocouple at 4 mm, for tests 15 and 25 having the same radius, reference heat flux but tested at 1500 and 20000 Pa respectively. Test duration for both tests was 37 s.

different. For Test 15 and 25, it is seen that the lower pressure, Test 15, swells during 19 seconds for 1.5 mm while the swelling time for higher pressure, Test 25, is 23 seconds and swells for 3 mm. The recession slopes are then the same for both cases. The same two behaviors were observed in Fig. 3.14 for three tests. This suggest that the swelling thickness and duration is dependent on pressure, thus enthalpy if the heat flux is kept constant. A different trend in the in-depth temperature is also observed as shown in Fig. 3.11.

3.5.4. Effect of Radius

After analyzing the effect of pressure, how the velocity gradient affects the surface temperature of the ablator is also investigated. The cases where different sized samples are exposed to the same free stream having the same pressure and reference heat flux are chosen. Fig. 3.25 shows how the temperature changes with different radii. It should be noted that since the free stream is the same, thus the samples are exposed to the same pressure and enthalpy at the boundary layer edge. However, when the *impinging* heat flux is measured with a heat flux probe that has the same geometry as the sample, the heat flux gets higher with smaller sample radius as shown by the Damköhler probes campaign in Appendix B. It is seen that, in the ablative tests, the velocity gradient affects only by a maximum of 82 K except the high pressure high heat flux case where the difference between the mean temperatures is 150 K. The error margins however are observed to be large at the points with high differences.

The boundary layer profiles of temperature and oxygen are plotted for a cold wall in Fig. 3.26 for Test 14R, 15 and 16. These are cases exposed to the same pressure and reference heat flux, thus free stream enthalpy,

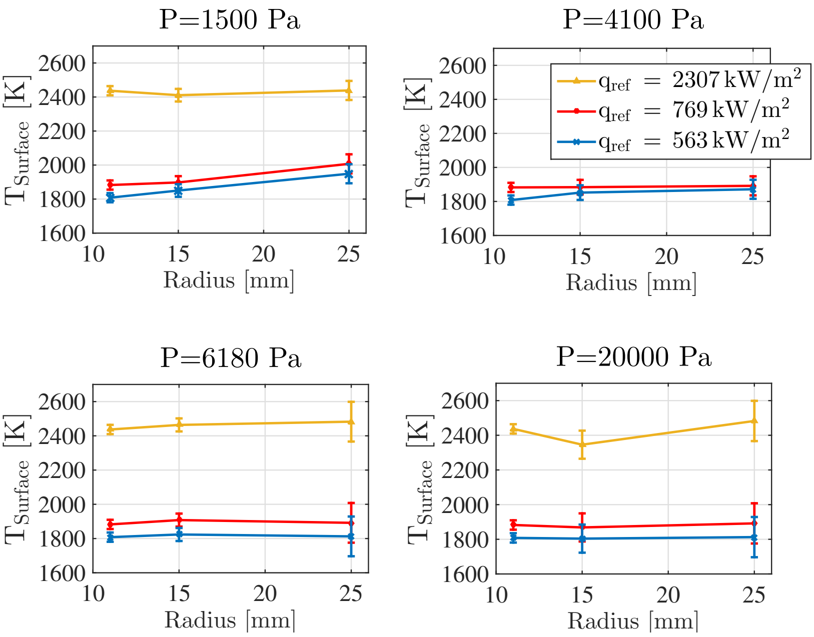

Figure 3.25.: Effect of radius for fixed reference heat fluxes and pressures.

however they have 25, 15 and 11 mm probe radii respectively. As the radius gets smaller, the conduction in the fluid phase is increasing as given by the temperature profiles. The diffusion on the other hand is also increasing as shown by the species profiles. Indeed, this confirms the higher *impinging* heat flux on the smaller sample sizes since the conduction measured by the calorimeter is equal to the conduction in the fluid and diffusion as given in Eq. (3.14). Recalling the energy balance at the ablative surface given by Eq. (3.10), the first two terms on the left hand side can also be considered increasing for the ablative surfaces. The third term, $\dot{m}_g h_{g,w}$, would cancel out if a steady state conduction is assumed inside the material. The fourth term was shown to be equivalent to $\dot{s}\rho_{char}$. The high speed camera data, after swelling is over, showed that for 25 and 15 mm samples, the recession rates are similar (0.05 and 0.06 mm/s) however the smallest sample returned a rate of 0.28 mm/s. From here, using the char density data from TGA which is constant, one can see that the $\dot{m}_c$ is higher as the sample radius is getting smaller.

The first term on the right hand side of the Eq. (3.10) is again balanced by the recessing surface as it is the mass that has to leave the control volume with incoming solid, thus it is also increasing with higher recession, meaning smaller radius. The radiative heating is increasing by a very small factor

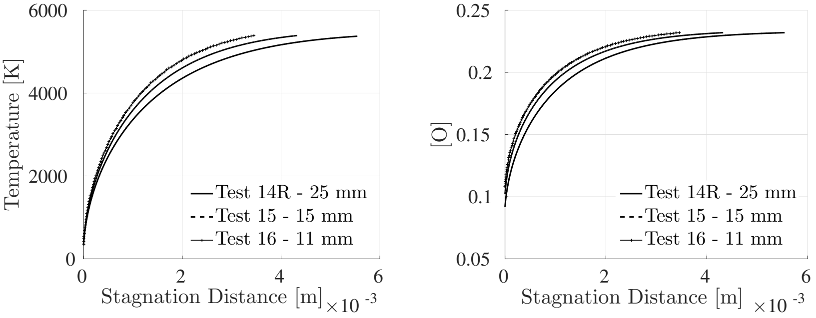

Figure 3.26.: The boundary layer temperature and oxygen mass concentration profiles, for tests 14R, 15 and 16 which are exposed to the same free stream pressure and enthalpy but having different probe radii of 25, 15 and 11 mm respectively.

due to the small increase in surface temperature. Similarly, the conduction in the solid increases as measured by the thermocouples. This suggests the hypothesis that the left and right hand sides of the equation balance each other to the point where the surface temperature does not change. When one considers the cold wall heat fluxes, since the impinging heat fluxes are higher for small radii, the first though is that the surface temperatures should be higher due to increasing heat flux. However it is observed and analyzed that the fluid conduction and diffusion are converted to conduction in the material which is a function of the chemical behavior of the ablator as discussed for Eq. (3.11). In order to see the effects on the blowing terms, a quantitative analysis has to be performed which requires a series of additional material properties testing that were not available at the time of this study.

In addition to the surface temperature analysis, it is also important to note the effect of radius on the recession/swelling profiles and the in-depth temperatures. It was shown in Fig. 3.15 that the smaller radii resulted in a bigger recession although the swelling durations were comparable. This may be due to the side heating of the smaller samples, but it necessitates further investigation before conclusion. The in-depth temperatures for changing the radius were plotted in Fig. 3.11 and it was seen that the heating slopes were steeper for the bigger sample.

3.5.5. Flight to Ground Duplication Mapping

The results of the ablation characterization campaign are analyzed in comparison to the QARMAN flight. The trajectory of QARMAN is computed with a ballistic coefficient for a constant squared cross sectional area. Even though it does not include the nose curvatures or material information, the altitude, velocity, thus enthalpy and pressure profiles are accurate enough for the baseline design. The CFD computations tell us more on the flow properties around the vehicle. However, the available CFD computations did not incorporate the surface chemistry and a radiative equilibrium surface was assumed, so the computed hot wall heat fluxes from CFD are not representative of the flight. Therefore, it is more relevant to predict how the surface temperature is going to change on an enthalpy-pressure map. The surface temperature then would allow us to predict other parameters knowing the altitude and velocity, thus stagnation pressure.

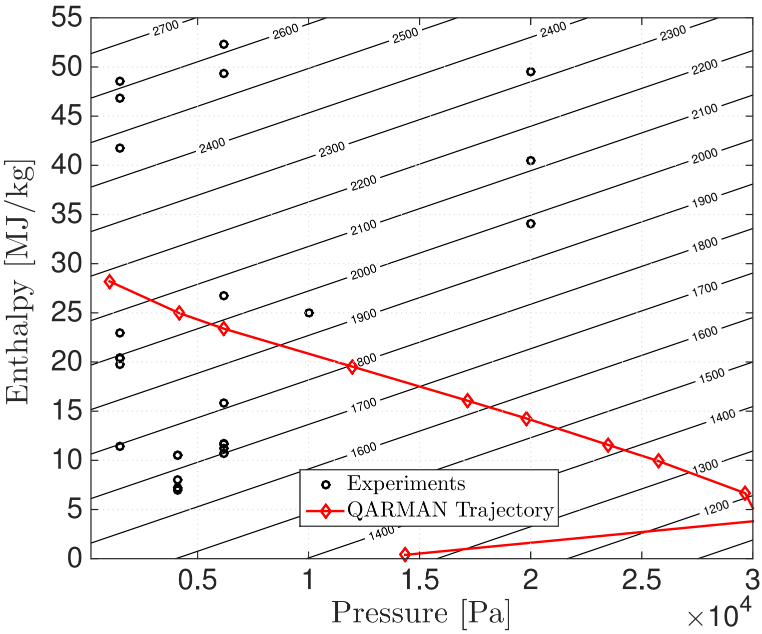

Figure 3.27.: Expected surface temperatures along QARMAN entry trajectory in Kelvin. Fitting rule: $T_{\text{Surface}} = 1568 - 0.01701 \times p_e + 22.1 \times h_e$. The errors of the fit are ±80 K with a 2σ margin.

The experimental data are correlated in a contour fit as depicted in Fig. 3.27 with the entry trajectory of QARMAN. It can be seen that in some cases, such as 20000 Pa, the expected trajectory is far below the experimental points. Despite the fact that the fitted surface temperature for lower enthalpies will be more erroneous, the operational envelope of the facility did not allow to make lower enthalpy measurements at those pressures. This covers a conservative test range in terms of heat flux. Furthermore, the shown trajectory is the nominal trajectory and the actual flight could follow a higher velocity one.

The map shows that the highest surface temperature will be around 2200 K on the surface. This gives us further information such as the surface emissivity will stay in the range above 0.8 for all trajectory.

It was shown in Sec. 2.3 that in order to duplicate the heat flux of the hypersonic entry in our ground facility, we need to respect the boundary layer edge enthalpy, pressure and velocity gradient. Due to the small radii, the altitudes below 66 km could not be tested with the actual sample radius. It was also shown that for a fixed free stream velocity, the temperature increase about a maximum of 80 K from 25 mm samples down to 11 mm. Since the needed sample radii are smaller, further increase in the surface temperature can be expected. One could take a rough linear approach and state that if the surface temperature increased by 80 K for a 2.3 factor decrease of radius, for 60 km which is the peak heating point, conservatively the change would be 150 K with comparison to the 25 mm radii.

A final remark should be made on the the fact that the experiments were conducted for a steady free stream condition. As a consequence, the data do not consider the transient heating history while during the flight, an accumulation of aerothermodynamic effects will act on the TPS. The next section covers the aspects and limitations of *dynamic testing* in ground facilities.

3.5.6. Dynamic Testing

The dynamic testing approach to simulate a full trajectory was discussed in Sec.2.4. Despite the added value of a conservative heat flux for TPS sizing, if the focus of the test is to accurately characterize the TPS along an entry trajectory, a trade-off study has to be performed based on the needs. Therefore, one has to analyze which parameters are representative during the experiments at constant pressure and radius but changing enthalpy. The effects of pressure and radius were discussed in detail in Sections 3.5.3 and 3.5.4. It was seen that the surface temperatures and emissivity mainly depended on the heat flux and are less affected by the pressure and radius. Within the envelope of the test matrix these effects on the surface temperature were shown in Figs. 3.22 and 3.25. On the other hand, it was seen that the changes in pressure and radius altered notably the material response in terms of recession and swelling profiles, as shown in Figs. 3.15 and 3.14. Similarly, the in-depth temperatures were also different for the same heat flux and radius but with different pressures, as plotted in Figs.3.11 and 3.24.

The dynamic testing has obviously its limitations with the existing wind tunnel capabilities. If the surface properties such as temperature and emissivity or a conservative heat flux are the focus of the study, then enthalpy stepping can be used. It was shown that the enthalpy steps with fixed radius and pressure provide conservative test conditions in terms of heat flux. However to accurately simulate the material behavior at changing conditions, a new pressure system should be designed for spontaneous modifications or an automated sample geometry design that can change nose geometry during the test. These constraints of ground facilities reveal once again the importance of performing flight tests, as they are currently the only feasible way for full dynamic tests. Next chapter discusses such small scale and low cost test platform, QARMAN.

3.6. Validation Strategy with Flight Data

Although the wind tunnel experiments can provide validation cases for material response models, they have limitations such as steady free streams, stagnation region etc. The validated material response codes can be run for transient entry trajectories however flight data are needed for a full validation. During the flight, we will only have access to in-depth temperature and pressure measurements by the in-flight experiments described in the next chapter. Since we cannot observe the TPS behavior externally during the flight, we will have to compute its response by the developed models using the available flight data. It was discussed in detail that some input parameters are necessary to run the material response codes. The surface temperature appears in both steps of the model development as described in Sec. 3.1.

If we can extract the evolution of the surface temperature at multiple locations of the vehicle nose, the shape change and recession information during the flight can be extracted. Here, first an inverse heat conduction method to determine surface temperatures using the in-depth temperature measurements is presented. Secondly, having access to the surface temperature, the material response model can be validated in the dynamic entry conditions.

It should be noted that the inverse method requires accurate knowledge of the thermal conductivity and the specific heat, therefore it can only be implemented once the material response model is finalized. Thus, the method is introduced here as a guideline as well as post-flight validation strategy.

3.6.1. Inverse Heat Conduction Method

The extraction of the surface temperature using the in-depth temperatures and surface pressure is an ill-posed mathematical problem and attracted a lot of attention in the literature [144, 162]. The inverse problem methodology consists of the usage of in-depth temperatures to solve the 1D heat conduction equation and estimate the surface temperature and heat fluxes. An overview of how to implement the procedure is provided in Fig. 3.28. It requires the knowledge of the material thermal conductivity which can be extracted from the material response model using the experimental data as described in this chapter. Pizzo et al. [162] developed a finite volume code for a C/C material test bench having 4 in-depth thermocouples. She used three deepest thermocouples to estimate the first thermocouple and surface temperature and heat flux with 0.8% and 1.14% errors. Once the material response model is finalized, one can apply the methodology of Pizzo on the experimental test cases where the computed wall temperatures, $T_{w,comp}$ can be cross checked with the pyrometer measurements, $T_{w,exp}$. How the material properties and the inverse methodology will be used in flight data processing is described in the next section.

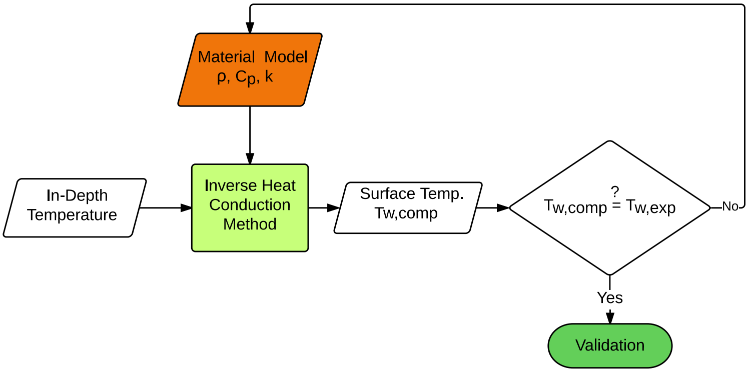

Figure 3.28.: Building the inverse heat conduction method for deducing the surface temperature from in-depth temperature measurements.

3.6.2. Material Response and CFD Validation

The validation of the material response models can be done simultaneously with the validation of the CFD computations. Although the hypersonic CFD computations were not performed by the author, a validation strategy is suggested. Fig. 3.29 shows a way to achieve such validation. The hypersonic CFD computational database for QARMAN is constructed with a lot of assumptions such as non-catalytic and radiative equilibrium walls, virgin TPS geometry, etc. A coupled simulation can be performed using the updated models with the flight data, where an ablative boundary condition can be applied to the correct geometry and actual flight conditions. The simulation schemes can be iterated until the best match with flight data is achieved. Similarly, the future material response models should be updated by flight data even if a good match is achieved with the ground test simulations. This is primarily important since during the flight, a temperature history with changing free stream conditions is present which cannot be simulated in ground test facilities.

To do so, a full entry trajectory simulation can be performed on virgin QARMAN geometry using the response model. The in-depth temperature history can be used as the comparison data like in the validation with the ground test data. Using the magnitudes determined by the inverse heat conduction method, recession can also act as a matching parameter. The thermal conductivity or other material properties as well as the transfer coefficients C_h and C_m can be iterated until a good agreement is found.

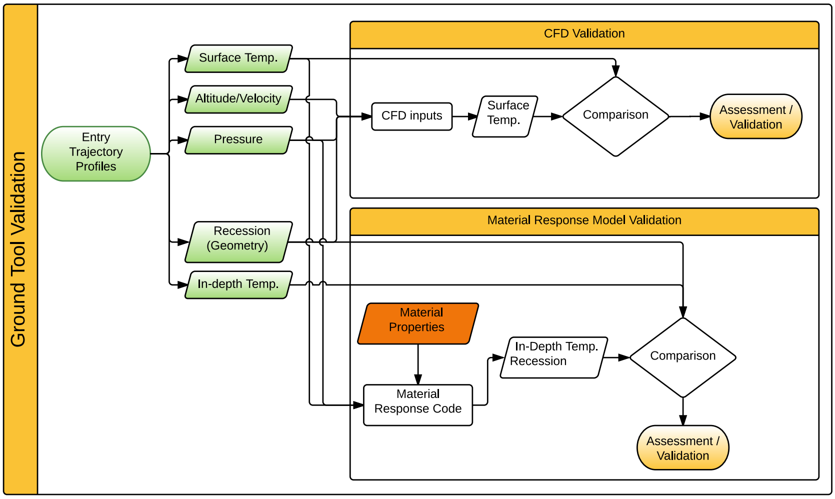

Figure 3.29.: CFD and material response model validation strategy.

3.7. Concluding Remarks

Material response models are necessary to predict TPS material efficiency and they can be validated by flight experiments. Although building the model and its implementation is out of the scope of this thesis, a model by Pinaud et al. [145] is detailed as example and how the mass, momentum, energy equation set can be solved using the surface energy balance boundary condition is discussed. A 2-step inverse methodology is proposed to provide the required material properties using plasma wind tunnel experiments. The first step consists of the determination of thermal conductivity, k, giving as input the measured recession profiles and the surface temperature by converging the measured in-depth temperatures to the computed ones. The second step is to determine the transfer coefficients C_h and C_m, giving as input the recession and by matching the computed and measured surface temperatures. Thus, a number of plasma experiments are performed with three objectives of providing experimental data for the material response model, investigating the effects of the LHTS parameters, pressure, enthalpy and velocity gradient, and proposing a strategy for validation by flight data. How each experimental result will be used in the response model equations are stated in Sec. 3.5.1, and the effects of the LHTS parameters are discussed in Sec. 3.5.2 to 3.5.4.

Using the results of the Flight-to-Ground duplication methodology and the free stream characterization techniques discussed in Chapter 2, the tests conditions are built to characterize QARMAN's TPS material Cork P50 in Plasmatron. A wider range of sample radii and heat fluxes are tested to allow interpolation between test conditions. Three sample sizes of 11, 15 and 25 mm radius are tested. The surface temperature was acquired by a pyrometer and radiometer, which allowed to extract emissivity. Three thermocouples were inserted in each sample at 4, 8 and 12 mm to monitor the in-depth heating. A video camera and a high speed camera were used to monitor the surface deformation and the swelling/recession profiles. The mass of each sample was measured before and after. Each sample was also sectioned to determine the char, pyrolysis and virgin layers. Two optical emission spectroscopy methods were implemented, one as a vertical line of sight in front of the sample and a second used three spectrometers aligned on the aft side of the sample to monitor the pyrolysis species outgassing.

In addition to the plasma wind tunnel experiments, a thermogravimetric analysis is performed to determine the virgin and char densities of the cork P50 material. The TGA results also reveal the temperatures where the major pyrolysis reactions occur. Arrhenius laws can be fit to the mass loss profiles to show how much mass is lost per reaction. This information is crucial to solve the mass conservation equation of the material response model.

The mass blowing rates and mass loss rates are studied. An important amount of pyrolysis outgassing is observed in agreement with the large virgin material left in the samples. An attempt to quantify the char blowing rates is made however it was seen that the swelling behavior of the material severely prevents from determining the char recession rates accurately.

The effect of each parameter of LHTS, being, heat flux, free stream enthalpy, pressure and radius are examined separately. Not all experiments were conducted at the same reference heat fluxes therefore surface temperature fits were performed for a more accurate comparison. It was seen that for a fixed sample geometry and pressure, the temperature linearly increased with the reference cold wall heat flux, so the free stream enthalpy. Furthermore, for a fixed sample geometry and fixed heat flux, the change of pressure is investigated. Note that to reach the same heat flux at a higher pressure, one must operate the facility at a higher power so the free stream enthalpy is also higher. It was seen that the surface temperatures did not change as much as the previous comparison. A maximum decrease of 80 K is observed when going from 1500 Pa to 20000 Pa. The effect of velocity gradient is also investigated by exposing different sized samples to the same free stream pressure, enthalpy and reference heat flux. If the cold wall heat fluxes were to measure at the given sample radii, one would measure higher cold wall heat flux with the small sample. However it was seen that reducing the sample size from 25 to 11 mm, the surface temperature only increased by 82 K. Studying the surface energy balance for an ablative wall, it was concluded that the conduction in the solid balances the increasing velocity gradient and the surface temperatures are not significantly affected.

A surface temperature map is built in terms of enthalpy and pressure and the QARMAN trajectory is superposed. The expected stagnation point temperatures are not higher than 2200 K. However one must take into account that the tests are performed on a single trajectory point, thus steady pressure and heat flux. The heating history of the material at dynamic free stream conditions is not present. This could change the material response, hence the shape change and in-depth temperatures as well as swelling/recession profiles.

The aspects of dynamic testing were discussed in the previous chapter and the effects of enthalpy or pressure stepping were shown. For the ablative test cases, it is shown that although the surface magnitudes do not depend highly on pressure and sample radius, the swelling/recession profiles and in-depth temperatures are affected significantly. Therefore a trade-off needs to be done for the stagnation material response, when simulating the temperature history in the plasma wind tunnel whether the surface or in-depth behaviors is the primary objective. The limitation of the current ground facility setup emphasizes on the importance of flight testing. The flight tests are the platforms where the material can be exposed to all the atmospheric entry dynamics of a spacecraft. Thus, improving the measurement techniques and the small sized entry probes are necessary for dynamic testing.

The validation of the material response models and CFD computations can be performed with flight data. The test case QARMAN will provide in-depth temperatures and surface pressure from the in-flight experiments. A perspective is given on how the flight data can be used for validation. The surface temperature appears in all steps of the material response models either as an input or as a matching parameter. A 1D inverse heat conduction method from [162] is mentioned as it is a method to extract surface temperature from in-depth temperature measurements. An iterative procedure is then introduced, using the determined surface temperatures, for the validation of the material model at dynamic entry trajectory conditions.

Chapter 4.

Flight: QARMAN In-Flight Experiments

The methods for understanding the physics of the atmospheric entry were presented in the Introduction as numerical simulations, ground tests and flight tests. Making atmospheric entry research on CubeSat platforms acts as an intermediate step between an actual mission and the wind tunnel tests on ground. Naturally, these small vehicles are probes designed for testing purposes. Despite their limitations, they can be sent to the actual trajectory, even to other planets or moons, partially with the actual configuration for data collection. The market availability of the off-the-shelf components (COTS) for these platforms highly reduces the design and development costs. Once these small probes are advanced enough for aerothermodynamic research, they can be launched almost as frequent as wind tunnel tests, and serve as the new method for experimental database construction.

Ground testing in wind tunnels has a long history. Wind tunnel designs, limitations and measurement techniques are well known and practiced. Oppositely, making the same research on CubeSat platforms is a new approach and is studied at VKI for its valuable return on flight data. The measurement techniques on-board of this new practice are detailed in this chapter similar to the wind tunnel techniques presented in Chapter 2.

The previous chapter covered the experimental treatment of ablators in a wind tunnel. Therefore, there is already an expertise on the techniques, such as measuring in-depth temperatures with thermocouples. This know-how is transferred to the design of the experimental payloads of QARMAN. In order to establish a solid ground for future development of new techniques, the payloads of QARMAN are presented in a way that allows the reader to design a payload from scratch, fit to fly on CubeSat like nano-platforms. For instance, how and why thermocouples are chosen for in-depth temperatures is elaborated although it is trivial based on wind tunnel experience.

Testing in flight environment is more demanding than wind tunnel experiments. To adapt a measurement technique or an experiment in a flight platform, strong interactions are required with the system level and the launch vehicle. Differently from other flights, the experimental payloads on the CubeSat platforms are the primary driving force on the design of the platform, of course, within the range of the constraints. Thus, the details of the technical aspects and more engineering work are included here providing the major steps.

First, the experimental payload design methodology is presented. It is later applied to the ablation related temperature and pressure experiments XPL01 and XPL02. XPL01 consists of thermal plugs making multiple depth temperature measurements at three locations on the ablative nose. Moreover, XPL02 is the pressure measurements at three locations on the blunt nose, consisting of bare pressure ports and a pressure spool at the back TPS surface. The trade-off study for placement scenarios is detailed. Finally, two successful test campaigns in VKI Plasmatron are presented where the payload heads and the acquisition electronics were placed in the test samples and were exposed to plasma.

4.1. In-Flight Experiment Design Methodology on Highly Constraining Platforms

Since the launch of the first CubeSat, these platforms have become highly interesting for educational, scientific and industrial use. The standardization of the launch pods allow CubeSat providers to work independently from the launch vehicles and this brought up a new philosophy for sending vehicles to space. The science application on CubeSats has specific difficulties due to the very strict mass, volume, power and data constraints. These constraints, however, are the reason of their relatively cheap costs and in fact pose scientifically interesting problems, such as the aerothermodynamic duplication of squared geometries as discussed in Chapter 2. Furthermore, a strong interdependence exists between the systems level and the payloads. Doing aerothermodynamic research on CubeSat platforms requires a dedicated payload design methodology. Such methodology is presented here based on the aerothermodynamics experience and references in literature concerning the space mission designs (e.g. [153]). One should keep in mind that the methodology is for design purposes and therefore does not include the flight model environmental tests, the deployer interface tests and the launch acceptance tests.

The methodology takes the “Mission Objectives” as input since the payloads of a space mission are derived from the mission objectives and requirements.

- **Stating the Problem and Defining the Payload Objectives**
  It is important to clearly explain why this phenomenon is interesting to investigate. The existing numerical, experimental and real flight test studies should be analyzed and the pros and cons as well as the open points should be well understood in order to point out the contribution of the proposed payload to science or engineering. Then, the quantitative payload objectives should be determined based on the mission objectives, concept, requirements and constraints.

- **Subject Trades: Measurement Parameters/Magnitudes**
  The mission "subjects" are defined under two groups: active and passive. Active subjects are the controllable quantities such as GPS navigation systems where the characteristics can be adapted during the design phase and/or the mission. Passive subjects are the measured quantities of the investigated phenomena, such as temperature or pressure in the case of QARMAN's in-flight experiments. The subjects are derived from the mission objectives. On a CubeSat platform, both types are used. In these constraining platforms, it is very important to determine the fundamental subjects to gain from volume, mass, power and data. Sometimes, the desired magnitude can be a combination of several subjects. A trade-off study should be conducted to reach the optimal number of subjects. How each subject can lead to the desired information should be detailed with references.

- **Preliminary Investigation**
  The existing models should be investigated and numerical/experimental simulations should be performed to have a first estimation on the magnitude at the desired location. Critical locations and moments of the flight should be pointed out with solid reasons.

  Based on the first estimations of magnitudes, the "performance thresholds" of one sensor unit should be determined. They should consist of all aspects of a measurement, such as measurement range, location, accuracy, frequency, mass, volume, power consumption, data size, TRL and cost. "Acceptable" and "Desired" performance requirements should be grouped in two parts which will be the criteria of the measurement technique selection. These two groups highly depend on the CubeSat platform design since the system level derives the available resources. The power, volume, mass and data budgets are the primary constraints.

- **Measurement Techniques**
  For each chosen subject, all the possible sensor types should be found and should be evaluated in terms of the specific items covered in the performance thresholds for the CubeSat platform feasibility analysis.

- **Preliminary Configuration and Operations Concept**
  The feasible measurement techniques should be assessed for whether they are suitable for measuring the parameter at the critical position and moments.

  Next, the measurement chain should be defined and mass, volume, power and data budgets should be assessed for the additional components. The selection of the measurement techniques or sensors should be made at this point. The concept of operations of the selected instrument should be defined stating in detail the operation timeline along the trajectory. How the user will get the end product/data and its format should be clarified. If the selected configuration no longer agrees with the performance thresholds, the procedure should be iterated with another candidate sensor.

- **Ground Testing Methodology and Extrapolation to Flight**
  Not all aspects of the hypersonic entry can be duplicated in one single facility. Therefore, the selection of the test facilities demands additional care. The range of free stream conditions should be compared to the mission entry trajectory. The maturity of the flow characterization methods of the selected facility is of great importance as well as the existence of a well-established extrapolation methodology, or similitude laws, between the flight and the ground conditions. If necessary, new measurement techniques should be proposed and developed.

  The test campaigns should be designed thoroughly. Prior to testing, a Test Readiness Review (TRR) may be required. After the experiments, detailed test reports should be prepared so that the whole team is informed and is updated on the developments. It is important to keep track of the events during each test. Post-processing data should include a sensitivity/uncertainty analysis. If necessary, complementary numerical simulations should be performed. The test data should be compared to the first estimations done at the beginning of the design process. In case of a discrepancy, the measurement technique may need to be changed or the tools for the preliminary investigations should be improved in case of need.

- **Risk Analysis**
  A risk analysis should be performed on two aspects: Mission Risks and Payload Risks. A number of approaches on detailed risk analysis on CubeSat platforms is available in literature [154, 155].

- **Success Criteria**
  The success criteria should be defined quantitatively or based on primary and secondary objectives. When applicable, full success and partial success criteria can be defined separately.

- **Document and Iterate**

In order to keep track of all development steps, it is important to document in detail all the above steps and explain what is decided and why it is decided. Due to the nature of the flight experiments and constraining CubeSat platforms, the system engineers should regularly be updated and be involved in the design process.

Additionally, each payload has to pass a number of review processes of Preliminary Design Review (PDR), Critical Design Review (CDR), System Acceptance Review (SAR), Operational Readiness Review (ORR) and Flight Readiness Review (FRR). The number of reviews may vary with the platform or payload owner, as well as the launch provider. The review data packages should consist of thorough documentation and each review may require an iteration to earlier documents.

4.2. QARMAN Mission Scenario

The details of the QARMAN mission were introduced in Sec. 1.2.1. Figure 4.1 shows the mission scenario. The mission has five main phases starting with the commissioning and detumbling after the deployment from the launcher. The first experimental phase is the Differential Drag Experiment, run by the University of Liege. During one month, this algorithm will use the reaction wheel to alter the vehicle's pitch angle, thus modifying its drag to perform an orbital rendez-vous maneuver. Later when the satellite arrives to 350 km, the Aerodynamic Stability and Deorbiting System (AeroSDS) will be activated by the deployment of four panels. The AeroSDS will make sure not only that QARMAN arrives at 120 km altitude with 7.7 km/s speed in a stable manner but also that the spacecraft follows the re-entry trajectory.

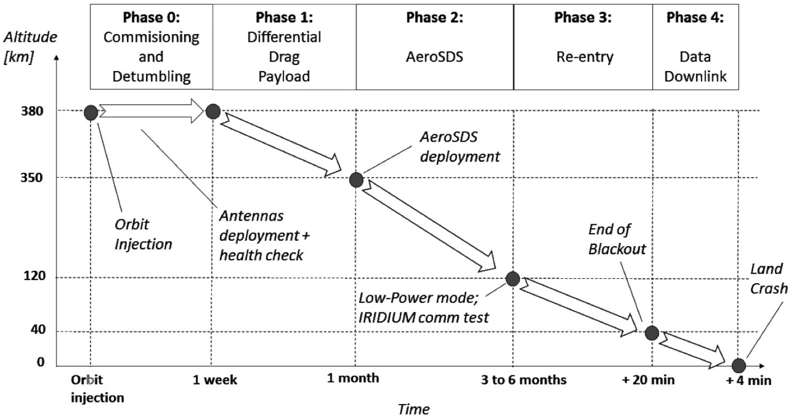

Figure 4.1.: QARMAN mission timeline.

At 120 km, the most critical and challenging phase, the re-entry begins. The entry trajectory is depicted in Figure 1.6. This is the core of the mission where the aerothermodynamic in-flight experiments will be performed. The strong bow shock and the high temperature plasma occurring in front of the vehicle will cause not only very high temperatures on the vehicle but will also prevent any means of communication. Therefore, in order to safely downlink the science data, QARMAN has to stand this harsh entry down to 40 km. QARMAN is designed in such a way that it will survive the reentry and after the blackout, send the data to the ground station through the IRIDIUM constellation. Not all systems onboard are required during the reentry phase. Those that requires electronics operational temperature ranges during the hot re-entry are put in two *Survival Units* that are titanium boxes filled with layers of FiberFrax thermal blanket and an insulating aerogel called Pyrogel. There is also an aluminum plate next to the PCBs to act as a heatsink to compensate the heat generated by the electronics.

All data collected during approximately 20 minutes of re-entry will be retrieved in a 3 to 5 minutes time window between the end of the telecommunications black-out and the landing of the satellite. To tackle this problem, data will be compressed and broadcasted in a pre-determined priority order. QARMAN will then make a crash land and will not be recovered.

The aerothermodynamic in-flight experiments are summarized in Table 4.1. The focus of this thesis is to perform a duplication of the stagnation region. Therefore only the stagnation region experiments of XPL01 and XPL02 will be detailed here. XPL01 will return the evolution of in-depth temperature inside Cork P50 at three locations at the nose. On the other hand, XPL02 consists of absolute pressure measurements at the nose to understand the aerothermodynamic environment in front of the TPS together with the XPL01. XPL02 will also contribute to the flush air data sensing system of QARMAN which is going to use the measured pressure data to construct the entry trajectory.

Table 4.1.: QARMAN aerothermodynamic in-flight experiments.

Payload	Objective	Parameter	Means
XPL01	TPS Efficiency	Temperature	Thermal Plugs
XPL02	TPS Pressure	Pressure	Absolute Pressure Sensor
XPL03	Vehicle Stability	Pressure	Absolute & Differential Pressure Sensors
XPL04	Laminar to Turbulence Transition	Pressure & Temperature	Thermocouples & Absolute & Differential Pressure Sensors
XPL05	Side Panel Heating	Temperature	Thermocouples
XPL06	Radiation	Species	Spectrometer

4.3. Aerothermodynamic Payloads, Development and Testing

4.3.1. XPL01: Thermal Plugs

The first experimental payload, XPL01, is described in detail following the steps of the payload design methodology explained in the previous section. While individual tests for XPL01 are presented here, the qualification test combined with XPL02 is described in Sec. 4.4.

4.3.1.1. Problem Statement

The numerical models, experimental tools and procedures for atmospheric entry can only be validated with real flight data. Due to the high costs of real flight tests, the aerospace community has access to very limited flight data. Flight data will lead to more accurate gas-surface interaction, material response, engineering models and accurate flight extrapolation methodologies that will eventually reduce the highly conservative safety margins for payload/crew protection and costs. In-depth and surface temperatures are of great importance to achieve these goals.

4.3.1.2. Objectives

The primary scientific objectives of this payload are to measure the following magnitudes:

1. Heating close to the hot corners
2. Stagnation region heating
3. Subsurface material response
4. TPS recession rate
5. TPS total recession

The baseline science requirement from the payload is to satisfy the first three objectives. The two recession measurements are classified as secondary scientific objectives.

4.3.1.3. Subject Trades

Two subjects that can satisfy the payload objectives are *temperature* and *recession*. Considering the strict constraints on the platform and to keep the vehicle design simple only one subject, temperature is chosen. Recession sensors are currently not sold commercially off-the-shelf and no budget is allocated within QARMAN project for a recession sensor development. It is known and practiced that temperature measurement devices can lead to recession measurements when implemented inside TPS materials. The temperature data will be used to reconstruct the parameters stated in the objectives.

For scientific objectives 1 and 2, the heat flux is simply deduced by the change of temperature in time:

$$\dot{q} = f\left(\frac{dT}{dt}\right) \tag{4.1}$$

The recession measurements required by the scientific objectives 4 and 5, will be based on the end-of-life of the sensor. The on-board clock of the spacecraft will provide the exact time of the last measurement from the sensor, which will be considered as end-of-life. The combination of temperature and time data gives information about the recession rate in time and the total recession throughout the atmospheric entry trajectory.

The scientific objective 3 is simply the temperature of the inner TPS environment. It imposes the requirement of making measurements at several depths in the TPS. These objectives also contribute directly to the justification of the QARMAN mission requirement of keeping the subsystems below $70°C$ for functional temperature range.

4.3.1.4. Preliminary Investigation

First Estimations

The selected TPS material Cork P50 was thoroughly investigated in Chapter 3. The surface temperatures as well as in-depth temperatures were measured at a wide range of free stream conditions. The in-depth temperature profiles were measured with a type K thermocouple, which is a technique that reads temperatures up to 1523 K and even to 1645 K for short term measurements. It was also seen that the thermocouples placed at 4 mm can reach its upper limit for the long duration tests.

In addition to the experimental data, the numerical aerothermodynamic database of QARMAN is examined to determine the expected surface temperature ranges. The simulations assume radiative equilibrium boundary condition to the surface with a constant emissivity 0.8. At the case close to the peak heating at 61 km altitude, QARMAN has the surface temperature of 2100 K which is comparable with the experimental cases mentioned previously. Figure 4.2 shows the CFD analysis at 66 km altitude (See Sec. 4.2 for QARMAN trajectory). The corners are the hottest surfaces and have a temperature of 2200 K while the stagnation region is 1950 K. To summarize, it can be stated that the expected measurement range from on board in-depth measurements has an upper limit of approximately 1650 K with 5% margin.

Critical Locations and Instants

The interesting location for these measurements are found to be the stag-

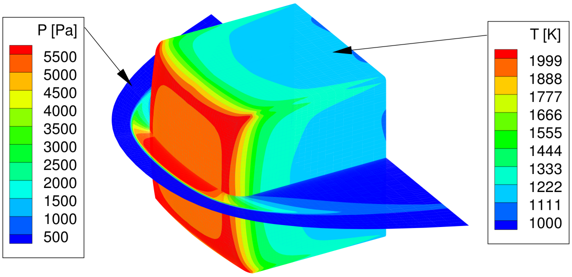

Figure 4.2.: QARMAN at 66 km. Contours of temperature and pressure on the body and the cross section respectively. The free stream conditions are $V_\infty = 6845.59$ m/s, $P_\infty = 8.66$ Pa, and $T_\infty = 228.925$ K as given in Table 2.6

nation region and the corners of the front unit, because the CFD simulations reveal gradients. However, the stagnation point is reserved for the spectrometer optical path as it is the only feasible configuration. Therefore, two locations are suggested in the diagonal direction between the stagnation point and the corner. The four diagonal directions are aerodynamically equivalent considering the angle of attack is 0°. The exact locations for the thermal plugs are determined by a trade-off study mentioned in Sec. 4.4 together with XPL02 for the frozen front unit design.

The critical instants for this payload to take measurements are below 150 km of altitude where a bow shock starts to occur in front of the vehicle due to the density increase of the atmosphere. The hypersonic flight at a denser atmosphere will result in exothermic reactions between the bow shock and the vehicle wall and there will be an increase of temperature. This payload is responsible for measuring the changes stated in the payload objectives. The critical time for measurement onset was determined to be when the vehicle goes below 150 km of altitude. However, frequent measurements are not needed until 120 km of altitude.

Performance Thresholds

The expected performance from this payload are summarized in the Table 4.2. Table 4.3 explains the selection criteria.

4.3.1.5. Measurement Techniques

The properties of possible sensors are summarized in Table 4.4. All XPL01 sensor candidates give the desired output: temperature, therefore the scientific objectives can be met directly.

Table 4.2.: Performance thresholds of one sensor unit for XPL01.

Type	Unit	Desired	Acceptable
Range	K	273 – 2200	273 – 1523
Accuracy	±K	$(0.0025 \times \mathrm{T}) + 273.15$	$(0.0075 \times \mathrm{T}) + 273.15$
Frequency 150-120km	Hz	1/60	1/240
Frequency <120 km	Hz	1	0.5
Response Time	s	0.1	0.5
Total Mass	g	9.9	16.8
Volume	cm^3	0.118	0.353
ADC Resolution	bit	12	11
Power	mW h	0.83	2.08
TRL	[-]	9	4

4.3.1.6. Preliminary Configuration and Concept of Operations

Measurement Technique Selection

Among the candidates, the most suitable ones are found to be thermocouples type K, R, S and B. Thermocouple type E can also be considered for the back of TPS where the temperature does not rise above 900°C. Type R, S and B thermocouples are currently not considered although they can measure a higher range, they are more expensive than type K, and require additional sheathing. Sheathed thermocouples are not of great interest for this application since they may alter the material response due to their thicker sizes. The rest of the sensors are ruled out for two reasons: Their ranges are not found to be suitable for XPL01 and secondly the sensor head geometry is not suitable for inner TPS accommodation to meet the scientific objectives. Finally, type K thermocouples, that have flight heritage, are chosen.

Measurement Chain Design

The output voltage signal of a type K thermocouple is very small, of order of $\mu V/°C$. The voltage change when temperature rises is called the *Seebeck effect*. For different types of thermocouples, the Seebeck coefficients are different. The most important feature of these coefficients is that they are not linearly changing with temperature. Figure 4.3 shows the Seebeck coefficients of the thermocouples considered in the previously. It can be stated that the voltage signal is fairly linear for types K, R and S over almost their entire ranges. These output values require a signal conditioning device with a gain of approximately 100. In addition, when the signal is amplified,

Table 4.3.: Details of performance thresholds for XPL01.

Type	Desired	Acceptable
Range	Surface temperature at peak heat flux (from CFD)	Range of TC Type K
Accuracy	TC Type R accuracy	TC Type K accuracy
Frequency 150-120km	Initial heating of TPS prior to re-entry	Safety factor 4.0 considering available power in the Low Power Mode
Frequency <120 km	Analogous to ground tests	Safety factor 2.0 considering available power
Response Time	Analogous to ground tests	Safety factor 5.0. Should be less than acceptable acquisition frequency
Mass	Sensor head 1 g + Cable 2.25 g (15 cm long at 0.015kg/m) + Installation 5 g + Safety factor 1.2	Sensor head 1 g + Cable 3 g (15 cm long at 0.015kg/m) + Installation 10 g + Safety factor 1.2
Volume	Diameter 1mm, Length 15cm	Diameter 1.5mm, Length 20cm
ADC Resolution	To achieve 1°C output resolution	To achieve 0.5°C output resolution
Power	Calculated for desired frequency, desired response time and 10 minutes acquisition time at 0.05 W	Calculated for accepted frequency, accepted response time and 10 minutes acquisition time at 0.05 W
TRL	Flight heritage	Tested in laboratory environment

it will be difficult to distinguish noise from the measurement itself. Therefore a low pass filter is required prior to signal amplifier.

Thermocouples are devices that generate a voltage that is a function of temperature *change*. Therefore, it is not trivial to make absolute temperature measurements unless a reference temperature is provided in the circuitry. This reference temperature is read at the junction of the two dissimilar metals with copper lines and is called the *reference junction*. In the laboratory environment, the reference junctions may be put in ice baths where the temperature is known to be 0°C. Since this is not practical, a method called *reference-junction compensation* or *cold-junction compensation (CJC)* is used nowadays. This method includes electronic circuits with an independent temperature sensing element close to the reference junction. The precision of the absolute temperature measurement highly depends on the reference temperature. The current integrated temperature sensors mounted close to the reference junction can have accuracies of small

Table 4.4.: Candidate sensors for XPL01.

Name	Range [°C]	Accuracy > 100 °C [°C]	Response Time [s]	Mass [kg]	Volume [mm^3]	Power [W]	TRL
TC Type K	-200 to 1250	±0.0075×T	0.1	0.0099	0.077	0.05	9
TC Type E	0 to 900	±0.0075×T	0.1	0.0099	0.077	0.05	9
TC Type R	0 to 1450	±0.0025×T	0.1	0.0099	0.077	0.05	8
TC Type S	0 to 1450	±0.0025× T	0.1	0.0099	0.077	0.05	8
TC Type B	0 to 1700	±0.0025× T	0.1	0.0099	0.077	0.05	8
TC Type N	0 to 1300	±0.0075×T	0.1	0.0099	0.077	0.05	8
SA1 RTD	-73 to 260	±0.35	< 2	0.0144	2x2x0.8 mm	0.05	6
SRTD1	-200 to 260	±0.0050×T	0.07	0.0144	15.7x25x0.64	0.05	6
SRTD2	-200 to 260	±0.0025×T	0.07	0.0144	15.7x25x0.64	0.05	6
RTD-F3102-36-G	0 to 480	±2.3 at 400°C	N/A	0.0156	4x5 mm	0.05	6

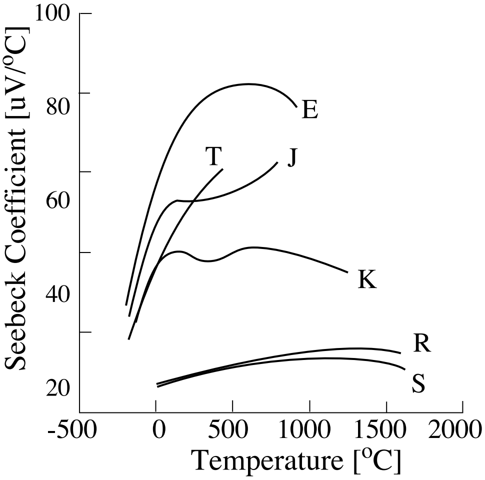

Figure 4.3.: Seebeck coefficients of different thermocouples [156].

fractions of 1°C. At high temperatures, as it is the case for QARMAN, the reference temperature sensor will already be more accurate than the thermocouple measurement itself. There are components off the shelf in the market (TRL 4) that include already the CJC and the signal conditioning providing the necessary gain. These devices are specific to thermocouples types and gives digital output so no processing is required. Several iterations are done for the measurement chain after the breadboard and Plasmatron tests [157]. The optimized chain is given in Fig. 4.4 which uses an additional low-pass filter, to cut the electromagnetic noise of the facility. The cut-off frequency of the low pass filter is 140 Hz.

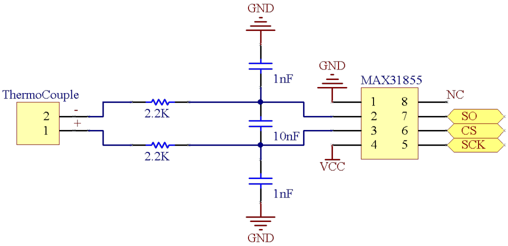

Figure 4.4.: Optimized thermocouple design with a low-pass filter.

Payload Head Design

It was seen in Chapter 3 that the temperature distribution inside the ablative TPS decreases away from the surface. In order to measure this trend in real flight, multiple thermocouples should be placed in the first 40% of the TPS thickness. Thermal plugs with multiple thermocouples mounted at several depths are considered. The concept of thermal plug is adopted from MEDLI; the Entry, Descent and Landing system of the Mars Science Laboratory [48].

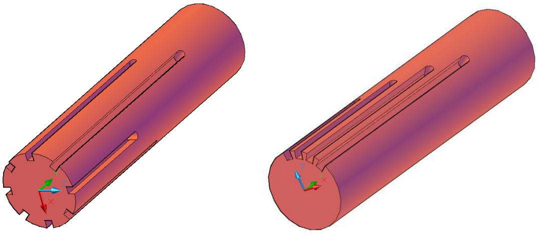

Figure 4.5.: Center (left) and corner (right) thermal plugs. The grooves are symmetric and the thermocouple cables pass through a perpendicular hole.

According to the initial TPS sizing, QARMAN TPS will have a thickness of 50 mm. Therefore the depths for thermocouple placing are proposed as 3, 5, 8, 11 and 18 mm. In order to catch the trend in the diagonal direction, three thermal plugs are foreseen. Due to the small size of the vehicle, the thermal plug diameters are limited. Diameters of 14 and 10 mm are found to be suitable. The thermal plug configurations for QARMAN are depicted in Fig. 4.5. Table. 4.5 shows the positions of the thermal plug center points. The XY-surface is the squared cross section of the vehicle, and Z is the longitudinal axis. While the thermal plug 1 (TP1) has 4 thermocouples, the TP2 and TP3 have 5 thermocouples.

Table 4.5.: Thermal plug locations.

Reference ID	Relative Position			Absolute Position		
REF_ID [-]	x [m]	y [m]	z [m]	x [m]	y [m]	z [m]
XPL-TP1	0.019	0.019	0.005	0.019	0.019	0.005
XPL-TP2	0.034	0.066	0.001	0.034	0.066	0.001
XPL-TP3	0.066	0.034	0.001	0.066	0.034	0.001

The thermocouples are proposed to be plugged in a U shape design. The plug will be drilled 1 mm sideways at the previously mentioned depths at three different angles. It should be reminded that the considered thermocouple diameter is 0.81 mm. This concept requires careful treatment because the thermocouple wires have to be split; one wire has to pass through the hole; the two wires are soldered outside and then the measuring junction has to be slid at the center of the plug. The U shape accommodation of thermocouples prevents thermocouples to come off the TPS during integration or during the mission where extreme loads will happen. One can question the strength of the solder while sliding the thermocouple in the plug but this can be checked a posteriori of the integration.

The measurement chain of XPL01, that is identical to XPL05, was sent to an orbit of 610 km altitude in June 2014 on board with both of the precursor missions of QB50 [54] QB50p1 and QB50p2. The payloads consisted of three XPL01 thermocouples and its measurement chains. The objective was to qualify the design even though the temperature measurement range will not be representative to an atmospheric entry flow. As a preliminary analysis, the measurement junction temperature and electronic board data are clean and the results show that the payload performed well in space environment and survived the launch loads without any damage.

Another important trial for this experiment was to monitor the behavior of the candidate insulating material for the thermocouple cables. The tests at Plasmatron were conducted with both teflon and fiber glass insulated wires. The two are further tested during the flight readiness testing for the QB50 precursor flight. Since the teflon insulation is much thinner than the fiberglass, teflon is chosen.

4.3.1.7. Breadboard and Ground Testing

The measurement chain with correct filtering and signal conditioning that can fit the constraints of the spacecraft bus is built and tested on a breadboard. This chain is further tested in the VKI Plasmatron facility, with two thermocouples inserted in a cork P50 sample exposed to plasma flow and the acquisitions are simultaneously made by identical sensors with the Plasmatron acquisition system for comparison (Fig. 4.6). The results showed very good agreement as seen in Fig. 4.7. The different cases correspond to filtering and grounding where the filtered thermocouple showed very good agreement with the reference thermocouple.

A qualification test of the measurement chain and the thermal plugs is conducted at the VKI Plasmatron on a setup, which also included XPL02. The details of this campaign are given in the dedicated Sec. 4.4.

4.3.1.8. Operations Concept

The payload is required to take minimum measurements with reduced frequency of 0.5 Hz above 120 km altitude and with higher frequency 1 Hz below 120 km. Since the measurement chain already gives a digital output, no onboard processing will be needed.

Figure 4.6.: Plasmatron test with conditions P=100 mbar and $\dot{q}$= 708; 1250; 1500; 1640 kW/m^2 with a sample of 15 mm radius.

4.3.1.9. Risk Analysis and Success Criteria

The risk analysis is an extensive and complex field for space systems as there is hardly a chance to perform thousands of tests for components. Especially, the low-cost CubeSat platforms do not allow exhaustive component testing. A risk analysis method for CubeSat platforms is developed by [158, 159] however is not discussed further in this thesis.

The payload will be considered *successful* if all the science objectives are met. The payload will be *partially successful* if only primary science objectives are met.

4.3.2. XPL02: Pressure on Ablator

This payload consists of pressure measurements in the front part of the vehicle to understand the aerothermodynamic environment together with the XPL01. It will allow us later to reconstruct the trajectory and will also act as input to understand the ablative material behavior and efficiency.

4.3.2.1. Problem Statement

The aim of the QARMAN mission is to collect flight data on the ablative thermal protection material behavior for improving our ground capabilities. The pressure is thus an important parameter to know simultaneously with the temperature measurements by XPL01 so that the flight can later be simulated numerically or experimentally on ground. On the other hand, knowing the local pressure, combined with temperature data, will allow us to determine the local flow conditions under LTE assumption during the

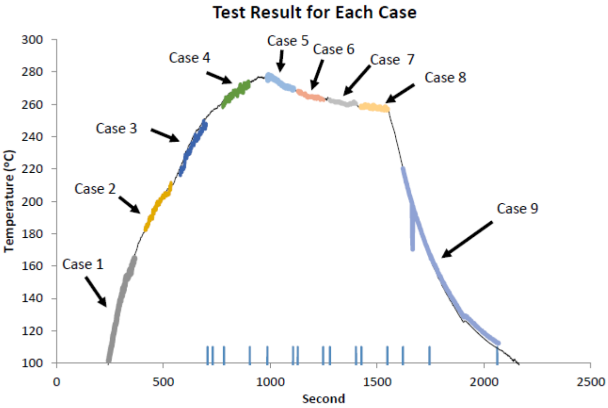

Figure 4.7.: VKI Plasmatron test with comparison to Plasmatron acquisition chain (Shown by black line).

flight. In addition to the ablation phenomenon, pressure measurements are directly related to the attitude and velocity of the vehicle and can be used to determine the flight speed as a part of the FADS system for trajectory reconstruction.

4.3.2.2. Objectives

The primary scientific objectives of the XPL02 payload are to measure:

1. Total pressure in the stagnation region
2. Total pressure close to the hot corners
3. Dynamic pressure, with comparison to the XPL03 experiment (XPL03 provides static pressure measurements on the side panels)

The baseline science requirement is to satisfy the first two objectives. The dynamic pressure measurement is a secondary objective.

4.3.2.3. Subject Trades

Since the total pressure is required by all objectives the intensive parameter *absolute pressure* is the subject of this payload.

4.3.2.4. Preliminary Investigation

First Estimations

The baseline of the expected pressure ranges comes from the CFD computations. Due to the sharp corners, the diagonal of the nose was determined as the relevant location for XPL02 measurements. Likewise, the pressure distribution along this line is examined. Fig. 4.8 shows the diagonal change of pressure at different altitudes using the virgin TPS geometry. On the other hand, the QARMAN TPS changes shape along the trajectory due to ablation. A very rough study is conducted to estimate the shape change, especially for the rounding of the sharp corners. The pressure distributions of the virgin TPS geometry are then compared to the ablated one for 66 km in Fig. 4.9. For all cases the maximum pressure in the stagnation region is 20000 Pa.

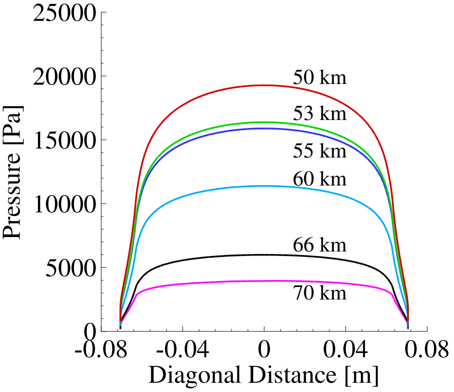

Figure 4.8.: Diagonal distributions of wall pressure at different altitudes for 0° angle of attack. All computations are done with the virging TPS geometry.

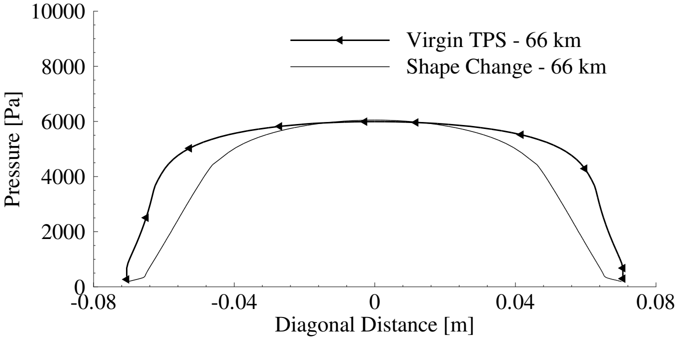

Figure 4.9.: Diagonal wall pressure distributions of virgin TPS and changed geometries at 66 km.

Critical Locations and Instants

The pressure measurements will be placed diagonally at two stations. The exact locations are also dependent on the front unit subsystems, XPL01 and XPL06. The measurement points should ideally allow the reconstruction of the pressure distributions of Figures 4.8, however a trade-off study is conducted due to the constraints of the CubeSat platform, which is presented in Sec. 4.4.

Between 120 km and 70 km altitudes, the pressure values are still too low for a *pressure sensor*, considering at 70 km the maximum pressure is lower than 4000 Pa. For such low pressures, vacuum sensors are more accurate but they are not considered due to the additional mass and volume budget on the mission. However since the relevant environment for aerothermodynamics start around 120 km altitude, the pressure measurements should also start at 120 km.

Performance Thresholds

The requirements of the XPL02 payload are summarized as the desired and acceptable performance thresholds in Table 4.6.

Table 4.6.: Performance thresholds for XPL02.

Type	Unit	Desired	Acceptable
Range	Pa	0-25000	0-100000
Accuracy	Pa	30	100
Frequency	Hz	1	0.2
Response Time	ms	10	50
Mass (sensor + cable + housing)	g	60	80
Volume	cm^3	1	1.5
Resolution	bit	10	12
Power	mW.h/piece	5	10
TRL	[-]	9	4

4.3.2.5. Measurement Techniques

The available pressure sensors compatible with CubeSat platform constraints are the piezoresistive sensing techniques. They come with analogue or digital outputs. For operation simplicity digital outputs are prioritized with the condition of good accuracy within the requirements in Table 4.6. Honeywell HSC series, (HSCMRNN015PASA3 model [160]) is chosen for XPL02 and also XPL04 payloads. The digital sensor includes also the temperature compensation circuit and the amplifier. The specifications are given in Table 4.7. Due to the wider measurement range of the sensor, the accuracy may drop at lower pressures. Therefore, a calibration campaign is conducted to monitor the actual behavior.

Table 4.7.: HSC-MRNN015PASA3 Specifications

Range	Pa	0-103421.36
Accuracy	% Full Span	0.25
Response Time	ms	0.46
Sensor mass	g	1
Volume	mm	10x13
Resolution	bit	12
Power	mW.h	1.7
TRL	[-]	6

4.3.2.6. Preliminary Configuration and Concept of Operations

Just like XPL01, the design of the pressure payload is also split into measurement chain and payload head designs.

Measurement Chain Design

The measurement chain of the pressure sensor is rather simple since it has a digital output. Unlike the XPL01, no low pass filter can be applied to this circuit, therefore the signal to noise ratio is experimentally determined during the breadboard tests.

Payload Head Design

The payload head of XPL02 consists of the pressure *spools* which make the connection with the pressure port at the TPS surface and the pressure sensor. The literature survey (e.g. [48]) showed no additional tubing inside the TPS is needed. Despite the fact that the ablation products may affect the pressure measurements, it was decided by MSL scientists to keep the pressure holes bare not to create heat sinks and affect the ablation of the TPS [161]. The bare hole diameter is chosen as 2 mm.

Therefore the pressure spool will be fixed on the bonding structure behind the TPS and it is sufficient to make sure the pressure tube and the pressure path are aligned. The spool is connected to an inconel tube behind the bonding structure. The inconel tube is a hard material and to ease the integration of the vehicle, a PTFE tube is attached behind it until the pressure sensor on the XPL data acquisition (DAQ) board. The pressure spool design depends on the location of the pressure port. As it is explained in Sec. 4.4, there are two diagonal positions and due to the bonding structure geometry, the spools need to be of different length. The spool design is depicted in Fig. 4.10.

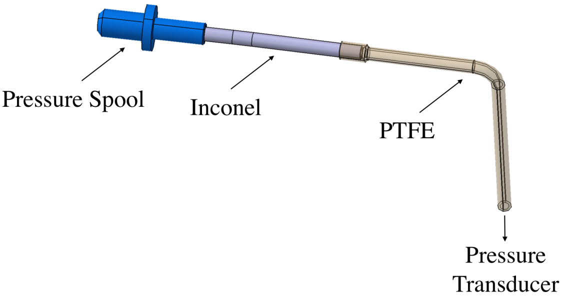

Figure 4.10.: Pressure spool connecting the sensor and the bonding structure with an insertion to the TPS material.

4.3.2.7. Breadboard Testing

Prior to an exposure to plasma in Plasmatron, a breadboard test is conducted in the VKI Minitorch facility. The aim was the determination of the calibration curve and sensitivity more accurately throughout the sensor's entire range using the measurement chain described previously. A mercury manometer and the low range pressure sensor of Minitorch have been used as a reference. Fig. 4.11 shows the results of the breadboard tests. The sub-atmospheric Minitorch chamber pressure is changed gradually by manually adjusting the three valves. Hysteresis effects were also checked and no significant error was found due to hysteresis only. The plot shows the data from the chosen sensor in comparison to the mercury manometer and the Minitorch sensor. A small discrepancy at very low pressures was observed when compared to the mercury manometer but matched well with the Minitorch sensor, which has a range of 0-20000 Pa. At higher pressures than 5000 Pa, all the points showed very good agreement. Pressure transducers are known to behave poorly in the lowest pressure ranges. Vacuum sensors have lower errors for lower ranges however they are not considered onboard QARMAN due to mass, volume and power constraints. The mercury manometer is the most trusted sensor among all and this curve acts as the calibration curve for the lower pressures. The digital output of the sensor can then be corrected accordingly. This configuration is used in the XPL01-XPL02 qualification tests, explained in Sec. 4.4.

4.3.2.8. Operations Concept

The payload is required to take measurements minimum with reduced frequency of 0.2 Hz above 120 km altitude and with higher frequency 1 Hz below 120 km. Since the output is digital, no on-board processing is needed.

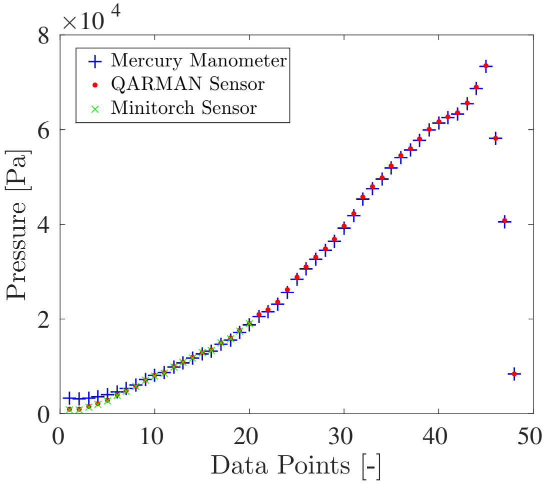

Figure 4.11.: Calibration Test of the absolute pressure sensor at VKI Minitorch.

4.3.2.9. Risk Analysis and Success Criteria

As was the case with XPL01, no thorough risk assessment study is reported in this thesis. The payload will be considered *successful* if all the science objectives are met. The payload will be *partially successful* if only primary science objectives are met.

4.3.3. XPL01-XPL02 Placement and Final Configuration

Different scenarios are considered for positioning the XPL01 thermal plugs and the XPL02 pressure ports on the front cork TPS. Figure 4.12 shows four considered scenarios where T# and P# correspond to the thermal plugs and pressure port locations respectively. A trade off analysis is performed based on criteria given in Table 4.8.

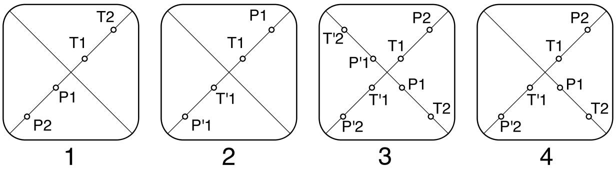

Figure 4.12.: XPL01 and XPL02 positioning scenarios.

The selection criteria consist of redundancy, weight, mission risk, dependency. integration, simplicity, DAQ simplicity and scientific contribution. The ratings of each case are given in Table 4.9. The scenario 4 is chosen as

Table 4.8.: Trade off analysis criteria and its scale factors.

Criterion	Scale Factor		
	low	medium	high
Redundancy	0	1	2
Weight	2	1	0
Risk	2	1	0
	none	partial	complete
Dependency	2	1	0
	simple	medium	complex
Integration Simplicity	2	1	0
DAQ Simplicity	2	1	0
	lower	medium	very high
Scientific Contribution	0	1	2
	very important	medium	less important
Criteria weight	3	2	1

Table 4.9.: Scenario ratings.

Criteria	Weight	Scenario 1	Scenario 2	Scenario 3	Scenario 4
Redundancy	3	0	1	2	2
Weight	2	2	2	0	1
Mission Risk	3	2	2	0	2
Dependency	1	2	1	1	1
Integration Simplicity	2	2	2	0	1
DAQ Simplicity	1	2	2	0	1
Scientific Contribution	3	1	0	2	2
Overall		21	20	13	**24**

the optimum with the highest rank. The redundancy is depicted as T'1 and P'1 since they are placed symmetrically of T1 and P1 around the stagnation point.

According to the mass, volume, power and link budgets, QARMAN can accommodate 14 thermocouples and 3 absolute pressure sensors in XPL01 and XPL02 payloads. The two central thermal plugs can accommodate five thermocouples at 3, 5, 8, 11 and 15 mm depth and have the diameter of 14 mm. The corner thermal plug on the other hand will be 10 mm diameter in size and have only four thermocouples at 3, 5, 8 and 11 mm. The pressure ports are placed according to the scenario 4 discussed previously.

The front unit design is depicted in Fig. 4.13. The thermal plugs and the pressure spools are shown. The back frame is made of the same TPS material as the side panels and the inner circular orifice accommodates the XPL06 spectrometer payload. All the electronics and the pressure tubing of XPL02 shown in Fig. 4.10 are placed inside the *Survival Unit*. The pressure sensors and the thermocouple chips are situated on the data acquisition (DAQ) board. The components of the survival unit and how it is mounted on the front unit back frame are shown in Fig. 4.14.

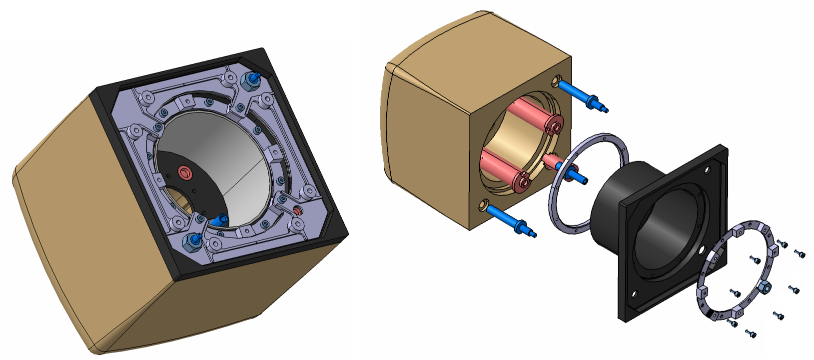

Figure 4.13.: QARMAN front unit (left) and the assembly breakdown (right). The thermal plugs and pressure spools are shown by pink and blue colors respectively. The back frame is made of the same ceramic TPS material as the side panels.

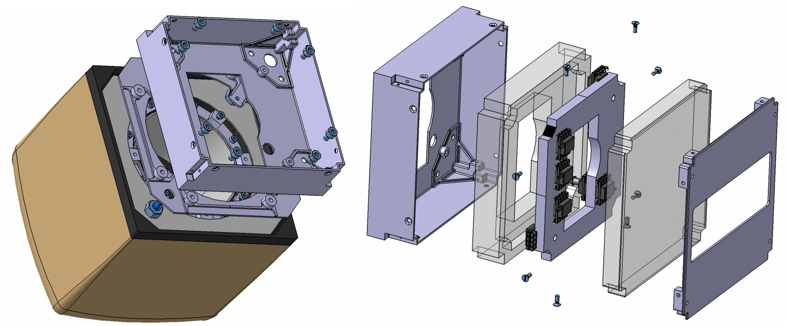

Figure 4.14.: QARMAN front unit (left) and the assembly breakdown of the survival unit (right). The titanium box, thermal insulation and the aluminum plate around the XPL DAQ board.

4.4. XPL01-XPL02 Qualification Tests

The qualification of the XPL01 and XPL02 payloads was achieved by tests in VKI Plasmatron facility. Initially, both payloads were tested in a 6/10 scale sample where a thermal plug with 3 thermocouples and a pressure sensor are placed together with the electronics. Later a full scale test of QARMAN's first unit was conducted. The test object with all three thermal plugs with 14 thermocouples in total, three pressure ports, the spectrometer, and the XPL survival unit, were exposed to plasma flow. Both tests are briefly presented here.

4.4.1. 6/10 Scale Test

The aim was to test XPL01 and XPL02 payload heads and measurement chains inside the Plasmatron chamber. It was shown in Chapter 2 that a correct duplication of the stagnation aerothermochemistry of the flight can be achieved by a correct Flight-to-Ground duplication methodology. In this test, a scaled model of the flight geometry was used. Therefore, no aerothermodynamic representation was sought. It was aimed to duplicate 50% of the heat load of the QARMAN trajectory, as it was the first time that electronic components would be exposed to plasma. The objectives are:

1. To monitor the behavior of the thermal plug configuration with radial thermocouples
2. To check the pyrolysis inside the bare pressure port
3. To monitor the surface temperature next to the pressure port
4. To monitor the recession of the sample at the center and at the corners
5. To check the char and pyrolysis layer
6. To monitor the back cavity temperature for electronics' operational range
7. To monitor the noise behavior of the temperature and pressure data under strong electromagnetic field effects
8. To investigate the circuit and component level stability in plasma environment

4.4.1.1. Experimental Setup

The sample is 6/10 scaled QARMAN geometry made of Cork P50 as depicted in Figure 4.15. There are two pieces held together by 4 screws at the corners to build the cavity where the PCB sits. The upper part of the

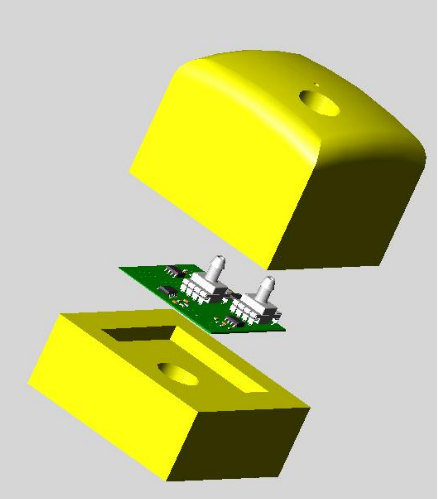

Figure 4.15.: Qualification test model.

sample has currently one thermal plug and one absolute pressure measurement station. The thermal plug is manufactured for XPL01 payload head. A bare pressure port is opened at the stagnation point for XPL02 testing.

Three pre-maid type K thermocouples with teflon insulation are used. The two wires are split and inserted to the thermal plug radially. The TC depths are 8, 15 and 22 mm away from the surface. The thermal plug has a diameter of 14 mm and its center is 13.51 mm away from the stagnation point in diagonal direction. It can be seen in Figure 4.16. A bare 2 mm diameter hole is opened where the pressure sensor tip is directly aligned and inserted at the back wall of the top part.

A double sided 4x4 cm PCB is designed to be put in the back of the Cork P50 and inside the Plasmatron. The PCB is capable to carry 2 absolute pressure sensors, 4 type K thermocouples including RF filters and also an MSP microprocessor; all identical to the original QARMAN DAQ board design. Remaining PCB areas are covered with ground plane in order to increase grounding and decrease plasma triggered noise effects. Flight configuration is fit on a smaller scale PCB, therefore hardware could be tested thoroughly. A simple code is written to pass the information over the UART (Universal asynchronous receiver/transmitter) bus. A UART to USB converter is used to pass the data to the PC. The data were logged using standard terminal software. This is considered as the first experiment for qualification of XPL01 and XPL02. The Figure 4.16 shows the top part and the Figure 4.17 shows the PCB before the screws are inserted.

The sample was mounted in the upper probe location in the Plasmatron inside the cooled box. The box temperature was measured and recorded by Plasmatron DAQ system.

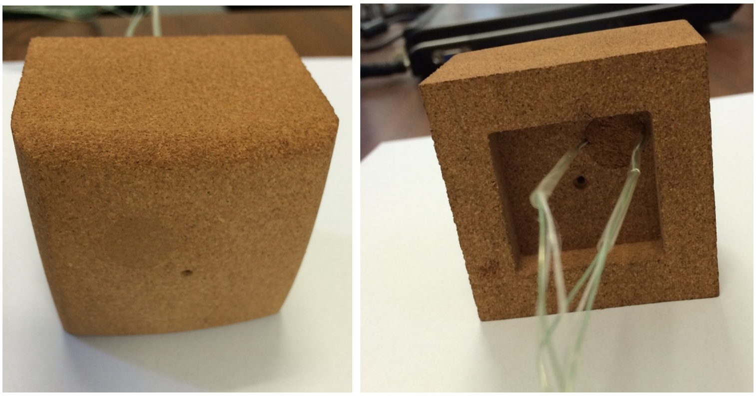

Figure 4.16.: Top part of the sample with pressure port and the thermal plug inserted.

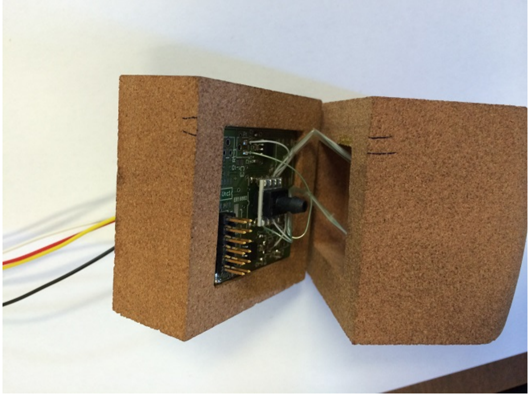

Figure 4.17.: The sample and the PCB before screws.

4.4.1.2. Plasmatron Test Conditions and Measurement Techniques

The Plasmatron operation conditions are given in Table 4.10. The given heat fluxes correspond to a heat load of 101960 kW.s which is the 50% of QARMAN trajectory. A conservative heat load for the electronics was chosen since there was no prior knowledge on whether the electronic components would survive the heat and the strong electromagnetic noise in the plasma wind tunnel.

4.4.1.3. Results

During the Test

The measurement with the sample PCB is started right after Argon is turned off. The pressure dropped due to the vacuum pump operation

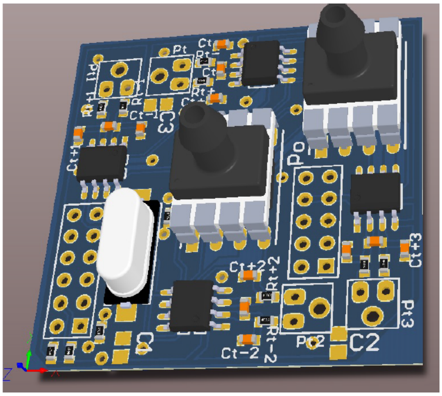

Figure 4.18.: PCB design.

Table 4.10.: Plasmatron Operations

Date	25.03.2014
Time	15.49
Pressure	100 mbar
Heat Flux by Standard Probe	708, 1250, 1500, 1640 kW/m2
Corresponding Ptron Power Efficiency	46.5, 55.05, 57.35, 58.3 %
Duration	20 s each heat flux, 80s in total
Air mass flow rate	16 g/s
Heat Flux Rotameter Info	level 15, $\dot{m} = 3.194$ g/s
Heat Flux Meas. Frequency	2 Hz
Pyrometer	Yes
Radiometer	Yes
Pyro & Radio Meas. Frequency	1 Hz
Spectrometer	No
High Speed Camera	Yes
Pitot Probe	No
Video Camera	No
Photo Camera	Yes
Sample Instrumentation	3 Type K TCs, 1 absolute pressure sensor
Instrumentation Frequency	1 Hz

while calibrating the heat flux, it is then recovered and the heat flux is re-calibrated. This drop in pressure is visible in the pressure transducer data of the sample. With the high speed camera, no recession was monitored at the stagnation point however the corners have recessed. All data were successfully acquired. A view of the sample exposed to plasma can be seen in Figure 4.19.

Visual Inspection

The connecting location of the bottom and the top side of the sample

Figure 4.19.: Sample exposed to plasma. The thermal plug is at the lower right corner.

seems to weld well and charred together. No significant step was formed initially and none occurred during the test. The side of the sample can be seen in Figure 4.20.

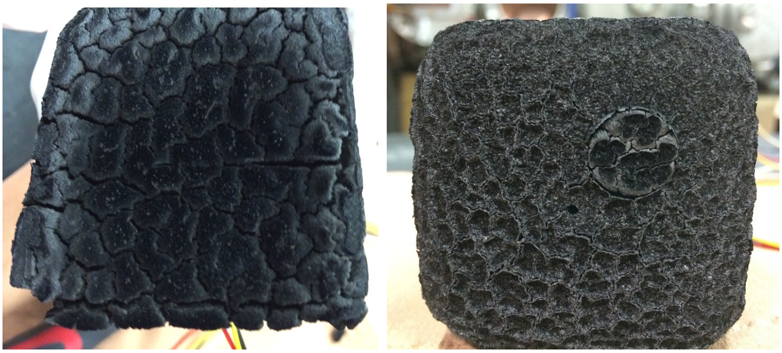

Figure 4.20.: Bottom and top parts interface (left) and the nose (right) after exposure to plasma.

The thermal plug can be seen as a different (darker) color during the test (Figure 4.19). The recession/swelling seems to be the same however a small hill can be seen at the circular border. The Figure 4.20 shows the nose surface of the sample after the test. The visual distinction is observed in other experimental campaigns when plugs are used within P50 material. It is believed that no matter how small the gap between the plug and the main material is, the swelling/recession and the pyrolysis is different. It is observed that after swelling, recession is slower in the interface similar to the cracks. Thus, an elevated interface is clearly visible in all cases. As also seen in the ablation campaign in Chapter 3, the pyrolysis products inside the material can find its way out towards the external flow through the interface cooling down this region and slowing down the char recession. Depending on the size of the plug, the recession at its center can still be equal to the main TPS but the interface always shows small hills.

When the sample is separated, it was seen that the PCB and the cavity still sit in the virgin layer and they are in good shape. The view from both sides can be seen in Figure 4.21.

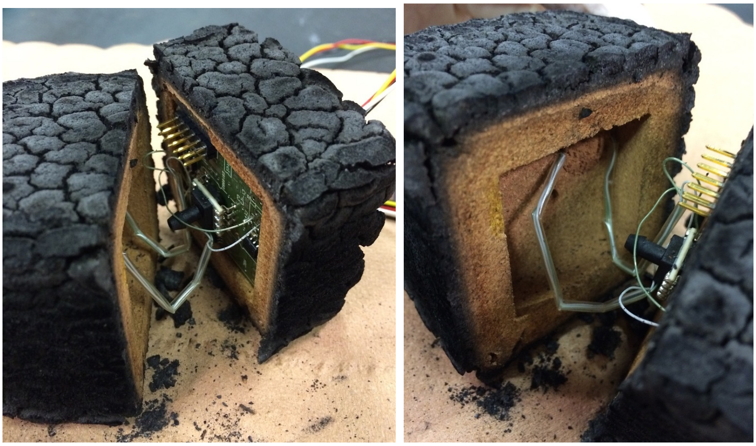

Figure 4.21.: Inside the sample after the test.

The sample is then cut to determine the char/pyrolysis/virgin layers, observe the pressure hole pyrolysis and determine the total recession. The cross section as well as the rounded corners can be seen in Figure 4.22. Due to manually cutting the sample, the char layer is partially missing however the layer thicknesses are measured and are given in Table 4.11. It is important to state that the first thermocouple of the plug is placed at 8 mm from the surface and therefore all thermocouples are in the virgin layer.

The pressure port seemed not to have the char/pyrolysis layer larger than the sample itself. The black dust is thought to come from the cutting means. No blockage due to swelling is observed along the pressure hole.

Table 4.11.: Sample and layer dimensions.

Initial Thickness (Top part)	48 mm
Final Thickness (Top part)	49.6 mm
Char layer	5.7 mm
Pyrolysis layer	0.24 mm
Virgin layer	43.66 mm

Heat Flux Measurements

Four heat flux levels are chosen from QARMAN entry trajectory. Once the chamber pressure is fixed, the operating power is set by measuring heat

Figure 4.22.: Sample cross section.

fluxes. The Figure 4.23 shows the heat flux measurements. The probe is injected later around $t = 630$ s.

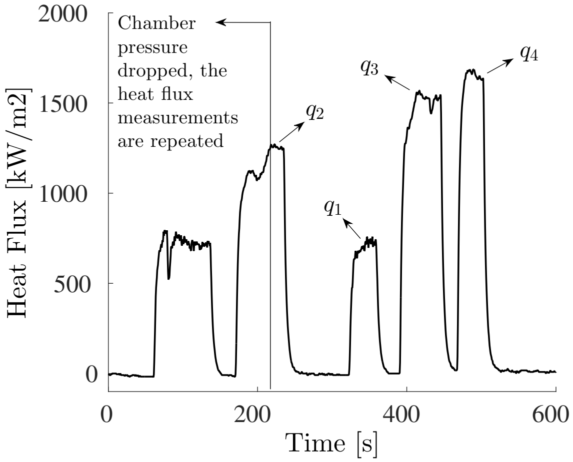

Figure 4.23.: Heat flux calibration for 4 different values of $q_1 = 708$, $q_2 = 1250$, $q_3 = 1500$, $q_4 = 1640\,\mathrm{kW/m^2}$.

Pyrometer and Radiometer Data

The pyrometer and the radiometer were pointed at the region between the thermal plug and the pressure port, however closer to the pressure port. The temperatures measured at that point are depicted in Figure 4.24. The radiometer showed very low temperatures. This was due to the scratched window which caused reflections and changed the transmissivity leading to a wrong measurement. A calibration of the setup with this damaged window is performed with a black body. However it was seen that the scratches refract the alignment laser and distort the path significantly. This could affect the measurements. In conclusion, the emissivity could not be determined. Nevertheless, it was shown in the previous chapter how surface temperature is related to the emissivity. At a surface temperature of 2240 K, the emissivity would read about 0.80.

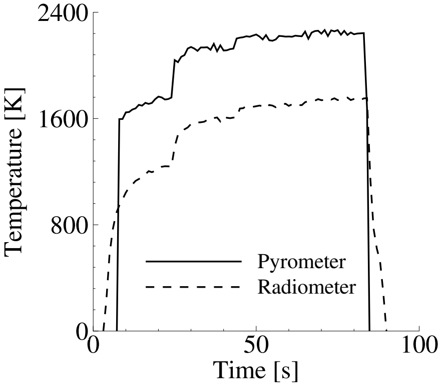

Figure 4.24.: Temperatures from pyrometer and radiometer (after calibration).

High Speed Camera

The High Speed Camera was used to monitor the recession rate and the shape change in the nose section. The Figure 4.25 shows the images taken at the beginning and at the end of plasma exposure. The high speed camera imaging showed a swelling of +1.6 mm as given in Table 4.11. The corner recession on the other hand is found to be 8.43 mm. For an engineering approach, the corner rounding data provided valuable input for the TPS shape change analysis although no representative aerothermochemistry can be achieved with the current setup.

Thermal Plug Measurements: XPL01

It was mentioned previously that all the thermocouples of the thermal plug lie in the virgin layer so no high temperatures were expected. Indeed the temperatures did not rise as much as the upper limit of the type K thermocouple. The temperatures measured by the thermal plug are given in Figure 4.26. The maximum temperature measured is around 240°C. The data are very clean as was the case in the breadboard testing and they do not seem to be affected by the electromagnetic noise of the facility.

On the other hand, the temperature sensor at the CJC on the PCB data are given in Figure 4.26. It can be seen that the temperatures in the back

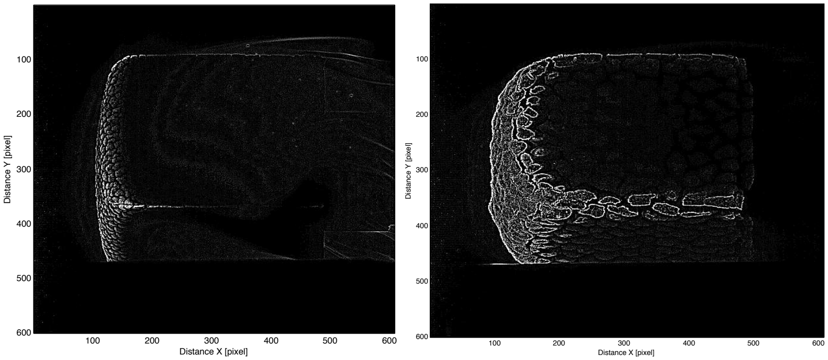

Figure 4.25.: High Speed Camera image at t=0 s (left) and at t=80 s (right). (1 pixel = 0.2273 mm)

of the TPS did not exceed the operational range of the electronics. The fact that the temperature keeps increasing after the sample is retracted from plasma flow is that the heat is still going inwards in the sample.

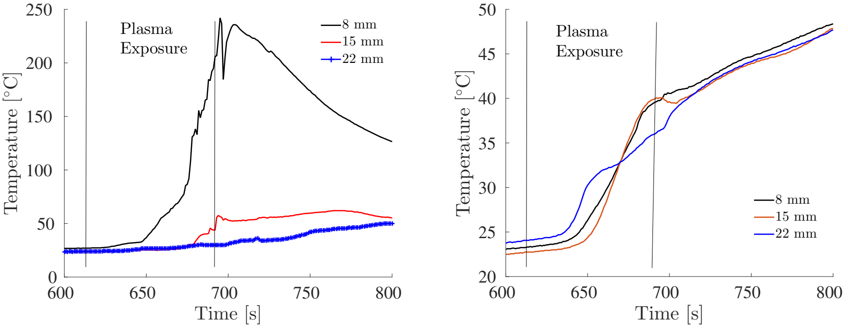

Figure 4.26.: Raw temperature data of the thermal plug (left). CJC temperatures on the PCB (right)

Pressure Measurements: XPL02

The measurement frequency was 1 Hz and the data can be seen in Figure 4.27 and it should be reminded that there is no low pass filter in its circuit. The fluctuations on the measurements are of the order ±30 Pa. However it is important to note that the chamber pressure is also fluctuation by ±100 Pa according to the static pressure sensor mounted in the chamber. Unfortunately there was no recorded reference measurement for this data therefore it cannot be validated. However it still reveals a more stable measurement than the Plasmatron static pressure measurements and the expected pressure is measured at the stagnation point. The expected total pressure order of magnitude would be the static pressure 10000 Pa + the dynamic pressure 20 Pa. Considering the pressure drop in the chamber due to the vacuum pump operation during the test, the total pressure can be considered in a good agreement.

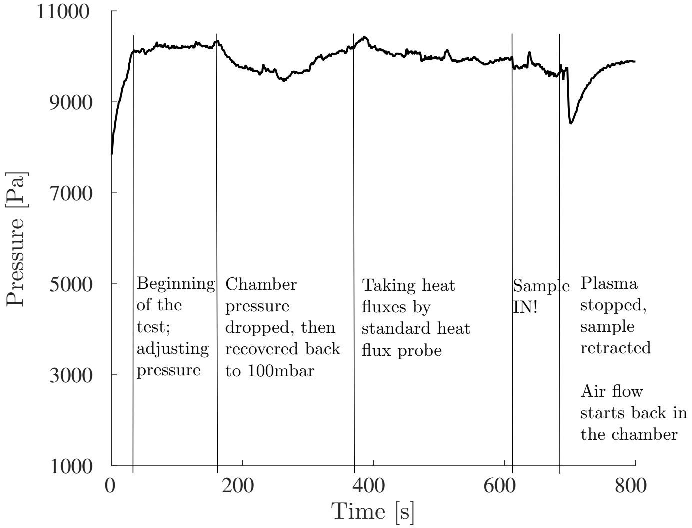

Figure 4.27.: Pressure sensor measurement at the stagnation point. The plasma exposure is between t=617 - 684 s.

Conclusions

The concluding remarks are summarized below in accordance with the objectives of the test mentioned in Section 4.4.1.

1. Notice: The uncertainties of the measurements are not included in this report. It is believed to be more meaningful by reference measurements and therefore only measurement fluctuations are mentioned throughout the text.
2. The thermal plug configuration allowed successful measurements. It was seen that the temperatures were not so high since the in-depth thermocouples were still in the virgin layer.
3. The bare pressure port is seen to work well. No blockage due to ablation was observed. The pyrolysis layer inside the hole is seen not larger than the rest of the stagnation region.
4. The temperature of the surface next to the pressure port is successfully measured by the pyrometer but not by the radiometer.

5. As expected the sample at the stagnation point did not recess but it is swollen by 1.6 mm. The corners however recessed by 8.43 mm.
6. The char and pyrolysis layers thicknesses are determined. It was seen that no thermocouple lay in the char/pyrolysis layers.
7. The back cavity temperatures were measured by the electronic components on the PCB and the temperatures did not exceed 70°C as required by all electronic components.
8. The temperature measurements are seen to be cleaner compared to the breadboard tests. The temperature and pressure measurement fluctuations were in acceptable ranges and they lay in the range of the sensor specifications.
9. No anomalies had been observed on the electronic board. Proper grounding will be ensured on future developments. Test showed that extra shielding and/or filtering is not required for accurate measurements.

4.4.2. Full Scale Test

QARMAN's first unit, meaning the first 10x10x10 cm^3 of the vehicle, is integrated to build an engineering model. An interface in the back is designed so that the EM can be mounted on Plasmatron sample holder. It included the entire front unit of QARMAN and the XPL survival unit. The main objectives of the test were to complete a first integration exercise, expose all the electronic and the sensor suite to plasma and especially test the performance of the XPL survival unit with all the sensors and the acquisition electronics in it, as a requirement for the Critical Design Review. It was shown in Chapter 2 that in order to simulate the stagnation aerothermochemisty of QARMAN flight in Plasmatron, smaller hemisphere cylinders are needed. Since the full scale squared model is exposed to a subsonic plasma, no aerothermo-chemistry duplication is expected. The test conditions aimed to duplicate the total heat load of the QARMAN entry trajectory at a constant pressure. This opportunity to test the XPL01 and XPL02 in scale one is taken mainly because the acquisition electronics are put inside the highly insulated survival unit and in order to see if there is any undesired effect coming from the surrounding components. Testing the electronics in the survival unit would not be possible in the samples computed with the Flight-to-Ground Duplication due to their small sizes.

The scope of this test was wider and the main objectives were related to the systems level, however in this thesis only the objectives and the test results concerning XPL01 and XPL02 are reported. The test objectives related to XPL01 and XPL02 are:

1. Complete integration exercise for the front unit and the XPL survival unit
2. Behavior of electronics in harsh electromagnetic field and high temperatures
3. Quantifying XPL board performance and XPL01, XPL02 functions
4. Provide data for inverse temperature problem for XPL01 post flight strategy

4.4.2.1. Experimental Setup

A test model with an interface to Plasmatron sample holder is designed and manufactured. Both XPL01 and XPL02 payloads were positioned in the suggested places by the trade-off study presented in the earlier sections. The central plugs had 5 type K teflon insulated thermocouples, and the corner one had 4. The XPL01 electronics and the pressure sensors were soldered to the XPL DAQ board located behind the back plate made of stainless steel (instead of ceramic TPS of the flight configuration). The pressure spool alignment with the bare pressure holes are checked prior to the integration of the sample. The pressure spool and sensor connection was altered due to unavailability of PTFE at the time of testing. Instead PVC tubes were connected to the Inconel tubes. The full scale cork (first unit) is extended with additional cork plates surrounding the survival unit instead of the ceramic TPS of QARMAN.

In addition to the QARMAN instrumentation, 11 thermocouples are placed in several locations for housekeeping data and are connected to the Plasmatron data acquisition system for redundancy. The Omegabond epoxy is used to mount the thermocouples. The finalized test model can be seen in Figure 4.28.

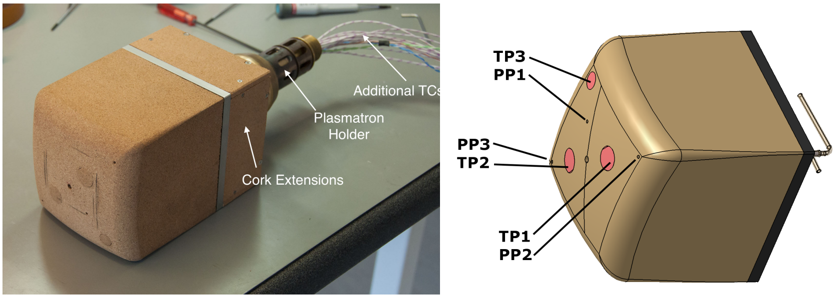

Figure 4.28.: Test Model and thermal plug/pressure port locations and labels.

4.4.2.2. Plasmatron Testing Conditions

Similar to the XPL01-02 scaled qualification test campaign, the pressure is kept constant at 100 mbar which is the mean pressure of the entry trajectory. The heat flux, on the other hand, is determined differently using the trajectory and CFD analyses with a rudimentary engineering approach. A reference cold wall heat flux is necessary since the Plasmatron free stream is adjusted with a cold wall heat flux calibration. Figure 4.29 shows the hot and cold wall heat fluxes of QARMAN computed by ASTOS trajectory propagator. It also shows the CFD computation results for a hot wall heat flux. The CFD computation originally gives the hot wall heat flux since a radiative equilibrium boundary condition is applied to the wall. Using the ratio of the cold wall and hot wall heat fluxes provided by ASTOS, a cold wall heat flux can be estimated. Additionally, it is known that the hot and cold wall heat fluxes can be related simply by the ratio of the differential enthalpies, $h_0 - h_w$, the enthalpy at the boundary layer edge and at the wall respectively. The cold wall heat flux computations return the values of 1023 and 997.5 kW/m^2 respectively by ASTOS and enthalpy difference method.

In order to keep the heat load of the re-entry the same in the Plasmatron test, the integral area is computed for a scaled cold wall heat flux trajectory. It can be seen in Figure 4.29 that ASTOS returns a maximum hot wall heat flux of 1620 kW/m^2 while the CFD returns 893 kW/m^2. [1] To define the heat load for the Plasmatron test, the peak heating of both trajectories are averaged and a scaled heat flux profile is obtained as plotted with dashed lines in Fig. 4.29. The peak heating of the averaged heat flux profiles is 1300 kW/m^2, which is considered as a conservative value. The integrated area under the newly defined heat flux profile, corresponding to the total heat load, returns 230.923 MW.s. This value can be reconstructed by a rectangular area, which means a constant heat flux. Thus the duration of plasma exposure can be determined accordingly by the heat load. The constant heat flux value is taken as the maximum of the enthalpy difference method, which is 1 MW/m^2. This equals a test duration of 230 s. The heat load duplication is depicted in Figure 4.29 together with the heat flux distributions.

The cold wall heat flux has to be adapted to the standard probe geometry since the given 1300 kW/m^2 is for 10x10 cm shape. The actual QARMAN geometry is comparable to the existing hemispherical equilibrium probe with

---

[1] The commercial ASTOS propagator computes the convective heat flux by a simplified Fay-Riddel formula by empirical values. It also uses a fixed cross section area and a rough *dimensionless radius* which includes the nose radius of curvature. It was demonstrated in Chapter 2 that the nose radius of curvature cannot be used in the case of QARMAN. In conclusion, ASTOS returned a higher heat flux than the CFD simulations. The ASTOS results are shown here as reference since the trajectory from which the enthalpy and the total pressure values are used in this thesis are computed with this program. It is the author's suggestion to use ASTOS for free stream parameters and CFD simulations for thermal quantities.

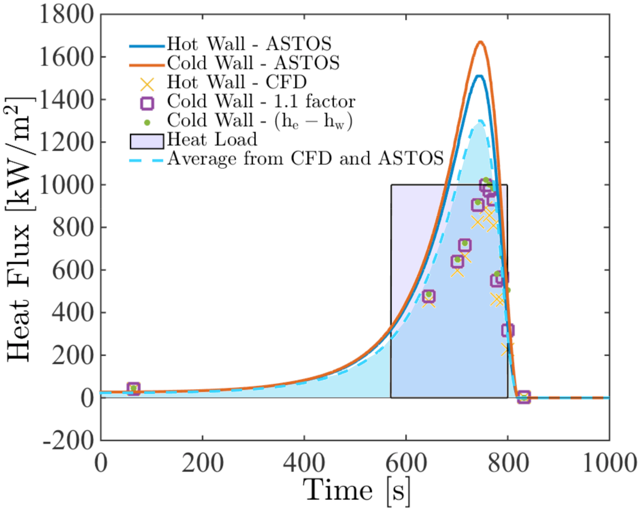

Figure 4.29.: Heat fluxes of the ASTOS trajectory and CFD analysis, and the heat load duplication.

115 cm diameter. At a static pressure of 100 mbar, when the equilibrium probe measures 1 MW/m^2, the standard probe measures 1.27 MW/m^2 as deduced from the experimental database.

4.4.2.3. Plasmatron Measurement Techniques

In addition to the full front unit instrumentation, 11 Type E thermocouples are placed. These additional thermocouples are connected to the Plasmatron acquisition system. Other facility measurement techniques are almost identical to the previous ablation campaigns and they are summarized in Table 4.12. The techniques and their results are discussed in the following section.

4.4.2.4. Results

Experiment Timeline

The test object is mounted on the lower probe holder and the standard heat flux probe is mounted on the top holder. First, the plasma is started and the pressure is adjusted to 100 mbar. Then the heat flux probe is injected and the Plasmatron power is adapted until the calorimeter measured 1270 kW/m^2. Once the free stream is stable, the pyrometer, radiometer, high speed and video cameras and the QARMAN EM acquisition are started and the full scale test model is injected.

The test is stopped before the target 230 s at 170 s since a short cut error message was received from the DAQ board and there was no longer data

Table 4.12.: Plasmatron Operations

Date	08.05.2015
Time	11.14
Pressure	100 mbar
Heat Flux by Standard Probe	1270 kW/m^2
Duration	Target: 230 s, Actual: 170 s
Air mass flow rate	16 g/s
Heat Flux Meas. Frequency	2 Hz
Pyrometer	Yes
Radiometer	Yes
Pyro & Radio Meas. Frequency	1 Hz
High Speed Camera	Yes
Video Camera	Yes
Photo Camera	Yes
Sample Instrumentation	Full Front Unit, XPL SU and 11 type E TCs
Additional Instrumentation Frequency	2 Hz

transfer after 110 s.

Heat Flux Measurements

The Figure 4.30 shows the heat flux measurement data. The probe is injected later around $t = 420s$. The heat flux probe is not left for longer time in plasma on purpose. The cork sample could not be placed in the cooled box because of its size and it was already heating up with the chamber temperature.

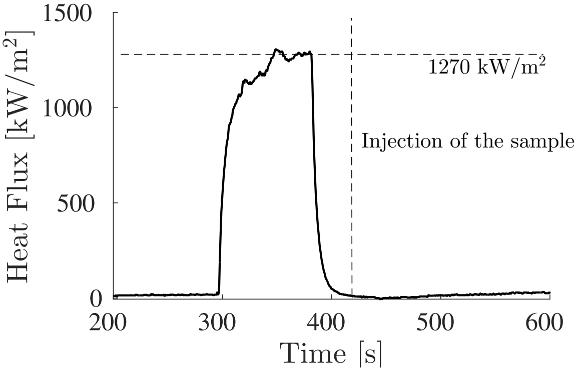

Figure 4.30.: Heat flux calibration for 1270 kW/m^2.

Visual Inspection - During the test

Initial visual inspection is performed during the plasma exposure. Figure 4.31 shows an overview of the sample throughout the test. Note that

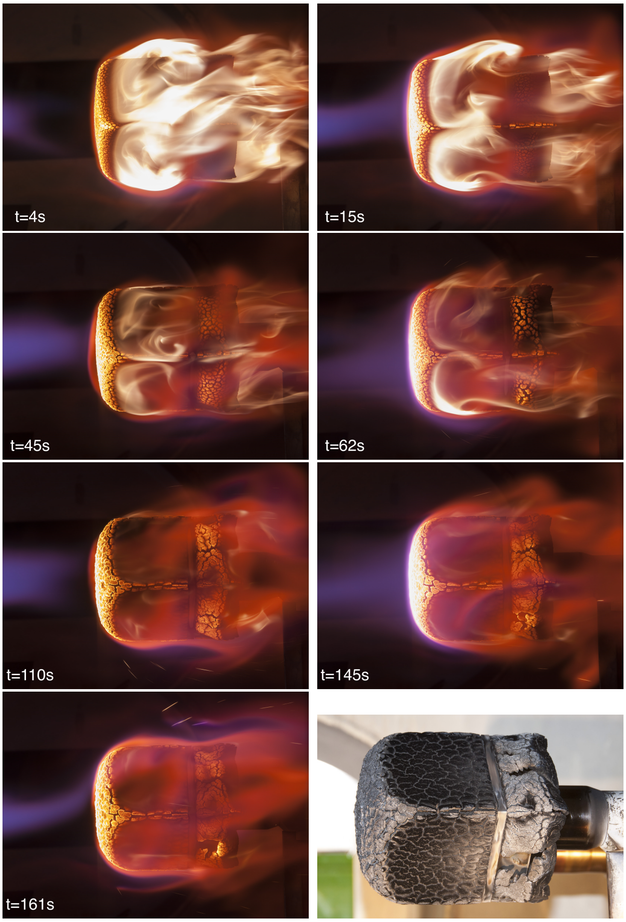

Figure 4.31.: Evolution of the sample during the test.

the time scale is changed from here on to t=0 s to the sample injection. It can be seen at t=4 s that the corners heated up, however still *sharp* and the cork extension at the back around the survival unit started to deform. At t=15 s, the sharp edges of the full unit was hot and the sharp corners were rounding. At 45 s, the cork extension started swelling in the center region. The heat-sink effect of the mounting screws next to the corners is clearly visible through the dark area around. The swelling continues until t=62 s, where the cracks started opening until around 110 s, where the swollen cracked char started to recess. At 145 s, the sample nose was significantly rounded and mechanical erosion started at the lower rearside that at 161 s, the survival unit wall was directly exposed to plasma from due to the missing piece. At the end of the test, the front TPS is intact and no mechanical erosion was observed however the cork extension is damaged.

It should be reminded that the cork extension was made solely for Plasmatron testing campaign as well as the stainless steal exposure to plasma. In QARMAN, the cork is in contact with the ceramic TPS which has a thermal conductivity 4 times lower and would make no cracks like Cork P50. The thin layer of cork swelled due to the incoming excessive heat from the exposed metal of the TPS-front-back plate and heat conduction through since it is stainless steel and not ceramics. Another reason would be the incoming heat from the tiny gap between the stainless steal and the cork, which was visible prior to the test. The primary assumption of this test was to provide a 1D heating from the stagnation point in axial direction. However, the *peeling* cork at the rear showed that there was significant heating from the side which could affect the performance of the survival unit.

Visual Inspection - After the Experiment

After the test, the sample is disassembled step by step for inspection and comparison to the measured data. Figure 4.32 shows the front cork. The thermal plugs are visible as reported for the scaled sample tests in Section 4.4.1. The cork is virgin in the back of the sample as expected. No damage on the pressure spools or the thermal plug thermocouples are seen.

The DAQ board on the left picture in Figure 4.33 is unchanged except the pressure pipes which melted at the corners. The right image shows the corner heating on the pyrogel as well which is caused by the heat conduction from the stainless steal corner due to direct plasma exposure.

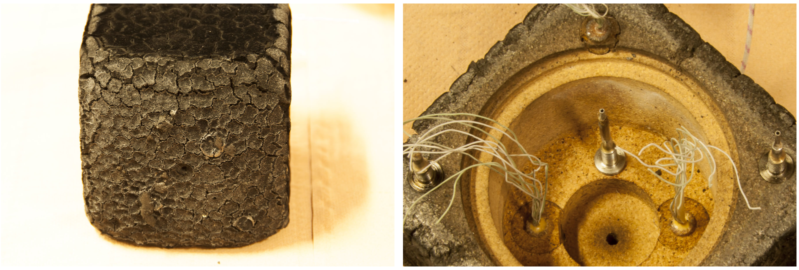

Figure 4.32.: Visual inspection during disassembly.

The cork is then sectioned diagonally to determine the charred and pyrolyzed portions of the cork P50. Figure 4.34 shows the cutting axis. Since the thermocouples are placed in U-shape inside the thermal plugs, it was not possible to cut through without removing the thermocouple cables. However, given the size of the test object, the thicknesses will not be different within a range of 1 cm. It can be seen that the cross section is just outside of the central plugs.

Figure 4.34 also shows three red lines where the char and pyrolysis layers are measured. The left and right lines corresponds to thermal plug 2 and 1 respectively. The layers are also measured on the lower sides shown in

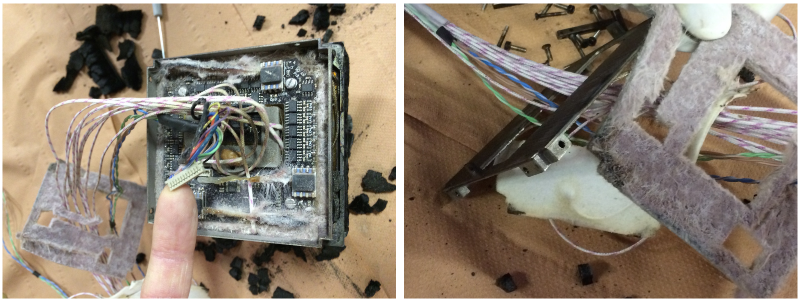

Figure 4.33.: Visual inspection during disassembly - continued.

Figure 4.34.: Cork P50 cross sectioning for layers inspection.

dashed squares. The layer thicknesses are given in Table 4.13. In the front face only char layer is visible at all three locations while on the sides some pyrolysis regions are visible. The char thicknesses on the front face are larger than the thermocouple depths of the thermal plugs and are observed in their data.

Table 4.13.: Char and pyrolysis layer thicknesses for locations given in Figure 4.34.

Location	Char Thickness [mm]	Pyrolysis Thickness [mm]
TP1	8.4	None
TP2	9.1	None
Center	5.9	None
Lower left side	9.5	7.5
Lower right side	0.4	N/A

Pyrometer and Radiometer Data

The pyrometer and the radiometer are pointed to the surface of the thermal plug 1 (TP1), that is closer to the center point. The alignment can be seen in Figure 4.35. The combination of both instruments gives the emissivity of the sample following Eqs. (3.21) and (3.22).

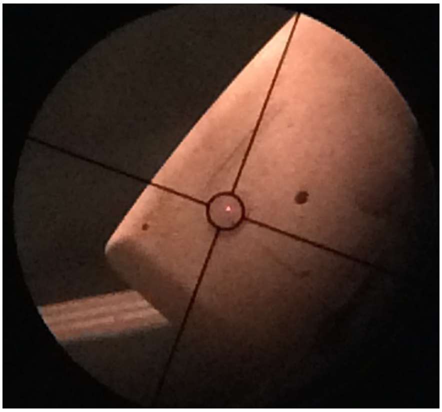

Figure 4.35.: Pyrometer and radiometer alignment. Note: pyrometer reverses the image in two axes.

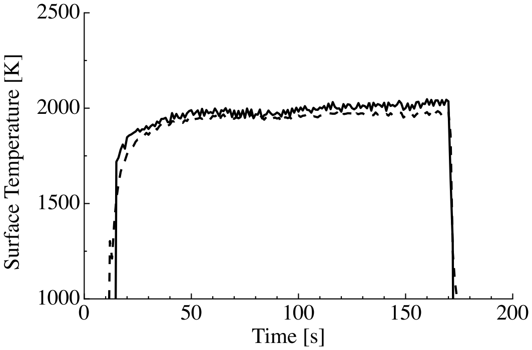

Figure 4.36.: Surface temperature measurements by pyrometer (solid line) and radiometer (dashed lines).

The average emissivity on the steady temperature plateau at 2015 K is computed as 0.89. The correlations given in the ablation characterization campaign in the previous chapter can be used to guess the surface temperature and the emissivity. To do that, the reference heat flux is used. The surface temperature is found to be 2094 K and the emissivity 0.83. This is considered a good agreement since the thermal plug is not located at the stagnation point but slightly off, making it exposed to a different heat flux.

The surface emissivity and the surface temperature together with the thermal plug data will provide valuable input for the post flight data processing of QARMAN.

XPL DAQ Board

The XPL board design was identical to the flight configuration and is shown in Figure 4.33. After the probe is injected in the plasma, the XPL board sent data from all sensors for 110 s. The temperature and pressure were acquired at 1 Hz. Then the interface card gave a partial short circuit error and couple of seconds later the card is fully short circuited. At the visual inspection after the test, it was seen that the spectrometer's photodiode amplifier circuit cables were melted and this was the reason for the short circuit. After the plasma test, a new functional test is conducted and data are successfully acquired from all sensors of XPL01 and XPL02.

As will be shown for thermal plug and pressure measurement results, the highest temperature of the electronics of XPL01 and XPL02 was 55°C. This shows that despite the high temperatures at the inner walls of the survival unit due to the side heat conduction, the fiberfrax and pyrogel insulators are sufficient to keep the electronics in their operational temperature range.

Thermal Plug Measurements: XPL01

Three thermal plugs were inserted in the test object identical to the QARMAN configuration. Two thermal plugs in the center have 5 type K thermocouples while the one in corner has 4. The depth of the thermocouples are 3, 5, 11, 18 and 25 mm from the surface. The Figure 4.28 shows the labeling of the plugs to match with the data. The temperatures of the CJC chips and the thermocouples are recorded at 2 Hz frequency. The sample is injected at 35 s. Figure 4.37 depicts that no temperature exceeded 55°C on the XPL board. It should also be noted that the initial temperatures were about 30 degrees due to the fact that the sample was exposed to heat before injection during the heat flux measurements. When the tested sample is small enough to fit in the cooling box, the initial temperatures are around 17-18°C which would make a difference of 12°C.

Figures 4.38 to 4.40 show the thermocouple data of the three thermal plugs (TPs). It is seen that the shallowest thermocouples reached their upper limit in all cases. No bare thermocouple junction is visible on the nose therefore it can already be guessed that the first thermocouples at 3 mm for all plugs were in the char layer with the surface temperature of 2000°C as shown in Figure 4.36. Indeed as given in Table 4.13 and shown in Figure 4.34, the char thicknesses were 9.1 mm for TP1 and 8.4 mm for TP2. The thermocouple depths were 3 and 5 mm away from the surface by design however during the mounting of the thermal plug, the depths are considered to be biased and could not be quantified since no X-ray measurement was performed. It can be seen from the data of TP1 and TP2 (in Figures 4.38 and 4.39) that the second thermocouple in TP1 also reached its upper limit while the one

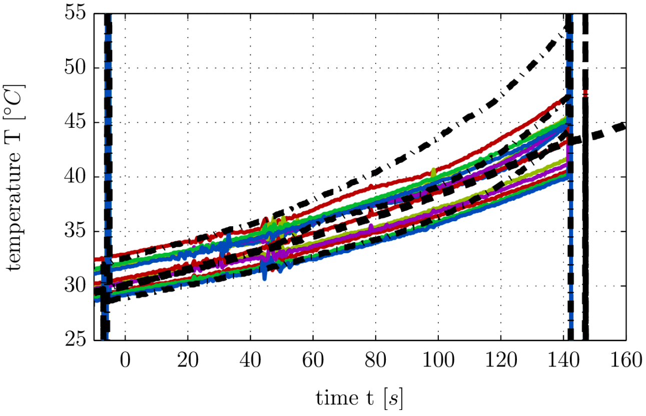

Figure 4.37.: Temperature sensor data on the XPL DAQ of TC measurement chain. Sample in: t=35 s. Legend is not given all curves stand for the 22 thermocouple CJC chips.

of TP2 has not. Although the plugs are symmetrical to the incoming flow and the second thermocouples were supposed to be at the same depth, the "hump" in the data (which is discussed in the later paragraphs) suggests the fact that thermal plug 2 thermocouples were at a lower depth than the thermal plug 1 or the plug surface temperatures were different.

On the other hand, the sample was slightly tilted downwards on the probe holder and the thermal plug 1 was more directly exposed in the stagnation point than the thermal plug 2. This can explain the increase of the temperature at the second thermocouple up to its limits in thermal plug 1 by having a thicker char layer.

The thermal plug 3 showed grounded loops for the second thermocouple after the surface thermocouple reached its upper limit in the char layer and later for others.

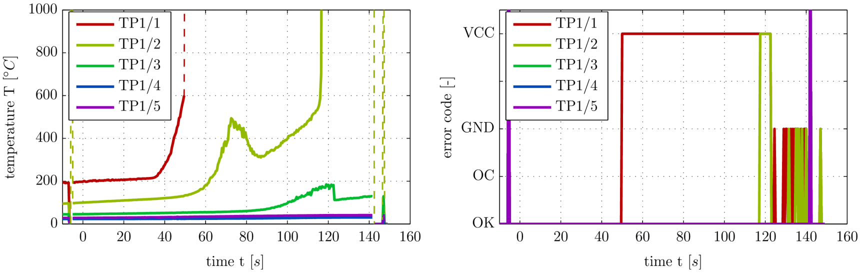

Figure 4.38.: Thermocouple data and the digital output of the thermal plug 1 which is in the center. Sample in: t=35 s.

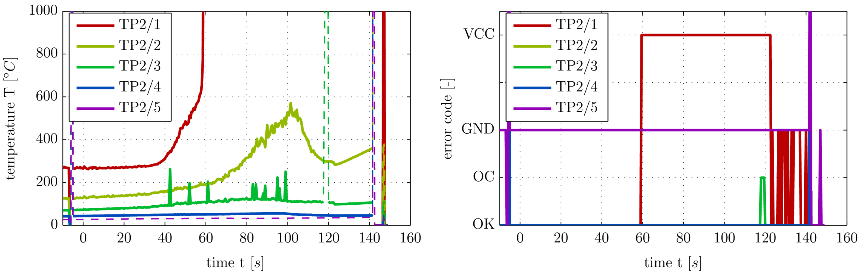

Figure 4.39.: Thermocouple data and the digital output of the thermal plug 2 which is in the center. Sample in: t=35 s.

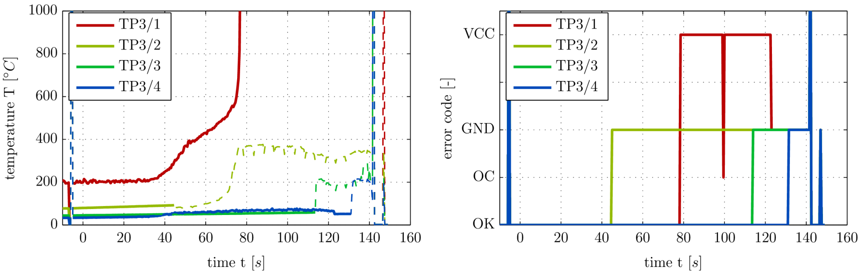

Figure 4.40.: Thermocouple data and the digital output of the thermal plug 3 which is in the corner. Sample in: t=35 s.

Moreover, for thermal plug 1 and 2, a “hump” can be seen in the second thermocouple at 5 mm at 72 and 100 s respectively in Figs. 4.38 and 4.39. These humps are visible in other ablative material plasma tests and flight data as discussed in Chapter 3. The temperatures where they occur are consistent with the TGA data shown in Section 3.4.1.

It was shown that the reason behind these humps are the exothermic chemical reactions inside the material at a given temperature which were measured by the TGA analysis. An important finding from the humps is that it was shown previously in the Cork P50 characterization campaign that even at different chamber pressures, if the surface temperature is the same, the humps occur at the same time given the thermocouple depths are the same. Although the TP1 and TP2 were placed symmetrically, the humps occurred about 28 s apart. This may be an evidence that the plug surfaces were at different temperatures therefore, it is expected that the first thermocouples had different heating slopes and that the second thermocouples showed different behavior in both plugs.

Finally, a temperature plateau is observed in Fig. 4.40 for thermal plug 3 about the same time that the first thermocouple reached its upper temperature limit. This is the plug which has 4 thermocouples and placed at the corner. Normally, during a phase change the temperature can be steady for a pure element however no direct sublimation is expected in depth therefore it suggests that this is an acquisition error rather than a physical phenomenon.

In summary, it should be noted that the test objective was to acquire healthy data from the XPL01. Since the aerothermodynamic environment was not fully representative of the flight, the biased location of the thermocouples in the plugs or the slight tilt of the probe in the Plasmatron chamber did not affect the objectives of the experiment. Thus, the test objective is considered met despite the two erroneous thermocouples (TP2/5 and TP3/2) and the shorter test duration.

Pressure Measurements: XPL02

There were three absolute pressure sensors on the test object. The labels and locations are depicted in Fig. 4.28. The measurement chain consisted of the bare holes, pressure spools, plastic tubes and the sensors. Fig. 4.41 shows the data from the three sensors. It is expected that all three sensors show the chamber pressure of 100 mbar before injection which is at about 37 s. The pressure in Plasmatron chamber fluctuates ±2 mbar due to the vacuum pumps. The sensor 1 and 2 do show a good match of about 98 mbar while the center sensor showed a higher value. Although identical sensors were used in the EM, the calibrations of individual sensors can be different. The plotted data in Fig. 4.41 come from the digital output of the sensor without any calibration. The difference can therefore be corrected with a calibration campaign.

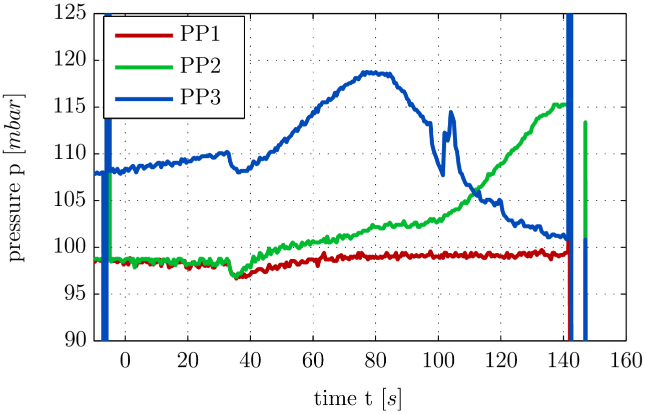

Figure 4.41.: Pressure sensor data. Sample in: t=35 s.

It is seen in Figure 4.41 that the pressure values changed for sensor 2 and 3 after injection at t=0 s. Since the sample has a certain nose geometry, after the injection the wall pressure would change from 100 mbar to another value but should change only due to the shape change of the nose. A rounding corner would suggest a decreasing pressure. However a change of 20 mbar as in the case of the Sensor 3 is too high and rapid when compared to the shape change. It could be the swelling/recession of the cork material that opened or blocked the bare holes of 2 mm diameter. This issue was not seen in the previous campaign of XPL01-02 qualification tests with 6/10 scaled test model. These changes in the data are, in fact, due to the melting of the plastic tubes. It was mentioned previously that instead of the PTFE tubes of the original QARMAN configuration, PVC tubes were used in this campaign. PVC has a melting point about 100°C while the PTFE melts between 260 and 327°C. The additional thermocouples placed in the test object revealed that the temperature at the corners inside the survival unit exceeded the melting point of the PVC due to the steel back frame conducting more heat than the original ceramic TPS would. The full scale testing will be repeated with the ceramic back frame and PTFE tubing, and the detailed thermal analysis will be performed with the new dataset.

As a housekeeping data and survival unit health monitoring, the temperatures of the pressure sensors are also recorded using the embedded temperature sensors. Figure 4.42 shows that the highest temperature reach throughout the test was 53°C. It should also be noted that the initial temperatures were about 30 degrees due to the fact that the sample was exposed to heat before injection during the heat flux measurements. When the tested sample is small enough to fit in the cooling box, the initial temperatures are around 17-18°C which would make a difference of 12°C.

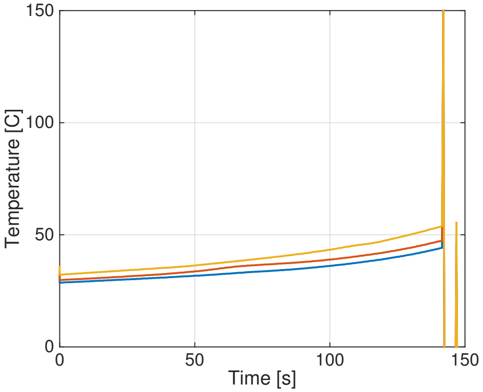

Figure 4.42.: Pressure sensor temperatures on XPL DAQ board. Sample in: t=35 s.

In summary, no error in data acquisition from XPL DAQ board was observed. However, the measurement chain in the next test needs improvement concerning the spool-sensor tubing with actual flight configuration.

Conclusions

The engineering model of the front unit of QARMAN was exposed to plasma flow at VKI Plasmatron facility. The free stream conditions were 100 mbar and 1.27 $\mathrm{MW/m^2}$ with the standard heat flux probe. The sample was injected for 170 s which corresponds to 73% of the re-entry total heat load.

The primary assumption of the experiment was to provide a 1D heat to the sample, which could not be established due to the test model design. There was severe additional heat conduction through the stainless steal plate between the front unit and the cork extension. Also, due to the small gap between the metal plate and the cork, the extension cork plates swelled and mechanical failure was observed which let the survival unit directly exposed to plasma. Despite this additional heat, it was seen that the electronic temperatures did not rise above their operational ranges. The front cork was still virgin with a small charred layer in front. No pyrolysis layer was formed at the stagnation region.

The thermal plugs worked well except a grounding error on the thermal plug 3. The temperature data agreed well with the char layer thicknesses measured. The plastic tubes used in pressure measurements were not identical to the flight configuration and could not resist the high temperatures. It is foreseen to repeat the experiment with the proper tubing material to avoid melting. Furthermore, the digital outputs of each pressure sensor will be calibrated prior to the full EM test to provide more reliable data.

Although the data connection failed during the test because of the melted photodiode cables, the XPL board performed successfully. The test will be repeated with the space qualified photodiode cables and no short cut is expected since the cable melting was the only problem. The objective about quantifying the XPL board performance under high heat loads and electromagnetic noise is therefore considered met.

The last objective was to provide high quality data for XPL01 performances for the post flight procedures discussed in Sec. 4.5. Several thermal plug experiments were already performed in Plasmatron. This objective is therefore considered successful with the new additions to the database.

Finally, it is important to state that radiation tests are also performed for the payloads XPL01 and XPL02, and QARMAN vehicle. This increases the Technology Readiness Level (TRL) of both payloads to 9. Recalling that the XPL01 measurement chain was successfully launched on board of two CubeSats and is still operational for over a year now. Recently QARMAN vehicle, including the two payloads XPL01 and XPL02, successfully passed the Critical Design Review (CDR) process. Currently, the flight model is being built for the launch in 2016.

As a future work, a link can be established between the full scale test in the subsonic plasma testing and the ablation characterization campaign.

However, this is not a direct connection since the in-depth temperature and swelling/recession measurements are in the off-stagnation region. This link can be made through the material response model once it will be built using the experimental data during the ablation characterization campaign. The material model can be fed to a 3D code to extract the in-depth ablation behavior of this test and its output can be validated by the XPL01 and XPL02 data.

4.5. Flight Data Reduction and Post-Flight Data Analysis Strategy

QARMAN flight will only provide in-depth temperatures from XPL01 and the pressure measurements from XPL02 in addition to the attitude and entry trajectory data from its IMU. It is important to relate the flight data to the ground test data for comparison to the Flight-to-Ground duplication procedure, and validation of the material response models and CFD computations that were discussed in Sec. 2.3.8 and 3.6 respectively. Before the validation, one must first plan on how to deal with the flight data once the vehicle is flown successfully.

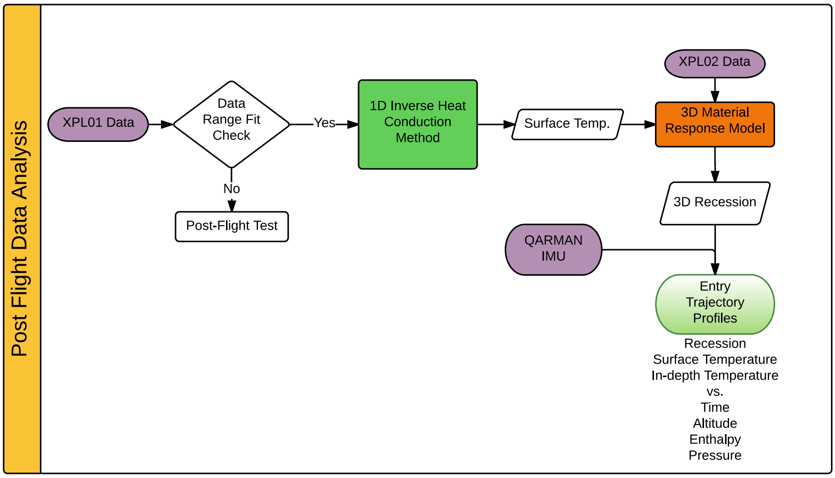

Figure 4.43.: Postflight data reduction from the experimental payloads and the extraction of the entry profiles.

The temperature and pressure data bits coming from XPL01 and XPL02 will be first converted to legible information. A noise reduction procedure may be needed for the pressure data as seen by the ground test results. During the ground tests, the temperature data were not noisy and less noise is expected during the flight since the strong Plasmatron electromagnetic field will not be present.

An analysis approach is given in Fig. 4.43 for after the data clean-up. Initially, the temperature data should be checked whether it fits the range of the ground test measurements to ensure validity of the inverse heat conduction method and the material response model. Although the ground tests were conducted at a larger envelope than the nominal QARMAN entry trajectory, the actual flight trajectory may generate a new set of data. If the flight data are too far out from the testing envelope, post-flight ground tests should be performed and the inverse and material response models should be updated. Later, by using the inverse methods, the surface temperature can be determined. In combination with the pressure data from XPL02, the material response model can be used to determine the recession profiles over the entire nose. QARMAN IMU will provide the location, velocity and attitude of the vehicle therefore the re-entry profiles of the surface recession and all other ablative behavior such as surface and in-depth temperatures can be determined.

4.6. Concluding Remarks

QARMAN, the atmospheric entry experiment CubeSat, is planned to be launched to 380 km altitude in early 2016. It will perform an atmospheric entry to Earth with 7.7 km/s speed at 120 km. On the way down, it will perform a number of aerothermodynamic experiments amongst which the XPL01 and XPL02 discussed in this study. XPL01 consists of three thermal plugs made of cork P50 that are insertions to the front TPS with 5 thermocouples at several depths. As for XPL02, three pressure ports are placed to measure the total pressure along the trajectory. The XPL01 and XPL02 configurations are established with the experience from the flight experiments discussed in Sec.1.2.2 and wind tunnel tests that were covered in Chapter 3. However both in-flight experiment designs are explained from square one, based on the payload design methodology presented, to provide guidelines for future in-flight experiments. The breadboard and plasma tests were detailed.

A scaled sample is manufactured and tested in Plasmatron, which was the first time electronic components were put in the test chamber. It was seen that the thermal plug and the pressure port concepts were successful. The electronics performed well even though the sample was exposed to high temperatures and strong electromagnetic noise. Then a full scale model of QARMAN's first unit is manufactured. It was an integration exercise and a first plasma test for the front unit subsystems for the CDR review. It included the survival unit and the full data acquisition board, as well as XPL01, XPL02 and the spectrometer. The results that are related to the thermal plugs and pressure measurements are detailed. Thermal plugs performed very well however the pressure measurements on two stations were damaged. The reason was the PTFE tubing that was replaced by a plastic one during the test which was affected by a stainless steel back frame. Originally the back frame material should have been titanium, however during the experiment a stainless steel plate was used and it conducted more heat than the titanium one would. The two replacement materials caused a damage in the tubing. The test will be repeated due to other unexpected results on the spectrometer and the back frame. In this test, correct tubing will be used to increase the TRL level.

Finally, a post-flight analysis strategy is proposed on how to deal with the flight data for validation of the ground experiments and numerical tools.

Chapter 5.

Conclusions and Perspectives

5.1. Contributions of this Thesis

This thesis provides an extensive study on the entire procedure of the TPS testing for an atmospheric entry vehicle, from pre-flight plasma wind tunnel experiments to in-flight aerothermodynamic experiments and finally a post-flight analysis strategy. Although the pre-flight to post-flight analysis processes were developed on QARMAN vehicle as a test case, each step is applicable to any other mission, that will perform an atmospheric entry.

For efficient TPS designs, accurate ground experiments are indispensable. Therefore, in this thesis it has been attempted to provide a complete Flight-to-Ground Duplication methodology in order to make sure the hypersonic entry flow conditions are duplicated in the ground facility. The stagnation region was the priority since it is subjected to high heat fluxes. Following the LHTS approach, pressure, enthalpy and velocity gradient parameters of the stagnation region are the main parameters to be duplicated in the ground facility. Plasmatron facility capabilities are extended with a novel enthalpy probe and an optical emission spectroscopy tool for enthalpy characterization. The enthalpy probe setup is built and tested in a wide range of testing conditions. The spectroscopy tool, which uses the ratio of two emission lines is developed as a non-intrusive realtime enthalpy measurement technique. The results from the two techniques are presented in comparison to the existing methods.

This work aimed especially to provide an accurate duplication of the velocity gradient parameter, that depends on the geometry of the hypersonic vehicle, its entry trajectory and the sample probe used in the ground facility. It is seen that all existing methodologies accounted for axisymmetry and generally spherical noses. An iterative four step procedure is proposed for arbitrary spacecraft geometries, providing the sample model geometry to be used in a particular moment of the entry trajectory. The required sample shapes are presented for QARMAN entry trajectory. The aspects of a full entry trajectory simulation in a plasma wind tunnel, called dynamic testing, were given within the facility capabilities.

A large data set of experiments and numerical simulations of the facility is produced and documented. The experimental database consists of heat flux measurements by four different heat flux probes, static and dynamic pressures, ICP powers and enthalpy measurements by different methods. For a wider range of operating conditions, numerical simulations of the VKI Plasmatron facility were performed. The numerical database, including the non-dimensional parameters (NDPs), were used in the Flight-to-Ground duplication and also for the classical rebuilding procedure of experiments for determining the boundary layer edge conditions. These data can be used by any experimentalist working in subsonic plasma wind tunnels for a range of heat flux probes.

A thorough ablation characterization campaign is conducted to provide experimental data as input to material response model development, with an emphasis on the effect of LHTS parameters on ablation phenomena. The variety of the experimental techniques used in the campaign provides a baseline for ablation measurement setups at VKI Plasmatron. Guidelines for the future material response model validation both with ground test and flight data are provided.

Finally an aerothermodynamic in-flight experiment design methodology is developed for constraining platforms such as QARMAN. Based on the existing flight experiments and following the payload design methodology, two experimental payloads for QARMAN, being thermal plugs for in-depth temperature measurements and a pressure payload, are designed, developed and tested in breadboards and in VKI Plasmatron environment. Three XPL01 measurement chains and sensors were flown in QB50p1 and QB50p2 satellites, launched in 2014. They performed well and are still operational. The measurement chain and the thermocouples are now at TRL9.

Additionally, a post-flight data analysis procedure is presented for data reduction with the aim of validation of the ground tools after the launch in 2016. The data analysis and validation procedures can be applied to any mission carrying onboard basic temperature and pressure instrumentation.

5.2. Conclusions

Plasma Flow Characterization

The enthalpy probe is a heat exchanger tube connected to a vacuum pump, that provides a direct measurement of local enthalpy. The incoming plasma flow suction rates are unique and determined only after the test by an iteration on density. The tests on relatively low heat fluxes (below $\sim$1040 kW/m^2) and pressures above 6100 Pa performed well, provided enough suction rate samples were acquired for an accurate hyperbolic curve fit. A preliminary set of suction rate ranges is provided so that the follow-up campaigns can rely. The obtained results showed a good agreement with existing methods such as rebuilding procedure and the OES method probing the O777 atomic line.

Secondly, an optical emission spectroscopy tool is developed making use of CN violet and N_2^+ emission line measurements. The ratios of the peaks or the integrated areas under the features are compared to a theoretical spectra to extract temperature. Assuming local thermodynamic equilibrium, the temperature data are converted in realtime to enthalpy. It was seen that this method always overshoots the enthalpy values when compared to the enthalpy probe, rebuilding and O777. Further investigation showed that the exposure time of the spectrometer integrates the plasma fluctuations in the facility which results in a higher temperature estimation.

Experimental and Numerical Databases

In addition to the enthalpy measurements, a wide range of heat flux measurements were performed with four different copper calorimeter probes: hemispherical probes of 15, 25 and 57.5 mm radii and the flat faced standard probe of 25 mm radius. The heat fluxes are measured at pressures from 1500 Pa to 23400 Pa. For these heat fluxes, the pressure-power operating conditions are determined and dynamic pressure measurements are taken. All measurements were performed with 16 g/s air mass flow rate and the probes were always placed at 445 mm away from the torch.

For the same probe position and 16 g/s flow rate, a numerical database is built using the in-house ICP CoolFluiD code. The classical 25 mm hemispherical probe mesh is used. New meshes are generated with 6, 15 and 57.5 mm radii probes based on the 25 mm reference one. A very large range of pressure and ICP power conditions were simulated and the non-dimensional parameters were computed. These simulations are quite time consuming (a new mesh takes about 4 to 5 days and a new operating condition 5 to 6 hours) thus the produced NDPs are valuable and are currently being implemented in a neural network so that NDPs can be determined without solving the entire plasma flowfield.

Flight-to-Ground Duplication Methodology

The iterative Flight-to-Ground Duplication methodology includes the passage from an arbitrary hypersonic vehicle geometry to its “hypersonic equivalent sphere”, then to a “subsonic equivalent sphere” for subsonic plasma, and finally to the probe geometry where the thermal protection systems and the instrumentation of the spacecraft can be tested. The procedure is applied to QARMAN entry trajectory at 66 km altitude. The flow fields along the stagnation line of the hypersonic vehicle, the hypersonic equivalent sphere, and the hemispherical probe for ground testing are compared and are shown to have a good agreement. The ground testing duplication, presented for QARMAN as a preflight analysis, is applicable to any spacecraft without a limitation on its geometry.

The whole procedure is developed for a fixed mass flow rate. It is seen that as the vehicle lowers the altitude, the required sample sizes get too small to make realistic tests in the facility. It is demonstrated that a way to overcome this is to reduce the mass flow rate so that bigger samples can still be used for accurate duplication.

The Flight-to-Ground duplication methodology can currently be used in steady free stream conditions which corresponds to a single point along the trajectory due to facility capabilities. However during the flight, the vehicle is subjected to a temperature history and a dynamic testing capability would allow us to make a full trajectory simulation in the plasma tunnel. This means that we have to modify pressure, enthalpy and radius at the same time, which is currently not possible. It is shown that if one keeps pressure and radius constant, but changes the enthalpy (or power) in a pre-defined and calibrated manner, the TPS materials can be tested with a higher, thus conservative, heat flux than it would be exposed to in an ideal dynamic test. Effect of mass flow rate changes are left as future work due to absence of experimental and numerical data at rates different than 16 g/s.

Ablation Characterization for Material Response Model Building

Within the wide range of testing conditions, it was seen that the reference cold wall heat flux is the parameter playing the major role on the surface temperatures. Changing solely pressure (thus edge enthalpy at fixed reference heat flux) or velocity gradient (thus impinging heat flux) did not affect the surface temperatures as much as the reference heat flux. For a fixed pressure and velocity gradient, it was seen that the surface temperature increases linearly with enthalpy, hence heat flux or power. These effects however were different for the in-depth response of the material. Even if the surface temperature does not change substantially when changing only the pressure or velocity gradient, but the in-depth temperatures, swelling and recession profiles and the mass loss rates showed a different behavior.

The swelling behavior makes the recession measurements rather difficult by the high speed camera. Once the swelling is over and the recession begins, it was seen that the recession profiles are linear. However often the test durations were not sufficient to determine the slope accurately. It was observed that at very high reference cold wall heat fluxes around 3 $\mathrm{MW/m^2}$, there is no swelling. It is also seen that with increasing pressure, the material swells more and for a longer time when the pressure and sample radius are kept constant. Furthermore, it was seen that for a constant pressure and heat flux, different sized samples swelled for an equal duration however the total recession of the smaller sample was bigger. This effect could be due to increasing influence of the side heating for smaller samples.

In addition to the plasma tests, a thermogravimetric analysis is performed to determine the mass densities for virgin and char together with the major pyrolysis reactions and the relevant Arrhenius laws. Although building the material response model was out of this thesis' scope, the necessary experimental data are provided. How each of the experimental results contribute to developing the model is explained in a synthetic manner.

Concerning the material response model validation in steady plasma tests as well as flight data once QARMAN is flown, the relation of the flight data and the ground data is established. It was seen that a 1D inverse heat conduction method is useful to extract the surface temperatures, thus recession, from the in-depth temperature flight data. Having this information, one can also validate the material response model in the transient entry trajectory conditions with a temperature history.

A mapping of the surface temperatures in the testing envelope is shown together with the QARMAN entry trajectory to estimate the surface temperatures. It was seen that the maximum expected temperature is about 2200 K. However it should be noted that the mapping is made for steady tests and the previously defined aspects of the dynamic testing is analyzed for ablation phenomena. The surface temperatures are mainly defined by the reference heat fluxes but the in-depth physics also rely on the pressure, enthalpy and velocity gradient. The conservative heat flux approach with power stepping, may be used for dynamic testing of the surface temperatures however more parameters must be simultaneously modified to simulate the full trajectory to match the in-depth phenomena such as temperature or the swelling/recession behaviors.

In-Flight Experiment Design and Qualification on Ground

Following the proposed payload design methodology, XPL01 thermal plugs and XPL02 pressure measurements are developed. The breadboard tests in Plasmatron showed that the temperature measurements are sensitive to the electromagnetic noise of the VKI Plasmatron. Therefore additional low pass filtering was necessary. This setup was successfully tested in samples exposed to plasma and it was launched onboard two satellites. The pressure measurement chain is also successfully tested in Plasmatron conditions. The fluctuations seen by XPL02 during the plasma tests are of similar range with the fluctuations measured by Plasmatron static pressure sensor.

The full scale testing for the front unit of QARMAN was overall successful for thermal plugs. The pressure tubes that are designed with PTFE materials were replaced by PVC because of time constraints of the experiment. Also due to the replacement of the titanium back frame with stainless steel, unexpected heat conduction occurred and two out of three pressure tubes melted. A more complete qualification of the complete XPL02 set will be left as future work.

Post-Flight Strategies

A post-flight strategy is given for the post-flight phase of QARMAN vehicle since the launch will be in 2016. A data reduction methodology is provided, allowing us to determine the surface temperature and recession profiles from the in-flight measurements. An inverse heat conduction method is described for surface temperature determination using XPL01 measurements. However, this method requires the thermal conductivity and the specific heat of the cork P50 material, thus left as future work after the material response modeling.

Having the entry data in combination to the attitude and altitude data from the IMU measurements, one can validate the material response models simultaneously with the numerical tools validation. Additionally, one can iterate the Flight-to-Ground Duplication procedure with the actual flight trajectory that may be different than the expected one.

5.3. Perspectives

- **Flow Characterization:**

  The enthalpy probe method could be further extended to high heat fluxes and low pressures. A primary improvement to the current setup would be on the heat exchanger design. Roughness elements could be added to the inner surface to induce turbulence and increase the efficiency of heat exchange. Secondly, a flow stabilization element can be added to the experimental setup for low pressure cases.

  In addition to the enthalpy probe, the improvement of non-intrusive techniques is also crucial as they can provide real-time measurements and perform as a calibration tool. High speed emission spectroscopy techniques are highly recommended for Plasmatron facility, that can study different atomic or molecular spectral lines.

  In order to increase the accuracy and confidence on the optical techniques, the jet unsteadiness should be characterized for Plasmatron operating conditions. Radial and axial mapping of the jet enthalpy and velocity would be of great benefit for all ongoing studies.

- **Extending Numerical and Experimental Databases:**

  An effort is made to extend the existing experimental and numerical databases to different sized probes. Broadening the databases further with different mass flow rates or probe positions would allow a novel approach to dynamic testing of the entry trajectories as well as the use of bigger samples for the Flight-to-Ground duplication methodology.

- **Flight-to-Ground Duplication:**

  The entire procedure was made with a fixed mass flow rate and a fixed location of the probe. With a wider experimental/numerical database, the current facility capabilities would allow bigger sample sizes and a proper dynamic testing if the mass flow rate can be modified instantaneously. The change of the axial position of the probe is amongst the capabilities of VKI Plasmatron however there is currently not enough data on how enthalpy or β changes axially. With additional information, both mass flow rate and the probe position may lead to a different duplication configuration than just modifying the free stream and the sample geometry.

In addition to the sensitivity analysis on the iterative procedure, an uncertainty quantification (UQ) can be conducted.

- **Ablation Campaign:**

  Longer test durations are suggested for future test campaigns of cork P50 material for more accurate recession rate measurements. Also, the bigger sample sizes should be considered with a new numerical/experimental database and a more accurate flight mapping can be achieved in dynamic conditions.

  Although a TGA analysis could be carried out at VKI, more material properties, such as specific heat, thermal diffusivity, thermal conductivity, permeability, tortuosity, etc. can be measured in collaboration with material science experts to build higher fidelity material response models.

  Assessment and validation of the surface measurements should be done for the case of ablators. More focused effort should be made on the validity of the gray body assumption used for the emissivity measurements with the infrared pyrometer and radiometer. Wider range spectral radiance measurements can be conducted to match the radiometer wavelengths. This would be very useful for VKI Plasmatron experiments since radiometer device is much more practical than spectroscopic or infrared camera measurements.

- **In-Flight Experiment Design:**

  For future re-entry test flights on CubeSat platforms may carry a different TPS material, different attitude control and de-orbiting devices. Most importantly, it may carry different miniature instrumentation for more accurate or more interesting measurements, such as recession sensors, vacuum sensors, infrared thermography etc.

Appendices

Appendix A.

Enthalpy Measurements

A.1. Enthalpy Probe Measurements

Table A.1.: Case H-4b. Pressure 6180 Pa; $\dot{q}_{std} = 651.73$ kW/m^2.

$\overline{\dot{m}_g}$	$\sigma_{\dot{m}_g}$	$\dot{m}_w$	$\overline{T_{in}}$	$\sigma_{T_{in}}$	$\overline{T_{out}}$	$\sigma_{T_{ou}t}$	$\overline{T_3}$	σ_{T_3}
g/s	g/s	g/s	C	C	C	C	C	C
0.0133	0.00015	8.87	22.3	0.1020	28.1	0.3199	300.3	0.1425
0.0154	0.00015	8.87	22.5	0.0336	29.0	0.1923	300.9	0.1250
0.0180	0.00025	8.87	22.6	0.0368	29.8	0.1447	301.4	0.1253
0.0214	0.00020	8.87	22.7	0.0430	30.8	0.0585	302.2	0.1370
0.0162	0.00020	8.87	22.7	0.0310	29.7	0.1503	302.5	0.0609
0.0104	0.00010	8.87	22.6	0.0468	28.2	0.3297	302.5	0.0438
0.0089	0.00020	8.87	22.6	0.0315	27.3	0.0612	302.6	0.0000
0.0058	0.00015	8.87	22.6	0.0000	26.8	0.1233	302.4	0.0144

Table A.2.: Case H-4bbis6. Pressure 10000 Pa; $\dot{q}_{std} = 460.50$ kW/m^2.

$\overline{\dot{m}_g}$	$\sigma_{\dot{m}_g}$	$\dot{m}_w$	$\overline{T_{in}}$	$\sigma_{T_{in}}$	$\overline{T_{out}}$	$\sigma_{T_{ou}t}$	$\overline{T_3}$	σ_{T_3}
g/s	g/s	g/s	C	C	C	C	C	C
0.0187	0.00037	6.58	22.1	0.0686	27.6	0.7060	306.9	0.1005
0.025	0.00043	6.58	21.9	0.0461	30.9	0.4110	306.6	0.0000
0.0303	0.00046	6.58	22.0	0.0471	33.0	0.4500	306.7	0.0000
0.0371	0.00049	6.58	22.0	0.0499	34.8	0.3688	307.6	0.1212
0.0401	0.00050	6.58	22.1	0.0000	36.0	0.1996	308.7	0.1867
0.0434	0.00048	6.58	22.2	0.0304	37.4	0.1960	310.9	0.3363
0.0285	0.00046	6.58	22.3	0.0496	35.0	0.7849	309.2	0.1415
0.0127	0.00029	6.58	22.1	0.0507	30.4	0.8057	308.2	0.1221
0.009	0.00022	6.58	22.0	0.0465	27.5	0.4536	307.4	0.1050
0.0045	0.00012	6.58	21.9	0.0213	26.2	0.0512	306.8	0.0973

Table A.3.: Case H-4bbis. Pressure 10000 Pa; $\dot{q}_{std} = 642.68$ kW/m^2.

$\overline{\dot{m}_g}$ g/s	$\sigma_{\dot{m}_g}$ g/s	$\dot{m}_w$ g/s	$\overline{T_{in}}$ C	$\sigma_{T_{in}}$ C	$\overline{T_{out}}$ C	$\sigma_{T_{ou}t}$ C	$\overline{T_3}$ C	σ_{T_3} C
0.003	0.00008	8.87	22.3	0.0647	26.0	0.0337	298.7	0.0690
0.0065	0.00016	8.87	22.4	0.0427	26.8	0.1371	299.1	0.0673
0.0112	0.00025	8.87	22.5	0.0167	28.0	0.1433	299.6	0.0950
0.0154	0.00030	8.87	22.5	0.0501	29.3	0.2738	300.1	0.0716
0.0188	0.00034	8.87	22.6	0.0362	30.6	0.1608	300.7	0.1043
0.0215	0.00034	8.87	22.7	0.0262	31.7	0.1913	301.4	0.1475
0.0238	0.00034	8.87	22.8	0.0000	32.8	0.0913	302.5	0.1340
0.0305	0.00041	8.87	22.9	0.0202	34.6	0.0772	304.5	0.2190
0.0349	0.00041	8.87	23.1	0.0503	36.0	0.0856	307.3	0.3391

Table A.4.: Case H-4bbis4. Pressure 10000 Pa; $\dot{q}_{std} = 858.06$ kW/m^2.

$\overline{\dot{m}_g}$ g/s	$\sigma_{\dot{m}_g}$ g/s	$\dot{m}_w$ g/s	$\overline{T_{in}}$ C	$\sigma_{T_{in}}$ C	$\overline{T_{out}}$ C	$\sigma_{T_{ou}t}$ C	$\overline{T_3}$ C	σ_{T_3} C
0.0145	0.00025	8.87	23.3	0.0352	32.0	0.0946	307.1	0.0896
0.0153	0.00025	8.87	23.3	0.0000	32.4	0.0606	307.5	0.0686
0.0174	0.00026	8.87	23.3	0.0000	33.1	0.2037	307.8	0.0781
0.0254	0.00033	8.87	23.4	0.0468	35.7	0.3692	308.6	0.2054
0.0356	0.00042	8.87	23.6	0.0887	39.5	0.8119	311.5	0.9781
0.0135	0.00026	8.87	23.4	0.0747	32.1	0.2611	310.9	0.1119
0.0048	0.00012	8.87	23.3	0.0459	29.1	0.4000	309.8	0.1373

Table A.5.: Case H-4bbis5. Pressure 10000 Pa; $\dot{q}_{std} = 1039.65$ kW/m^2.

$\overline{\dot{m}_g}$ g/s	$\sigma_{\dot{m}_g}$ g/s	$\dot{m}_w$ g/s	$\overline{T_{in}}$ C	$\sigma_{T_{in}}$ C	$\overline{T_{out}}$ C	$\sigma_{T_{ou}t}$ C	$\overline{T_3}$ C	σ_{T_3} C
0.0058	0.00010	8.87	23.0	0.1017	29.1	0.5819	308.1	0.0828
0.012	0.00025	8.87	23.2	0.0625	31.7	0.4814	308.7	0.1103
0.0169	0.00025	8.87	23.3	0.0183	34.0	0.2744	309.2	0.0885
0.021	0.00095	8.87	23.4	0.0841	36.3	0.4541	309.9	0.1317
0.0266	0.00025	8.87	23.6	0.0515	38.4	0.4892	310.9	0.2289
0.0302	0.00025	8.87	23.6	0.0497	40.2	0.2439	312.5	0.2828
0.0381	0.00045	8.87	23.8	0.0497	43.2	0.4657	315.6	0.5928

Table A.6.: Case H-5a. Pressure 11967 Pa; $\dot{q}_{std} = 375.59$ kW/m^2.

$\overline{\dot{m}_g}$ g/s	$\sigma_{\dot{m}_g}$ g/s	$\dot{m}_w$ g/s	$\overline{T_{in}}$ C	$\sigma_{T_{in}}$ C	$\overline{T_{out}}$ C	$\sigma_{T_{ou}t}$ C	$\overline{T_3}$ C	σ_{T_3} C
0.0067	0.00017	8.87	22.7	0.0420	25.1	0.1230	304.4	0.0318
0.0120	0.00027	8.87	22.8	0.0485	26.1	0.1305	304.4	0.0135
0.0148	0.00029	8.87	22.8	0.0213	27.2	0.3096	304.4	0.0394
0.0176	0.00031	8.87	22.9	0.0296	28.0	0.0982	304.5	0.0000
0.0172	0.00027	8.87	22.9	0.0000	28.2	0.1336	304.5	0.0236
0.0215	0.00031	8.87	22.9	0.0000	28.6	0.1767	304.7	0.0505
0.0325	0.00043	8.87	23.0	0.0646	31.1	0.3873	307.2	1.4509
0.0418	0.00050	8.87	23.1	0.0486	32.8	0.5170	311.8	0.4806

Table A.7.: Case H-5c. Pressure 11967 Pa; $\dot{q}_{std} = 727.43$ kW/m^2.

$\overline{\dot{m}_g}$ g/s	$\sigma_{\dot{m}_g}$ g/s	$\dot{m}_w$ g/s	$\overline{T_{in}}$ C	$\sigma_{T_{in}}$ C	$\overline{T_{out}}$ C	$\sigma_{T_{ou}t}$ C	$\overline{T_3}$ C	σ_{T_3} C
0.0389	0.00030	8.87	23.1	0.1502	37.5	0.8332	312.0	0.5687
0.0325	0.00025	8.87	23.4	0.0354	37.3	0.1622	312.1	0.1388
0.0229	0.00025	8.87	23.4	0.0376	34.3	0.8077	311.2	0.1441
0.0140	0.00025	8.87	23.3	0.0388	31.1	0.5390	310.5	0.1148
0.0063	0.00015	8.87	23.2	0.0451	28.7	0.3974	309.9	0.0802
0.0025	0.00010	8.87	23.1	0.0000	27.4	0.1318	309.4	0.0650
0.0118	0.00010	8.87	23.1	0.0302	29.1	0.4941	309.6	0.0408
0.0202	0.00015	8.87	23.2	0.0354	32.1	0.4002	309.6	0.0668
0.0298	0.00020	8.87	23.3	0.0000	35.0	0.6055	310.4	0.2116
0.0366	0.00025	8.87	23.4	0.0476	37.6	0.3979	312.3	0.3386

Table A.8.: Case H-6a. Pressure 17143 Pa; $\dot{q}_{std} = 324.83$ kW/m^2.

$\overline{\dot{m}_g}$ g/s	$\sigma_{\dot{m}_g}$ g/s	$\dot{m}_w$ g/s	$\overline{T_{in}}$ C	$\sigma_{T_{in}}$ C	$\overline{T_{out}}$ C	$\sigma_{T_{ou}t}$ C	$\overline{T_3}$ C	σ_{T_3} C
0.0064	0.00017	8.87	21.6	0.0000	23.6	0.1466	298.0	0.0462
0.0155	0.00036	8.87	21.6	0.0273	24.5	0.3109	298.1	0.0504
0.0252	0.00049	8.87	21.7	0.0164	26.0	0.3219	298.5	0.0681
0.0288	0.00049	8.87	21.8	0.0202	27.4	0.2100	299.4	0.1728
0.0338	0.00051	8.87	21.9	0.0209	28.2	0.1226	300.5	0.2095
0.0347	0.00047	8.87	22.0	0.0520	28.8	0.0913	302.1	0.3843
0.0416	0.00048	8.87	22.1	0.0497	29.7	0.2509	305.1	0.5728

Table A.9.: Case H-6b. Pressure 17143 Pa; $\dot{q}_{std} = 582.97$ kW/m^2.

$\overline{\dot{m}_g}$ g/s	$\sigma_{\dot{m}_g}$ g/s	$\dot{m}_w$ g/s	$\overline{T_{in}}$ C	$\sigma_{T_{in}}$ C	$\overline{T_{out}}$ C	$\sigma_{T_{out}}$ C	$\overline{T_3}$ C	σ_{T_3} C
0.0066	0.00018	8.87	22.1	0.0298	25.6	0.0471	303.2	0.2136
0.0178	0.00040	8.87	22.2	0.0536	27.3	0.5302	302.8	0.1029
0.0253	0.00050	8.87	22.3	0.0354	29.4	0.3679	302.7	0.0328
0.0309	0.00053	8.87	22.4	0.0425	31.2	0.4272	303.4	0.1597
0.0354	0.00054	8.87	22.5	0.0000	32.6	0.2655	304.9	0.2799
0.039	0.00052	8.87	22.6	0.0649	33.5	0.1720	307.1	0.5111
0.0402	0.00049	8.87	22.7	0.0110	33.8	0.1135	309.0	0.3637
0.0279	0.00052	8.87	22.7	0.0483	31.6	0.5010	307.3	0.2735
0.0125	0.00030	8.87	22.5	0.0561	28.2	0.7718	305.9	0.2677

Table A.10.: Case H-6c. Pressure 17143 Pa; $\dot{q}_{std} = 813.49$ kW/m^2.

$\overline{\dot{m}_g}$ g/s	$\sigma_{\dot{m}_g}$ g/s	$\dot{m}_w$ g/s	$\overline{T_{in}}$ C	$\sigma_{T_{in}}$ C	$\overline{T_{out}}$ C	$\sigma_{T_{out}}$ C	$\overline{T_3}$ C	σ_{T_3} C
0.0041	0.00015	8.87	22.2	0.0522	26.5	0.5906	303.0	0.0629
0.0103	0.00015	8.87	22.3	0.0325	28.4	0.4302	303.0	0.0229
0.0154	0.00025	8.87	22.4	0.0329	30.1	0.3342	303.3	0.0817
0.0227	0.00030	8.87	22.4	0.0486	32.5	0.4944	303.8	0.1206
0.0275	0.00025	8.87	22.6	0.0495	34.4	0.4303	304.7	0.1772
0.0333	0.00030	8.87	22.7	0.0504	36.5	0.4139	306.5	0.3586
0.0378	0.00010	8.87	22.7	0.0503	38.2	0.2804	309.0	0.4388
0.0399	0.00025	8.87	22.8	0.0195	39.1	0.1666	311.1	0.4282

Table A.11.: Case H-7a. Pressure 19815 Pa; $\dot{q}_{std} = 381.79$ kW/m^2.

$\overline{\dot{m}_g}$ g/s	$\sigma_{\dot{m}_g}$ g/s	$\dot{m}_w$ g/s	$\overline{T_{in}}$ C	$\sigma_{T_{in}}$ C	$\overline{T_{out}}$ C	$\sigma_{T_{out}}$ C	$\overline{T_3}$ C	σ_{T_3} C
0.0064	0.00018	8.87	22.0	0.0402	24.5	0.2480	304.3	0.0627
0.0121	0.00030	8.87	22.0	0.0335	25.6	0.1969	304.2	0.0390
0.0200	0.00045	8.87	22.1	0.0300	26.8	0.2405	304.0	0.0250
0.0254	0.00052	8.87	22.1	0.0470	28.1	0.2580	304.2	0.0785
0.0342	0.00060	8.87	22.2	0.0189	29.8	0.3426	305.6	0.3323
0.0382	0.00062	8.87	22.3	0.0216	30.8	0.1313	307.6	0.3471
0.0418	0.00059	8.87	22.3	0.0425	31.8	0.1726	310.5	0.5095
0.0469	0.00057	8.87	22.5	0.0451	32.8	0.1349	314.2	0.6243
0.0490	0.00056	8.87	22.6	0.0502	33.0	0.0674	316.4	0.3860

Table A.12.: Case H-7b. Pressure 19815 Pa; $\dot{q}_{std} = 425.87$ kW/m^2.

$\overline{\dot{m}_g}$ g/s	$\sigma_{\dot{m}_g}$ g/s	$\dot{m}_w$ g/s	$\overline{T_{in}}$ C	$\sigma_{T_{in}}$ C	$\overline{T_{out}}$ C	$\sigma_{T_{ou}t}$ C	$\overline{T_3}$ C	σ_{T_3} C
0.0065	0.00020	8.87	22.0	0.0394	24.7	0.4382	305.6	0.0396
0.0141	0.00005	8.87	22.1	0.0501	26.6	0.3229	305.4	0.0489
0.0239	0.00030	8.87	22.2	0.0192	28.2	0.3083	305.4	0.0552
0.0348	0.00050	8.87	22.3	0.0567	30.7	0.4480	307.1	0.3946
0.0284	0.00060	8.87	22.4	0.0000	29.9	0.0780	307.2	0.0492
0.0401	0.00005	8.87	22.5	0.0470	32.0	0.3694	309.7	0.4712
0.0429	0.00075	8.87	22.6	0.0510	33.2	0.2939	313.1	0.6801
0.0476	0.00010	8.87	22.7	0.0500	33.9	0.0923	316.1	0.5074
0.0485	0.00055	8.87	22.8	0.0000	34.2	0.1242	318.5	0.5581

Table A.13.: Case H-7c. Pressure 19815 Pa; $\dot{q}_{std} = 714.68$ kW/m^2.

$\overline{\dot{m}_g}$ g/s	$\sigma_{\dot{m}_g}$ g/s	$\dot{m}_w$ g/s	$\overline{T_{in}}$ C	$\sigma_{T_{in}}$ C	$\overline{T_{out}}$ C	$\sigma_{T_{ou}t}$ C	$\overline{T_3}$ C	σ_{T_3} C
0.0068	0.00019	6.58	21.7	0.0426	27.0	0.1437	303.1	0.0469
0.0110	0.00028	6.58	21.8	0.0000	28.4	0.3227	303.2	0.0359
0.0205	0.00046	6.58	21.9	0.0288	30.9	0.6287	303.3	0.0778
0.0317	0.00062	6.58	22.1	0.0489	34.6	0.8097	304.3	0.1447
0.0406	0.00068	6.58	22.2	0.0506	38.8	0.9676	307.8	0.5266
0.0556	0.00079	6.58	22.4	0.0483	42.9	0.8496	315.0	0.7940
0.0667	0.00082	6.58	22.7	0.0683	48.1	0.8470	324.9	0.8540
0.0707	0.00080	6.58	22.9	0.0850	51.2	0.5115	333.5	1.4245
0.0778	0.00080	6.58	23.3	0.0693	54.3	0.6065	346.5	1.5732

Table A.14.: Case H-8a. Pressure 23482 Pa; $\dot{q}_{std} = 364.85$ kW/m^2.

$\overline{\dot{m}_g}$ g/s	$\sigma_{\dot{m}_g}$ g/s	$\dot{m}_w$ g/s	$\overline{T_{in}}$ C	$\sigma_{T_{in}}$ C	$\overline{T_{out}}$ C	$\sigma_{T_{ou}t}$ C	$\overline{T_3}$ C	σ_{T_3} C
0.0138	0.00035	8.87	22.2	0.0502	25.6	0.1860	307.6	0.1155
0.022	0.00050	8.87	22.3	0.0000	26.8	0.2500	307.0	0.0791
0.0271	0.00057	8.87	22.3	0.0227	27.7	0.1630	307.0	0.0000
0.0317	0.00062	8.87	22.4	0.0448	28.8	0.2455	307.6	0.1418
0.0367	0.00067	8.87	22.4	0.0503	29.7	0.2884	309.0	0.3218
0.0421	0.00070	8.87	22.5	0.0378	30.7	0.1565	312.2	0.5774
0.0467	0.00071	8.87	22.6	0.0000	31.5	0.1886	315.5	0.5365
0.051	0.00073	8.87	22.7	0.0503	32.3	0.2449	318.7	0.5421
0.0556	0.00071	8.87	22.8	0.0494	32.6	0.2914	322.7	0.7219
0.0578	0.00066	8.87	22.9	0.0449	33.5	0.1804	327.1	0.7675

Table A.15.: Case H-8b. Pressure 23482 Pa; $\dot{q}_{std} = 559.32$ kW/m^2.

$\overline{\dot{m}_g}$ g/s	$\sigma_{\dot{m}_g}$ g/s	$\dot{m}_w$ g/s	$\overline{T_{in}}$ C	$\sigma_{T_{in}}$ C	$\overline{T_{out}}$ C	$\sigma_{T_{out}t}$ C	$\overline{T_3}$ C	σ_{T_3} C
0.0057	0.00020	8.8935	22.4	0.0381	25.5	0.4554	300.9	0.0685
0.0113	0.00025	8.8935	22.5	0.0000	27.0	0.1432	301.3	0.0981
0.0163	0.00015	8.8935	22.6	0.0407	28.2	0.1927	301.7	0.0930
0.0219	0.00040	8.8935	22.6	0.0505	29.5	0.1768	302.2	0.0775
0.0267	0.00065	8.8935	22.8	0.0496	30.9	0.1244	302.8	0.1453
0.0324	0.00035	8.8935	22.9	0.0422	32.4	0.0767	304.2	0.2073
0.036	0.00030	8.8935	22.9	0.0562	33.6	0.1911	306.0	0.3610
0.0397	0.00035	8.8935	23.1	0.0474	34.5	0.1041	308.5	0.5523
0.043	0.00030	8.8935	23.2	0.0380	35.2	0.0569	310.7	0.3275
0.044	0.00100	8.8935	23.3	0.0000	35.5	0.0998	312.2	0.3307
0.0459	0.00010	8.8935	23.3	0.0000	35.6	0.1288	313.3	0.1492

Table A.16.: Case H-8c Pressure 23482 Pa; $\dot{q}_{std} = 781.97$ kW/m^2.

$\overline{\dot{m}_g}$ g/s	$\sigma_{\dot{m}_g}$ g/s	$\dot{m}_w$ g/s	$\overline{T_{in}}$ C	$\sigma_{T_{in}}$ C	$\overline{T_{out}}$ C	$\sigma_{T_{out}t}$ C	$\overline{T_3}$ C	σ_{T_3} C
0.0123	0.00032	8.8935	22.9	0.0263	29.0	0.3295	306.5	0.1000
0.0186	0.00044	8.8935	23.1	0.0516	31.0	0.3504	306.2	0.0503
0.0236	0.00052	8.8935	23.2	0.0502	32.6	0.1528	306.2	0.0482
0.0288	0.00058	8.8935	23.3	0.0390	34.6	0.2559	306.9	0.1330
0.0335	0.00063	8.8935	23.3	0.0181	35.9	0.1604	308.0	0.2469
0.0364	0.00065	8.8935	23.4	0.0453	36.9	0.1456	309.5	0.2902
0.0395	0.00066	8.8935	23.4	0.0549	37.6	0.1318	311.2	0.3524
0.0413	0.00064	8.8935	23.6	0.0436	38.8	0.1521	313.5	0.4610
0.0438	0.00062	8.8935	23.7	0.0000	39.3	0.1863	315.5	0.3506
0.0457	0.00059	8.8935	23.7	0.0259	39.8	0.1752	316.7	0.2406
0.0468	0.00055	8.8935	23.7	0.0499	40.0	0.1217	317.6	0.1389

A.2. ARTEmiS

ARTEmiS is initially developed for Argon-Hydrogen plasma and it uses H_α (656.27 nm) and H_β (484.12 nm) atomic emission lines in the Balmer series [124]. These two features correspond to the first Balmer transitions between hydrogen electronic levels and the transitions are considered not self-absorbed. Another important assumption is that the measurements are conducted in optically thin plasma. The optically thin directional emission intensity, J_{ul}, associated with a radiative transition due to spontaneous emission, from an upper emitting level u to a lower level l can be expressed by [132]:

$$J_{ul} = \frac{A_{ul}}{4\pi} \times n_u \times \frac{hc}{\lambda_{ul}} \; [W.m^{-3}.sr^{-1}] \tag{A.1}$$

where A_{ul} (in s^{-1}) is the Einstein coefficient associated with the spontaneous emission from level u to level l, with energy E_u and E_l (in cm^{-1}), $\lambda_{ul} = 10^7/(E_u - E_l)$ (in nm) denotes the line position, and n is the population. The treatment of the H atomic transitions required spectroscopic data taken from the atomic spectra database NIST [163] and they are summarized in Table A.17.

Table A.17.: Spectroscopic data of H_α and H_β. A_{ul} is the Einstein coefficient, E_u and E_l are the upper and lower level energies respectively and g is the degeneracy.

Line	Position nm	A_{ul} s^{-1}	E_u cm^{-1}	E_l cm^{-1}	g
H_α	656.27	4.41×10^7	82258	97492	18
H_β	486.12	9.6×10^6	82258	102823	36

Assuming the probed plasma medium is a homogeneous isotherm column of length equal to the plasma diameter, the local intensity in column $J(x)$ can be rebuilt using the intensity recorded by the spectrometer. The temperature can then be extracted by means of the common Boltzmann diagram method since at thermal equilibrium the electronic levels population follows a Boltzmann distribution as given in Eq. A.2.

$$n_i = \frac{N(T)}{Q(T)} \times g_i \times exp\left(\frac{-E_i}{k_B T}\right) \tag{A.2}$$

where N(T) and Q(T) are respectively the concentration and partition function of the hydrogen species and g is the degeneracy of a given electronic level i, E_i is the energy of the considered level and k_B is the Boltzmann constant. Introducing Eq. A.2 in Eq. A.1, and taking the ratio of the two hydrogen line intensities as J_1/J_2, the temperature can be deduced from Eq. A.3 as the slope of J_1/J_2 vs. $(E_{k2} - E_{k1})$.

$$T = \frac{-hc}{k_B} \frac{(E_{k2} - E_{k1})}{log\left[\frac{J_1}{J_2}\frac{E_{k2}\Delta E_2 g_2}{E_{k1}\Delta E_1 g_1}\right]} \tag{A.3}$$

The uncertainty on the temperature can be evaluated from Eq. A.4.

$$\Delta T = \frac{T^2}{\frac{hc}{k_B} \times (E_{k1} - Ek2)} \left(\frac{\Delta J}{J} + \frac{\Delta A}{A}\right) \tag{A.4}$$

where the Δ values correspond to the absolute uncertainties. For convenience, a 10% measurement error is associated to the intensity and the error on the data coming from NIST database is taken 0%.

Using Mutation++ library [116], the enthalpy corresponding to the measured temperature and the measurement pressure can be found. As the Mutation++ is a validated in-house code, its error is neglected in the enthalpy error computation. Finally the error on enthalpy results from the pressure and temperature measurements only.

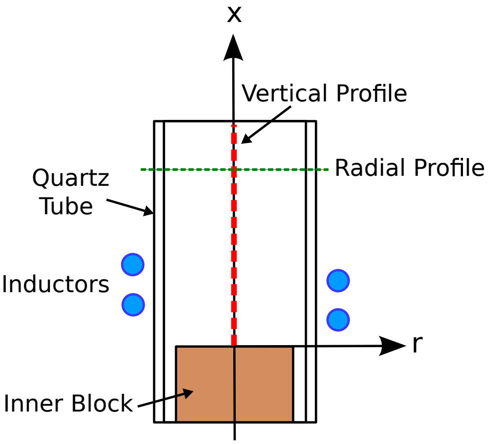

Figure A.1.: Minitorch test section and measured profiles.

A test campaign is conducted in the VKI Minitorch facility due to the simplicity of its operation. An Argon-H_2 plasma is used as test species. Different H_2 concentrations, pressures and powers are tested to monitor the radial and vertical temperature profiles of the torch as shown in Fig. A.1. The test setup consists of an Ocean Optics HR4000 spectrometer, an optical fiber with a lens to to produce a collimated beam. A traverse mechanism is used to move the beam. The alignment is made with a laser. The results along the radial profile of a test case at 2300 Pa pressure and 3694 W power is presented in Fig. A.2. It can be seen that in the jet center where the radiation intensity is strong, the error in temperature is around 1.4% and 3% in enthalpy. However, as the spectrometer is moved to the sides of the quartz tube at about r=0 and r=25 mm, the intensity is significantly reduced therefore the measurement uncertainty increases to 20% in temperature and 36% in enthalpy. For this specific case, no Abel inversion is applied to the line of sight measurements to find local values. Similar to the minitorch experiments of Laux [164], only the central part of the small homogeneous plasma jet is dominating the emission and the edges do not contribute as strong.

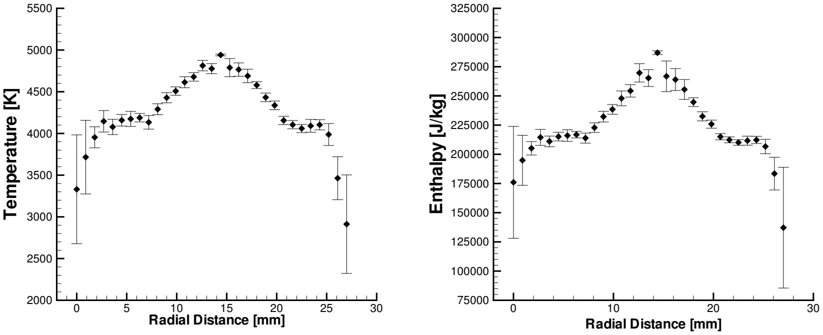

Figure A.2.: Test case with chamber pressure of 2300 Pa, Power %40 with 369 W and intensity 1.39A. Hydrogen concentration is unknown due to lack of rotameter calibration.

A.3. REDES Data

A.4. Enthalpy Measurement Comparison Data

Table A.18.: Enthalpy measurements by Optical Emission Spectroscopy tool: REDES.

Pres.	Power	$\dot{q_{std}}$	$2\sigma\,\dot{q}$	Peak Ratio	Error	Integral Ratio	Error	P$_{dyn}$	Error
Pa	kW	$\frac{kW}{m^2}$	$\frac{kW}{m^2}$	$\frac{MJ}{kg}$	$\frac{MJ}{kg}$	$\frac{MJ}{kg}$	$\frac{MJ}{kg}$	Pa	Pa
1600	120	233	4.79	37.20	1.56	24.30	1.65		
1600	160	498	3.05	36.70	0.53	35.89	0.41		
1600	200	800	3.75	37.40	0.27	38.28	0.21		
1600	250	948	7.15	37.70	0.18	38.71	0.19		
1600	300	1329	8.53	37.60	0.14	38.48	0.12		
2130	120	243	3.76	33.23	3.11	32.12	4.94	71.07	7.45
2130	150	382	5.47	33.74	0.99	34.09	0.99	103.41	6.34
2130	170	487	4.15	35.53	0.46	35.82	0.43	112.05	4.92
4160	120	224	9.25	29.81	4.60	27.83	6.16	32.46	8.38
4160	170	500	6.04	31.61	0.60	32.45	0.52	59.08	9.56
4160	190	599	4.55	33.63	0.39	34.20	0.32	69.20	12.24
5000	250	1058	11.84	35.79	0.14	37.95	0.14		
5000	300	1482	12.81	37.34	0.10	39.35	0.11		
6180	120	230	9.78	28.49	3.17	25.08	4.03	18.16	9.05
6180	150	360	5.63	31.78	0.59	28.90	0.70	26.01	8.90
6180	170	659	10.62	32.10	0.29	31.03	0.41	33.79	9.53
6180	190	785	8.30	33.35	0.33	33.23	0.31	41.22	11.29
10000	120	120	3.17	33.22	6.17	30.88	8.30		
10000	160	607	8.51	26.14	0.75	26.67	0.61	13.59	4.60
10000	200	970	8.53	31.33	0.35	31.58	0.33	23.05	5.88
10000	250	1318	13.84	35.03	0.24	35.23	0.22	38.52	8.39
10000	300	1723	14.46	36.72	0.21	37.23	0.22		
11970	130	183	3.77	32.42	5.60	28.93	7.90	6.17	3.14
11970	150	407	5.56	23.50	0.91	24.86	0.72	8.74	15.61
11970	170	583	16.39	26.43	0.34	28.11	0.31	14.71	8.40
11970	190	725	38.69	28.22	0.33	29.97	0.31	19.61	9.99
15000	120	104	5.44	35.10	7.86	33.26	10.58		
15000	170	707	7.54	26.28	0.29	27.11	0.24	8.64	6.26
15000	200	948	10.50	29.95	0.21	30.39	0.21	14.36	5.52
15000	250	1287	13.80	33.35	0.46	33.61	0.46	26.24	5.70
15000	300	1865	7.95	35.87	0.17	37.30	0.22		
17140	130	158	5.21	25.04	3.48	21.96	3.84		
17140	150	274	6.58	23.05	0.61	24.31	0.44	8.01	10.57
17140	170	638	5.74	24.27	0.32	25.63	0.22	11.00	9.90
17140	190	820	8.52	25.85	0.29	27.37	0.22	17.50	5.96
19820	190	815	17.30	25.47	0.65	26.32	0.55	13.78	3.44
19820	250	1447	7.79	30.31	0.33	31.86	0.32	24.65	6.17
19820	300	1954	12.31	33.04	0.47	35.21	0.51		
23482	150	368.72	18.37	27.11	4.71	23.77	5.42	2.54	3.85
23482	170	559.85	26.06	21.44	0.83	23.45	0.84	3.93	3.35
23482	190	783.19	17.86	26.23	0.29	27.89	0.27	6.53	4.93

Table A.19.: Comparison of enthalpy measurements with the numerical rebuilding. Data for the plot in Fig. 2.16.

Case	Hprobe	Error	Peak Ratio	Error	Integral Ratio	Error	O777	Error	Rebuilding
4a			31.78	0.59	28.90	0.70			13.33
4b	19.02	2.81	32.10	0.29	31.03	0.41	18.28	4.10	17.98
4bbis6	17.42	3.18			12.57	4.58			12.61
4bbis	20.42	3.05			18.75	4.58	18.56	4.10	15.91
4bbis4	28.24	3.08			23.65	4.64			20.22
4bbis5	28.01	3.18			19.18	4.64			23.21
4bbis7			36.72	0.21	37.23	0.22	34.03	2.90	34.43
5a	12.77	3.14	23.50	0.91	24.86	0.72			11.32
5b			26.43	0.34	28.11	0.31			17.52
5c	23.56	4.04	28.22	0.33	29.97	0.31			17.38
6a			23.05	0.61	24.31	0.44			9.42
6b	18.10	8.36	24.27	0.32	25.63	0.22			15.40
6c	23.39	10.71	25.85	0.29	27.37	0.22			19.80
7a	13.75	1.91							11.50
7b	13.09	4.79							10.92
7c	17.07	4.25	25.47	0.65	26.32	0.55	20.64	5.90	17.05
8a	14.87	12.36	27.11	4.71	23.77	5.42			11.59
8b	17.91	13.77	21.44	0.83	23.45	0.84			15.13
8c	21.12	2.59	26.23	0.29	27.89	0.27			18.58

All units are in [MJ/kg].

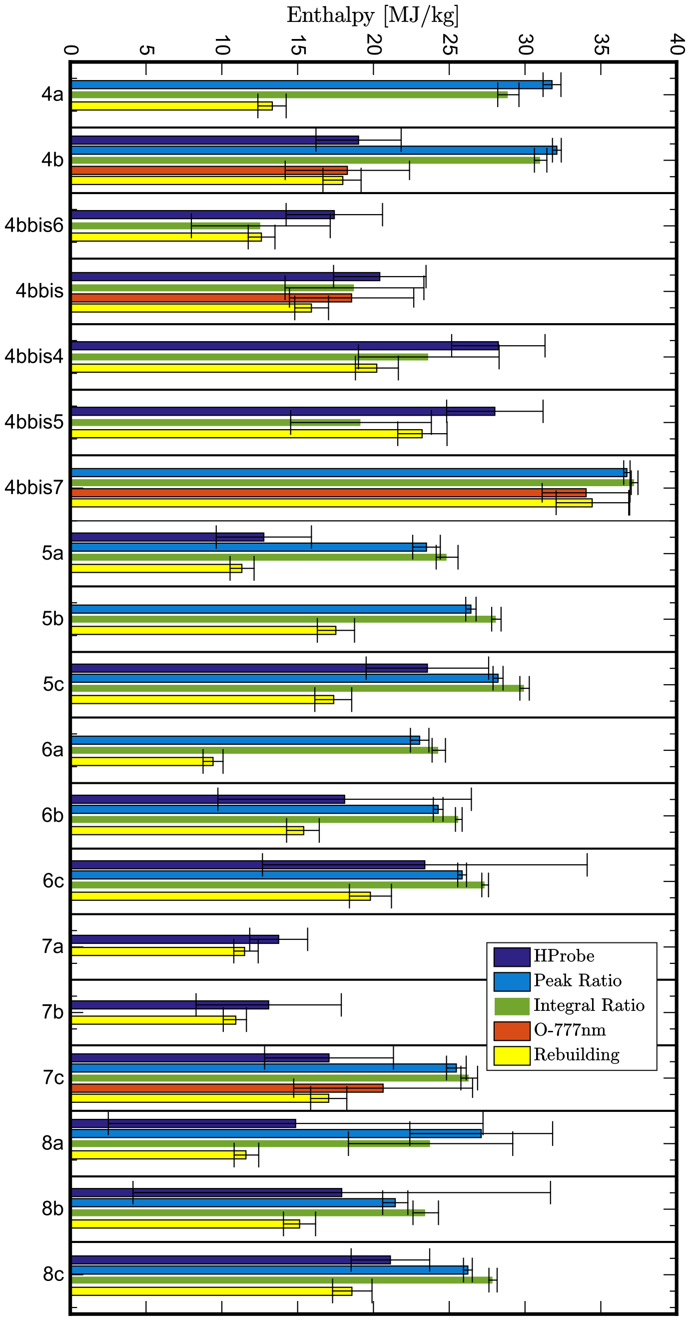

Figure A.3.: Comparison of enthalpy measurements.

Appendix B.

Testing Conditions - Experimental Data

Heat Flux Measurements

Table B.1 summarizes the testing conditions of all the experiments. The test names starting by "H" and "Da" correspond to enthalpy probe Damkohler campaigns respectively. The heat flux is measured by flat faced standard probe, and three hemispherical probes of 15, 25 and 57.5 mm radii. All the heat flux measurements are conducted with a water cooled copper calorimeter.

Table B.1.: Testing conditions for enthalpy characterization campaigns and for numerical database inputs.

						Std. Prb.		Hemi. 15mm		Hemi. 25mm		Hemi. 57.5mm	
Name	Press. Pa	Pwr kW	Effcy %	P_{dyn} Pa	2σ Pa	$\dot{q}$ kW/m^2	2σ kW/m^2	$\dot{q}$ kW/m^2	2σ kW/m^2	$\dot{q}$ kW/m^2	2σ kW/m^2	$\dot{q}$ kW/m^2	2σ kW/m^2
2a	2127	120		65.54	3.94	291.48	7.09	451.44	8.72				
2b	2127	150		92.47	4.93	464.39	11.67	625.43	11.64				
2c	2127	170		107.59	4.97	586.73	16.56	703.08	10.99				
-	2127	190		121.03	6.35	827.15	16.89	1140.91	12.23				
-	2127	220		141.87	5.97	985.97	10.67	1333.19	8.18				
3a	4156	120		28.01	10.19	275.88	9.95	362.05	13.91				
3b	4156	150		39.59	9.89	529.30	13.13	640.01	12.59				
3c	4156	170		50.76	10.10	630.67	12.37	754.95	9.70				
3d	4156	190		59.21	10.37	746.38	13.46	859.13	14.81				
-	4156	210		65.65	8.94	939.55	17.17	1342.41	14.48				
-	4156	240		82.83	8.72	1248.45	27.03	1699.05	13.37				
Da-1	5000	193	47.2					1485.84	22.76	1156.70	12.77	730.01	19.58
4d	6180	130		18.16	9.05	320.74	6.80	430.37	26.47				
4a	6180	150		25.09	8.23	462.03	10.02	582.18	17.59				
Da-4a	6180	124	39.7					598.23	46.16	463.03	21.91	177.53	22.96
H-4b	6180	164	44.7			651.73	13.20						
4b	6180	170		29.30	11.49	651.52	7.85	803.50	13.15				
Da-4b	6180	137	41.4					857.30	45.11	705.70	21.82	340.07	24.25
4c	6180	190		35.92	15.21	850.71	19.26	999.01	10.13				
-	6180	210		43.12	7.03	1035.48	15.99	1409.39	23.43				
-	6180	240		55.26	9.07	1195.71	20.58	1681.01	15.75				
-	6180	270		68.61	10.85	1319.22	36.56	1816.67	25.70				
4bbis6	10000	150		11.46	4.84	457.16	27.72	658.38	23.71				

Continued on next page

Table B.1 – *Continued from previous page*

						Std. Prb.		Hemi. 15mm		Hemi. 25mm		Hemi. 57.5mm	
Name	Press.	Pwr	Effcy	P$_{dyn}$	2σ	$\dot{q}$	2σ	$\dot{q}$	2σ	$\dot{q}$	2σ	$\dot{q}$	2σ
	Pa	kW	%	Pa	Pa	kW/m^2	kW/m^2	kW/m^2	kW/m^2	kW/m^2	kW/m^2	kW/m^2	kW/m^2
H-4bbis6	10000	146	44.4			460.50	13.29						
Da-4bbis6	10000	132	42.3					673.61	56.61	534.16	32.43	161.98	40.55
4bbis	10000	170		15.71	4.21	630.42	36.96	800.88	27.78				
H-4bbis	10000	168	47.5			642.68	16.39						
Da-4bbis	10000	139	43.4					840.19	57.97	650.36	94.83	236.36	30.77
4bbis4	10000	190		20.28	5.92	852.58	33.62	1097.22	13.23				
H-4bbis4	10000	192	49.3			858.06	24.77						
Da-4bbis4	10000	164	46.9					1119.04	91.86	915.81	32.01	434.50	39.38
Da-4bbis5	10000	175	47.8					1277.69	105.29	1112.45	66.74	531.45	35.17
4bbis5	10000	210		25.82	5.84	1030.92	24.76	1274.78	13.71				
H-4bbis5	10000	214	51.5			1039.65	12.42						
Da-F4	10000	199	50.3					1849.01	25.25	1620.51	25.25	1019.25	32.57
-	10000	230		30.90	8.40	1132.34	27.90	1549.52	19.89				
-	10000	250		38.52	8.39	1276.00	29.13	1807.54	18.18				
5d	11967	130		6.17	3.14	264.09	11.49	397.01	23.92				
5e	11967	140		7.21	4.39	292.59	18.48	403.62	35.91				
Da-5a	11967	138	43.7					604.81	172.38	472.46	86.35	26.17	50.25
H-5a	11967	140				375.59	29.44						
5a	11967	150		8.68	4.29	384.24	31.97	612.35	27.95				
5b	11967	170		10.49	3.30	646.34	19.85	845.27	20.71				
H-5b	11967	170	47.9			649.97	20.42						
Da-5b	11967	145	44.7					877.72	51.81	701.11	24.53	219.98	33.80
5c	11967	190		16.47	5.63	716.88	64.74	982.34	32.63				
H-5c	11967	175	48.2			727.43	18.73						
Da-5c	11967	154	45.7					1008.10	45.47	819.47	22.85	298.29	30.35

Continued on next page

Table B.1 – *Continued from previous page*

						Std. Prb.		Hemi. 15mm		Hemi. 25mm		Hemi. 57.5mm	
Name	Press. Pa	Pwr kW	Effcy %	P_{dyn} Pa	2σ Pa	$\dot{q}$ kW/m^2	2σ kW/m^2	$\dot{q}$ kW/m^2	2σ kW/m^2	$\dot{q}$ kW/m^2	2σ kW/m^2	$\dot{q}$ kW/m^2	2σ kW/m^2
-	11967	210		19.83	6.14	992.64	25.15	1367.72	21.00				
-	11967	230		24.63	7.54	2308.50	18.33	1733.54	28.13				
-	11967	250		31.52	6.79	1479.86	22.40	2006.47	21.23				
6abis6	15000	150		5.79	2.63	344.37	14.96	490.81	26.84				
6bbis	15000	170		8.64	6.26	640.00	18.46	800.22	21.34				
6abis3	15000	190		11.70	4.92	828.57	16.75	1059.59	18.35				
6abis5	15000	210		17.03	6.13	1043.12	23.60	1278.94	29.63				
-	15000	230		20.20	4.67	1256.55	31.56	1742.92	18.26				
-	15000	250		26.24	5.70	1499.13	19.21	1996.70	34.99				
6d	17143	130		3.49	3.09	263.69	21.29	368.11	33.94				
6e	17143	140		3.26	3.65	323.87	25.89	449.62	36.50				
6a	17143	150		4.78	4.63	306.78	26.51	446.98	35.94				
H-6a	17143	132	45.75			324.83	22.79						
Da-6a	17143	119	43.9					453.44	48.95	330.01	24.31	147.50	23.94
Da-6b	17143	142	47.05					745.26	59.45	532.44	34.20	243.54	35.77
6b	17143	170		6.68	5.18	576.74	24.34	727.33	44.19				
H-6b	17143	162	49.3			582.97	20.92						
Da-6c	17143	161	48.9					1041.32	74.76	797.45	36.78	418.57	32.13
H-6c	17143	184	51.2			813.49	19.69						
6c	17143	190		9.51	6.35	819.80	20.04	1058.11	20.11				
-	17143	210		13.33	4.84	1059.91	22.94	1448.63	18.12				
-	17143	230		17.86	5.00	1233.78	32.36	1706.34	25.49				
H-7a	19815	142	47.1			381.79	14.06						
7a	19815	150		3.88	3.19	382.91	18.70	530.71	32.46				
Da-7a	19815	131	45.55					551.00	50.13	434.91	31.84	195.86	29.16

Continued on next page

Table B.1 – *Continued from previous page*

						Std. Prb.		Hemi. 15mm		Hemi. 25mm		Hemi. 57.5mm	
Name	Press.	Pwr	Effcy	P$_{dyn}$	2σ	$\dot{q}$	2σ	$\dot{q}$	2σ	$\dot{q}$	2σ	$\dot{q}$	2σ
	Pa	kW	%	Pa	Pa	kW/m^2	kW/m^2	kW/m^2	kW/m^2	kW/m^2	kW/m^2	kW/m^2	kW/m^2
H-7b	19815	147	47.4			425.87	24.30						
7b	19815	170		7.46	4.25	428.46	25.03	608.40	34.93				
Da-7b	19815	135	45.95					611.57	62.91	481.80	28.36	221.29	29.40
Da-7c	19815	152	48.1					911.33	49.93	692.24	47.12	327.07	58.30
7c	19815	190		8.07	3.68	711.17	18.80	923.60	19.70				
H-7c	19815	184	51.75			714.68	17.56						
-	19815	210		13.46	5.54	1043.03	29.30	1403.72	21.29				
-	19815	230		18.06	7.24	1281.35	52.09	1691.85	41.63				
-	19815	250		24.65	6.17	1536.18	23.23	1998.56	14.77				
8bbis2	21415	150		3.66	3.60	356.99	23.51	545.09	29.72				
8bbis	21415	170		5.42	5.92	553.47	25.37	790.27	38.01				
8cbis	21415	190		8.96	4.49	630.68	18.48	913.93	26.46				
-	21415	210		11.85	4.49	913.39	22.07	1300.82	31.83				
-	21415	230		16.04	5.71	1260.98	13.45	1686.78	32.17				
-	21415	250		21.12	3.74	1480.23	41.14	2049.90	20.35				
Da-8a	23482	138	46.75					545.25	51.80	405.01	32.07	177.51	86.07
H-8a	23482	142	47.05			364.85	26.36						
8a	23482	150		2.54	3.85	368.72	18.37	566.34	37.75				
H-8b	23482	163	50.5			559.32	23.47						
8b	23482	170		3.93	3.35	559.85	26.06	813.50	37.38				
Da-8b	23482	150	48.1					828.28	62.08	645.70	29.88	298.45	27.10
H-8c	23482					781.97	11.40						
8c	23482	190		6.53	4.93	783.20	17.86	1096.12	39.52				
Da-8c	23482	164	49.65					1104.83	64.19	830.11	32.90	408.49	30.03
-	23482	210		10.80	4.55	888.72	58.99	1303.28	26.75				

Continued on next page

Table B.1 – *Continued from previous page*

						Std. Prb.		Hemi. 15mm		Hemi. 25mm		Hemi. 57.5mm	
Name	Press.	Pwr	Effcy	P_{dyn}	2σ	$\dot{q}$	2σ	$\dot{q}$	2σ	$\dot{q}$	2σ	$\dot{q}$	2σ
	Pa	kW	%	Pa	Pa	kW/m^2	kW/m^2	kW/m^2	kW/m^2	kW/m^2	kW/m^2	kW/m^2	kW/m^2
-	23482	230		13.51	4.43	1180.44	23.21	1550.61	16.61				
-	23482	250		18.01	5.06	1409.65	10.61	1933.44	17.26				

Appendix C.

Numerical Database

C.1. ICP Computations

Used Mesh

The classical mesh with the 25 mm radius hemispherical probe is used in this study. In addition, based on the 25 mm probe mesh three new meshes are generated for 6, 15 and 57.5 mm radii probes.

The boundary conditions are given in Fig. C.1. The reference grid with 25 mm radius hemispherical probe is depicted in Fig. C.2. Other mesh made by the author based on the reference mesh are given subsequently with probes of 57.5, 15 and 6 mm radii. The new grids are coarser because of the long computation times of ICP. Yet, the smooth inflection point regions are well captured and the resolution allows an accurate interpolation of the exact inflection point location when necessary. The velocity gradient profiles are shown in Fig. C.6 for Case 4c. The grid independence study on the presented meshes is left as future work. However it should also be noted that it is shown by Sartori [117] that the NDPs are very insensitive to grid convergence.

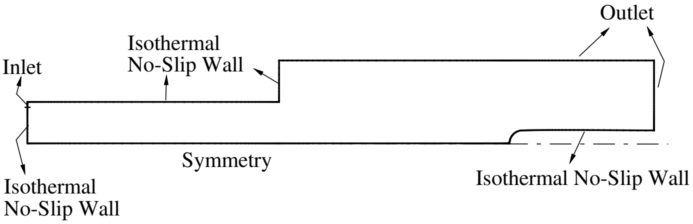

Figure C.1.: Boundary conditions.

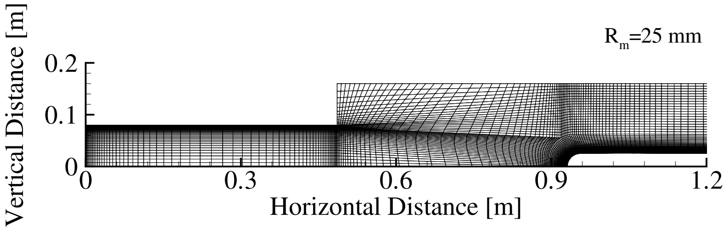

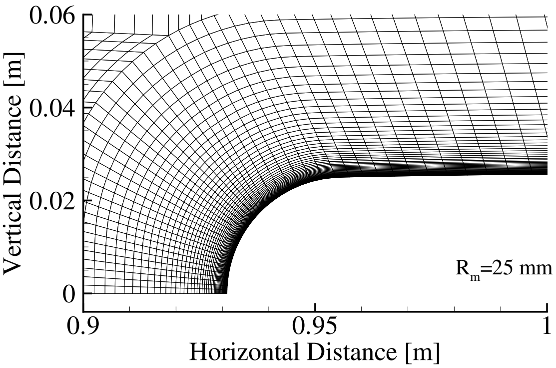

Figure C.2.: The reference grid with 25 mm hemispherical probe (top) and the region zoomed in the stagnation point region (bottom). 7830 nodes and the first grid point from the wall at the stagnation point is at 50 μn.

C.2. Non-Dimensional Parameters

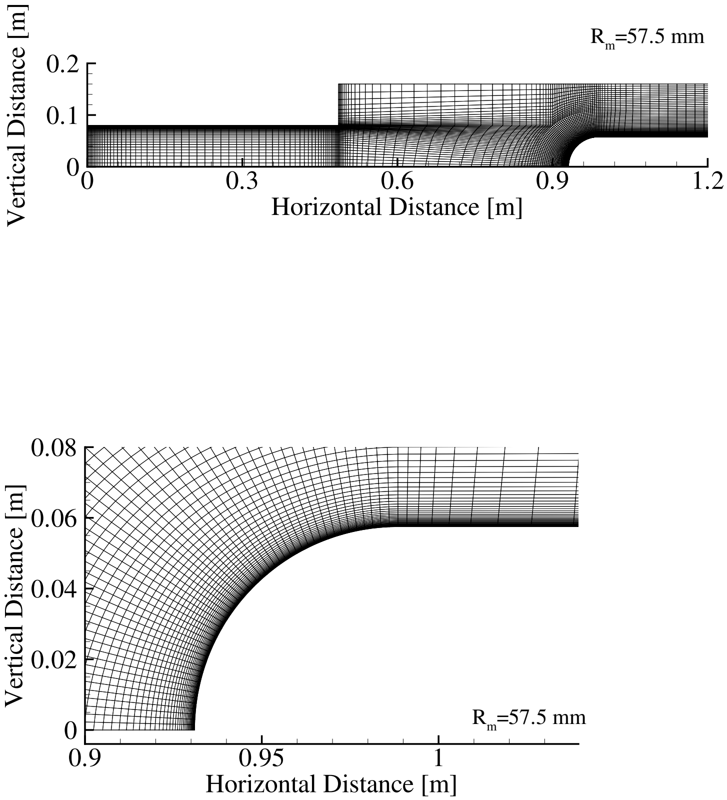

Figure C.3.: The mesh with 57.5 mm hemispherical probe (top) and the region zoomed in the stagnation point region (bottom). 6905 nodes and the first grid point from the wall at the stagnation point is at 100 μn.

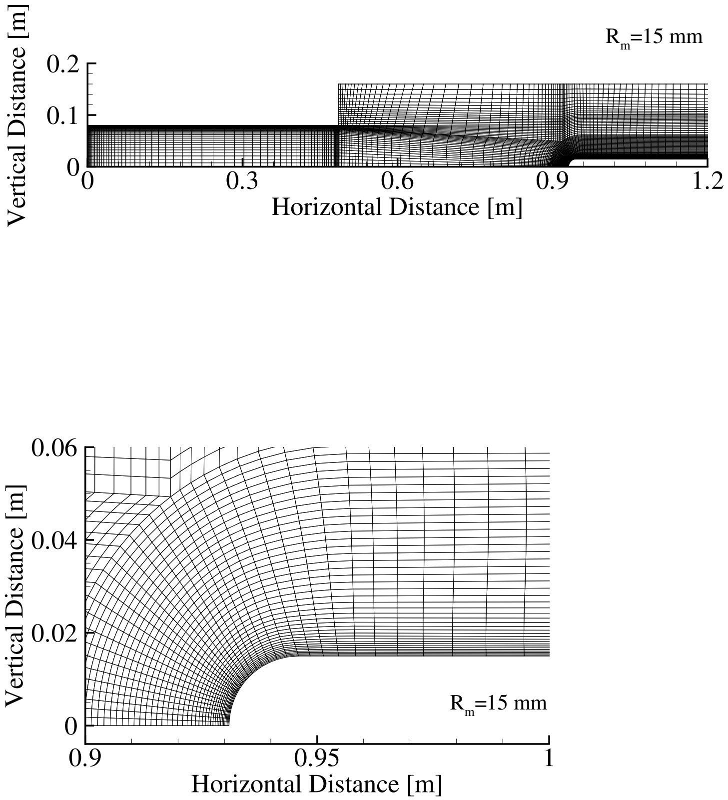

Figure C.4.: The reference grid with 15 mm hemispherical probe (top) and the region zoomed in the stagnation point region (bottom).6204 nodes and the first grid point from the wall at the stagnation point is at 200 μn.

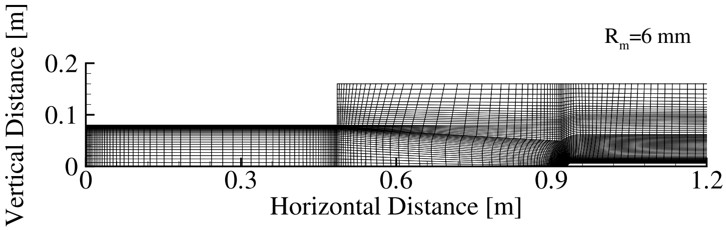

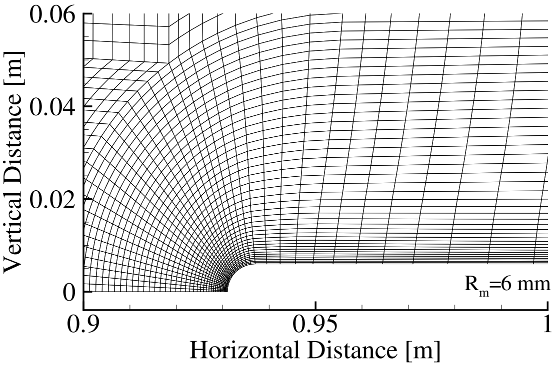

Figure C.5.: The reference grid with 6 mm hemispherical probe (top) and the region zoomed in the stagnation point region (bottom). 6420 nodes and the first grid point from the wall at the stagnation point is at 100 μn.

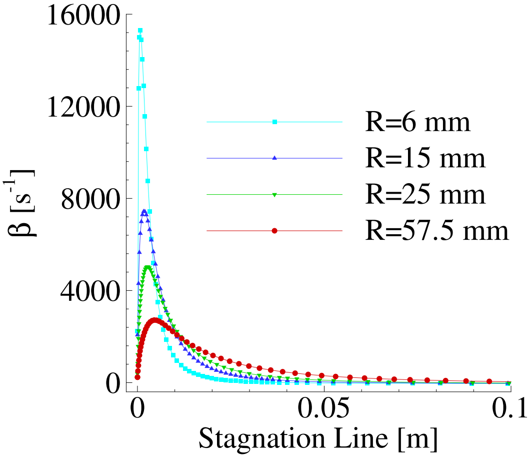

Figure C.6.: Velocity gradient profiles - the cell-centered values along the stagnation line for the reference (25 mm) and the new meshes (57.5, 15 and 6 mm). The computations are done for Case 4c.

Table C.1.: Plasmatron flow non-dimensional parameters by ICP computations. Given probe radii are all for hemispherical probes except “Std-25” refers to the ESA standard flat faced probe.

Radius mm	Mass Flow g/s	Pressure Pa	ICP Power kW	NDP1 -	NDP2 -	NDP3 -	NDP4 -	NDP5 -
6	16	4156	60	0.3456690135	0.3573651368	0.6496855121	0.3444338298	0.4251847882
6	16	4156	75	0.3342348047	0.3115829573	0.5773124175	0.2881978233	0.4066766937
6	16	4156	85	0.3342336611	0.3115872632	0.5773217474	0.2882007503	0.4066761728
6	16	4156	95	0.3249002004	0.3018008062	0.5692274839	0.2744292524	0.3982745343
6	16	6180	65	0.3482735	0.1574557187	0.3924058745	0.3025619344	0.4233862263
6	16	6180	75	0.34141324	0.1484558011	0.3756878453	0.2799142495	0.4145393335
6	16	6180	85	0.3353610667	0.1449329196	0.3716930005	0.2698951691	0.4095546431
6	16	6180	95	0.3308377667	0.1448977822	0.3753261683	0.2676179995	0.4074039935
6	16	6180	105	0.3274957667	0.1466996019	0.3831979466	0.2694205836	0.4056453384
6	16	7500	85	0.3209781174	0.2896092752	0.5496166152	0.25669999	0.3972684378
6	16	7500	95	0.3275315	0.1435683996	0.3743596294	0.2617975365	0.4056183699
6	16	10000	95	0.3221804	0.1431466831	0.3773874381	0.2556531985	0.4045920523
6	16	11967	75	0.3129152567	0.28416421	0.5464975766	0.2437129254	0.3936436737
6	16	11967	85	0.3129150386	0.2841648082	0.5464988876	0.2437132398	0.3936433882
6	16	11967	95	0.3186465167	0.1432517102	0.3804035637	0.2523187676	0.4027305921
6	16	12500	95	0.3178065333	0.1432625666	0.3811254712	0.2515116892	0.4022576466
6	16	13500	95	0.316666925	0.1431791941	0.3821161832	0.2502770744	0.4018001905
6	16	15000	95	0.31506495	0.1431766094	0.3838299601	0.2487482131	0.4012853632
6	16	16000	95	0.3140648833	0.1432844186	0.3851869331	0.2479807291	0.4011191013
6	16	17143	95	0.3129831083	0.1435068309	0.3869213177	0.2473276316	0.4015646084
6	16	18015	75	0.317425489	0.2819690831	0.5402692092	0.2439718555	0.3969613869
6	16	18015	85	0.3052875335	0.2860038249	0.5604011259	0.2372759803	0.3887543799
6	16	18015	95	0.3122064833	0.1437369907	0.3883598225	0.2469741383	0.4012092546

Continued on next page

Table C.1 – *Continued from previous page*

Radius mm	Mass Flow g/s	Pressure Pa	ICP Power kW	NDP1 -	NDP2 -	NDP3 -	NDP4 -	NDP5 -
6	16	19815	85	0.3177260333	0.141194876	0.3760638509	0.2455863891	0.403349443
6	16	19815	95	0.3107225833	0.144316073	0.3914636336	0.2465217097	0.4010659487
6	16	21415	85	0.3168006833	0.1415101319	0.3779022643	0.2452640664	0.4032926473
6	16	21415	95	0.30951505	0.1449090312	0.3943048996	0.2463509795	0.4006980686
6	16	21415	105	0.3030439	0.1494776562	0.4131335238	0.2494321959	0.3992875233
6	16	23482	85	0.3148176667	0.1422434175	0.3811298241	0.2445585839	0.4022686562
6	16	23482	95	0.3106943667	0.1449079748	0.0003954627	0.2476917722	0.4030628026
6	16	23482	105	0.301258	0.1504255771	0.4175484444	0.2491999923	0.3988111234
15	16	2127	60	0.23439056	0.545961406	1.4411480179	0.355408398	0.3924543546
15	16	4156	60	0.2330472	0.4949280599	1.3114775639	0.3215360357	0.3892733289
15	16	4156	75	0.2482490467	0.3372586592	0.8915950924	0.246207102	0.4042922583
15	16	4156	95	0.2762235533	0.37292002	0.8883415663	0.2803629905	0.3991387144
15	16	4156	105	0.2731420667	0.3714745816	0.8878156949	0.277485945	0.3987880537
15	16	4156	67.5	0.2574281667	0.3546431191	0.9088113666	0.2695850301	0.4139121711
15	16	6180	75	0.2806848667	0.3663212689	0.8650498386	0.2789009041	0.4080675312
15	16	6180	85	0.2755839067	0.3596353994	0.8588919586	0.2691723988	0.4024458732
15	16	6180	65	0.2881565333	0.3827141903	0.8880798902	0.3032037683	0.4198649239
15	16	6180	95	0.2707911333	0.3615298859	0.8692568424	0.2659992636	0.3973027638
15	16	6180	105	0.2671955333	0.366353905	0.8844726317	0.2670063476	0.3949931232
15	16	11967	75	0.2706581667	0.3580118639	0.8620279915	0.2635740106	0.4435795845
15	16	11967	85	0.2607772	0.3733313158	0.9170109254	0.2630591011	0.4121814102
15	16	11967	95	0.2557538	0.3797937879	0.9403302167	0.2626500535	0.3936748449
15	16	15000	85	0.2592282667	0.3650579221	0.8996437314	0.2558236038	0.3953306539
15	16	17143	75	0.2664381333	0.3569489712	0.8658113366	0.2586360619	0.4146375842
15	16	17143	85	0.2575965333	0.3651896431	0.903119789	0.2542845304	0.3952378933
15	16	17143	95	0.2501474667	0.3787847766	0.9483730063	0.255809432	0.3907468998

Continued on next page

Table C.1 – *Continued from previous page*

Radius	Mass Flow	Pressure	ICP Power	NDP1	NDP2	NDP3	NDP4	NDP5
mm	g/s	Pa	kW	-	-	-	-	-
15	16	19815	75	0.2647008667	0.3563174452	0.8672214772	0.2564745301	0.3987615161
15	16	19815	85	0.25584448	0.3655286204	0.907082627	0.252757103	0.3970022587
15	16	19815	95	0.2477804667	0.3800722022	0.9560122744	0.2540495788	0.3903572612
15	16	21415	85	0.2550007333	0.3659520628	0.9099663002	0.252173483	0.3963213745
15	16	21415	95	0.2464741333	0.3813233436	0.9614085353	0.2533780809	0.3890419831
15	16	23482	85	0.2537347333	0.3666863794	0.9140693541	0.2514072928	0.3942662631
15	16	23482	95	0.2447301333	0.3831571327	0.9693946366	0.2526997602	0.3867137042
15	16	23482	105	0.2390201	0.3897318074	0.991368996	0.2511242125	0.3843076088
25	16	1500	60	0.2313108021	0.5723867378	1.5166467537	0.3668160676	0.3891419177
25	16	1500	85	0.2247445811	0.4754721453	1.2990459117	0.2951890126	0.3633300137
25	16	1500	95	0.2217880025	0.4663069228	1.28831594	0.2879087128	0.3662127258
25	16	1500	105	0.220096385	0.4537881407	1.2671903983	0.2816256048	0.3699114941
25	16	1500	115	0.2215778961	0.4358980441	1.264269914	0.2786698647	0.3590120251
25	16	1500	125	0.2242054255	0.4088871472	1.191801312	0.2729638969	0.3452764012
25	16	1500	135	0.2118064627	0.4169314382	1.1044759447	0.266244351	0.3269720774
25	16	1500	145	0.2396177799	0.4044798249	1.1021452287	0.323874337	0.3683525067
25	16	1500	155	0.2314153203	0.4332756992	1.2030551937	0.3303114712	0.3771322588
25	16	1500	165	0.221136892	0.4637101484	1.3013756135	0.3339572385	0.3888527778
25	16	1500	175	0.2155904509	0.4893732198	1.3886582823	0.3440844806	0.3992207358
25	16	1500	185	0.2186271892	0.5029166307	1.4439345486	0.3639400897	0.4102706057
25	16	2127	60	0.23439056	0.545961406	1.4411480179	0.355408398	0.3924543546
25	16	2127	75	0.230971104	0.478516352	1.2853871128	0.3044868481	0.3770043207
25	16	2127	85	0.228203892	0.459434769	1.2489442769	0.2897731734	0.3747780336
25	16	3127	85	0.22658536	0.4430018482	1.2084383999	0.2773617777	0.3761969537
25	16	4156	60	0.2330472	0.4949280599	1.3114775639	0.3215360357	0.3892733289
25	16	4156	75	0.22827	0.4401786098	1.1906020566	0.2772311193	0.3775134471

Continued on next page

Table C.1 – *Continued from previous page*

Radius mm	Mass Flow g/s	Pressure Pa	ICP Power kW	NDP1 -	NDP2 -	NDP3 -	NDP4 -	NDP5 -
25	16	4156	85	0.22452328	0.4324975274	1.1856624841	0.2682214696	0.3763211093
25	16	4156	95	0.2207522	0.4299197854	1.1939405594	0.2633994768	0.3763025239
25	16	6180	75	0.22516912	0.4227169948	1.1527184044	0.2626992164	0.3767561412
25	16	6180	85	0.22036388	0.4188800433	1.1601030852	0.2546524821	0.3753791033
25	16	6180	95	0.21603848	0.4224714639	1.1866535381	0.2527074497	0.375920704
25	16	6180	65	0.2296216	0.4424655493	1.1869925512	0.2819918063	0.3815312487
25	16	6180	60	0.23137212	0.4648163452	1.2374830763	0.3003833102	0.3865278515
25	16	6180	105	0.2125676	0.4264858503	1.2132176125	0.252644083	0.3724773821
25	16	11967	75	0.21740796	0.4065565162	1.1301422048	0.2435391309	0.3743833914
25	16	11967	85	0.21171644	0.4106872908	1.1634234193	0.2392205408	0.3743354426
25	16	11967	95	0.20672616	0.4193128596	1.2080239594	0.2389784715	0.3754891236
25	16	11967	65	0.2241586	0.4163955121	1.1331303548	0.2593701223	0.3785796545
25	16	11967	70	0.2208468	0.4090579852	1.1251361423	0.2497574095	0.3760168475
25	8	11967	75	0.20889912	0.4148140111	1.1862872932	0.2382543757	0.3848336879
25	16	15000	85	0.2086922	0.4109760327	1.1743264334	0.2357629192	0.3703710076
25	16	15000	95	0.20289092	0.4230241664	1.2312274319	0.2360613071	0.3676033504
25	16	17143	75	0.2131018	0.4061761464	1.1419922224	0.2383348559	0.3737833461
25	16	17143	85	0.2067944	0.4126637842	1.185278299	0.2343978673	0.3742612754
25	16	17143	95	0.20043628	0.4258479699	1.2473069185	0.2343704126	0.3744042487
25	16	17143	65	0.22043104	0.4111535879	1.1288430299	0.2518207998	0.3772128959
25	16	18015	75	0.2124852	0.4065444337	1.1448448929	0.2378287842	0.3730017438
25	16	18015	85	0.20607692	0.4135443789	1.1900915427	0.2340073967	0.3694569576
25	16	18015	95	0.19950012	0.4270960339	1.2539278222	0.2338037008	0.3665895424
25	16	19815	75	0.21145516	0.4074366537	1.150685223	0.2371835474	0.3737099295
25	16	19815	85	0.2046756	0.4155341349	1.2002353055	0.2333776128	0.373952561
25	16	19815	95	0.1976588	0.4299178114	1.2679787583	0.2328561506	0.3737182792

Continued on next page

Table C.1 – *Continued from previous page*

Radius mm	Mass Flow g/s	Pressure Pa	ICP Power kW	NDP1 -	NDP2 -	NDP3 -	NDP4 -	NDP5 -
25	16	21415	95	0.196157168	0.4325950938	1.2805140334	0.2322578462	0.3731848122
25	16	23482	75	0.2096316	0.4105341512	1.1651376664	0.2368870908	0.3737917639
25	16	23482	85	0.20210336	0.4199924912	1.2210632079	0.2325984907	0.3734665386
25	16	23482	95	0.19496272	0.4354227264	1.2936339272	0.2322361287	0.373314328
25	16	23482	105	0.190062	0.451290027	1.3649148823	0.235001929	0.3631001435
57.5	16	4156	75	0.1755386087	0.2537591747	0.9039273834	0.2331309162	0.312484539
57.5	16	4156	85	0.1702669565	0.2581448115	0.9442170168	0.2308998272	0.315533466
57.5	16	4156	95	0.166618087	0.2649713262	0.9873902829	0.2327915985	0.3232630254
57.5	16	6180	75	0.1711707826	0.2514904829	0.9172727671	0.2259784207	0.3140852831
57.5	16	6180	85	0.1651215652	0.2580929843	0.9717956683	0.2242906881	0.3211581201
57.5	16	6180	65	0.1805483478	0.2459339195	0.8587322919	0.2336412352	0.3142788873
57.5	16	6180	95	0.1603330435	0.2668307391	1.0277598428	0.2254107245	0.3218822913
57.5	16	6180	105	0.1570295652	0.2761977784	1.0800989687	0.2281678362	0.3293325496
57.5	16	6180	120	0.1561113043	0.2811389746	1.0960149343	0.2319014873	0.3287471227
57.5	16	7500	85	0.1621384348	0.2601560802	0.9944186442	0.222028688	0.3208126233
57.5	16	8500	85	0.1599502609	0.2617361873	1.0106495907	0.2203102057	0.321249858
57.5	16	8500	95	0.1541866087	0.2726876196	1.0813136514	0.2210533066	0.3230790571
57.5	16	10000	85	0.1567478261	0.2639352585	1.0337203986	0.2175699448	0.322518184
57.5	16	10000	95	0.1518523478	0.2763148631	1.1108846733	0.2205672896	0.3259356938
57.5	16	11967	75	0.1619634783	0.2531770838	0.9693766567	0.2160261514	0.3212576402
57.5	16	11967	85	0.1537346087	0.2665496212	1.0599480626	0.2155154018	0.3241866093
57.5	16	11967	95	0.1490841739	0.2806640297	1.1467350689	0.2198313912	0.3272298342
57.5	16	12500	75	0.1612504348	0.2538601046	0.9751739852	0.2156607247	0.3213250536
57.5	16	12500	85	0.1531478261	0.2672461258	1.0665673428	0.2152883358	0.325374976
57.5	16	12500	95	0.1483756522	0.2817031524	1.1555606463	0.2195489903	0.3266362599
57.5	16	13500	95	0.1470805217	0.2836257879	1.17170962	0.2190147506	0.3269694677

Continued on next page

Table C.1 – *Continued from previous page*

Radius mm	Mass Flow g/s	Pressure Pa	ICP Power kW	NDP1 -	NDP2 -	NDP3 -	NDP4 -	NDP5 -
57.5	16	15000	95	0.1451048696	0.2866685894	1.1956991235	0.2181579378	0.3266919575
57.5	16	16000	95	0.1438201739	0.2888031108	1.2117555594	0.2176609574	0.3260138031
57.5	16	17143	75	0.1558086957	0.259780246	1.0217765091	0.2131835032	0.3235718193
57.5	16	17143	85	0.1486982609	0.2746281591	1.1239575242	0.2148884047	0.327164819
57.5	16	17143	95	0.1424215652	0.291308839	1.2298656639	0.2172094866	0.3257821067
57.5	16	18015	85	0.1479391304	0.2760638136	1.1339646651	0.2148788232	0.3267024966
57.5	16	18015	95	0.1414069565	0.2932557094	1.2434409076	0.2169488948	0.3273975857
57.5	16	19815	85	0.1464391304	0.278967323	1.1540549206	0.2148529323	0.3279781894
57.5	16	19815	95	0.1394921739	0.2972644332	1.2705346749	0.2166443419	0.3288836354
57.5	16	21415	85	0.1451833043	0.2814700401	1.171175266	0.2148321953	0.3280652435
57.5	16	23482	85	0.1437008696	0.2845733853	1.1918314184	0.2148594351	0.3278535371
57.5	16	23482	95	0.1367130435	0.3041997853	1.3173855896	0.2169608688	0.3282723833
57.5	16	23482	100	0.1355405217	0.3116934034	1.3616606676	0.2200564774	0.3309691648
Std-25	16	2127	75	0.4489064	0.3157670561	0.5182579622	0.3552767989	0.436489534
Std-25	16	2127	85	0.4426492	0.3046111611	0.5025234946	0.3370595027	0.432834987
Std-25	16	4156	75	0.4449844	0.2894580318	0.4776550858	0.3252410298	0.4377814388
Std-25	16	4156	85	0.43805128	0.2859403689	0.4747147081	0.3135249868	0.4348285052
Std-25	16	6180	75	0.440742	0.2771407608	0.4593895667	0.3093318755	0.4388504715
Std-25	16	6180	85	0.43224664	0.2759704958	0.4602673611	0.2987208828	0.4355774024
Std-25	16	6180	95	0.4230248	0.2787768974	0.4659956391	0.2954851258	0.434935569
Std-25	16	11967	75	0.4293182	0.2649838203	0.4429219622	0.2885729025	0.4369516127
Std-25	16	11967	85	0.4168548	0.2698129219	0.453903568	0.2809913211	0.4335201981
Std-25	16	11967	95	0.405922	0.2758921433	0.4656993109	0.2795115924	0.4337943651
Std-25	16	11967	65	0.437992	0.2722933833	0.45582881	0.307344984	0.4420093092
Std-25	8	11967	75	0.4089944	0.2739894927	0.4630157311	0.2795795571	0.447538566
Std-25	20	11967	75	0.4399588	0.2644207761	0.4418300321	0.2973514845	0.4339204206

Continued on next page

Table C.1 – *Continued from previous page*

Radius mm	Mass Flow g/s	Pressure Pa	ICP Power kW	NDP1 -	NDP2 -	NDP3 -	NDP4 -	NDP5 -
Std-25	16	17143	75	0.421104	0.2646087873	0.4442990129	0.2824185524	0.4363545683
Std-25	16	17143	85	0.40771808	0.2706732818	0.4575501375	0.2753420872	0.4344226162
Std-25	16	17143	95	0.3966432	0.2834672139	0.4813411274	0.2801675118	0.434427637
Std-25	16	19815	75	0.4175792	0.2655099176	0.4465991423	0.280868427	0.4360661491
Std-25	16	19815	85	0.4046832	0.2719497571	0.4605450306	0.2745848862	0.4345091556
Std-25	16	19815	95	0.3925296	0.2805224565	0.4774392156	0.2740797916	0.434623623
Std-25	16	23482	75	0.4136128	0.2676194114	0.4509915426	0.2803070958	0.4357521326
Std-25	16	23482	85	0.40105248	0.2838844543	0.4651293366	0.274238805	0.4351913925
Std-25	16	23482	95	0.3876132	0.2838062609	0.4842116787	0.2733824153	0.4344789454

Appendix D.

Ablation Campaign - Emissivity Measurements

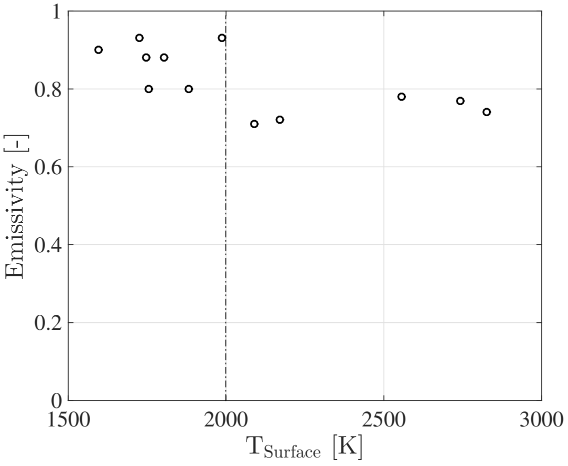

Figure D.1.: Steady state surface temperatures and emissivities.

Table D.1.: Steady state emissivity values computed from Eq. (3.21).

Test Name	Emissivity [-]
3Rep	0.88208
5	0.71632
7Rep	0.74448
9Rep	0.79607
14Rep	0.78472
17	0.78432
18RepRep	0.77093
19	0.93323
20	0.90006

Bibliography

[1] Francesco Panerai. *Aerothermochemistry Characterization of Thermal Protection Systems.* PhD thesis, Universite degli Studi di Perugia and von Karman Institute for Fluid Dynamics, 2012. 3, 23, 28, 29, 34, 48, 96, 112

[2] J. T. Howe. Hypervelocity atmospheric flight: Real gas flow fields. Technical Report Technical Momerandum 101055, NASA Ames Research Center, 1989. 3

[3] G. A. Bird. *Gas Dynamics and the direct simulation of gas flows.* Oxford University Press, 1994. 4, 111

[4] G. G. Chernyi and R. F. Probstein. *Introduction to Hypersonic Flow.* Academic Press, 1961. 2

[5] John J. Bertin. *Hypersonic Aerothermodynamics.* AIAA Education Series, 1994. 2, 3, 4

[6] Ali Bulent Cambel, Donald P. Duclos, and Thomas P. Anderson. *Real Gases.* Academic Press, 1963. 2

[7] J.D. Anderson. *Hypersonic and High Temperature Gas Dynamics.* McGraw-Hill, 1989. 2, 9, 19, 25, 30, 35

[8] Walter G. Vincenti and Charles H. Kruger Jr. *Introduction to Physical Gas Dynamics.* Krieger, 1967.

[9] Chul Park. *Nonequilibrium Hypersonic Aerothermodynamics.* John Wiley and Sons, 1990. 4

[10] Chul Park. Assessment of two-temperature kinetic model for ionizing air. In *AIAA Paper 82-1574*, Honolulu, HI, June 1982.

[11] J. H. Lee. Basic governing equations for the flight regimes of aeroassisted orbit transfer vehicles. In AIAA New York, editor, *Thermal Design of Aeroassisted Orbit Transfer Vehicles, Progress in Aeronautics and Astronautics*, volume 96, pages 3–53, 1985.

[12] Olivier Chazot. Gas-surface interaction lectures. VKI Research Master Course Notes, 2015. 5

[13] Georges Duffa. *Ablative Thermal Protection Systems Modeling.* AIAA Education Series, 2013. 5, 7

[14] B. Laub and E. Venkatapathy. Thermal protection system technology and facility needs for demanding future planetary missions. In *Proceedings of the International Workshop Planetary Probe Atmospheric Entry and Descent Trajectory Analysis and Science*, Lisbon, Portugal, 2003. 5, 7

[15] William H. Dorrance. *Viscous Hypersonic Flow.* McGraw-Hill, 1962. 6

[16] I. Sakraker and C. O. Asma. Experimental investigation of passive/active oxidation behavior of sic based ceramic thermal protection materials exposed to high enthalpy plasma. *Journal of the European Ceramic Society*, 33(2):351–359, 2013. 6

[17] Toshiyuki Suzuki, Kazuhisa Fujita, and Takeharu Sakai. Graphite nitridation in lower surface temperature regime. In *47th AIAA Aerospace Sciences Meeting Including The New Horizons Forum and Aerospace Exposition, Orlando, Florida*, number AIAA-2009-260, 2009. 7

[18] B. Helber, I. Sakraker, D. Lequang, and O. Chazot. Absolute radiation measurements of ablation products in the boundary layer of an composite ablator. In *8th European Symposium on Aerothermodynamics for Space Vehicles*, Lisbon, Portugal, 2015. 7, 105

[19] F.S. Milos and Y.K. Chen. Comprehensive model for multicomponent ablation thermochemistry. *AIAA-97-0141*, 1997. 7

[20] Alexandre Martin. Preliminary numerical and experimental analysis of the spallation phenomenon. In *8th European Symposium on Aerothermodynamics for Space Vehicles*, Lisbon, Portugal, 2015. 7

[21] Y.K. Chen and F.S. Milos. Ablation and thermal response program for spacecraft heatshield analysis. *Journal of Spacecraft and Rockets*, 36(3):475–483, May-June 1999. 7

[22] Jean Lachaud, T. E. Magin, I. Cozmuta, and N. N. Mansour. A short review of ablative material response models and simulation tools. Technical Report ARC-E-DAA-TN3517, NASA Ames Research Center, 2011. 7, 78

[23] Alessandro Turchi. *A gas-surface interaction model for the numerical study of rocket nozzle flows over pyrolyzing ablative material.* PhD thesis, Universita di Roma La Sapienza, 2013. 7, 80, 81

[24] Y.K. Chen and F.S. Milos. Navier-stokes solutions with finite rate ablation for planetary earth reentries. *Journal of Spacecraft and Rockets*, 42(6):961–970, November-December 2005. 7

[25] D. Bianchi and F. Nasuti. Carbon-carbon nozzle erosion and shape change in full-scale solid-rocket motors. *Journal of Propulsion and Power*, 28(4):820–830, 2012. 7

[26] Antonio Viviani and Giuseppe Pezzella. *Aerodynamic and Aerothermodynamic Analysis of Space Mission Vehicles.* ISBN 978-3-319-13926-5. Springer, March 2015. 8

[27] D.L. Cauchon. Radiative heating results from the fire ii flight experiment at a re-entry velocity of 11.4 km/s. Technical Memorandum NASA-TM-X-1402, NASA, July 1967. 9

[28] R.L. Wright and E.V. Zoby. Flight measurements of boundary-layer transition on a 5 degree half-angle cone at a free-stream mach number of 20 (reentry f). Technical Memorandum NASA-TM-X-2253, NASA, May 1971. 9

[29] Al Seiff, D.E.Reese, S.C. Sommer, D.B. Kirk, E.E. Whiting, and H.B. Niemann. Paet, an entry probe experiment in earth's atmosphere. *ICARUS*, 18:pp 525–563, April 1973. 10

[30] G. Lozino-Lozinsky and V. Timoshenko. Lessons learned from the bor flight campaign. In *Proceedings of the 3rd European Symposium on Aerothermodynamics for space vehicles*, Noordwijk, The Netherlands, 24-26 November 1998. ESA ESTEC. 10

[31] Y. Yamamoto and M. Yoshioka. Cfd and fem coupling analysis of orex aerothermodynamic flight data. In *30th Thermophysics Conference*, number AIAA-1995-2087, San Diego CA, June 1995. 10

[32] G. Schmitt and R. Kasper. Mirka micro re-entry capsule. In *IAF-94-V.2.532, 45th Intl Astronautical Congress*, Jerusalem, Israel, October 1994. 10

[33] P. Tran and J. Soler. Atmospheric reentry demonstrator post flight analysis: Aerothermal environment. In *Proceedings of the 2nd Intl Symposium on Atmospheric Reentry Vehicles.* Arcachon, France, March 2001. 10

[34] J.M.A. Longo, Th. Eggers, A. Gülhan, J. Turner, and H. Weihs. Designing flight experiments for hypersonic flow physics. In *NATO RTO AVT VKI Lecture Series "Flight Experiments for Hypersonic Vehicle Development"*, Rhode Saint Genese, Belgium, October 2005. 10

[35] M. S. Murbach et al. Summary of soarex 6 and 7 flight experiments. In *International Planetary Probe Workshop 7*, Barcelona, Spain, 2010. 10

[36] Thom Stone, Marcus Murbach, Richard Alema, and Ray Gilstrap. Soarex-8 suborbital experiments 2015-a new paradigm for small spacecraft communication. In *IEEE Aerospace Conference*, 2015. 10

[37] A.D. Gardner, Klaus Hannemann, A. Pauli, and Johan Steelant. Ground testing of the hyshot supersonic combustion flight experiment in heg. *Shock Waves, Springer Berlin Heidelberg*, pages 329–334, 2005. 10

[38] Hendrik Weihs, J. Longo, and J. Turner. The sharp edge flight experiment shefex ii, a mission overview and status. In *Proceedings of the 15th AIAA International Space Planes and Hypersonic Systems and Technologies Conference*, 2008. 10

[39] Karen T. Berger et al. Aerothermodynamic testing and boundary-layer trip sizing of the hifire flight 1 vehicle. *Journal of Spacecraft and Rockets*, 45(6):1117–1124, 2008. 11

[40] Kevin R. Jackson, Mark R. Gruber, and Todd F. Barhorst. The hifire flight 2 experiment: An overview and status update. In *45th AIAA/ASME/SAE/ASEE Joint Propulsion Conference & Exhibit*, number AIAA 2009-5029, August 2009.

[41] Thomas R. Smith, Kevin G. Bowcutt, John R. Selmon, Luis Miranda, Brandin Northrop, Ron Mairs, , Eric R. Unger, Kei Y. Lau, Todd Silvester, Hans Alesi, Allan Paull, Ross Paull, and Douglas J. Dolvin. Hifire 4: A low-cost aerodynamics, stability, and control hypersonic flight experiment. In *17th AIAA International Space Planes and Hypersonic Systems and Technologies Conference*, number AIAA 2011-2275, San Francisco, California, April 2011.

[42] R.L. Kimmel, D. Adamczak, and T.J. Juliano. Hifire-5 flight test preliminary results. In *51st AIAA Aerospace Sciences Meeting including the New Horizons Forum and Aerospace Exposition*, number AIAA 2013-0377, January 2013. 11

[43] Suzanne Smrekar et. al. Deep space 2: The mars microprobe mission. *Journal of Geophysical Research*, 104(27):13–27, 1999. 11

[44] Michael A. Weaver and H. AilorWilliam. Reentry breakup recorder: Concept, testing, moving forward. In *AIAA Space Conference and Exposition*, pages 11–13, 2012. 11

[45] Jean-Pierre Baumann, Adam S. Pagan, and Georg Herdrich. Aerothermodynamic re-entry analysis of the cubesat-sized entry vehicle mirka2. In *8th European Symposium on Aerothermodynamics for Space Vehicles*, Lisbon, Portugal, March 2015. 11

[46] David A. Spencer, Nicole Bauer, Jessica R. Juneau, Jenny Kelly, Amit Mandalia, Matthew Nehrenz, Allison Willingham, Justin McClellan, and James Sisco. Small probes for orbital return of experiments. In *50th AIAA Aerospace Sciences Meeting including the New Horizons Forum and Aerospace Exposition*, number AIAA-2012-0213, Nashville, Tennessee, January 2012. 11

[47] Bryan Chan, Nicole Bauer, Jessica R. Juneau, Stephanie Stout, Kento Masuyama, and Dave Spencer. Recovery of in-space cubesat experiments (rice) project. In *7th International Planetary Probe Workshop*, Barcelona, Spain, June 2010. 11

[48] N. Cheatwood, M. Wright, M. Munk, E. Martinez, and J. Herath. Medli: From instrumentation concept to flight hardware. 7th International Planetary Probe Workshop, Barcelona, Spain, June 2010. 11, 136, 142

[49] P. Agrawal, A. Cassell, N. Mangini, K. Peterson, D. Prabhu, K. Skokova, G. Swanson, D. Empey, S. Gorbunov, A. Howard, J. Arnold, and E. Venkatapathy. Sprite: A tps test bed for ground and flight. In *5th Ablation Workshop, U Kentucky, Lexington*, Feb-Mar 2012. 11

[50] Timothy Cichan, Scott D. Norris, and Paul Marshall. Orion: Eft-1 flight test results and em-1/2 status read more: http://arc.aiaa.org/doi/abs/10.2514/6.2015-4414. In *AIAA SPACE 2015 Conference and Exposition*, number AIAA-2015-4414, 2015. 12

[51] G. Tumino, E. Angelino, F. Leleu, R. Angelini, P. Plotard, and J. Sommer. The ixv project. the esa re-entry system and technologies demonstrator paving the way to european autonomous space transportation and exploration endeavours. In *IAC-08-D2.6.01*, Glasgow, Scotland, 29 September - 3 October 2008. 12

[52] Isil Sakraker, Ertan Umit, Thorsten Scholz, Paride Testani, Gilles Baillet, and Vincent Van der Haegen. Qarman: An atmospheric entry experiment on cubesat platform. In *8th European Symposium on Aerothermodynamics for space vehicles*, Lisbon, Portugal, March 2015. 12

[53] CalPoly. Cubesat design specification, revision 13, the cubesat program, issued 20.01.2014. 12

[54] Qb50 project. `www.qb50.eu`. last accessed: 10.06.2015. 12, 137

[55] J. M. Bouilly, G. Pinaud, J. Carvalho, and A. Coelho. Aerofast: Development of innovative thermal protections. In *7th European Workshop on TPS & Hot Structures*, Noordwijk (NL), April 8-10 2013. 13

[56] Heat transfer near the forward stagnation point of a body of revolution. Merwin sibulkin. *Journal of the Aeronautical Sciences*, 19(8):570–571, 1952. 18

[57] Irving Korobkin. Local flow conditions recovery factors and heat-transfer coefficients on the nose of a hemisphere-cylinder at a mach number of 2.8. Aeroballistics research-175, U.S. Naval Ordnance Lab White Oak Md, 1953. 18

[58] G. R. Eber. Recent investigation of temperature recovery and heat transmission on cones and cylinders in axial flow in the nol aeroballistics wind tunnel. *Journal of the Aeronautical Sciences*, 19(1):1–6, 14, 1952. 18

[59] Howard A. Stine and Kent Wanlass. Theoretical and experimental investigation of aerodynamic-heating and isothermal heat-transfer parameters on a hemispherical nose with laminar boundary layer at supersonic mach numbers. Technical Report TN-3344, National Advisory Committee for Aeronautics, 1954. 18

[60] Lester Lees. Laminar heat transfer over blunt nosed bodies at hypersonic flight speeds. *Jet Propulsion*, 26(4):259–269, 274, 1956. 18, 19, 20, 24

[61] Clarence B. Cohen and Eli Reshotko. Similar solutions for the compressible laminar boundary layer with heat transfer and pressure gradient. Technical Report NACA-TN-3325, National Advisory Committee for Aeronautics, 1955. 18

[62] Wallace D. Hayes. On laminar boundary layers with heat transfer. *Journal of Jet Propulsion*, 26(4):270–274, 1956. 18

[63] Davis H. Crawford and William D. McCauley. Investigation of the laminar aerodynamic heat-transfer characteristics of a hemisphere-cylinder in the langley 11-inch hypersonic tunnel at a mach number of 6.8. Technical Report NACA Report 1323, National Advisory Committee for Aeronautics, 1957. 18, 20, 24

[64] James A. Fay and Frederick R. Riddell. Theory of stagnation point heat transfer in dissociated air. In *VKI, An Introduction to Hypersonic Aerodynamics 13 p(SEE N 90-13334 05-02)*. 1958. 18, 19, 21, 24

[65] Peter H. Rose and W. I. Stark. Stagnation point heat-transfer measurements in dissociated air. *Journal of the Aeronautical Sciences*, 25(2):86–97, 1958. 19, 24, 58

[66] J.C. Boison and A.C. Curtiss. An experimental investigation of blunt body stagnation point velocity gradient. *ARS Journal*, 29(2):130–135, 1959. 19, 25, 27, 56

[67] William E. Stoney Jr. Aerodynamic heating of blunt nose shapes at mach numbers up to 14. Technical Report NACA RM L58E05a, National Advisory Committee for Aeronautics, 1958. 19

[68] R. Goulard. On catalytic recombination rates in hypersonic stagnation heat transfer. *Jet Propulsion*, 28(11):737–745, 1958. 19, 21, 24

[69] Ivan E. Beckwith and Nathaniel B. Cohen. Application of similar solutions to calculation of laminar heat transfer on bodies with yaw and large pressure gradient in high-speed flow. Technical Report TN D-625, National Aeronautics and Space Administration, 1961. 19, 20

[70] W. E. Moeckel and Kenenth C. Weston. Composition and thermodynamic properties of air in chemical equilibrium. Technical Report TN-4265, National Advisory Committee for Aeronautics, 1958. 19

[71] James A. Fay and Nelson H. Kemp. Theory of stagnation-point heat transfer in a partially ionized diatomic gas. *AIAA Journal*, 1(12):2741–2751, 1963. 20, 24

[72] A. Pallone and W. Van Tassell. Stagnation point heat transfer for air in the ionization regime. *ARS Journal*, 32:436–437, 1962. 20

[73] S. M. Scala and W. R. Warren. Hypervelocity stagnation point heat transfer. *ARS Journal*, 32:101–102, 1962. 20

[74] W. L. Bade. Stagnation-point heat transfer in a high temperature inert gas. *Phys. Fluids*, 5(2):150–154, 1962. 20

[75] T. E. Horton and T. L. Babineaux. Influence of atmospheric composition on hypersonic stagnation-point convective heating. *AIAA Journal*, 5(1):36–43, 1967. 20, 58

[76] R. M. Nerem, C. J. Morgan, and B. C. Graber. Hypervelocity stagnation point heat transfer in a carbon dioxide atmosphere. *AIAA Journal*, 1(9):2173–2175, 1963. 20

[77] James P. Reilly. Stagnation-point heating in ionized monoatomic gases. *The Physics of Fluids*, 7(12):1905–1912, 1964. 20

[78] Ronald. B. Pope. Stagnation-point heat transfer in arc-heated helium and argon. *AIAA Journal*, 7(6):1159–1161, 1969. 20

[79] P. H. Rose and J. O. Stankevics. Stagnation-point heat transfer measurements in partially ionized air. *AIAA Journal*, 1(12):2752–2763, 1963. 20, 58

[80] D. J. Collins and T. E. Horton. Experimental convective heat-transfer measurements. *AIAA Journal*, 2(11):2046–2047, 1964. 20

[81] Ernest V. Zoby. Empirical stagnation point heat transfer relation in several gas mixtures at high enthalpy levels. Technical Report TN D-4799, NASA Langley, 1968. 20, 24, 25, 55, 58

[82] Kenneth. K. Yoshikawa. Linearized theory of stagnation point heat and mass transfer at hypersonic speeds. Technical Report TN D-5246, National Aeronautics and Space Administration, 1969. 20

[83] Kenneth Sutton and Randolph A. Graves Jr. "a general stagnation-point convective heating equation for arbitrary gas mixtures. Technical Report NASA TR R-376, National Aeronautics and Space Administration, 1971. 20, 21, 24

[84] Paul F. Holloway and James C. Dunavant. Heat-transfer and pressure distributions at mach numbers of 6.0 and 9.6 over two reentry configurations for the five-stage scout vehicle. Technical Report D- 1790, National Aeronautics and Space Administration, 1963. 20

[85] P. Calvin Stainback. Convective and equilibrium radiation heat-transfer predictions for project fire reentry vehicle. Technical Report NASA TN D-2867, National Aeronautics and Space Administration, 1965. 21

[86] Michael E. Tauber. A review of high-speed convective heat-transfer computation methods. Technical Report TN-2914, National Aeronautics and Space Administration, Ames Research Center, 1989. 21

[87] Aaron M. Brandis and C. O. Johnston. Characterization of stagnation-point heat flux for earth entry. In *45th Plasmadynamics and Lasers Conference*, number AIAA 2014-2374, Atlanta, GA, USA, June 2014. AIAA Aviation. 21

[88] A.F. Kolesnikov. Extrapolation from high enthalpy tests to flight based on the concept of local heat transfer simulation. RTO AVT Course on "Measurement Techniques for High Enthalpy and Plasma Flows", Rhode-Saint-Genese, Belgium, October 1999. 22, 27

[89] P. Barbante. *Accurate and Efficient Modelling of High Temperature Nonequilibrium Air Flows.* PhD thesis, Universite Libre de Bruxelles and von Karman Institute for Fluid Dynamics, 2001. 23, 30, 33, 34, 52, 59, 61, 90, 91

[90] P. F. Barbante and Olivier Chazot. Flight extrapolation of plasma wind tunnel stagnation region flowfield. *Journal of thermophysics and heat transfer*, 20.3:493–499, 2006. 23

[91] A. Guelhan, B. Esser, A. Del Vecchio, S. Loehle, N. Sauvage, O. Chazot, and C.O. Asma. Comparative heat flux measurements on standard models in plasma facilities. In *13th International Space Planes*

Conference, number AIAA 2005-3324, Capua, Italy, June 2005. 23, 28, 35

[92] M. S. Holden. Studies of potential fluid-mechanical mechanisms for enhanced stagnation-region heating. In *Thermophysical Aspects of Re-Entry Flows, American Institute of Aeronautics and Astronautics*, pages 281–309, New York, 1986. 24

[93] Herbert Olivier. Influence of the velocity gradient on the stagnation point heating in hypersonic flow. *Shock Waves*, 5:205–216, 1995. 24, 26

[94] Lester Lees. Recent developments in hypersonics. ARS Semi-Annual Meeting, San Francisco, California, June 1957. 24

[95] W. T. Obryant and R. M. Machell. An experimental investigation of the flow over blunt-nosed cones at a mach number of 5.8. *Journal of the Aeronautical Sciences*, 23:1054–1055, 1956. 24

[96] L.L. Trimmer and E.L. Clark. Stagnation-point velocity gradients for spherical segments in hypersonic flow. *AIAA Journal*, 7(10), 1969. 25

[97] D. G. Fletcher and M. Playez. Characterization of supersonic and subsonic plasma flows. In *25th AIAA Aerodynamic Measurement Technology and Ground Testing Conference*, number AIAA-2006-3294, San Francisco, California, 5-8 June 2006. 25

[98] Frank M. White. *Viscous fluid flow*, volume 3. New York, McGraw-Hill, 1991. 25

[99] R. W. Truitt. *Fundamentals of Aerodynamic Heating.* The Ronald Press Company, 1960. 25

[100] D. R. Topham. An empirical formula for stagnation point velocity gradient for spheres and circular cylinders in hypersonc flows. *Journal of Royal Aeronautics Society*, 60:407–408, 1965. 25

[101] Ernest V. Zoby and Edward M. Sullivan. Effects of corner radius on stagnation-point velocity gradients on blunt axisymmetric bodies. Technical Report NASA-TM-X-1067, NASA, 1965. 25

[102] James C. Ellison. Experimental stagnation point velocity gradients and heat transfer coefficients for a family of blunt bodies at mach 8 and angles of attack. Technical Report TN D-5121, NASA Langley, 1969. 25

[103] L. Howarth. The boundary layer in three dimensional flow, part ii, the flow near stagnation point. *Phil. Mag.*, 42(335):1433–1440, 1951. 26

[104] E. Reshotko. Heat transfer to a general three dimensional stagnation point. *Jet Propulsion*, 28:58–60, 1958. 26

[105] Paul A. Libby. Heat and mass transfer at a general three-dimensional stagnation point. *AIAA Journal*, 5(3):507–517, March 1967. 26

[106] Fred R. DeJarnette and F. McNeil Cheatwood. A review of some approximate methods used in aerodynamic heating analyses. *Journal of Thermophysics*, 1(1):5–11, January 1987. 26

[107] V. Lunev. *Hypersonic Aerodynamics*. Mashinostroyeniye (in Russian), Moscow, Russia, 1975. 26

[108] W.D. Hayes and R.F. Probstein. *Hypersonic flow theory*. Academic press, 1959. 26

[109] B. Bottin. *Aerothermodynamic Model of an Inductively-Coupled Plasma Wind Tunnel*. PhD thesis, Universite de Liege and von Karman Institute for Fluid Dynamics, Belgium, October 1999. 27

[110] H. Schlichting and K. Gersten. *Boundary Layer Theory*. Springer, 7 edition, 1979. 30, 52, 53, 59

[111] A.F. Kolesnikov. An efficient modeling stagnation point heat transfer for subsonic aerothermal test conditions. Technical Report TN-200, von Karman Institute For Fluid Dynamics, January 2001. 30

[112] Jan Thoemel. Local heat transfer simulation of air and co2. Master's thesis, von Karman Institute For Fluid Dynamics, 2005. 30

[113] Gerard Degrez, Paolo Barbante, Marta de la Llave, Thierry Magin, and Olivier Chazot. Determination of the catalytic properties of tps materials in the vki icp facilities. In *European Congress on Computational Methods in Applied Sciences and Engineering*, Swansea, Wales, UK, September 2001. ECCOMAS Computational Fluid Dynamics Conference 2001. 31

[114] H. W. Krassilchikoff. Procedures for the determination of the cold copper catalycity. Master's thesis, von Karman Institute for Fluid Dynamics, 2006. VKI-PR2006-18. 31

[115] G. Degrez, D.P. Vanden Abeele, P. Barbante, and B. Bottin. Numerical simulation of inductively coupled plasma flows under chemical non-equilibrium. *International Journal of Numerical Methods for Heat & Fluid Flow*, 14(4):538–558, 2004. 31, 34

[116] J. B. Scoggins and Thierry Magin. Development of mutation++: Multicomponent thermodynamics and transport properties for ionized gases library in c++. In *11th AIAA/ASME Joint Thermophysics*

and Heat Transfer Conference,16-20 June, number AIAA 2014-2966, Atlanta, GA, 2014. 31, 37, 42, 73, 192

[117] E. Sartori. Numerical simulation of chemical reactive flows in inductively coupled plasma windtunnels. Technical Report VKI-SR-2010-01, von Karman Institute For Fluid Dynamics, October 2009. 32, 203

[118] C. Park. Radiation enhancement by nonequilibrium in earth's atmosphere. *Journal of Spacecraft and Rockets*, 22:22–36, 1985. 33, 51, 53

[119] B. Bottin, D.P. Vanden Abeele, M. Carbonaro, G. Degrez, and G.S.R. Sarma. Thermodynamic and transport properties for inductively plasma modeling. *Journal of Thermophysics and Heat Transfer*, 13(3):343–350, 1999. 33

[120] Nadege Villedieu, Francesco Panerai, Olivier Chazot, and Thierry Magin. Uncertainty quantification for gas-surface interaction in plasmatron facility. In *7th European Symposium on Aerothermodynamics, ESA SP-692*, Brugge, Belgium, 9-12 May 2011. 34, 72, 73

[121] A. Nawaz, D.M. Driver, I. Terrazas-Salinas, and S. Sepka. Surface catalysis and oxidation on stagnation point heat flux measurements in high enthalpy arc jets. In *44th AIAA Thermophysics Conference*, San Diego, CA, USA, 24-27 June 2013. 35

[122] Thomas Rees. Development of an enthalpy probe for the plasmatron. Technical Report VKI SR 2014-44, von Karman Institute For Fluid Dynamics, 2014. 37

[123] M. Barker. On the use of very small pitot-tubes for measuring wind velocity. In *Proceedings of the Royal Society of London. Series A, Containing Papers of a Mathematical and Physical Character (1905-1934)*, volume 101, pages 435–445, 1922. 38

[124] J. J. Balmer. Notiz uber die spectrallinien des wasserstoffs. *Annalen der Physik*, 261(5):80–87, 1885. 42, 191

[125] D. G. Fletcher. Nonintrusive diagnostic strategies for arcjet stream characterization. RTO AVT Course on Measurement Techniques for High Enthalpy and Plasma Flows, Rhode-Saint-Genese, Belgium, October 1999. 43

[126] Alessio Cipullo. *Ground Testing Methodologies Improvement in Plasma Wind Tunnels Using Optical Diagnostics.* PhD thesis, Seconda Universite degli Studi di Napoli and von Karman Institute for Fluid Dynamics, 2012. 43, 44

[127] Cristophe O. Laux. Radiation and nonequilibrium collisional-radiative models. Technical report, von Karman Institute for Fluid Dynamics, 2002. 43, 45, 73

[128] D. Le Quang Huy. *Spectroscopic Measurements of Sub- and Supersonic Plasma Flows for the Investigation of Atmospheric Re-entry Shock Layer Radiation.* PhD thesis, Universite Blaise Pascal and von Karman Institute for Fluid Dynamics, 2014. 45, 47

[129] Jose Pedro Pinto Leite. Assessment of ground testing conditions for in-flight experiment development. Master's thesis, PR2013-08, von Karman Institute for Fluid Dynamics, Rhode-Saint-Genese, 2013. 45

[130] B. Bachmann, R. Kozakov, G. Gott, K Ekkert, J-P. Bachmann, J.L. Marques, H. Schopp, D. Uhrlandt, and J. Schein. High-speed three-dimensional plasma temperature determination of axially symmetric free-burning arcs. *JOURNAL OF PHYSICS D: APPLIED PHYSICS*, 46, 2013. 45

[131] Pablo Solano Lopez. Plasmatron testing conditions characterizations. Master thesis, vki pr 2014-13, von Karman Institute For Fluid Dynamics, 2014. 45

[132] H. R. Griem. *Principles of Plasma Spectroscopy.* Cambridge University Press, isbn-9780511524578 edition, 1997. 47, 191

[133] Dr. Zuheyr Alsalihi. Personal communication, April 2015. 49

[134] Cfd++ software, metacomp technologies, www.metacomptech.com/. Online. Last Checked 26.05.2015. 51

[135] A. Turchi, J.J. Matesanz Saiz, T.E. Magin, and O. Chazot. On the flight extrapolation of stagnation-point ablative material plasma wind tunnel tests. In *Proceedings of 8th European Symposium on Aerothermodynamics for Space Vehicles*, Lisbon, Portugal, March 2015. 52

[136] A. Munafo. *Multi-Scale Models and Computational Methods for Aerothermodynamics.* PhD thesis, Ecole Centrale Paris and von Karman Institute for Fluid Dynamics, 2014. 53

[137] L. Landau and E. Lifchitz. *Physique Theorique tome 6: mecanique des fluides.* Chapter 1, ISBN : 5-03-000197-2. Editions MIR, Moscow, Russia, 1989. 56

[138] O. Chazot, R. Regnier, and A. Garcia Munoz. Simulation methodology in plasmatron facility and hypersonic wind tunnels. In *12th International Conference on Method of Aerophysical Research*, Akademgorodok, Novosibirsk, Russia, June 28 - July 4 2004. 58

[139] L. Yee, H.E. Bailey, and H.T. Woodward. Ballistic range measurements of stagnation-point heat transfer in air and in carbon dioxide at velocities up to 18000 feet per second. Technical Report TN D-777, NASA, 1961. 58

[140] G. Zuppardi and A. Esposito. Recasting the fay-riddell formulae for computing the stagnation point heat flux. *Proc. Instn. Mech. Engrs.*, 214(Part G, TN):115–120, 2000. 58

[141] P. Sagnier and J-L. Verant. Flow characterization in the onera f4 high-enthalpy wind tunnel. *AIAA Journal*, 36(4):522–531, April 1998. 58

[142] F. De Fillipis and M. Serpico. Air high enthalpy stagnation point heat flux calculation. Technical Report TN 96-014, CIRA, January 1996. 58

[143] Dean A. Kontinos and Michael J. Wright. Introduction: Atmospheric entry of the stardust sample return capsule. *Journal of Spacecraft and Rockets*, 47(5):705–707, 2010. 78

[144] Milad Mahzari, Robert D. Braun, Todd R. White, and Deepak Bose. Preliminary analysis of the mars science laboratory's entry aerothermodynamic environment and thermal protection system performance. In *51st AIAA Aerospace Sciences Meeting including the New Horizons Forum and Aerospace Exposition, Grapevine, Texas*, volume AIAA 2013-0185, 7-10 January 2013. 78, 98, 118

[145] Gregory Pinaud and A.J. van Eekelen. Thermo-chemical and mechanical coupled analysis of swelling charring and ablative materials for re-entry application. In *5th Ablation Workshop*, Lexington, Kentucky, Feb. 28th – Mar. 1st 2012. 78, 79, 120

[146] Daniele Bianchi. *Modeling of ablation phenomena in space applications.* PhD thesis, Universita degli Studi di Roma "La Sapienza", 2007. 82, 83

[147] Amorim cork composites, www.amorimcorkcomposites.com. Online. Last Checked August 2015. 78

[148] E. Smith, B. Lamb, R. Beck, and E. Fretter. Thermal/ablation model of low density cork phenolic for the titan iv stage i engine thermal protection system. In *AIAA 27th Thermophysics Conference*, number AIAA 92-2905, 1992. 89, 101, 102, 103

[149] F.S. Milos and Y.K. Chen. Ablation and thermal response property model validation for phenolic impregnated carbon ablator. In *47th*

AIAA Aerospace Sciences Meeting Including The New Horizons Forum and Aerospace Exposition, Orlando, Florida, volume AIAA 2009-262, 5 - 8 January 2009. 98

[150] T. Kruse and P. Roth. Kinetics of c2 reactions during high-temperature pyrolysis of acetylene. *J. Phys. Chem.*, 101:2138–2146, 1997. 105

[151] B. Helber, A. Turchi, O. Chazot, T. E. Magin, and A. Hubin. Gas/surface interaction study of low-density ablators in sub- and supersonic plasmas. In *11th AIAA/ASME Joint Thermophysics and Heat Transfer Conference*, Atlanta, GA, USA, 16-20 June 2014. AIAA Aviation. 97, 110

[152] J. W. Metzger, M. J. Engel, and N. S. Diaconis. Oxidation and sublimation of graphite in simulated re-entry environments. *AIAA Journal*, 5(3):451–460, 1967. 103, 104

[153] JR Wertz and WJ Larson. *Space Mission Analysis and Design.* Microcosm Press, 1999. 124

[154] K.B Gamble and E.G. Lightsey. Cubesat mission design software tool for risk estimating relationships. *Acta Astronautica*, 102:226–240, 2014. 126

[155] K.M. Brumbaugh Gamble. *A Software Tool Suite for Small Satellite Risk Management.* PhD thesis, University of Texas at Austin, May 2015. 126

[156] Seebeck coefficients of thermocouples, aviatechno.free.fr/thermo/thermo04.php. Online. Last Checked 26.05.2015. 135

[157] Isa Eray Akyol. Design of data acquisition subsystem of qarman payloads and validation in plasma facilities-hardware. Technical report, SR 2013-16, von Karman Institute for Fluid Dynamics, 2013. 135

[158] K.M. Brumbaugh and E.G. Lightsey. Application of risk management to university cubesat missions. *Journal of Small Satellites, JoSS*, 2(1):147–160, July 2013. 138

[159] K.M. Brumbaugh Gamble and E.G. Lightsey. Cubesat mission design software tool for risk estimating relationships. *Acta Astronautica,*, 102:226–240, 2014. 138

[160] Honeywell hsc pressure sensors. `http://sensing.honeywell.com`. 141

[161] M. J. Gazarik, A. Little, F. Cheatwood, M. J.Wright, J. A. Herath, E. R. Martinez, F. M. Munk, J. Novak, and H. S. Wright. Overview of the medli project. IEEE Aerospace Conference, Montana, USA, 2008. 142

[162] Michelle E. Pizzo, David E. Glass, and Kim Bey. Development of a one-dimensional, centered, finite volume computational code to solve direct and inverse heat conduction problems with time-varying temperatures and temperature dependent thermal properties. In *12th International Planetary Probe Workshop*, Cologne, Germany, June 2015. 118, 122

[163] Nist atomic spectra database, http://www.nist.gov/pml/data/asd.cfm. Last Checked: 25.05.2015. 191

[164] Christophe O. Laux, Laurent Pierrot, and Richard J. Gessman. State-to-state modeling of a recombining nitrogen plasma experiment. *Journal of Chemical Physics*, 398:46–55, 2012. 193